Modelling high-speed rail induced vibrations around tunnels (jointed rock masses)

Harry Thomas Holmes

School of Earth and Environment

University of Leeds

A thesis submitted for the degree of

Doctor of Philosophy

July 2023

Intellectual Property and Publication Statements

The candidate confirms that the work submitted is his own, except where work which has formed part of jointly authored publications has been included. The contribution of the candidate and the other authors to this work has been explicitly indicated below. The candidate confirms that appropriate credit has been given within the thesis where reference has been made to the work of others.

1. **Chapter 4 –** Holmes, H.T., Paraskevopoulou, C. and DeMoraes, R. 2020. Determining the Relative Influence of Joint and Rock Properties on the Propagation of Planar Waves in Jointed Rock Masses Using Multivariate Statistical Techniques In: 54th US Rock Mechanics/Geomechanics Symposium.
2. **Chapters 5, 6, 7 –** Holmes, H., Paraskevopoulou, C., Hildyard, M., Neaupane, K. and Connolly, D.P. 2023. Jointed rock masses as metamaterials-implications for railway tunnel vibrations. Transportation Geotechnics. 41, p.101033.
3. **Chapters 4, 5, 6** – Holmes, H., Paraskevopoulou, C., Hildyard, M., Neaupane, K. and Connolly, D.P. 2023b. Numerical modelling of resonance mechanisms in jointed rocks using transfer functions. Journal of Rock Mechanics and Geotechnical Engineering. 15(5), pp.1076–1089.
4. **Chapter 5** – Holmes, H., Paraskevopoulou, C., Hildyard, M., Neaupane, K. and Connolly, D.P. 2023c. Equivalent material modelling of fractured rock mass resonance effects In: Expanding Underground-Knowledge and Passion to Make a Positive Impact on the World: Proceedings of the ITA-AITES World Tunnel Congress 2023 (WTC 2023), 12-18 May 2023, Athens, Greece., p.268.
5. **Chapter 8** – Holmes, H., Paraskevopoulou, C., Hildyard, M., Neaupane, K. and Connolly, D.P. 2023d. Effect of joint dip on the transmission of stress waves from a moving point load in a parallel jointed rock mass (in press) In: 15th ISRM Congress.

For all the papers listed above the candidate has contributed the data collection, data analysis, numerical modelling, literature search, figure creation and preparation of the manuscript. Other authors have provided support in the form of supervisors, giving advice on concepts and proofreading.

Chapter title page illustrations have been created my Graham Pilling from Army of Cats Creative Studio.

Copyright Declaration

This copy has been supplied on the understanding that it is copyright material and that no quotation from the thesis may be published without proper acknowledgement.

The right of Harry Holmes to be identified as Author of this work has been asserted by him in accordance with the Copyright, Designs and Patents Act 1988.

Copyright ©2023. The University of Leeds and Harry Holmes

Chapter illustration © Army of Cats Creative Studio 2023

Acknowledgments

This work has been funded by the Engineering and Physical Sciences Research Council (EPSRC) under the grant number EP/R513258/1. I am eternally grateful to EPSRC for the opportunity to undertake this research which the grants funding has allowed. This work was also supported by the industrial partner AECOM, who provided additional funding. I am especially indebted to Steve Hodgetts for making this happen.

I would like to thank Chrysothemis Paraskevopoulou for proposing the project, applying for the funding and generally making a friendly working environment for me. It really wouldn’t have happened without you.

My supervision team was made up of a number of no less important supervisors, including Mark Hildyard, David Connolly, Krishna Neaupane and Roberto deMoraes. Without your help and some very patient feedback my project would not have been the same. I would like to give a special mention to Mohammed Hussein who introduced me to the whole world of fun which can be had with Green’s Functions.

Thanks to my numerous friends who have provided support and listened to my ruminations about the academic world. Thanks especially to Dan, Billy, Alasdair and Jennie.

Abbreviations

1D	One Dimensional
2.5D	Two and a half Dimensional
2D	Two Dimensional
3D	Three Dimensional
BEM	Boundary Element Method
DEM	Discrete Element Method
DEM-FDM	Combined Discrete Element – Finite Difference Method
DFT	Discrete Fourier Transform
DM	Discrete representation of joints
DMA	Dynamic Mechanical Analysis
EDZ	Excavation Damage Zone
FDM	Finite Difference Method
FEM	Finite Element Method
FEM-BEM	Combined Finite Element – Boundary Element Method
HEM	Homogenous equivalent medium
LEM	Localised equivalent medium
LHEM	Locally homogenous equivalent medium
PiP	Pipe-in-Pipe Method
PML	Perfectly Matched Layers
PPV	Peak Particle Velocity
P-wave	Compressional Wave
S-wave	Shear Wave
UDEC	Universal Discrete Element Code
VdB	Velocity Decibels
VDV	Vibration Dose Value

Preface

© Army of Cats 2023

A poem, A poem, A poem for my thesis

Chapter 1

All theses need a grand depart,
So this is a convenient start.
A story four years in the making,
It has been a battle, there is no mistaking.

From trains in tunnels to vibrations in rocks,
This thesis covers a number of scientific stocks.
Written on pages, leaf over leaf,
I hope your seat is comfy, this isn't that brief.

Chapter 2

A thorough review is presented here,
Completed largely in the formative year.
Studies which have provided inspiration,
To build this work on a solid foundation.

Chapter 3

A review of anisotropic material,
A vein of work, almost arterial.
From stress and geological creation,
This provides a background for my studies fixation.

Chapter 4

One-dimensional jointed rocks,
Made of repeated joints and blocks.
Impulsive sources, they were subject,
With attempts to see any resonance effect.

Actions of springs and superposition,
Give the transmitted waveform through coalition.
Presented with formulae which are analytical,
These are, to my thesis, hyper-critical.

Chapter 5

Further models with added complexity,
Are seen as a scientific necessity.
To verify the mechanisms presence,
Encapsulates this chapter in its essence.

Chapter 6

An extra dimension is introduced,
To see if the effects can be reproduced.
Models containing a cavity,
Give this chapter a realistic gravity.

Chapter 7

A jointed rocks frequency response,
Is shown to be a metamaterial in nuance.
Matching experimental results shows validity,
Of the resonance's physical applicability.

Chapter 8

Viewing the model from the side,
A moving load is applied.

Transfer functions provide the evidence,
Of frequencies which have precedence.

Chapter 9

This concludes this projects scope,
With the findings which are kinda dope.
From a beginning with numerical models,
The outcomes finally viewed from realistic goggles.

Spring and superposition resonance occurs,
Giving the frequencies a material prefers.
These are found in various situations,
And discussed for different applications.

I hope this summary was illuminating,
A novel way of a study communicating.
I thank you for your perusal,
And I hope it has your approval.

Harry Holmes

Abstract

This research studies the role of joints within rock masses on the transmission of stress waves. The motivation for this comes from vibrations generated by high speed trains running in tunnels, excavated in jointed rock masses. This will allow industrial partners to better understand how vibrations from high speed rail can impact receptors located close to a railway line. Based on this mitigation measures can be engineered to reduce their impact in the design phase of new railway lines or buildings close to railway lines.

The combined discrete element – finite difference code in the software UDEC and the finite difference code in the software WAVE2D are used throughout this research to study jointed materials. Both software's are modelled with explicitly jointed models as well as equivalent continuum models in order to understand how their effect on the transmission of stress waves through 1D and 2D models.

In particular resonance effects in parallel jointed rocks subject to stress waves are investigated. This is undertaken using transfer functions, derived from signals generated by numerical modelling. Resonance is important for a range of engineering situations as it identifies the frequency of waves which are favourably transmitted through a material. The different numerical codes used are shown to be able to model jointed rock masses in similar ways showing two distinct resonance mechanisms, spring resonance and superposition resonance. Spring resonance implies that jointed materials oscillate like masses between springs, with joints acting as springs and blocks acting like masses. This occurs are relatively low frequency and is unrelated to the wave speed of a material. The superposition resonance shows that constructive interference can occur between reflected waves within jointed bounded blocks. This effect operates at higher frequencies that the spring resonance effects, typically allowing the two effects to be distinct within transfer functions.

Equations are developed which can accurately predict the two resonance mechanisms identified in jointed materials. Using increasingly complex models, including 2D models and moving loads, the continuity of the resonance mechanisms are proved, showing that the resonance mechanisms first identified in highly simplified 1D models are not a consequence of the modelling assumptions. This indicates that the spring resonance effect will prevail in complex rock masses under a range of geological settings. The effects of the spring resonance mechanism operating within a range of realistic jointed rock masses are appraised in the context of vibrations from railway tunnels. It is shown that vibrations generated from train

excitations are likely to be transmitted through all jointed rock masses, while sources from the track are less likely.

The similarity of the spring resonance mechanism to the resonance characteristics of periodic metamaterials is appraised. It is shown that jointed materials can operate as a band-pass or low-pass filter, depending on the number of joints within the material. Evidence is presented showing that periodic metamaterials exhibit spring resonance with results from a laboratory scale frequency sweep test on a periodic metamaterial are shown to feature high transmission zones occurring at the predicted spring resonant frequency for that material.

The outcomes of this work, especially the resonance mechanisms and associated analytical equations, can be used in industry to inform scoping studies as to the vibrations which will be preferentially transmitted from vibrational sources embedded in jointed rock masses. This is not limited to vibrations from high speed rail but it also applicable to vibrations from any manmade or natural source. With knowledge of the resonant frequencies of a rock mass, prior to operation of new vibrational source or construction of a new building which could be subject to vibrations, designs can be modified to limit the impact of such preferentially transmitted frequencies.

“Vibrate joints and blocks,
Equations for resonance
Applied to fast trains”

Contents

List of Figures

List of Tables

1. Introduction

"All theses need a grand depart,
So this is a convenient start.
A story four years in the making,
It has been a battle, there is no mistaking.

From trains in tunnels to vibrations in rocks,
This thesis covers a number of scientific stocks.
Written on pages, leaf over leaf,
I hope your seat is comfy, this isn't that brief."

© Army of Cats 2023

1.1. Problem Statement

Railways present a popular fix to many societal problems, promising to reduce congestion on roads and provide an environmentally friendly form of transport. They have even been used as a convenient vehicle for the UK government's attempts to level up the North of England with HS2, although this is rapidly becoming a less extensive construction than its initial promise (Meighan, 2022). Despite the uncertain state of high speed rail in the UK, its study is of relevance to countries across the globe. One particularly important aspect of new railway lines is the generation of ground vibrations, which can have negative impacts on people and structures near an active railway line.

This thesis investigates the transmission of vibrations through jointed rock masses, a ground material which is often neglected in such studies. The work presented considers jointed rock masses using discontinuum and equivalent continuum models. This has been undertaken with the extensive use of numerical modelling, although attempts were made to run a physical experiment to verify the findings. The findings indicate that resonance mechanisms within jointed rock masses can lead to high transmission of certain frequencies, while others are significantly reduced. The resonance mechanisms are presented in the form of explicit analytical Equations, with physical analogies given to enhance their understanding.

"And now, Harry, let us step out into the night and pursue that flighty temptress, adventure." – Albus Dumbledore
(Rowling, 2005, pg. 62)

1.2. Purpose of this Research

The global drive to cut carbon emissions has created the need to develop environmentally friendly forms of transport. Moving large numbers of people or goods at the same time is recognised as a less energy intensive means of transit, than doing the same work using personal transport. Light urban railways, like the London Underground, have successfully transported people across relatively short distances and higher speed surface lines have covered significant cross-country distances since the Victorian era (Atkinson et al., 2020). The increased speed of movement of people and goods since the advent of the railway has allowed significant social and economic benefits to areas linked by these transport arteries (Wynn, 2004). The significance of railways at the time of their construction was in part due to their speed. However, as the safety, speed and reliability of personal transport, such as cars, has improved the pull of railways has waned. In the United Kingdom, this culminated in the closure of numerous railway lines in the 1960s, commonly known as the Beeching cuts after the influential report written by Dr Richard Beeching for the UK Government (Patmore, 1965). Future improvements in transport infrastructure therefore need to compete with the ease of use and cost of personal transport, while also improving on it, such as by being more environmentally friendly. Although there are numerous advantages of railway lines, they can also negatively impact communities which these lines run through. The work presented here investigates potential side effects of an increased usage of high speed rail, namely ground vibrations.

High speed rail provides a mass transport option which, assuming effective management, can have a low environmental footprint potentially fulfilling the transport needs of large numbers of people (Hanson et al., 2012). The speeds at which high speed rail operates at makes it impractical for small urban lines, with the main advantages seen when covering vast distances. In order to create a maximum return on investment it is necessary to have significant and varied draws for commuters at either end of the line, with easy to reach stations. Therefore, the most practical siting for a high speed railway station is close to the centre of an urban area, with the other end of the line in the centre of an equally significant urban area (Calder, 2023). Trains, especially those travelling at high speed, require flat and straight track alignments to allow efficient movement as well as assuring passenger comfort. Therefore, the need to penetrate already congested urban environments and to overcome topographical constraints require efficient engineering solutions. A common engineering solution to both constraints are tunnels, which this thesis will consider.

Before a tunnel is constructed, planners and designers need to answer a variety of questions about the proposed excavation, including:

- How deep should the tunnel be?
- How long should the tunnel be?
- How steep can the tunnel approach ramps be?
- Does the geology constrain the construction techniques that can be used? Does it dictate what support is appropriate?
- Should a single large bore tunnel or double twin bore tunnels be used? Should these be side by side or piggy backed?
- Will the tunnel operation or construction have impacts on buildings and residents nearby?

Despite robust planning there are some effects of tunnel excavation which cannot be eliminated. Tunnel construction can cause settlement at the ground surface as the ground surrounding the tunnel relaxes into the newly created void. This surface settlement is dependent on the depth of the tunnel, the method of construction and the properties of the ground surrounding the tunnel. A deep tunnel will have a reduced surface expression of ground relaxation around the tunnel as the ground above the tunnel will increase in volume by a process known as bulking. Changing the tunnel construction method or sequence by using short advance lengths in NATM or by using EPB Shield boring machines will reduce surface settlement, although this will not eliminate the problem. Ground conditions such as a very stiff layer of soil or rock overlying the tunnel will effectively cause a beam to be formed, reducing settlement (Brady and Brown, 2006). In high permeability ground the settlement would be expected to occur quite quickly, whereas in low permeability soils the settlement may be ongoing for some time (Craig, 2004). This can cause damage to buildings constructed close to the tunnel, which was observed with the Shanghai Metro (Shen et al., 2014). All the above stated problems are a consequence of tunnel construction, which can the thought of as a static problem. This static loading case has been well studied in literature and modelling of such scenarios is routinely carried out during the design of new tunnels and is not of concern in this thesis. This thesis considers the dynamic effects of the train running in the tunnel and how these dynamic effects could impact upon buildings and residents.

As trains run along a track the train wheel interacts with the rails, causing vibrations. These are transmitted to the track and surrounding structure, through a propagation pathway, such as soil or rock, and can reach a receptor, such as a building, which causes the receptor to vibrate (Figure 1-1). These vibrations can create ground-borne noise, where elements of a receptor vibrate which causes the displacement of air, transforming the vibrations of the structure into vibrations in the air, or noise. This typically occurs between the excitation frequencies of 16 to 250 Hz (Connolly et al., 2015). Vibrations can also cause a mechanical nuisance, whereby objects or persons upon which a vibration is incident can also vibrate. This occurs at lower frequencies of 1 to 80 Hz (Andersen and Jones, 2006). Both forms of vibration, ground-borne noise and vibration, can cause annoyance to residents. From a human perspective ground-borne noise is likely to be felt before ground-borne vibrations, as lower amplitudes of the former are required for human perception (Kurzweil, 1979). Ground-borne vibrations do not just cause a subjective degree of annoyance, they can also cause sensitive scientific or medical equipment to malfunction rendering a building unsuitable for its intended purpose, such as could be the case with recording studios or concert venues. Sporting venues could also be impacted. If a railway line is located close to a snooker hall a delicately poised ball could be caused to fall into a pocket through unseen forces, possibly affecting the outcome of a match which could have consequences for a player's future. Vibrations can also have economic consequences of a more profound and far-reaching effect than niche sporting prize money. Nuisance vibrations can affect real estate values surrounding the line, increasing the number of stake holders who have a vested interest in new railway lines (Connolly et al., 2016).

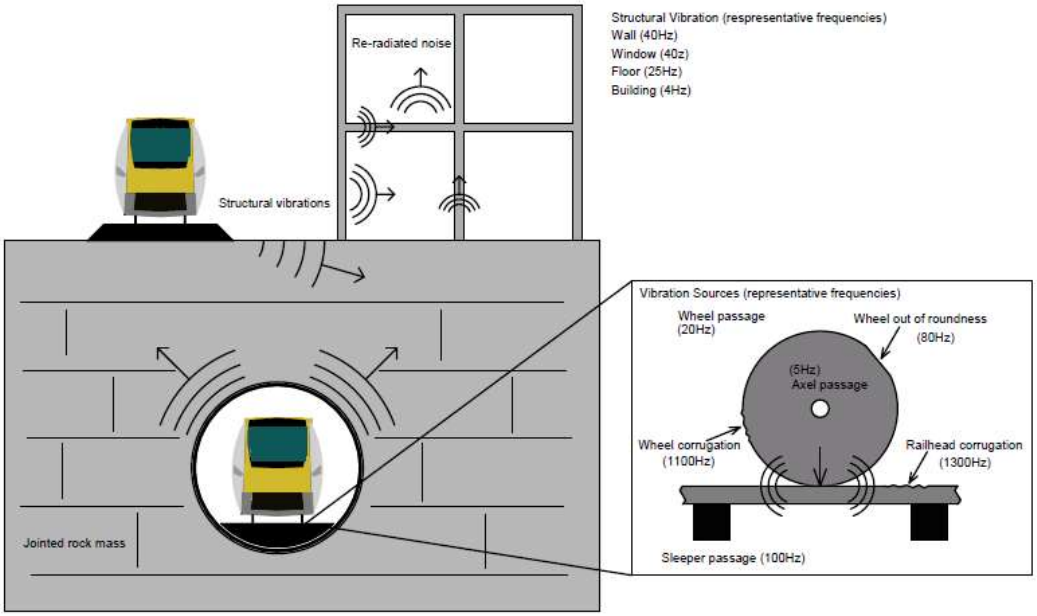

Figure 1-1 Ground borne vibration and structure borne noise from a train in a tunnel with typical resonant frequencies. From Holmes et al. (2023a) *Figure 1*

The structure which ground vibrations interact with can cause vibrations to be amplified or attenuated. Heavy structures, such as masonry buildings, or buildings on piled foundations are less sensitive to ground borne vibrations than lightweight buildings or those on slab foundations (Kurzweil, 1979). Modern construction practices, allowing wider span buildings, have been found to have an amplifying effect on ground vibrations (Connolly et al., 2015).

The vibrations induced by movement of the train along a track are a type of seismic wave. Seismic waves are usually associated with earthquakes and the term is derived from the Greek word "seien", meaning "to shake". The origin of the shaking is not confined to natural sources; therefore, the shaking can also have anthropogenic origins. The vibrations from the track transfers energy into the surrounding ground as stress waves. The designation of these vibrations as stress waves is clear when it is considered that the tunnel does not lose mass when it vibrates, indicating that only energy, or stress, is transmitted to the surroundings. These stress waves are dampened through material and geometrical damping, which logarithmically reduce the amplitude of waves with increasing distance from the source (Gupta et al., 2009). Material damping is the reduction in the amplitude of vibrations over each cycle, or wavelength, of the vibrations. Given the same distance a high frequency wave reduces in amplitude more than a low frequency wave as more cycles of the high frequency wave will occur over the same distance, due to the associated lower wavelength. Geometrical damping is where energy becomes spread out over distance. On a two dimensional (2D) flat surface, at the source of the vibration, if there is a single unit of energy, and assuming the wave is not constrained at all, the wave will spread with a circular wave front. Therefore, at 1m from the source the same unit of energy will spread over a wave front equal to 2πr, where r is the radius of the circular wave front, which is 1 m in this case. Therefore, at each point in the ground the wave front will have 1/2πr of a unit of energy. The combined effect of these damping mechanisms means that at large distances from the source the effect of ground vibrations is of no consequence, meaning that the problem of train vibrations is a function of the proximity to the source. For a three dimensional (3D) scenario the wave front spreads as the surface of a sphere, with the energy density decaying proportional to $1/r^2$.

Although this thesis will consider high speed railway vibrations, the sources of the vibrations are the same for lower speed lines. With railways being almost ubiquitous throughout the world railway vibrations are a widely known problem. In order to control them, standards have been created throughout the world which dictate what acceptable levels of vibration are for different situations. Although this does provide a useful means of determining whether vibrations are of an acceptable level, different countries use different methods for determining what threshold levels should be, which hinders cross comparison of standards. The most common assessment methods include velocity decibels (VdB) from the US, vibration dose value (VDV) from the UK, peak particle velocity (PPV) and human exposure standard from Germany (Connolly et al., 2016).

Much previous research into vibrations from railway tunnels has been conducted in soft ground tunnelling conditions, with little research into hard rock tunnelling conditions. Hard rock masses often contains joints, which equally have received little interest from rail vibration studies. Generalised studies have been conducted into how jointed rock masses affect vibrations. Despite these generalised studies, there exists a niche which studies transfer functions through rocks, which can be used to determine the relative transmission of a wide range of frequencies.

1.3. Scope of Thesis

This work attempts to study how stress waves are transmitted through jointed rock masses. Numerical modelling is used throughout the work presented here. The methods used are the finite difference method (FDM) and the combined discrete element – finite difference method (DEM-FDM). These methods have been used previously for modelling stress wave transmission through jointed materials and are considered to be of use in this study. A range of different sources are used, including planar and nonplanar sources, and moving loads.

A range of data analysis techniques are used through the thesis, although much of the analysis is undertaken using transfer functions. These decompose a time series signal into its frequency components and compare the response of a model to a reference frequency spectrum, with the difference indicated by the transfer function. These are often displayed as transmission coefficients, which show the relative difference between a recorded and reference waveform as a fraction. However, insertion losses, which are given in decibels (dB) are also used where appropriate. In terms of transmission coefficient, an unaltered signal has the value of one, with a signal of half the strength a value of 0.5 and a signal of twice the strength a value of two.

1.4. Significance

The research presented in this study is relevant not just to applications of train vibrations from tunnels excavated in jointed rock masses, but also to the wider rock engineering community. The resonance mechanisms found in this study and the analytical Equations used to predict them are easily applicable to a wide array of rock engineering problems which involve vibrations, such as machine foundations, blasting from quarrying and other forms of transport.

1.5. Aims and Objectives

This thesis aims to investigate the role which the material in a vibration sources is excited within affects the transmission of induced stress waves. The effect of the ground on stress waves can have consequences for receptors which could lead to preferential transmittance of certain frequencies. High transmittance of non-desirable frequencies could lead to unacceptable levels of vibration in buildings located nearby to a railway line. While this may not lead to structural damage it could render the building unsuitable for its intended purpose. Being able to accurately characterise the ground will allow these vibrations to be predicted at the design phase, allowing suitable and targeted mitigation measures to be installed. This will reduce the impact on receptors as well as potentially reducing the costs of such measures as the problematic frequencies will become evident.

This thesis will answer the aims, detailed above, through the following objectives:

- How does a jointed rock mass affect vibrations which are transmitted through it?
- Can joints and blocks within a rock mass cause resonances to develop?

- Can a jointed material be treated as an equivalent medium?
- Will jointed rock masses pose any particular issues for trains running through a tunnel excavated within them?

The work presented here is limited to only considering the response of the ground, specifically jointed rock masses, and does not consider the response of structures or the ground-building interaction.

1.6. Thesis Outline

The work in this thesis is split into 9 Chapters, including the introduction and conclusion Chapters. The chapters follow a logical progression adding more complexity to the modelling scenarios in each subsequent Chapter.

Chapter 1: Introduction

This Chapter presents a general overview of the motivation behind the work undertaken in this thesis. The thesis aims and objectives are outlined and the structure of the proceeding Chapters is introduced.

Chapter 2: Literature Review

This Chapter provides a general overview of train vibrations, providing context about why it is considered that vibrations from trains in jointed materials are a worthwhile niche to be explored.

Chapter 3: Anisotropic Materials

This is an additional literature review Chapter, focussing entirely on anisotropic materials, of which jointed rock masses are one. This investigates their formation and consequences for vibrations which are transmitted through them.

Chapter 4: One Dimensional Rock Masses

One dimensional (1D) models are introduced which can be used to investigate rock mass resonance. A thorough model development section is undertaken for the DEM-FDM method, analysing continuum models and investigating the effect of different setups and waveforms. Following this transfer functions are introduced and used to investigate the transmission of stress waves through a jointed material. Finally, the jointed rock mass resonance mechanisms of spring and superposition resonance are isolated and analytical functions are introduced which can be used to predict the frequency of the resonances.

Chapter 5: Verification of One Dimensional Rock Mass Resonance Effects

The analytical functions for jointed rock mass resonance are verified in this Chapter. This is achieved by breaking some of the modelling assumptions used in the previous Chapter. An FDM is introduced which is shown to perform similarly to the DEM-FDM model in Chapter 4. Equivalent material models are introduced and analysed to determine how well they perform in comparison to discretely jointed models. A physical experiment and modelling methodology to determine whether the resonances exist in reality is introduced and solved numerically to show its potential. Finally, the models used in this study are compared to the outcomes of previous studies to understand why different conclusions were reached previously.

Chapter 6: Resonance in Two Dimensional Rock Masses

The previous 1D models are extended to 2D with nonplanar waves used as the source. These are solved in a time domain FDM model. A modified approach to calculating transfer functions is introduced. Models containing unlined cavities are introduced. The jointed rock mass resonance mechanisms are shown to occur in all 2D models being analysed.

Chapter 7: Jointed Rocks as Metamaterials

Jointed rock masses are compared to periodic metamaterials. Both materials are shown to have frequency related responses, although it is determined that jointed rock masses are natural periodic materials, while metamaterials are artificial periodic materials. However, the resonance mechanisms identified in jointed rock masses are shown to occur in periodic metamaterials, with results presented from a published physical experiment. Finally, a conceptual wave barrier is introduced which employs the resonance characteristic of jointed materials to reduce vibrations.

Chapter 8: Moving Loads

Results from moving load sources within jointed materials are presented. The response of jointed materials and equivalent transversely isotropic continua are compared. The angle of joints and the plane of isotropy are varied indicating that the load direction, in relation to the dip of joints, do affect the amplitude of stress waves in jointed materials. Finally, transfer functions are generated showing that the jointed rock mass resonance mechanisms persist when a moving load source is used.

Chapter 9: Conclusions

This Chapter put the findings from this thesis into context, suggests potential areas of further research, as well as indicating the limitations in the research presented in the previous Chapters.

"I'm going to keep going until I succeed—or I die. Don't think I don't know how this might end. I've known it for years." – Harry Potter
(Rowling, 2007, pg. 568)

2 Literature Review of Underground Railway Vibrations

"A thorough review is presented here,
Completed largely in the formative year.
Studies which have provided inspiration,
To build this work on a solid foundation."

© Army of Cats 2023

2.1 The Source

"When in doubt, go to the library." – Ron Weasley
(Rowling, 1998, pg. 283)

All vibrations from train passage originate at the wheel-rail interface. There are numerous different sources of vibration, which are given in Figure 2-1 with the range of frequencies associated with them. The sources of vibration can be decomposed into quasi-static loading and dynamic excitation (Milne et al., 2017). Quasi-static vibrations are most significant for low frequency vibrations, while dynamic excitation causes higher frequency vibrations.

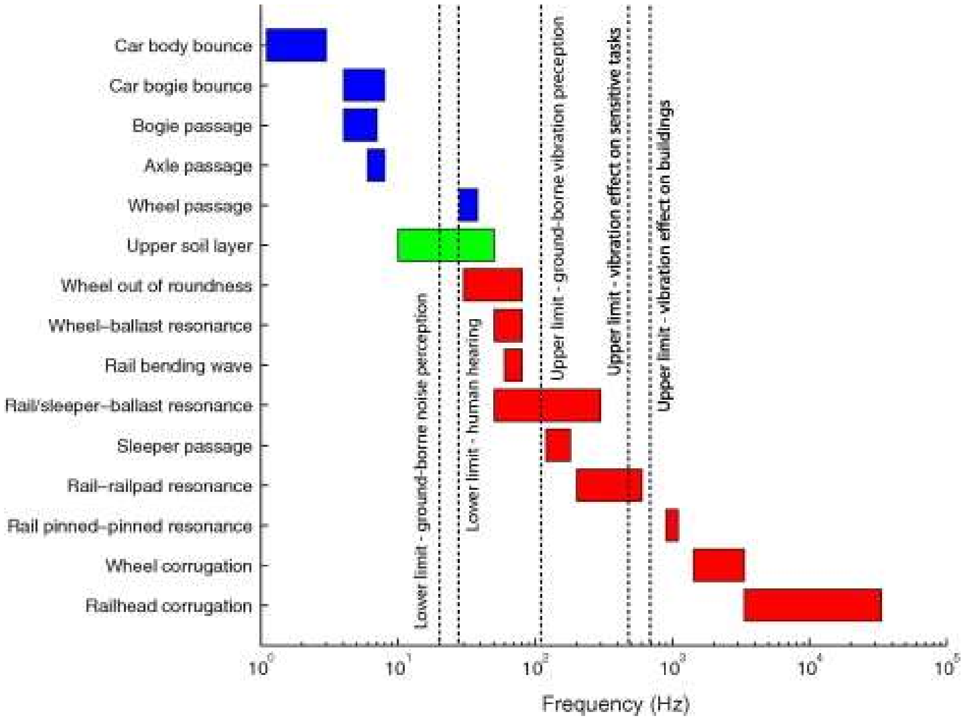

Figure 2-1: Typical frequency range of excitation from high speed rail lines. From Connolly et al. (2015) *Figure 5*

Quasi-static loading is derived from the weight of the train transferred to the track through each wheel (Milne et al., 2017). Quasi-static loading varies from zero to a maximum, underneath the train axle, and back to zero every time a wheel axle moves over a point. This gives the basic stress propagation pattern from the transit of a train and is of a constant magnitude, given by the axle weight (Chua et al., 1992). The amplitude of the quasi-static loading therefore stays constant, regardless of the speed of the train.

As the quasi-static loading is induced underneath train axles, for a point on the rail considered in the time domain, rail deflections are related to the spacing of axles and bogies on the train carriage (Milne et al., 2017). Milne et al. (2017) shows that the composition of the vehicle affects the dominant frequency of the vibration. Some trains are composed of a standard car that gives a repeated sequence of high amplitudes at regular frequencies relating to the axel spacing. Vehicles composed of different cars have a noisier vibration spectrum. The Euro-Star for example has a combination of power car, end car and articulated car, each with a different vehicle length, bogey spacing and axles spacing, giving a noisy and complex vibration spectrum.

Dynamic excitation occurs due to random imperfections such as unevenness of the rail or from impact excitation from wheel flats or joints in the rail (Gupta et al., 2009). Dynamic excitation is related to wheel and rail roughness which alters the ground reaction by virtue of the un-sprung mass of the train riding over these irregularities (Chua et al., 1992). Therefore, two trains with the same quasi-static loading of the ground will not experience the same dynamic excitation if their suspension systems differ. A train with no suspension will have its whole weight subject to excitation from a rough surface. Conversely, a train with effective suspension will reduce the affective weight experienced by dynamic excitation forces, therefore reducing the amplitude of the dynamic excitation. The poorer the state that the rail and train wheels are in, the rougher each of these surfaces is, so the effect of the dynamic excitation will increase.

> *"Poor Thomas was going faster than he had ever gone before. He was out of breath and his wheels hurt him, but he had to go on. 'I shall never be the same again,' he thought sadly. 'My wheels will be quite worn out.'" – Thomas the Tank Engine*
>
> *(Awdry, 1993, pg. 16)*

2.2 The Transmission Pathway

Figure 1-1 shows the full transmission pathway for vibrations from tunnels. Vibrations can be modified at any stage through the transmission pathway, from the source at the train-wheel interface, at the tunnel-ground interface or in the ground, to the receptor at the structure-ground interface or in the structure itself. The goal of modifications is to reduce the effect of the vibrations on the receptor. Modifications in the transmission pathway or at the receptor are called passive mitigation strategies and are typically less effective than modifications to the vibration source, known as active mitigation strategies (Connolly et al., 2016). Passive mitigation strategies include resilient couplings between the ground and structure to dampen vibrations; moving furnishing away from the centre of floors to reduce the effect of amplification from wide spans; and wave barriers in the transmission pathway (Connolly et al., 2016).

Active mitigation strategies can include: resilient wheels, which have been found to reduce vibration frequencies between 40 and 250 Hz (Kurzweil, 1979); improving the wheel or rail conditions, which can lead to reductions of 10 to 20 dB between very poor and good conditions; introducing floating slab tracks or ballast which can substantially reduce vibration levels, especially at high frequencies (Connolly et al., 2016); more effective train suspension, although this is only effective at suppressing low frequency vibrations (Gupta et al., 2009). The mitigation strategies listed do not always have the intended effect. For instance, the use of floating slab track can lead to an amplification at frequencies synonymous with the resonant frequency of the resilient fasteners in the floating slab (Hussein and Hunt, 2009).

2.3 Predicting Underground Railway Vibrations

Predicting vibrations from underground railways is an issue in the construction of new lines and new buildings near existing lines. Before substantial changes are made to existing rail tracks or new tracks and structures close to tracks are constructed, it is important to investigate the potential vibration levels at sensitive locations. These are known in industry as environmental impact assessments and involve a multi-step process; including an initial scoping study, followed by more in depth analysis.

Scoping models are used to predict vibration levels across large sections of track in order to identify the areas which are likely to be affected by elevated vibration levels (Connolly et al., 2014). Scoping models typically use an empirical approach by taking observations from existing railways and using these to inform the possible vibration levels at new sites (Kurzweil, 1979). Using empirical models for engineering design is common practice, with the empirical Q system for tunnelling (Barton et al., 1981) and empirical models for deep excavations from Long (2001) and Holmes et al. (2019). In rail engineering, Hood et al. (1996) introduce an empirical model for the assessment of ground vibrations from the Channel Tunnel Rail Link (CTRL), the UK's first high speed rail line (HS1). These methods can give accurate results, although it does have severe limitations if the new setting is not the same as the original setting from which the model is developed. Due to the advent of modern computing power, it is possible to generate empirical models generated from artificial data. This is more accurately referred to as a semi-empirical approach. This approach is adopted by Connolly et al. (2014) in the development of ScopeRail. ScopeRail is a scoping model that uses a machine learning approach, adopting a neural network to analyse a large database of vibration predictions generated using a three-dimensional finite element model. It is capable of quickly predicting ground vibration levels and can more accurately predict potential problem areas, compared to previous empirical approaches.

2.4 Railway Vibration Modelling

Once initial scoping studies have been carried out, models that are more specific are generated to predict vibration levels for a site. These can be conducted either numerically or physically. Physical models induce representative vibrations on the as-built structure from which a physical transfer function for the vibration pathway can be determined. This provides a highly accurate result, although they are sometimes impractical to carry out (Connolly et al., 2016). Numerical modelling encompasses a range of computer-based modelling techniques to simulate vibrations from a tunnel, including numerical and analytical methods. Finite Element Modelling (FEM) is a numerical modelling method commonly used to study railway vibrations, allowing accurate predictions of railway vibrations. This is computationally expensive; so, techniques have been developed to reduce the computational cost of these simulations. More advanced models combine different numerical modelling techniques, such as: FEM with Boundary Element Modelling (BEM), where FEM is used for the tunnel and BEM is used for the soil (Gupta et al., 2009); and FEM with Perfectly Matched Layers (PML) (Ruiz et al., 2019). These methods reduce the computational costs of the model but still require longer run times and computing power than analytical methods, where the system performance is described using mathematical Equations. An example of the analytical method is the Pipe-in-Pipe (PiP) method, developed by Forrest & Hunt (2006a), which can generate a vibration spectrum for a circular tunnel on even a modest home computer in less than a minute. This is a significant advantage over the expensive numerical methods whose run times can be on the order of 10's of hours to days. However, there are still advantages of using FEM and combined FEM-BEM or FEM/PML models. These models can simulate a wider range of tunnel geometry or ground layering, providing accurate results in a range of complex situations.

Modern numerical modelling software allows for modelling tunnels with or without considering the out of plane dimension of the tunnel. In a static analysis it is usually reasonable to model a tunnel which is invariant in the out of plane dimension in two dimensions (2D). However, when a tunnel is subject to a moving load the 2D approach is less suitable. To investigate the differences in the dimensions used in modelling Yang et al. (2017) conduct a comparative study into 2D and two and a half dimensions (2.5D) finite / infinite element approaches to modelling long underground tunnels subject to moving train loads in an isotropic half space. A 2.5D approach is the same as a three-dimensional (3D) approach, when the tunnel is invariant or periodic in the out of plane direction, allowing for computationally efficient solutions to be used. This approach assumes that the train induced response at two locations along the tunnel are identical except for a time shift (Ba et al., 2019). A single 2D cross-section is analysed which is extrapolated into 3D using numerical techniques. These models can be used with either dry or saturated materials. For a dry model, Ba et al. (2019) find that a 2D model gives a greater soil response than a 2.5D model, unless the speed of the train is assumed to be infinite and running on a smooth track, where the two solutions converge. Therefore, the 2D approach can be considered as the limit of a 2.5D response for a train of an infinite speed. The results of any 2D analysis are therefore of limited quantitative value.

The following sections represent a review of the recent history of railway tunnel modelling as well as what can be considered the “state of the art”. The review is split into different domains of vibration prediction by the designation of the ground and the number of tunnels present in the analysis.

2.5 Modelling Vibrations in Circular Tunnels

2.5.1 Single Circular Tunnel – Full Space

Forrest & Hunt (2006a) presented a major step in the prediction of vibrations from underground railways with the development of the PiP model, a fully 3D analytical model computed in the frequency domain to study vibrations in the ground generated by the passage of trains in tunnels with a circular cross section, in an isotropic soil of infinite extent. The PiP model uses a full space so cannot accurately predict displacements at receptors on the surface, as there is no free surface present which would allow surface waves to form. The presence of the free surface is unlikely to affect the near field tunnel response allowing the model to provide information on how different configurations of tunnel support and track composition affect the propagation of waves into the ground. In the model, it was assumed that the only body forces acting on the tunnel are due to gravity, which is a reasonable assumption in the soft ground tunnelling conditions for which this model was developed. These body forces are ignored, with the force component in the governing Equations set to zero, as they are not required for the calculation of vibrations about an equilibrium position.

Forrest & Hunt (2006a) showed that radial displacements from an unbounded tunnel, assumed to be an infinitely long thin-walled cylinder, reaches a peak when standing waves can develop within the cylindrical cross section of the tunnel. Figure 2-2 a shows these peaks for an unbounded tunnel, with *n* representing the mode number of each peak. When the thin-walled tunnel is modelled inside an isotropic full space (Figure 2-2 b) the pattern shown in Figure 2-2 a for the tunnel invert is lost, instead giving a smooth line which decreases with increasing frequency. This loss of resonance is due to radiation damping of the infinite soil surrounding the tunnel. At points away from the tunnel invert, troughs in the displacement pattern are observed separated by a constant value frequency to *c/2L*, where *c* is the soil wave velocity and *L* is the distance from the tunnel invert. These represent points of interference between P and S-waves in the soil body.

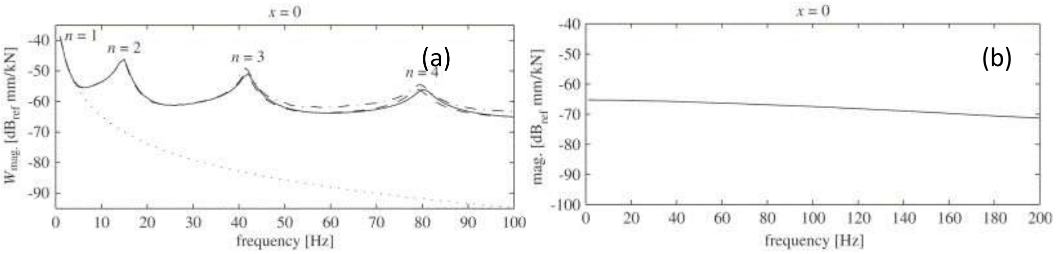

Figure 2-2: (a) Radial driving-point response (at invert) for an infinitely long, free thin-walled cylinder (radius 3.125 m and shell thickness 0.25 m). Resonant peaks are marked with mode numbers (n). – Shell theory, --- Continuum theory, -.-. FE periodic structure approach, …. free Euler beam (Forrest & Hunt (2006a), Figure 6). (b) Radial driving-point response at invert for an infinitely long thin-walled cylinder embedded in a full space (radius 3.0 m and shell thickness 0.25 m) (Forrest & Hunt (2006a), Figure 9).

Forrest & Hunt (2006b) extended the PiP model to account for a floating slab track, finding that resilient bearings do not reduce vibrations as much as simple theories predict. The softest slab bearings were found to reduce vibrations by only 6 dB and at some positions around a tunnel, floating slab tracks have been found to increase vibrations at high frequencies.

In a state of the art review into the effect of seismic loading from earthquakes Tsinidis et al. (2020) shows that earthquakes have the potential to allow residual forces to develop in tunnels, which indicates that multiple earthquakes may exacerbate such problems through time. Viewing this from the context of train vibrations, if vibrations are capable of inducing residual forces in tunnels, even if they are minor, the frequency which a train tunnel is subject to vibrations could lead to long term issues in the liner.

2.5.2 Single Circular Tunnel – Half Space

Hussein et al. (2014) presents an updated version of the PiP model which extends the previous isotropic homogenous full space approach to an isotropic multi layered half space, incorporating boundaries within the soil as well as a free surface. Despite the added complexities in the model, it was still solved using a fully analytical approach. The near field tunnel displacements are calculated for a tunnel inside a full space, as the near field response of the tunnel-soil interaction is assumed not to be affected by layer interfaces or the free surface. This technique is synonymous with the method used for the full space PiP method. Soil displacements in the multi layered half space are calculated using Green's functions using the direct stiffness method.

In order to verify the method, Hussein et al. (2014) use several different modelling cases to compare results against a FEM-BEM model. Both methods give the same predicted vibrations for an isotropic full space, while in an isotropic half space there is found to be up to +/-10dB difference in the displacement at low overburden depth and frequency, which reduces to almost unity when the overburden depth and / or the frequency increases.

Figure 2-3 shows the results for a layered half space for the FEM-BEM method and extended PiP method against the insertion gains comparing the two results. This shows that when the layer boundary is above the tunnel (at an elevation of -10 m) the two methods give comparable results; however, when the layer boundary is within the tunnel (at an elevation of -20 m) the two results show substantially different results. This second case disobeys the assumption that the tunnel response is not affected by soil layers, as that cannot be the case when the tunnel bisects a layer interface. This highlights a flaw in the method, with complex ground profiles not being suitable for the analytical PiP model. When a multi-layered half space is modelled using the extended PiP method and compared with FEM-BEM results, both give comparable ground responses (M.F.M. Hussein et al., 2014).

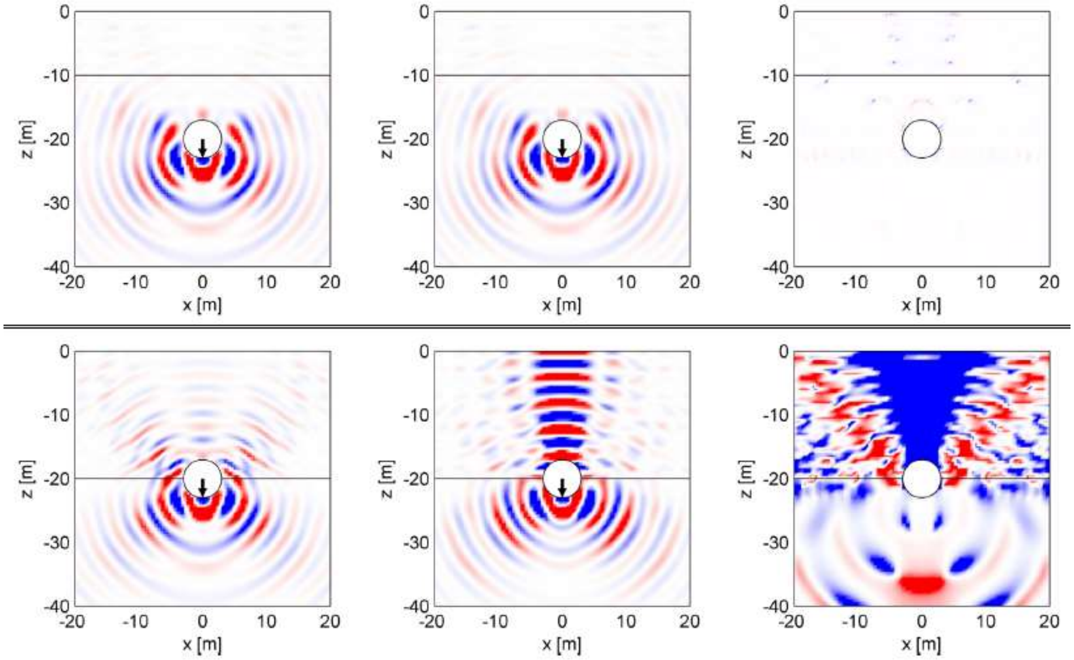

Figure 2-3: Comparison of FE-BE model (column 1) against extended PiP (column 2) and insertion gains (column 3). Red = -ve, Blue =+ve, white=0. Modified from Hussein et al. (2014) Figure 17

The soil layers modelled by Hussein et al. (2014) are horizontal; however, it is common for soil layers to be inclined following geological process. This is investigated by Jones et al. (2012) for a dry two layer system with a variable interface inclination angle and relative velocity of the two layers. It is found that these changes lead to differences in the velocity of vibrations at different locations. If the upper layer has a velocity greater than the lower layer, the amplitude of vibrations are greater at the down dip side (Figure 2-4). If the converse situation is modelled the opposite occurs. This is because the waves refract at the inclined layer interface. The response agrees with the theoretical response predicted by the law of refraction for a wave passing through two layers of different seismic velocities at a non-normal angle of incidence.

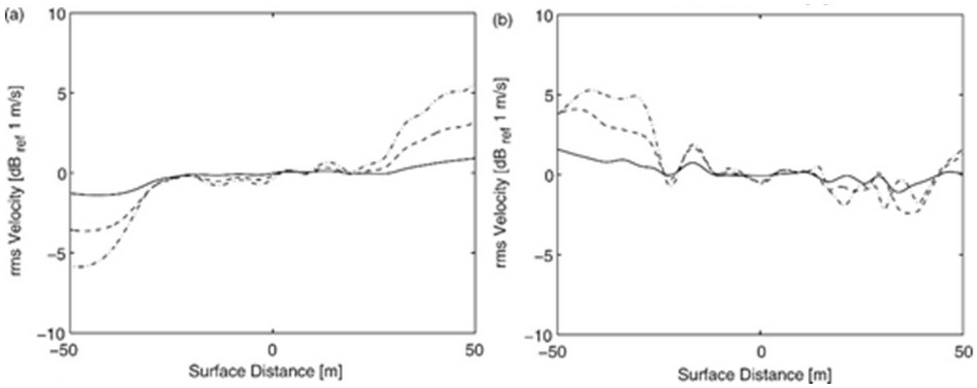

Figure 2-4: rms velocity along a surface with a 5 m layer inclined at various angles (solid line, 1^{o}; dashed line, 3^{o}; dash-dotted line, 5^{o}). (a) C-upper layer > C-lower layer, (b) C-upper layer < C-lower layer. Modified from Jones et al. (2012) Figure 15

Yuan et al. (2017) presented a semi analytical solution for vibrations due to a moving point load in a tunnel embedded in an isotropic half space. This model shows a similar accuracy to that of Hussein et al. (2014) for deep tunnels, but also gives a comparable solution to the FEM-BEM method for shallow tunnels. Therefore, this form of semi analytical method would be more suitable than that of Hussein et al. (2014) if a tunnel is within two tunnel diameters of the ground surface.

Yuan et al. (2017) determine the critical velocity for tunnels by applying different velocities to moving loads in the tunnel. It is found that the critical velocity of the ground is equal to the Rayleigh wave velocity for shallow tunnels. Critical velocity is defined as when the speed of the train is equal to the speed of the slowest seismic wave in the soil, typically the Rayleigh wave speed. When a train approaches the critical velocity the amplitudes of vibrations dramatically increase. This is because a feature, equivalent to a mach cone in front of a super-sonic plane, develops in front of the train causing a resonant effect to occur (Kece et al., 2019). This is a major problem for tracks founded on soft underlying geology, which have low Rayleigh wave velocity. Such effects have been found at Stilton Fen, United Kingdom, where even a modest train speed causes unsatisfactory vibration amplitudes (Connolly & Forde, 2015). Tunnels excavated in rocks are likely to have a wave velocity sufficiently large to effectively remove this issue, with seismic velocities of rocks often being over 1000 m/s (Bandis et al., 1983).

2.5.3 Single Circular Tunnel – Saturated Full Space

The previously described models all consider a tunnel embedded in dry soil, whereas there is likely to be water within the soil. Zeng et al. (2014) and Di et al. (2016) apply the PiP method to model a poroelastic full space. Di et al. (2016) use Biot's saturated porous medium to simulate the soil and allow for the presence of a grouted layer, a common construction technique when tunnelling in saturated ground, by adding an additional shell around the shell which represents the tunnel. It is found that neglecting pore water pressures could lead to erroneous predictions of shear and normal dynamic stresses.

In order to investigate the effect of this water on vibration transmission, Yuan et al. (2015) use a theoretical study of a tunnel buried in a 2D full space composed of saturated poroelastic soil subject to a moving point load. His allows the critical velocity and the dynamic characteristics of the system to be investigated. The model used in the study was conducted longitudinally to the tunnel, with the tunnel and track modelled as a single Euler-Bernoulli beam. The method of modelling a Euler-Bernoulli beam for a tunnel with an internal dynamic load is also adopted by Metrikine & Vrouwenvelder (2000) and Koziol et al. (2008); however, these studies only model dry cases. This method is only valid for very low frequency vibrations, as a large wavelength is required in the ground for the tunnel not to significantly interfere with the wave. This low frequency cut off is higher for smaller tunnels and stiffer ground, although it cannot capture the entire response of the system. Equally, propagation of waves out of the plane of the model are not modelled, further diverging the model results from reality. Despite this, results can be inferred with Yuan et al. (2015) finding that the critical velocity of the tunnel system studied was equal to 0.7 times the S-wave velocity of the surrounding medium. The peak response of the system is found to reduce with an increase in permeability. A higher permeability is also found to slightly lower the critical velocity of the system.

Yuan et al. (2016) used a semi-analytical method to investigate the effect of a harmonic point load in a tunnel embedded in a saturated poroelastic full space on pore pressure, displacements and stresses surrounding a tunnel. The sensitivity of these metrics were compared to different loading frequencies and soil permeability. This study extends the earlier work of Yuan et al. (2015) to 3 dimensions. A full space is adopted as surface waves are not likely to influence the near tunnel response of a deeply buried tunnel. Therefore, the results of this study are likely to only be correct for deeply buried tunnels. The tunnel is assumed to have an impermeable liner, which was fully bonded to the surrounding soil.

Figure 2-5 shows the free field response to a point load applied at tunnel invert for radial displacement, circumferential displacement, and pore pressure for a deep tunnel. All plots in Figure 2-5 show a symmetrical pattern about the tunnel centreline, as the models are symmetrical about this point.

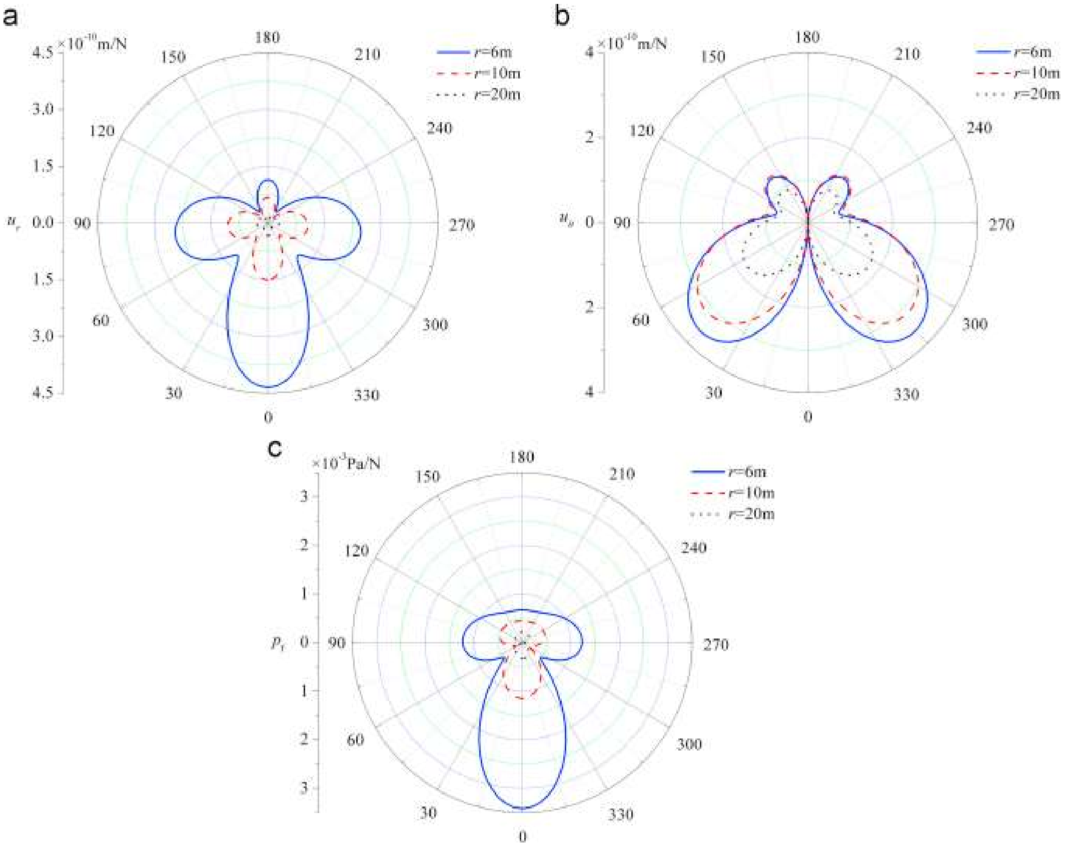

Figure 2-5: The response amplitude in the free field for a loading frequency of 10 Hz. (a) solid radial displacement; (b) solid circumferential displacement; (c) pore pressure. From Yuan et al. (2016), Figure 8.

Figure 2-6 shows how the distribution of pore pressure changes with a change in the loading frequency. At 10 Hz, shown by the left hand plot in Figure 2-6, the increase in pore pressure is in the invert and side walls, while at 80 Hz, shown by the right hand plot, the increases occur all around the tunnel, including the tunnel crown. Therefore, as the excitation frequency increases the influence of pore pressure on the tunnel lining is likely to increase.

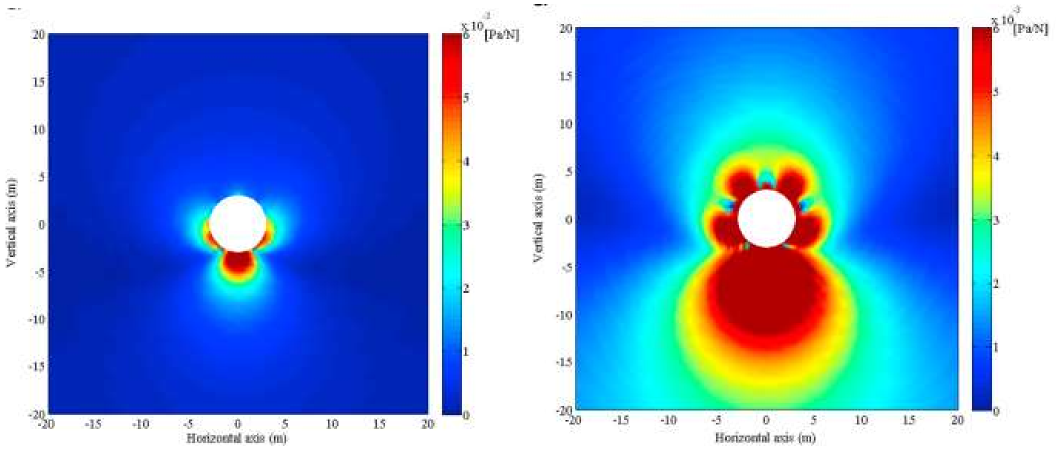

Figure 2-6: Pore Pressure surrounding the tunnel. Left hand plot loading frequency of 10 Hz. Right hand plot loading frequency of 80 Hz. Modified from Yuan et al. (2016) *Figures 12 and 13*

Radial stresses around a tunnel are also found to be affected by the loading frequency. Figure 2-7 shows the effect of a low load frequency (10 Hz) and a high load frequency (80 Hz) on radial stresses. At low frequencies, the maximum stresses radiate downwards and outwards from the tunnel invert and walls, with only a small amount of stress radiated upwards. At higher frequencies, the stresses can radiate outwards at more locations around the tunnel due to interaction between the shorter wavelength waves and the tunnel lining.

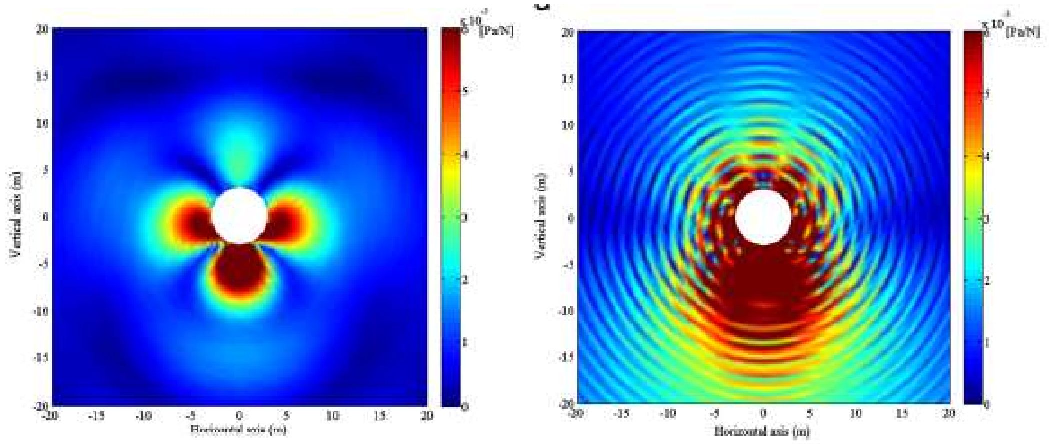

Figure 2-7: Radial stress surrounding the tunnel. Left hand plot loading frequency of 10 Hz. Right hand plot loading frequency of 80 Hz. Modified from Yuan et al. (2016) *Figures 14 and 15*

2.5.4 Single Circular Tunnel – Saturated Half Space

Zhou et al. (2017) introduced an efficient method for calculating the vibration from a poroelastic half space in 3D, by modifying the PiP method. This method considers the effect of the ground surface, so is more likely to represent a real-world scenario when the tunnel is not deeply buried, compared to Yuan et al. (2016) who considered a full space. Similar to other approaches, the tunnel / soil interaction is modelled in an initial step by assuming that the near field response of the soil is not affected by the free surface.

Zhou et al. (2017) found that surface displacements are greatest at low excitation frequencies but reduce as the frequency increases (Figure 2-8). The reduction occurs in an undulating fashion with peaks and troughs at regular intervals related to the interference between P and S-waves. The permeability of the soil changes the spacing of these peaks and troughs by changing the P-wave speed, with the S-wave speed being largely unaffected by increased permeability, and therefore water content. A highly permeable soil will have closer spaced peaks than a less permeable soil, as this is manifested as a slower P-wave velocity. The reduction of the magnitude of displacement with a higher frequency is due to increased material damping. Figure 2-8 also shows that a single phase, dry, soil has a higher displacement than the two-phase saturated soils modelled. This is particularly evident at higher frequencies leading to over prediction of surface displacements if ground water is not considered.

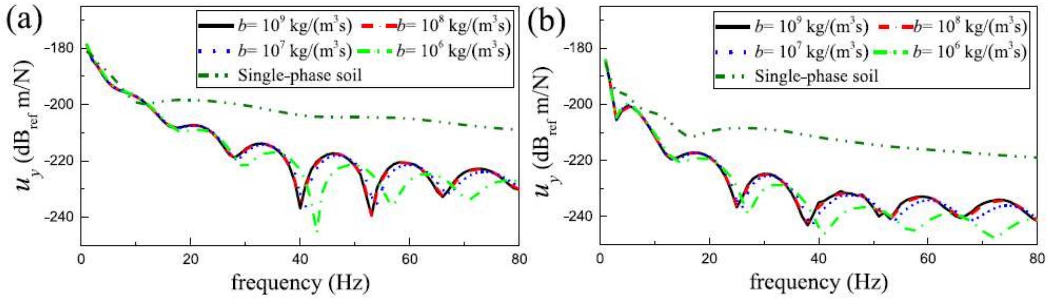

Figure 2-8: Displacement magnitude of soil surface above a tunnel at 10 m depth. (a) 0 m offset; (b) 20 m offset. From Zhou et al. (2017) *Figure 6*

Yuan et al. (2018) develop a model for vibrations from a tunnel within a layered half space using a semi-analytical solution under the influence of hydraulic boundary conditions at scattering surfaces. The layering of the model comes from a variable thickness dry soil layer on top of a saturated poroelastic half space, which also allows for a moving ground water table. This situation of having a moving ground water table can give uncertainties in vibrations of up to 20dB.

Yuan et al. (2018) investigate the influence of different boundary conditions at the fluid boundaries in a model; the tunnel-soil boundary and the soil-soil boundary between the saturated soil and dry soil. When encountered in a real soil body, neither of these boundaries are fully permeable or fully impermeable, but both end member cases have been studied to determine the effect that these common modelling assumptions have on vibration levels and therefore modelling uncertainty. It is found that a fully impermeable soil-soil boundary gives 20 dB greater vibrations than a fully permeable boundary. Regarding the tunnel-soil boundary, at low frequencies the response of both boundary types is the same with differences found at frequencies over approximately 40 Hz. At this frequency, the impermeable boundary shows vibrations approximately 5 dB greater than the permeable boundary. However, the effect of the boundaries depends on the orientation of the displacement being measured, with a greater effect for vertical and longitudinal displacement than transverse displacement. Interference was present in the frequency-displacement domain but occurring at different frequencies depending on the boundary type, indicating that some degree of phase change occurs due to the different hydraulic boundary conditions.

The tunnel-soil boundary is found to cause changes in pore pressure, with a sealed boundary giving greater pore pressures at frequencies higher than 20 Hz (Yuan et al., 2018). Below this frequency, the wavelength is too large to be affected by the tunnel.

Yuan et al. (2018) found that changing the depth to the water table changes the response of the ground to vibrations in the transverse and vertical directions. It is found that a deeper ground water level causes greater soil displacement in both directions studied. The interference pattern also alters, increasing the lateral distance between the maximum points of interference. However, the displacement in the far field is not affected by the ground water level. The difference between fully saturated ground and dry ground is found to be up to 20 dB (Yuan et al., 2018).

2.6 Modelling Vibrations in Twin Circular Tunnels

The effect of a neighbouring tunnel is often neglected in vibration prediction studies. Twin tunnels are common in urban environments, allowing separate bores for inbound and outbound trains. Twin tunnels can be studied in both a static setting and dynamic setting with incident seismic waves; however, the interaction between internally dynamically loaded twin tunnels typically receives less attention. Sheng et al. (2005) use a wavenumber FEM-BEM model to compare surface vibrations of a single double-track tunnel and a pair of single-track tunnels. It is found that the single double-track tunnel produces greater surface vibration levels than twin single track tunnels.

2.6.1 Twin Circular Tunnels – Full Space

Kuo et al. (2011) assess the effect of a twin tunnel on the propagation of ground borne noise form railway tunnels embedded in a homogenous elastic full space. It is assumed that there is a dynamic load in only one tunnel at a time. This model adopts the techniques applied in the

Pipe-in-Pipe model, developed by Forrest & Hunt (2006a), for a twin tunnel model and therefore represents a fully 3D analytical model, therefore being a more efficient method than that employed by Sheng et al. (2005). The vibrations response of the two-cavity system is calculated from the super position of two single cavity displacement fields (Figure 2-9).

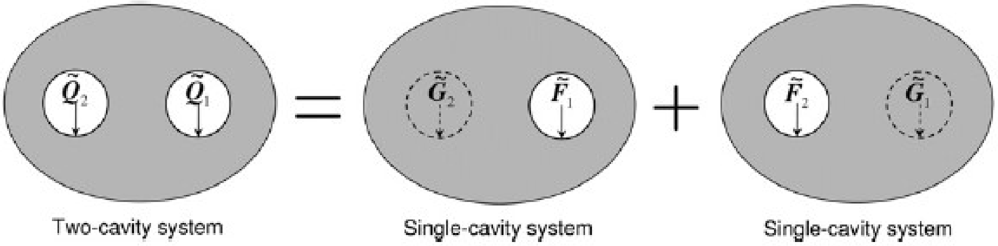

Figure 2-9: Tractions (Q_1 and Q_2) are the sum of two single cavity systems with traction vectors acting on a single cavity (F_1 F_2) and the traction vectors induced by the neighbouring cavity (G_1 G_2). From Kuo et al. (2011) *Figure 5*

Kuo et al. (2011) investigate the effect of tunnel position and support thickness in twin tunnels. The effects of each of these are found to be frequency dependent, with higher frequencies interacting more with the secondary tunnel due to a shorter wavelength, when compared to low frequency waves. Both increases and decreases in vibration amplitude are observed, depending on the location of the measurement point. Greatest increases are found on the free field side of the second tunnel.

He et al. (2018) developed an innovative approach to modelling a 3D full space containing twin tunnels by splitting the full space along a vertical line between the two tunnels creating two half spaces. With each half space therefore containing a single tunnel. Wave transformations were used to satisfy the boundary conditions between the half space and the tunnel. It was found that if the separation between neighbouring tunnels is less than three times the tunnel diameter the interaction between the tunnels can cause insertion gains on the order of 20 dB at the ground surface with a greater difference observed at higher frequencies, supporting the conclusions of earlier work.

2.6.2 Twin Circular Tunnels – Half Space

Hamad et al. (2015) investigate the dynamic interaction of twin tunnels in a homogenous half space using two different models: a fully coupled model where two cavities are modelled in the half space and a superposition model where two single tunnel models are superimposed giving the ground response of a twin tunnel model. The composition of both models is otherwise the same, with the tunnel modelled using the cylindrical thin shell theory and the half space soil simulated using the boundary element method. The model is assumed to be invariant in the out of plane direction allowing a 2.5D approach to be adopted. Insertion gains of up to +/-10 dB in the transverse direction, +/-20 dB in the longitudinal direction and +/- 10 dB in the vertical direction could be found when a second tunnel is modelled. Additionally, it is shown that the more computationally efficient superposition method gives comparable results to the fully coupled method, with negligible errors of less than 0.5 dB, suggesting that the analytical method of Kuo et al. (2011) also gives a high degree of accuracy.

He et al. (2019) improve on previous work by developing a 2.5D semi-analytical twin tunnel model with a multi layered half space (Figure 2-10). An entirely new modelling approach is needed from He et al. (2018) as the coupled half spaces used previously will not allow for internal layering or a free surface. The second tunnel, layer boundaries and free surface created in this model provide multiple scattering surfaces giving significant difference in ground vibrations, when compared to a single tunnel model. The solution for the dynamic interaction between twin tunnels is obtained by means of the compatibility of displacements and equilibrium of stresses at the tunnel-soil interfaces.

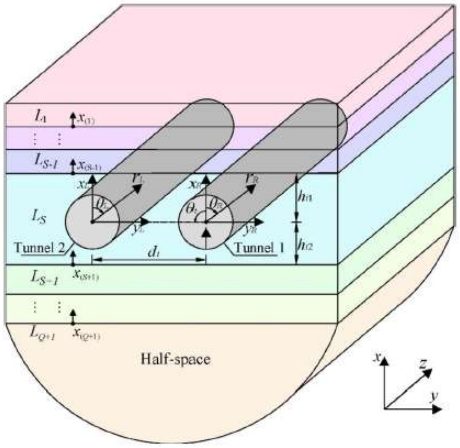

Figure 2-10: Model of a multi-layered half space with twin tunnels embedded in a single isotropic layer. From He et al. (2019) *Figure 1*

He et al. (2019) investigate the scenarios where a single tunnel contains a dynamic source, like previous studies, as well as the scenario where both tunnels contain a dynamic source. The results for the single tunnel case are similar to those of other researchers, with increased surface displacements being observed on the free field side of the second tunnel with these displacements also being frequency dependent. When a train is running in the second tunnel it is found that surface displacements reduce on the free field side of the second tunnel, although there are greater displacements between the twin tunnels (Figure 2-11).

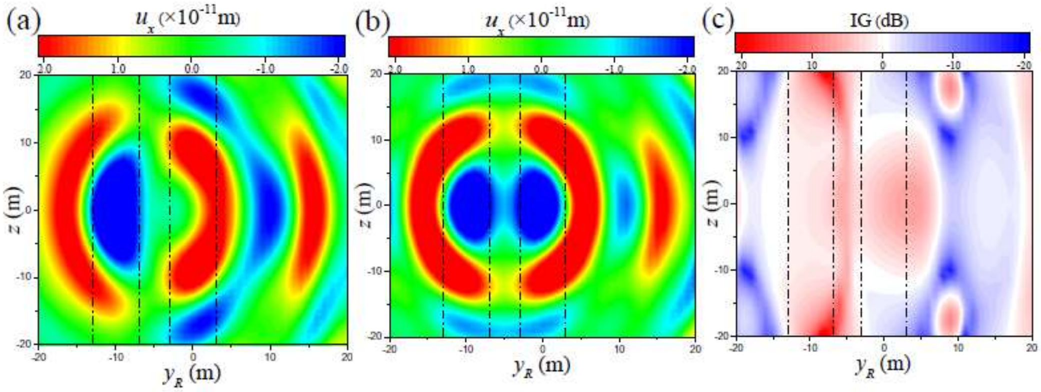

Figure 2-11: Vertical displacements on the ground surface by (a) line load applied to right hand tunnel, (b) line loads applied to both tunnels, (c) Insertion Gains comparing a and b. From He et al. (2019) *Figure 11*

He et al. (2019) find that the stiffness of the soil layers effects the surface displacements from dynamic loading of the tunnels. This is investigated using a three-layer model, where the tunnels are embedded wholly in the central layer. The stiffness of the soil above and surrounding the tunnel has a significant impact on the dynamic interaction of the twin tunnels, while the soil below the tunnel has a minor impact on the dynamic interaction.

Yuan, Boström, Cai, et al. (2019a) present a solution for calculating the effect of a neighbouring tunnel on vibrations using an analytical approach. The solution uses a novel way of accounting for the multiple scattering effects of the two tunnels, in an otherwise simple model of elastic hollow cylinders within a full space with two cavities. Although it is less advanced geometrically than the multi-layered approach used by He et al. (2019) it should be more computationally efficient for modelling similar situations. The method of Yuan, Boström, Cai, et al. (2019a) also allows for arbitrary angles between the two tunnels. It is found that the separation angle has little effect on the vertical displacement of the dynamically loaded tunnel invert but can induce large differences at locations away from this. Results for piggy-backed tunnels are given using the PiP method by Clot et al. (2016), although this study does not give results for arbitrary angles and is modelled as a full space. The results for side-by-side tunnels from Yuan, Boström, Cai, et al. (2019a) are contemporary with the previously described research, finding that the location of measurement and the excitation frequency dictate the differences between a single tunnel model and a twin tunnel model.

2.6.3 Twin Circular Tunnels – Saturated

Yuan, Boström, Cai, et al. (2019b) develop an analytical wave function method for calculating vibrations from two tunnels embedded in a saturated poroelastic full space. The wave field in the full space was assessed using the principles of superposition. Due to the presence of water in the model it is necessary to adopt hydraulic boundary conditions for the tunnel-soil interface, where an impermeable boundary is assumed. It is found that the soil permeability has no effect on the tunnel inverts vertical displacement; however, an increase in the permeability and excitation frequency causes a decrease in displacement magnitudes for transverse movement. Directly above the tunnels in the model it is found that an increase in soil permeability leads to a decrease in displacement, both vertically and transversely, at high frequencies. Pore pressure is found to increase at the tunnel invert in low permeability soils with a low excitation frequency, while only high excitation frequencies cause a difference in pore pressure for different permeabilities at points further away from the tunnel.

Yuan, Boström, & Cai (2019) extend the work of Yuan, Boström, Cai, et al. (2019b) by developing a semi-analytical solution for twin tunnels embedded in a saturated poroelastic half space. It is found that the half space model predicted up to 20dB greater displacements than the full space model, when measured at the same equivalent ground surface elevation.

2.7 Modelling Jointing and Discontinuities

Tunnels are not only excavated through materials that can be considered as a continuum. Tunnels excavated through rocks will be affected by the presence of joints in the rock mass. Such situations are studied by Eitzenberger (2012) and Eitzenberger et al. (2011) who use the coupled discrete element-finite difference method in the Universal Discrete Element Code (UDEC) to assess how joints in a rock mass affect transmission in 2D models solved in the time-domain. Eitzenberger et al. (2011) models a square, unsupported tunnel to determine the effect of a changing overburden and the presence and properties of single horizontal discontinuities on the peak particle velocity (PPV) at a horizontal free surface. It is found that as the overburden increases the PPV reduces, with the maximum vertical PPV found directly above the tunnel and maximum horizontal PPV at two to three tunnel widths from the centre of the tunnel. When a joint is modelled above the tunnel floor the PPV at the free surface decreases, while if the joint is modelled below the tunnel floor the PPV increases. It is also found that when a joints stiffness is high, vibrations from the tunnel are not affected by the presence of the joint, while low stiffness joints exacerbate the effects found when the joint location is changed. Eitzenberger (2012) built upon this work by modelling further cases to assess the effect of tunnels. Using a horseshoe shaped tunnel with a flat invert, the effects of the discontinuity position, dip angle, joint spacing and the number of sets of discontinuities are assessed. It is found that inclined joints give local maxima and minima in different places to horizontal joints, with energy transmitted along intact blocks. It is also found that when the joint spacing is small (5m) the model performs equivalently to an isotropic continuum model.

When two sets of dipping discontinuities, which run perpendicular to one another, are modelled it is found that the model performs similarly to the isotropic continuum as well. This is taken as meaning that as the joint spacing decreases or the number of joint sets increases the model will behave more like a continuum. A final model assesses how the effect of large, disturbed zones, like faults, and weakened surface zones, like a weathered rock mass, affect PPV at a free surface. It is found that when a faulted zone is modelled energy can become trapped in this zone, increasing the PPV where the zone daylights the surface. When a weakened horizontal layer is modelled, a low material stiffness and a high thickness increases the PPV at the free surface. In Eitzenberger (2012) and Eitzenberger et al. (2011) the tunnel is dynamically loaded using a velocity history comprising of a sine wave of a single frequency. The frequency modelled is 100 Hz in Eitzenberger et al. (2011) and 125Hz in Eitzenberger (2012). These cannot be considered as realistic train loading, so the study does lose some relevance to the field from this. However, as a first of its kind analysis of the dynamic interaction of train tunnels in jointed rock masses it does have some scientific merit. Avci et al. (2020) also study vibrations from trains in tunnels embedded in rock using a 2D plane strain finite element model. This study only considers the rock to be a very stiff continuum rather than a discontinuum, and arguably could be considered to not capture the inherent heterogeneity of a realistic rock mass. Other more generalised studies of vibrations in jointed rock masses are conducted by Pyrak-Nolte et al. (1990), Cai & Zhao (2000) and Zhao et al. (2006), among others. These studies are conducted using physical and numerical models, with generalised analytical Equations derived for a range of situations. There is considerable scope to study the role of joints and realistic rock masses in vibrations from train tunnels, building on the early work which is highlighted above. A more detailed overview of stress wave transmission through jointed rock masses is given in Chapter 3.

2.8 Further Influences on Tunnel Vibrations

The single tunnel studies already discussed cover a wide range of cases including full spaces, half spaces and saturated ground. However, there are numerous different scenarios possible in tunnelling which can influence ground vibrations.

Jones & Hunt (2011) include the presence of voids at the tunnel-soil interface. Other models discussed assume a perfectly bonded tunnel-soil interface; however, in reality this is seldom the case. A semi-analytical model is used which is based upon the PiP method. Voids are incorporated by uncoupling nodes along the tunnel-soil interface, which itself is within a fully 3D isotropic full space. This approach is to determine how voids affect transmission of energy into the soil, so modelling a full space is an appropriate simplification. The effect of the void is related to the size of the void and the excitation frequency, which gives different wavelengths. When a void has a comparable size to that of the wavelength of an incident wave, the void affects transmission, while if the void is considerably smaller than the wavelength there is negligible effect. Examples given in this study are that a 2 m long void will not affect a 25 m wavelength wave while it will affect a 13 m wavelength wave. Therefore, higher excitation frequencies tend to be affected more by voids with uncertainties of up to +/-5 dB in the near field (i.e. directly surrounding the tunnel). The changes in vibration levels are brought about by transmission of vibrations being supressed around a void, with energy concentrated outside of this, giving minimum areas of transmission in the void and maximum areas of transmission outside of the void.

Another hitherto unconsidered cause of possible error in ground vibration predictions from single underground railways is the effect of the excavation damage zone. During tunnel excavation the ground surrounding the tunnel relaxes, causing large strains to develop in the soil which reduces the strength of the remaining material. This is a well-known phenomenon in tunnelling and is referred to as the excavation damage zone (EDZ) (Brady and Brown, 2006). Ruiz et al. (2019) includes the effects of an EDZ in a railway vibration model by modelling the tunnel in two connected pieces of software. Initially the commercial FEM software Plaxis is used to model the reduction in stiffness due to the tunnel excavation. From this, the reduced ground stiffness is output and input as the ground stiffness in a railway vibration model. The railway vibration model is run with both disturbed and undisturbed parameters in order to assess the effect a disturbed zone had on the transmission of vibrations from the tunnel. It is found that the disturbance increases the transmission of high frequency waves directly above the tunnel, but with minor change at low frequencies. Troughs in the transfer function caused by interference of P and S-waves are moved to lower frequencies as the disturbance increases. The changes in vibration amplitude and the movement of the interference pattern in transfer functions reduce as the lateral distance increases. This is because at large lateral distances the transfer function is dictated by the original soil properties, while at small distances much of the ground in the wave transmission pathway is disturbed, so the disturbed properties dictate the response of the transfer function.

The previously described case studies only consider tunnels of a circular cross section. While this may be the case for bored tunnels, it is less likely to be an efficient construction profile for tunnels constructed using other approaches. The need to drive machinery into a tunnel will necessitate a flat invert in these situations, giving rise to other shapes such as horseshoes. Gupta et al. (2009) investigates this with the use of a coupled FEM-BEM model with tunnels of a circular, horseshoe and square cross section of equivalent area. It is found that the tunnel shape does not have a large effect on the vibrations of the ground in the far field, provided an equivalent circular cross section is modelled, as shown by Figure 2-12. However, close to the tunnel the geometry of the tunnel should be considered, as a square tunnel behaves differently to a circular / ovoid tunnel in this area.

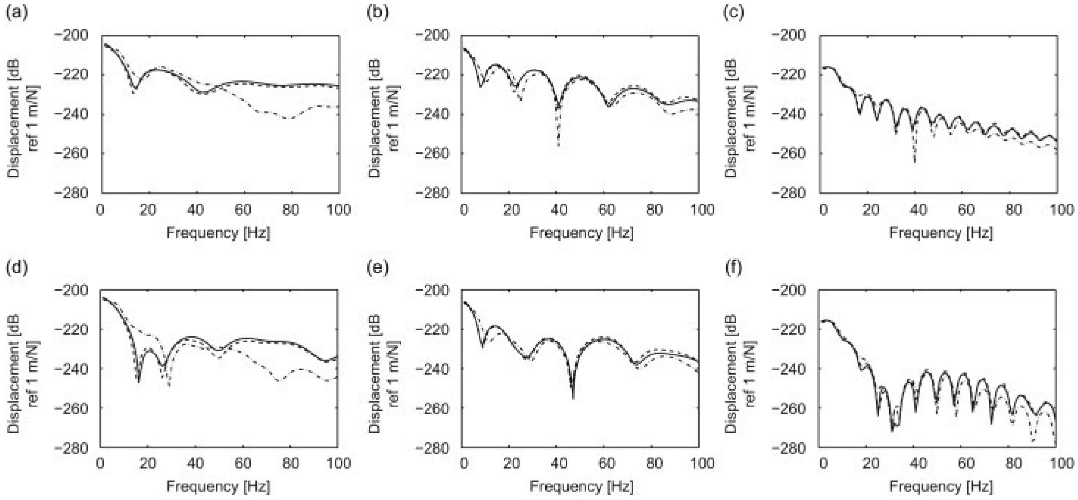

Figure 2-12: Effect of different tunnel shapes of an equivalent size at points in the free field. A) free surface, 0 m offset; b) free surface, 16 m offset; c) free surface, 64 m offset; d) 4 m below free surface, 0 m offset; e) 4 m below free surface, 16 m offset; f) 4 m below free surface, 64 m offset. Free surface 24 m above tunnel invert. Circular tunnel has a radius of 4.56 m and a 0.7 m thick liner. Circular tunnel (solid line), ovoid tunnel (dashed line), square tunnel (dash-dotted line). From Gupta et al. (2009) *Figure 31*

2.9 Tunnel Vibrations in Anisotropic Conditions

There has been a small body of research which tries to examine the effect of anisotropic ground conditions on railway vibrations, most of which has been conducted in soft ground conditions (Rieckh et al., 2012; Ai and Ren, 2016; Gao et al., 2018; Ba et al., 2019). Anisotropy in the ground is an aspect of the seismic response of tunnels which Tsinidis et al. (2020) identified as being an unexplored. This study does not concern vibrations from within the tunnel, such as trains, but looks into the effect of earthquakes and other external seismic loadings. Despite this difference in scenario, the same factors are likely to be important in the response of tunnels regardless of the source of the vibration.

Rieckh et al. (2012) presents a study of vibrations from an underground railway in a layered anisotropic half space using a 3D BEM model. The model contains a transversely isotropic layer using the boundary element method in 3D. The model is set up with three layers, two of which are isotropic and the upper layer being transversely isotropic, which is directly below the free surface. The tunnel is embedded in all layers, with the invert and tunnel walls in the isotropic layers and the crown in the transversely isotropic layer. The results for this show that on the ground surface directly above the tunnel an increase in the E_h:E_v ratio increases displacement, while at a lateral offset of 5m the opposite is true. The results are not discussed in any depth and no mechanisms are proposed for the observed effects. Studies considering truly anisotropic ground conditions, where the entire model is anisotropic, are limited to embankment lines and have studied both dry (Lu et al., 2006) and saturated mediums (Zhan et al., 2014; Gao et al., 2018) as well as multi layered ground (Ba et al., 2019).

Gao et al. (2018) investigates the effects of saturated anisotropic material properties on ground vibrations and excess pore pressure, excited by a moving train load on an embankment. This is not in a tunnel, so the quantitative results are unlikely to be directly applicable to the subject of this thesis; however, the qualitative results will highlight possible effects from underground tunnels due to soil anisotropy. The soil in this study is modelled as transversely isotropic with anisotropic ratio's (E_h:E_v) of between 0.7 and 1.15. It is found that there is an increase in the peak vertical displacement of up to 1.5mm when the E_h:E_v ratio increases from minimum to maximum across the studied range. This displacement effect is thought to be caused by the increase in E_h having a confining effect on the soil body. Excess pore pressure is found to increase below the track, when E_h:E_v increased from 0.7 to 1.15.

Ba et al. (2019) studies an embankment railway on a multi layered transversely isotropic half space using an efficient semi-analytical approach adopting Green's functions to model wave propagation in the soil. This study models E_h:E_v ratios of between 0.5 and 2.0. Similar to Gao et al. (2018), it is found that the E_h:E_v ratio causes the vertical displacement of a point near a railway track to increase when $E_h > E_v$ and to reduce when $E_h < E_v$ (Figure 2-13). The distance to the measurement point, shown by x/B in Figure 2-13, and the load speed, shown by c*, affect the vertical displacement response for different values of E_h:E_v. These studies show that an anisotropic material has a significant impact on ground vibrations from moving train loads, so the same is likely to be true for trains running in tunnels.

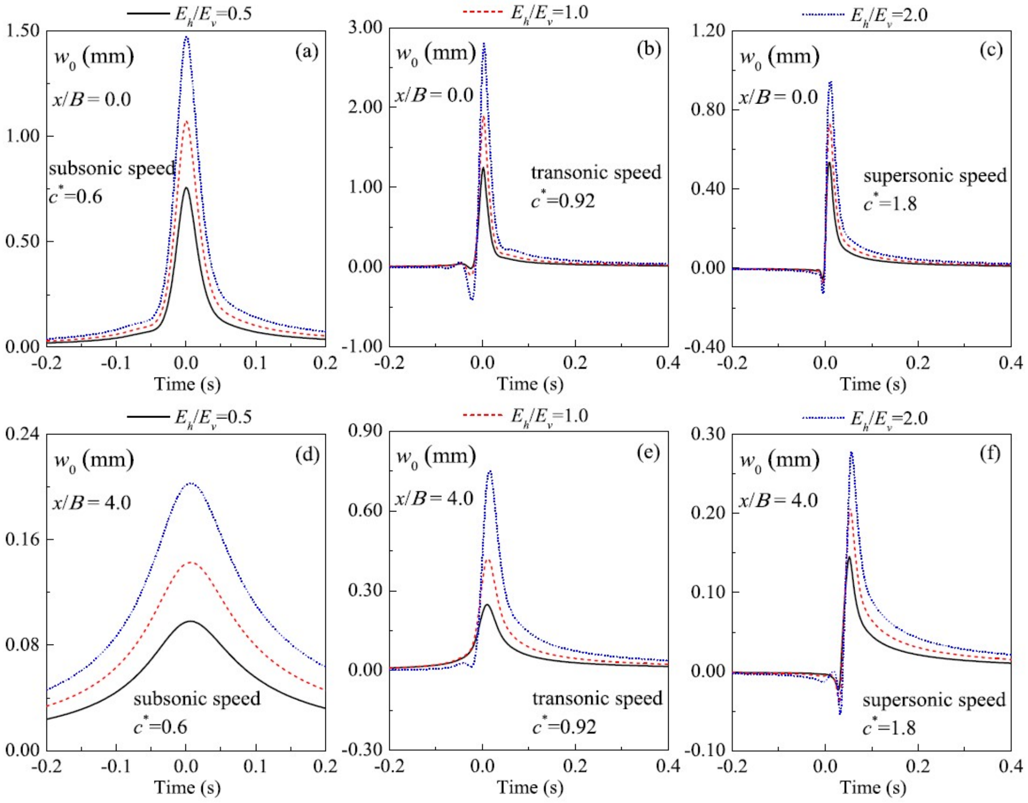

Figure 2-13: Effect of changing the TI (Transversely Isotropic) ratio on ground vertical displacement response for a homogenous transversely isotropic material. w_0 = vertical displacement of measurement point. From Ba et al. (2019) *Figure 4*

Additional considerations of tunnelling in anisotropic ground is the effect of strain softening during excavation. Zymnis et al. (2013) found that excavating a tunnel in transversely isotropic soil causes a greater degree of strain to develop perpendicular to the plane of isotropy. Ruiz et al. (2019) studies the effects of the excavation damage zone on future railway vibrations in an isotropic soil. Combining the approach of Ruiz et al. (2019) with an anisotropic soil model could lead to a greater degree of softening of the surrounding ground, which may amplify the effects of the excavation damage zone.

2.10 Possible Research Areas

As can be seen from the literature review and summarised in Table 2-1 (see below), there has been considerable research into tunnels in a variety of settings and ground conditions. This work is conducted solely in soils with isotropic material parameters. The above discussion also shows that anisotropic ground can cause a meaningful change in the response of the ground under excitation from a moving train load. With such little research conducted into train vibrations in anisotropic ground conditions there is a considerable scope for future research in the area.

There are many other avenues for research into tunnels in anisotropic ground conditions. These include analyses which consider:

- Full space and half space;
- Homogenous and layered;
- Wet and dry;
- Single and Double Tunnels.

Train vibrations in anisotropic ground conditions are an undeveloped vein of research. As such, there is scope to cover much of the work discussed in the literature review, which will be of scientific merit due to the new ground conditions being considered.

Jointed rock masses can have anisotropic material properties and are not extensively studied in the context of rail vibrations. This is with the exception of Eitzenberger (2012) who did studies the transmission of train vibrations through jointed materials; however, these are never considered as anisotropic materials. Therefore, there remains considerable scope to investigate train vibrations in anisotropic jointed rock masses. Jointed rock masses are common in nature and often have tunnels bored through them. As such it is highly likely that rail vibrations will be transmitted through jointed rock masses. There are a number of aspects of the transmission of stress waves through jointed materials which can be investigated. These include the relative roles of joint and block properties and geometries, and the potential presence of resonance, an effect which is eluded to by Eitzenberger (2012), although it is not studied. Another aspect of jointed rock masses which merits investigation is the use of equivalent materials. Modelling using equivalent materials has the potential to alter the transmission of stress waves from a source, despite both materials being considered as being the same. Therefore, investigation into what conditions can be modelled as equivalent materials is a useful aspect which requires further research.

"It is a capital mistake to theorize before you have all the evidence. It biases the judgment." – Sherlock Holmes
(Doyle, 2014, pg.21)

Table 2-1: Comparison of selected references showing their research area and how current state of the art research has progressed. Modelling assumptions are given in mutually exclusive pairs in the header. X shows that the model has applied a certain assumption.

Reference	Isotropic	Anisotropic	Full Space	Half Space	Homogenous	Layered	Dry	Wet	Single Track	Double Track	Tunnel	Embankment	Comments
(Forrest and Hunt, 2006a)	x		x		x		x		x		x		Initial presentation of PiP model.
(Forrest and Hunt, 2006b)	x		x		x		x		x		x		Extended the PiP model to include a floating slab track.
(Jones and Hunt, 2011)	x		x		x		x		x		x		Assessed the effects of voids present at the tunnel-soil interface.
(Yang et al., 2017)	x			x	x		x		x		x		Comparison of 2D and 2.5D FEM results.
(Yuan et al., 2017)	x			x	x		x		x		x		Similar to Hussein et al. (2014) but capable of modelling tunnels close to ground surface.
(Ruiz et al., 2019)	x			x	x		x		x		x		Assessing the effects of tunnel excavation damage on future vibrations.
(M.F.M. Hussein et al., 2014)	x			x		x	x		x		x		Extending PiP to multi layered half space.
(Yuan et al., 2015)	x		x		x			x	x		x		Tunnel in full space with water in a 2D long section.
(Yuan et al., 2016)	x		x		x			x	x		x		Tunnel in full space with water in 3D.
(Zhou et al., 2017)	x			x	x			x	x		x		Tunnel in half space with water in 3D.

(Yuan et al., 2018)	x			x		x		x	x		x		Tunnel in a layered half space with water in 3D.
(Kuo et al., 2011)	x		x		x		x			x	x		Twin tunnels in full space using superposition.
(He et al., 2018)	x		x		x		x			x	x		Novel approach using two vertically joined half spaces for Twin tunnels in full space.
(Yuan, Boström, Cai, et al., 2019a)	x		x		x		x			x	x		Twin tunnels in half space with water.
(Sheng et al., 2005)	x			x	x		x			x	x		Comparison of twin tunnel and equivalent double track single tunnel using FEM-BEM.
(Hamad et al., 2015)	x			x	x		x			x	x		Comparing superposition and a fully coupled models of twin tunnels in homogeneous half space.
(He et al., 2019)	x			x		x	x			x	x		Twin Tunnels in layered half space.
(Yuan, Boström, Cai, et al., 2019b)	x		x		x			x		x	x		Twin tunnels in full space with water.
(Yuan, Boström and Cai, 2019)	x			x	x			x		x	x		Twin tunnels in layered half space with water.
(Gao et al., 2018)		x		x	x			x	x			x	Embankment on a transversely isotropic half space.
(Ba et al., 2019)		x		x		x	x		x			x	Embankment on layered anisotropic soil.

3 Anisotropy

"A review of anisotropic material,
A vein of work, almost arterial.
From stress and geological creation,
This provides a background for my studies fixation."

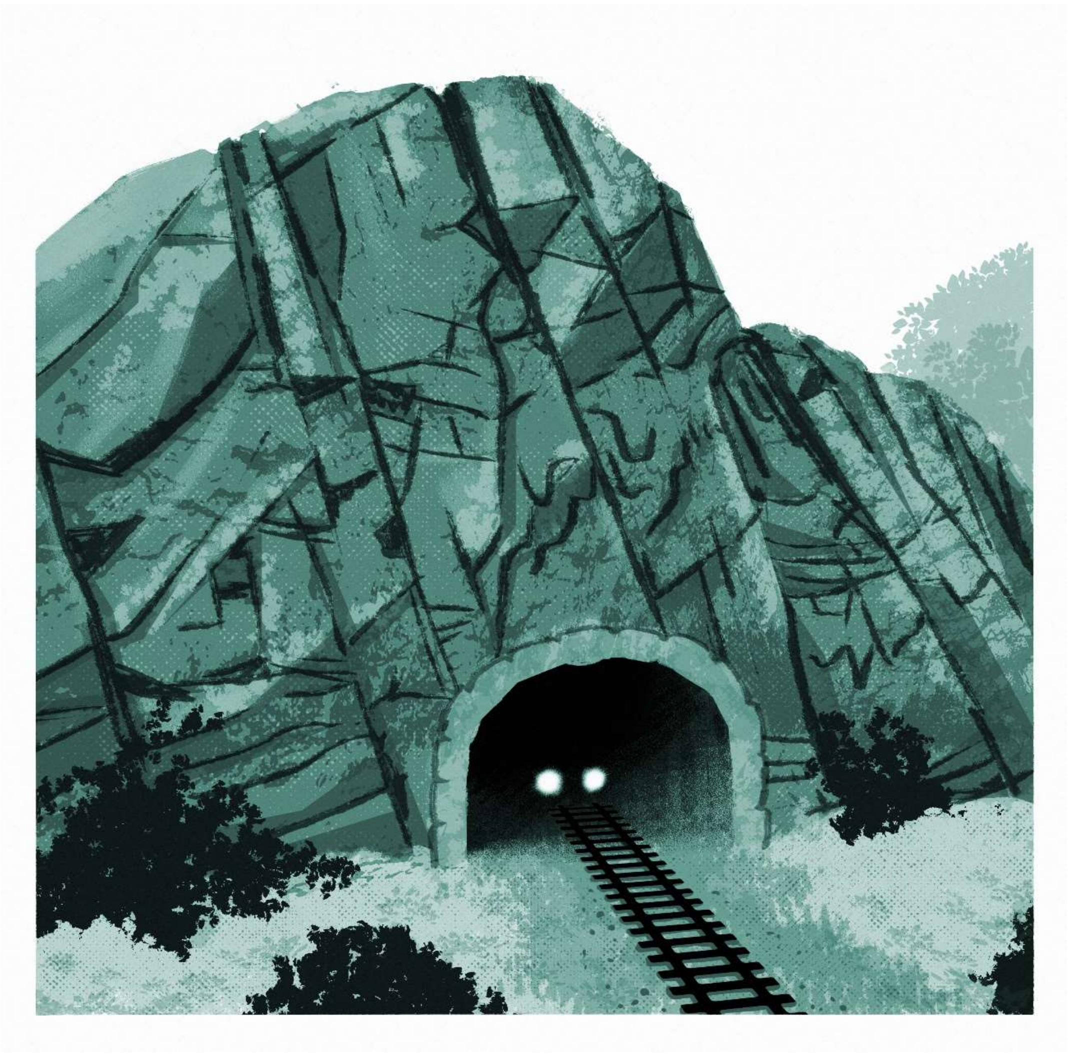

© Army of Cats 2023

3.1 Introduction

The previous Chapter introduces the train vibration research in anisotropic materials, although it does not go into how anisotropic materials form. This Chapter focuses on what is meant by a material being anisotropic.

3.2 What is Anisotropy

Anisotropy is the term used to describe materials which have different properties in different directions. Isotropic materials, which have largely been the subject of train vibration studies, have the same stiffness in all directions. However, it is possible for natural materials to have different material properties depending on the direction in which they are measured.

There are a range of different types of anisotropic materials. Three common types are transversely isotropic, orthotropic, and fully anisotropic materials (Schoenberg and Sayers, 1995). Transversely isotropic materials have a plane of isotropy, where the material properties in a plane are the same, with the out of plane direction having different properties. These are characterised by having five different independent material properties. Orthotropic materials have different material properties in three perpendicular planes, which require nine independent material properties to define them. Anisotropic materials have different material properties in all directions, requiring 21 independent material properties.

Anisotropy is the de facto condition of natural deposits in the real world (Barton and Quadros, 2015). All stages in the deposition and deformation of natural deposits can lead to the development of anisotropy. Consequently, it is unlikely that tunnels will be excavated solely in isotropic materials. Considering this, and in the context of this thesis, it begs the question: why has so much research into underground railway vibrations been conducted in isotropic materials? Perhaps the degree of anisotropy is not typically significant, or it has negligible effect on the propagation of vibrations. The following sections will try to answer this question, starting with an overview of how geological processes can cause anisotropy, followed by a discussion of current research into vibrations in anisotropic conditions.

3.3 Inherent Anisotropy

Anisotropy can be created in a natural deposit through a wide variety of geological processes. Anisotropy related to the geological history of a deposit is referred to as inherent anisotropy.

During sedimentary deposition, particles in a deposit may align due to the mode of deposition, with laminations and bedding forming due to changes in the sedimentation cycle. Figure 3-1 shows bedding and laminations in Devonian aged varved thermally stratified lake sediments of the Orcadian Basin (Andrews et al., 2010), exposed at Spittal Quarry in Caithness, Scotland. The changing shades of the deposits represent seasonal changes in the mode of deposition. The yellowy-brown laminations are clastic sediments which are deposited when storms bring material eroded from the land surrounding the basin in the winter, the light creamy coloured laminations are carbonates precipitated from the water body during the warm summer and the dark grey bands are organic carbon deposits from the death of living things in the lake water. This produces couplets or triplets of laminae representing annual deposition. Bedding in this rock mass is highlighted in Figure 3-1a by the small benches formed. The bedding represents a weakness in the rock mass not seen in the regular fine laminations and has been exploited during quarry workings as preferential weaknesses to aid excavation. These beds form where the lake periodically dried out and represent a disconformity. Due to these regular parallel horizontal weaknesses the rock mass will behave as a transversely isotropic material, having a lower elastic stiffness in the vertical direction than in the more continuous horizontal direction. Equally, the intact blocks between bedding will also behave as a transversely isotropic material due to the stiffness variations in the small-scale laminations. In the case of the rocks in Figure 3-1 the plane of isotropy is horizontal, with the vertical direction having different material parameters due to the presence of the sedimentary layering. The degree of anisotropy can be represented by the ratio between the stiffness in the plane of isotropy to the stiffness in the perpendicular direction. The rock mass in Figure 3-1 a will have significantly different stiffnesses, showing a large degree of anisotropy, in comparison to Figure 3-1b, whose material properties in the vertical and horizontal direction will be different although not significantly different from each other. This is due to the presence of the discontinuities representing the bedding planes. This difference in stiffness is shown schematically using the tensors in Figure 3-1. The pattern of horizontally orientated sedimentary features as shown in Figure 3-1 b are typical of sedimentary basins, so transversely isotropic material properties can be expected in natural deposits.

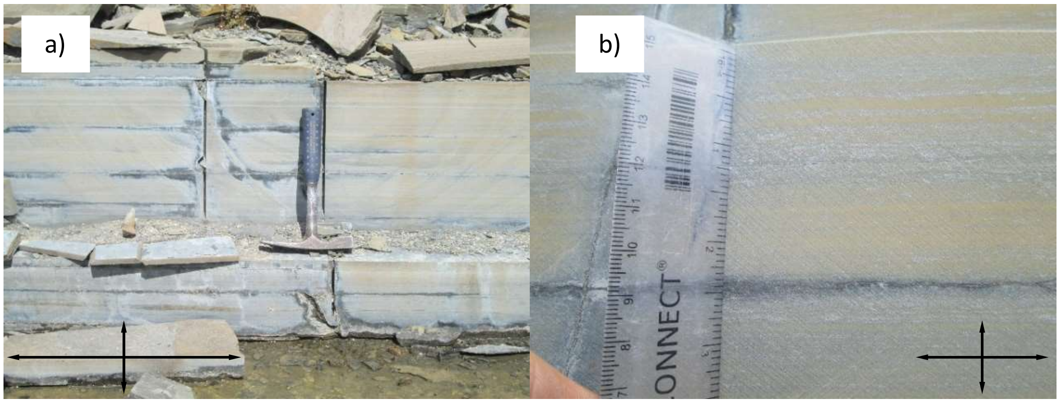

Figure 3-1: Laminations in a varved sediment of the Orcadian Basin shown on a saw cut quarry face. a) larger scale bedding features; b) smaller scale laminations, with diagonal striations formed due to the cutting process. Tensor arrows show the relative stiffness of the material. Spittal Quarry, Caithness, Scotland

It is not only deposition which can cause the persistent features which give rise to anisotropy. Metamorphism, the process by which a rock mass is modified by stress and / or temperature and can cause minerals to re-align to the local stress regime which the rock mass is subject to (Bucher and Grapes, 2011). This re-alignment is not dependent upon the orientation of anisotropy in the original material, the protolith. Slate is a common low-grade metamorphic rock with a well-developed foliated structure showing transversely isotropic behaviour, with the plane of isotropy aligned with the maximum principal stress during metamorphism.

Anisotropy can also be observed in igneous rock, such as columnar jointed basalt (Figure 3-2). Columnar joints form when an igneous body cools and contracts forming a series of circumferential cracks around a central, commonly hexagonal, intact body (Phillips et al., 2013). Although the intact body could be thought of as an isotropic material, it can itself show layering perpendicular to the columnar jointing (Figure 3-2 b). These features can be observed at many famous locations across the world including extensively on the isle of Staffa in the Hebrides.

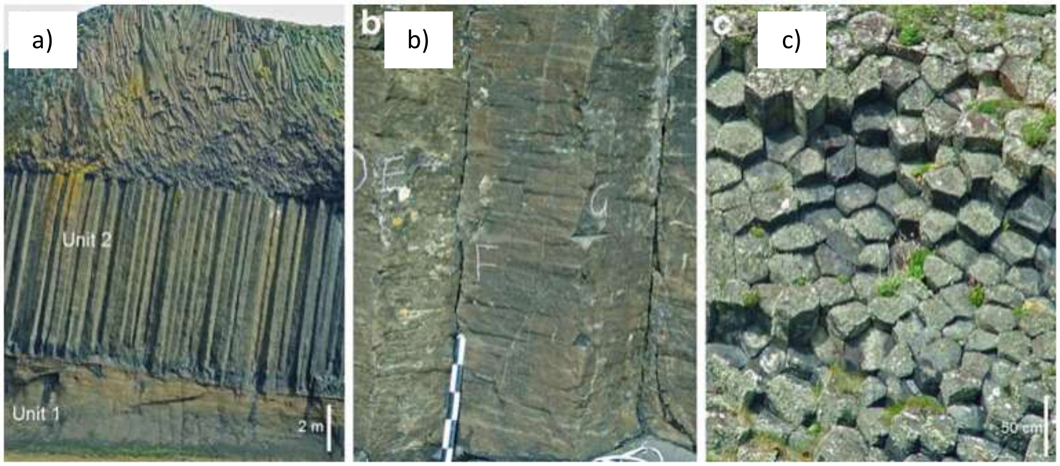

Figure 3-2: Columnar jointing from Staffa. A) clear columnar jointing in Unit 2; b) horizontal striae in columns; c) top view of columns showing hexagonal pattern. From Phillips et al. (2013) *Figure 5*

Anisotropy can develop in rock masses due to many other processes than those discussed above. One such process, which can lead to the development of jointing is the role of tectonics. Tectonic forces can cause changes in the stresses present within the earth's crust which can lead to stresses which can exceed the strength of the host rock, which are released through shearing and the development of joints. Additional joints will introduce weaknesses in a rock mass, causing a change in the material properties of the rock.

The above discussion briefly describes some causes of anisotropy which can be observed in natural deposits. This is by no means an exhaustive list, but it is hoped that it serves as an indication of the likely prevalence of anisotropic materials in nature created by the processes involved in their formation.

3.4 Anisotropy from Geological Structures

The previous section has described how geological processes can cause natural deposits to be anisotropic. In the case of laminations this is through the layering of different materials of different stiffnesses. Assuming each lamination behaves like a spring, the composite material can be thought of as several springs connected in series. A spring is an element with a single degree of freedom, so this analogy only applies in a single spatial dimension. The stiffness of a series of n springs (E_m) is given by Equation 3-1 (Ma et al., 2013).

$$\frac{1}{E_m} = \sum_{i=1}^{n} \frac{1}{E_i} \qquad \text{Equation 3-1}$$

Where E_i is the stiffness of each individual spring and *n* is the number of springs.

A rock mass with intact blocks separated by persistent joints can also be thought of as a series of connected springs. Although it may be clear how an intact body can behave like a spring, a joint acting as a spring, which is the absence of material, may not be so clear. A joint is defined as an interface between intact blocks. These interfaces allow movement in all spatial directions with the degree of sliding of blocks past each other dictated by the joints shear stiffness (k_s) and squeezing of joints controlled by the joint normal stiffness (k_n). These stiffness properties are related to the properties of the joint, such as infill material, roughness, joint separation, and degree of weathering (Bandis et al., 1983). Smooth joint walls lead to a low shear stiffness but can also cause the joints to be in contact in more places, leading to an increased joint normal stiffness. Weathering of joint walls will create an annulus of weakened material surrounding an intact block allowing blocks to effectively penetrate one another upon joint closure, leading to a reduced normal stiffness. A widely separated joint will allow more displacement than a joint with a smaller separation, meaning a narrow joint is likely to have a higher joint stiffness than a wide joint.

Considering a single set of joints with a spacing of *s*, Equation 3-1 can be re-written as Equation 3-2 (Itasca Consulting Group Inc., 2014).

$$\frac{1}{E_m} = \frac{1}{E_r} + \frac{1}{k_n s} \qquad \text{Equation 3-2}$$

The parallel jointed rock mass in Figure 3-1 will therefore have a rock mass stiffness in the vertical direction equal to E_m and in the horizontal plane of isotropy both directions will have a stiffness equal to E_r, assuming there are no vertical joints present. The shear stiffness of a rock mass (G_m) can be calculated in a similar way from the intact rock shear stiffness (G_r) and joint shear stiffness using Equation 3-3 (Itasca Consulting Group Inc., 2014).

$$\frac{1}{G_m} = \frac{1}{G_r} + \frac{1}{k_s s} \qquad \text{Equation 3-3}$$

The rock mass stiffness, given by Equation 3-2, can be used to determine the displacement of the rock mass from an applied stress using Equation 3-4.

$$u = \frac{E_m}{\sigma} \qquad \text{Equation 3-4}$$

Where u is displacement and σ is the applied stress.

The displacement of the rock mass in Equation 3-4 occurs through displacement of the intact blocks and joints. However, as previously stated, the normal stiffness is influenced by the joint separation. Therefore, joint stiffness is not a constant value, and instead changes as the applied stress changes. This effect is included in the Barton-Bandis non-linear joint model, where the joint stiffness is related to the stress applied on the joint (Bandis et al., 1983). The end members of this relationship are that at an infinitely large joint separation the joint stiffness tends to zero, and at an infinitely small joint separation the joint stiffness tends to infinity. An infinitely stiff joint will not have any effect on the stiffness of the rock mass, which can be seen by subbing the relevant values into Equation 3-2, meaning that in this end member case, the rock and rock mass have the same stiffness (E_m=E_r). Equation 3-5 shows how joint normal stiffness is calculated from the applied stress (σ_n), the maximum joint closure (V_m) and the initial joint stiffness (k_{ni}). The Δ symbol is not included in the original formulation of Equation 3-5 in Bandis et al. (1983); however, it is deemed a sensible addition as it implies that if σ_n is zero then k_{ni} equals k_n which, logically, it should do. Therefore, Equation 3-5 gives the new k_n when a joint is subject to a different stress than its original condition which has a joint normal stiffness of k_{ni}. Similar relationships were also derived for the joint shear stiffness by Bandis et al. (1983).

$$k_n = k_{ni}\left[1 - \frac{\Delta\sigma_n}{V_m k_{ni} + \Delta\sigma_n}\right]^{-2} \qquad \text{Equation 3-5}$$

3.5 Stress Induced Anisotropy

The Barton-Bandis joint model shows that changing the stress applied to a rock can influence the joint stiffness. Equation 3-2 shows how changes in joint stiffness can influence rock mass stiffness, which can have implications for the properties of a rock in a non-hydrostatic stress field. Consider, for instance, a homogeneous isotropic sample of rock with a random distribution of identical micro cracks at random angles (Figure 3-3). Under hydrostatic compression, where σ_1=σ_2=σ_3, all cracks in the sample will be closed equally and therefore the stiffness of the material will be the same in all directions. Now consider triaxial or uniaxial compression where σ_1>σ_2=σ_3, where σ_1 is orientated vertically in Figure 3-3. Cracks orientated perpendicular to σ_1 will close more than those parallel to it. Therefore, the stiffness of the sample in its long axis will be greater than the short axis, giving the material transversely isotropic properties, despite being isotropic when subject to hydrostatic conditions. Equally, under true triaxial conditions, where σ_1>σ_2>σ_3, the stiffness of the rock will be orthotropic. This anisotropy has been entirely created through the stress induced in the sample and will be lost if the stress is removed and the cracks can return to their original separation. Therefore, anisotropy, or at the very least the degree of anisotropy, is not necessarily a permanent feature of a rock mass.

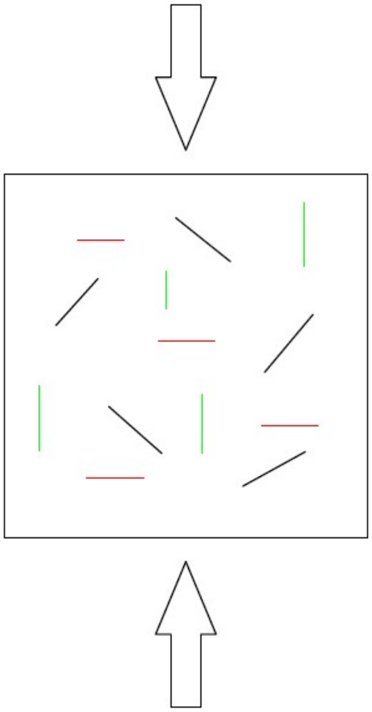

Figure 3-3: Closure of micro-cracks in an axially loaded rock sample. Under uniaxial loading (orientated vertically) red cracks are closed, green cracks are not closed and black cracks are partially closed.

3.6 Anisotropy in Natural Deposits

The previous Chapter shows that it is possible for a railway on an embankment to show a marked difference between the amplitude of vibrations when the ground is modelled as isotropic compared to transversely isotropic material. The E_h:E_v ratios which created these differences in the studies varied between 0.5 and 2. Ba et al. (2019) stated that the typical range of E_h:E_v given in literature is between 0.55 and 4.0. However, while it is possible to have highly anisotropic soils in extreme cases, are anisotropic conditions the norm? The above discussion regarding the causes of anisotropy in natural deposits indicates that anisotropy is commonplace, but it does not indicate the degree of anisotropy which will be found. If E_h:E_v ratios are typically close to one with a small variance, the potential effect of typical anisotropic soils will be reduced and the motivation to study its effects will be negated. To answer this question, it is necessary to consider the properties of a real soil body in which numerous train lines and train tunnels have been constructed.

London Clay is a stiff marine clay underlying the city of London and is the foundation for a considerable number of above ground and underground railway lines (Gasparre, 2005).

London Clay is regarded as being a transversely isotropic material, typically with a greater horizontal stiffness than vertical stiffness (Tan and Tan, 2003). Figure 3-2 shows the shear strength of London Clay in horizontal:horizontal (G_{hh}) and horizontal:vertical (G_{hv}) directions. This shows that the average ratio of $G_{hh}:G_{hv}$ is approximately 2.0. While this is measured using shear strength, instead of Young's Modulus as used in the study of Ba et al. (2019), these ratios will be equivalent to those used in the former study. Other studies have shown that the ratio can vary between less than one to greater than three (Tan and Tan, 2003), agreeing with the possible range of natural soil anisotropy previously stated. This shows that, for London Clay, the effects of soil anisotropy observed by Ba et al. (2019) is realistic. Therefore, considering the results of studies of surface embankments which have studied anisotropic material properties, it will be necessary to analyse vibrations in railway tunnels in comparable situation to reduce prediction uncertainties.

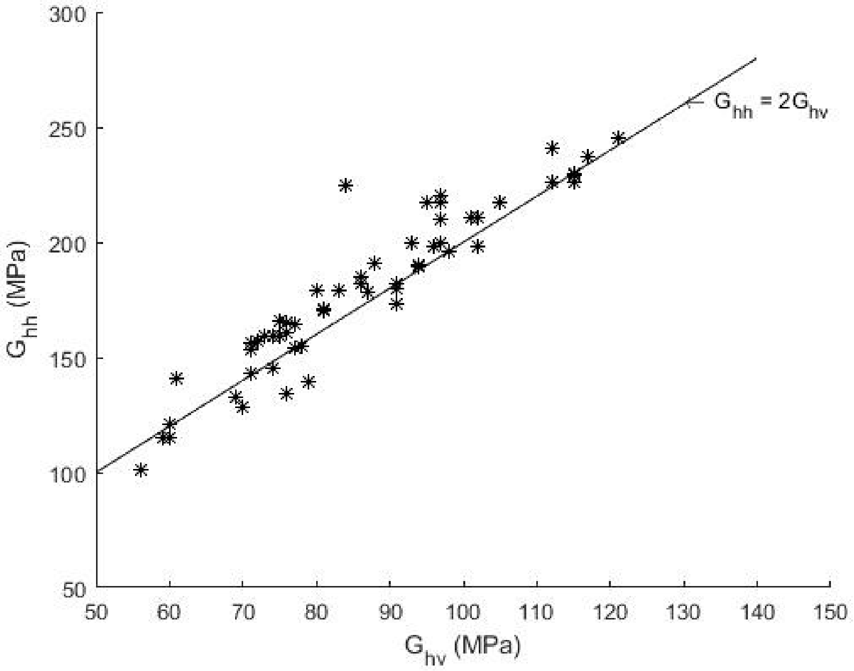

Figure 3-4: G_{hh} vs G_{hv} data for London Clay. (Gasparre, 2005)

3.7 Effect of Joints on Transmission of Stress Waves

Stress waves propagating through a body are affected by differences in the seismic velocity of blocks and the presence of discontinuities. Propagation of stress waves through a continuous solid can be refracted and reflected at interfaces where two blocks of different seismic velocity are in contact, following Snell's Law. Snell's Law dictates that the degree of refraction and reflection is also dependent on the angle of incidence of the wave upon the interface. When two blocks are in contact and their seismic velocity is the same, refraction and reflection can still occur if the two blocks are not perfectly bonded. If the blocks are perfectly bonded the interface is effectively not there and no refraction or reflection occurs. This will be the case in a homogenous jointed rock mass, where the rock mass is composed of blocks of the same properties separated by joints, such as those shown in Figure 3-5. In reality, joints will not be perfectly bonded due to roughness of the joint walls, infilling of the joint or weathered annulus in the blocks on either side of the joint (Bandis et al., 1983). Problems of stress wave propagation through joints have been widely studied in literature with analytical solutions being derived for a variety of situations, as well as more complex cases being investigated numerically (Pyrak-Nolte et al., 1990b; Pyrak-Nolte et al., 1990a; Cai and Zhao, 2000; Zhao et al., 2008; Deng et al., 2012; Varma et al., 2017; Fan et al., 2018). For single joints, it is found that the degree of reflection from a joint is related to the stiffness of the joint and the frequency of the incident wave. The degree of reflection increases as the stiffness of the joint reduces; with an extremely low stiffness joint reflecting all energy and an extremely high stiffness joint transmitting all energy. Incident waves of a high frequency will also show a greater degree of reflection than low frequency waves. Cai & Zhao (2000) found that when there are multiple parallel joints it is possible for a peak to occur in the transmission of waves through jointed materials. This only occurs at a limited range of ratios of joint spacing to wavelength, but it does indicate that there are many factors to consider between jointed rock masses and wave transmission. These factors are typically assumed to be brought about by the superposition of multiple reflections from joints.

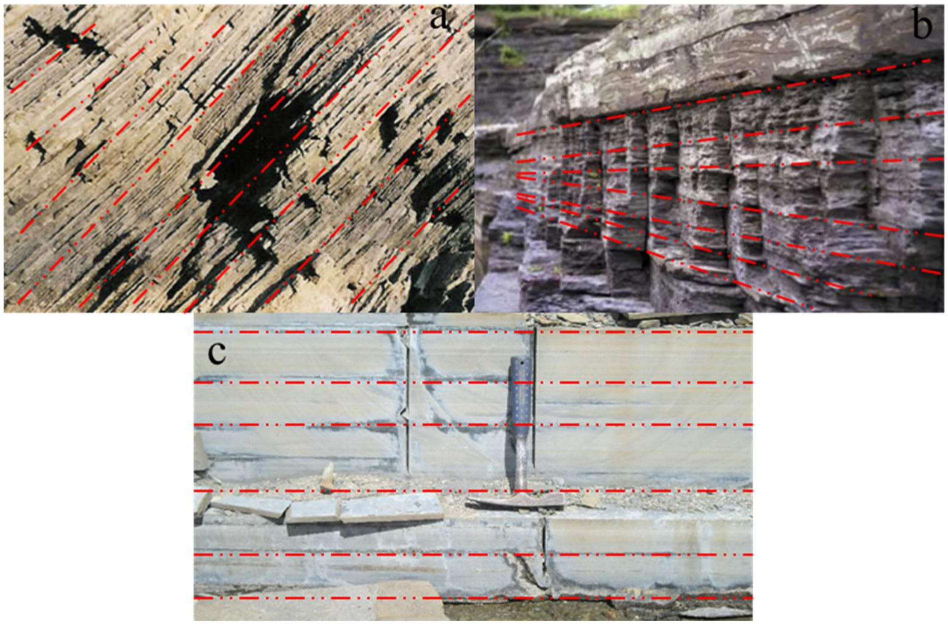

Figure 3-5 Parallel jointed rock masses which will show transverse isotropy. a) Sub-vertical joints in slate-like grits, Aberystwyth, western Wales, with a sub-vertical plane of isotropy (Barton and Quadros, 2015)*; b) Horizontal joints in alternating siltstone and shale from Appalachian Plateau, Fingers Lakes, New York, with a vertical plane of isotropy* (Germanovich and Astakhov, 2004)*; c) horizontal joints in Achanarras Limestone Member, Caithness Flagstone Group, Spittal Quarry, Caithness, Scotland. Joints within rock masses are highlighted by dashed lines*

Before more complex cases involving multiple reflections are studied it is necessary to introduce the empirical Equations for transmission and reflection given by Pyrak-Nolte et al. (1990b, 1990a). Equation 3-6 shows the transmission coefficient for normally incident stress waves through a single fracture. This can be applied to either Compressional or Shear waves (P or S-waves) by using the appropriate joint stiffness (shear stiffness for S-waves or normal stiffness for P-waves) and wave velocity in the seismic impedance term (S-wave velocity for S-waves or P-wave velocity for P-waves). Equation 3-7 shows the reflection coefficient, with similar alterations for the different wave types. These Equations have a common parameter, the normalised joint stiffness, given by $k/z\omega$. Figure 3-6 shows the transmission and reflection coefficients plotted against the normalised joint stiffness. When the normalised joint stiffness is low the transmission coefficient approaches zero and the reflection coefficient approaches one. As the normalised joint stiffness increases the transmission coefficient tends to one and the reflection coefficient tends to zero. For two rocks with the same seismic impedance (z) the normalised joint stiffness increases with an increasing joint stiffness or a reduction in wave frequency. These models do a very good job of explaining the characterisics of stress wave trasmission through individual blocks. The empirical formulae for transmission and reflection from single fractures are replicated in numerical software by a number of researchers (Cai and Zhao, 2000; J Zhao et al., 2006; J. Zhao et al., 2006).

$$T_1 = \frac{2\frac{k}{z\omega}}{2\frac{k}{z\omega} + i} \qquad \text{Equation 3-6}$$

$$R_1 = \frac{i}{2\frac{k}{z\omega} + i} \qquad \text{Equation 3-7}$$

T_1 and R_1 are the transmission reflection coefficients, respectively, k is the joint specific stiffness, z is the seismic impedance of the blocks on either side of the joints ($z=v\rho$, where v is the P or S-wave velocity) and ω is the angular frequency of the incident wave.

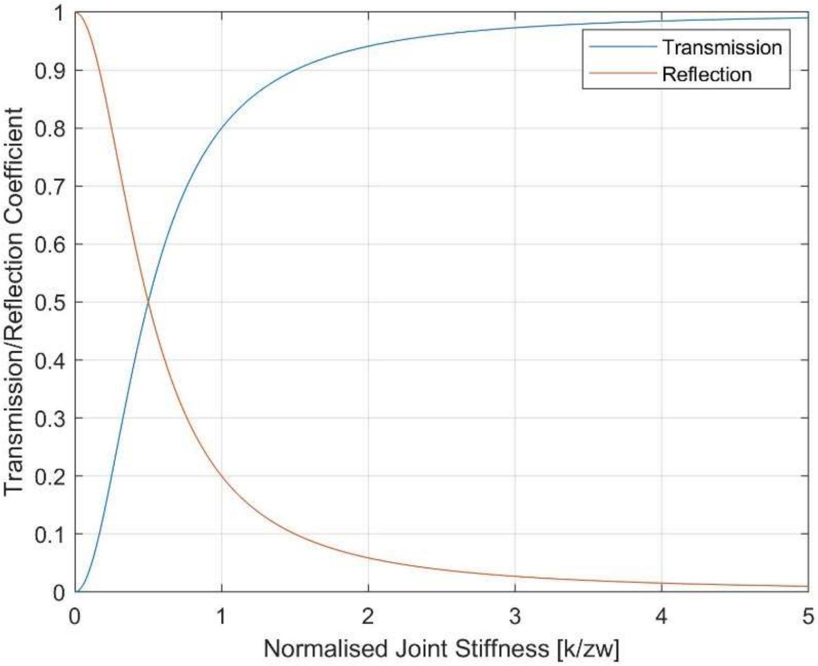

Figure 3-6 Transmission and reflection from a single joint plotted against normalised joint stiffness

The transmission of stress waves through multiple joints is also investigated empirically by Pyrak-Nolte et al. (1990b). An approximation of the transmission is given by $|T_N|=|T_1|^N$, where N is the number of fractures. This Equation will only ever be able to offer an approximation of the transmission coefficient as it ignores the effects of the superposition of multiple reflections, which are logically predicted to occur based on Equation 3-2. When the transmitted wave is contaminated by multiple wave reflections Zhao et al. (2006) shows that $|T_N|>|T_1|^N$.

Zhao et al. (2006) found that the transmission coefficient for multiple parallel fractures with a normally incident stress wave is governed by the non-dimensional fracture spacing (ξ=*joint* *spacing[s]/wavelength[λ]*), the normalised joint stiffness and the number of fractures. It was found that when the fracture spacing is much smaller than the incident wavelength the behaviour of the rock mass could be explained by an equivalent medium method. This effect was also found by Schoenberg & Sayers (1995). For example, in a parallel jointed rock mass this would be equivalent to transversely isotropic continuum.

Hildyard (2007) investigates the use of the finite difference method (FDM) to accurately model seismic waves through fractured rock masses surrounding cavities. This work uses the FDM software WAVE, developed by Hildyard et al. (1995). The laboratory experiments of Pyrak-Nolte et al. (1990b) are replicated using WAVE. Fractures within the FDM models are simulated explicitly as displacement discontinuities. A good agreement is found between the numerical and physical models. This work is the first time a numerical model had been shown to accurately show the transmission of non-planar waves through multiple fractures. Of particular importance, this work shows that non-uniform stress within a model can lead to a variation in the stiffness across individual joints, generating a complex wave behaviour and inducing focusing of waves through joints.

Parastatidis et al. (2017) also analyses wave propagation through parallel jointed rock masses using different material models, comparing them to experimental results. The different material models are: i) explicitly modelling fractures; ii) a homogenous transversely isotropic continuum, iii) localised transversely isotropic continuum. This work is also undertaken in the FDM code WAVE (Hildyard et al., 1995). It is found that the similarity between the physical and numerical results depends upon the direction of wave propagation; be that parallel to or perpendicular to the fractures. When waves propagate parallel to fractures it is found that the explicit modelling of fractures provides the best match, with a reasonable match for the localised transversely isotropic continuum and a poor match for the homogenous transversely isotropic continuum. When waves propagate perpendicular to fractures, none of the models were found to match the experimental results.

Zhu et al. (2013) investigate the transmission of stress waves through more complex rock masses, using a parametric analysis to study the effects of joint stiffness, non-dimensional joint spacing, joint spacing ratio, joint intersection angle, incidence angle and the number of joint sets. It is found that, depending on the wave type, different parameters affect the wave transmission through the joints. It is found that, in 2D plane strain, when the number of joint sets is equal to or greater than four a rock mass can be considered to be isotropic. A similar study is also conducted by Eitzenberger (2012), but with a focus on the spatial differences caused by differing joint angles, whereas Zhu et al. (2013) measure the PPV at an individual location in the model.

Most studies consider transmission and reflection coefficients, but not resonance. Resonance is an important consideration in many engineering studies, not least railway engineering. Resonance in buildings and the track structure are well known to accentuate vibration problems (Connolly et al., 2016). Resonance effects are studied by Li et al. (2019) who use a 3D finite element program to study the resonance of different sized and shaped intact blocks using different excitation frequencies. Resonance is identified in the study which depends on the block properties. It is found that increasing the size of the block reduces the frequency of resonant peaks and increasing the peak frequency of the excitation increased the resonant frequency of the blocks. These high transmission are identified as being resonant frequencies, which seems to be the correct conclusion, but the reasons behind them are not well identified. The resonant frequencies vary in a systematic manner when the block size increases, which indicates that the resonance may be due to the superposition of the incident wave and a reflected wave from the edge of the modelled block. This superposition effect has been identified in rock and concrete blocks (Nakagawa, 1998) and is the subject of a standardised test (EN, 2004). Eitzenberger (2012) also identifies that there could be resonance mechanisms in jointed rock masses, although these are not investigated.

Although looking at quite different phenomena, the work by Zhang et al. (2019) considers aspects of resonance. This study investigates rock burst conditions, which considers aspects of superposition of waves from a reflective surface. Field monitoring of rock bursts shows that peak ground motion at the surface of an excavation in fractured rock is amplified compared to the motion of solid rock. Although this study is applied to rock burst conditions, which typically will not be found in rail tunnels, the amplification of the vibrations at the tunnels free surface could have consequences for rail vibration in jointed rock tunnels. It was found that the amplification of seismic waves depends on the characteristics of the incident wave and the properties of the fractured rock. Zhang et al. (2019) found that fracture stiffness, fracture spacing, fracture number and wave frequency influence the amplification factor of stress waves.

The above review shows that joints do not just have the potential to cut waves out, through a filtering effect, but also amplify waves, through the superposition of incident and reflected waves. These effects will have the potential to modify a vibration signal as the vibrations travel through a jointed rock mass and merit further study.

3.8 Conclusions

This Chapter outlines a number of ways in which anisotropy can occur in natural deposits. This includes anisotropy from depositional processes, geological structures and that induced by stress. Finally, it is shown that some features which can cause anisotropy, namely joints, can also affect the transmission of stress waves through a material. Train vibrations in jointed materials have not been widely investigated, so will be an appropriate avenue of research for this thesis.

4. 1D Jointed Rock Masses

"One-dimensional jointed rocks,
Made of repeated joints and blocks.
Impulsive sources, they were subject,
With attempts to see any resonance effect.

Actions of springs and superposition,
Give the transmitted waveform through coalition.
Presented with formulae which are analytical,
These are, to my thesis, hyper-critical."

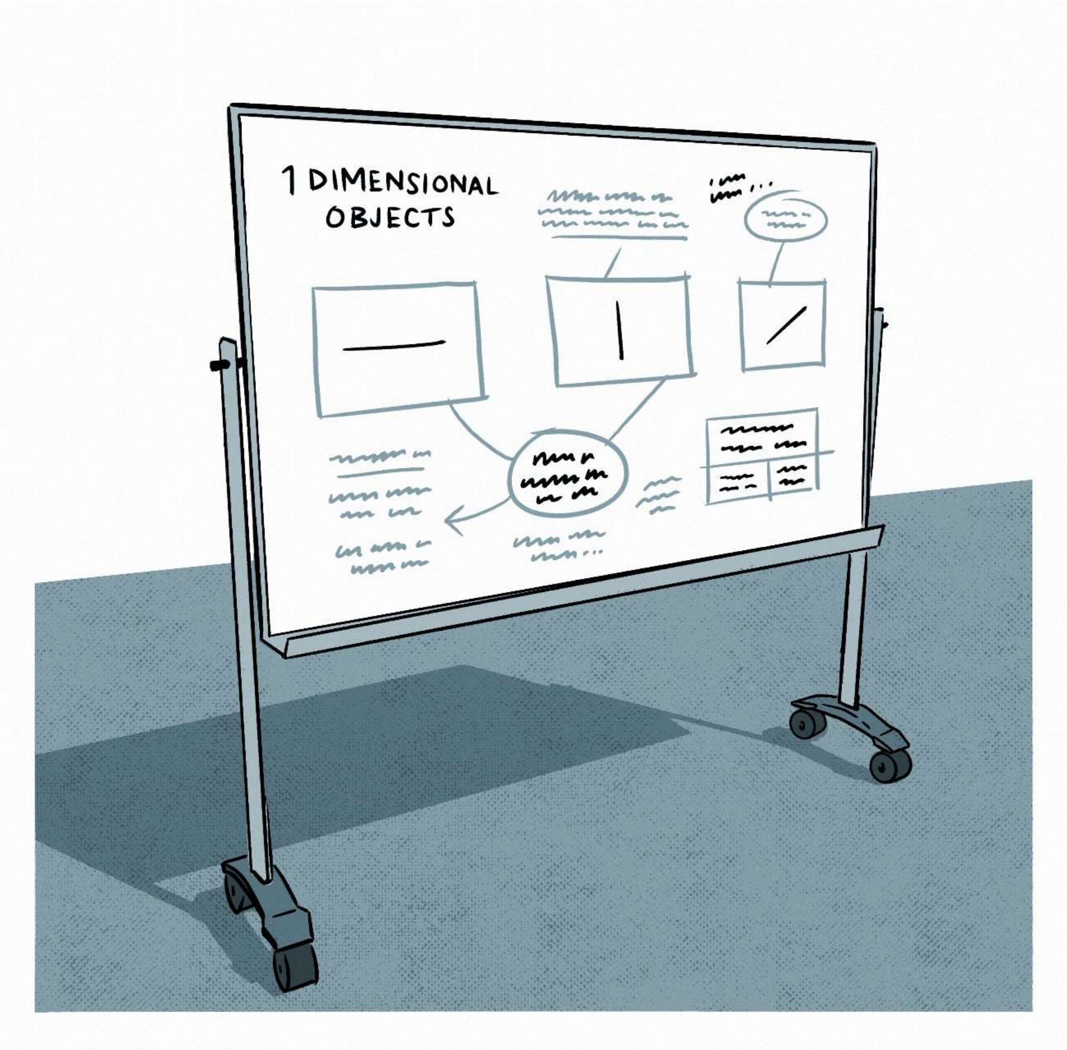

© Army of Cats 2023

4.1. Introduction

As shown in Chapter 2, vibrations from tunnels propagate through a complex transmission pathway on their way to a receiver, such as a building (Figure 4-1). There are various interactions between the rails and its substructure, the substructure and the tunnel, the tunnel and the ground and the ground and the building. Many aspects of this transmission pathway have been studied previously, which are outlined in Chapter 2; however, the interactions between blocks within a jointed rock mass have not been extensively studied in the context of rail vibrations, with the exception of the work by Eitzenberger (2012). This Chapter presents an initial investigation into jointed rock mass propagation pathways.

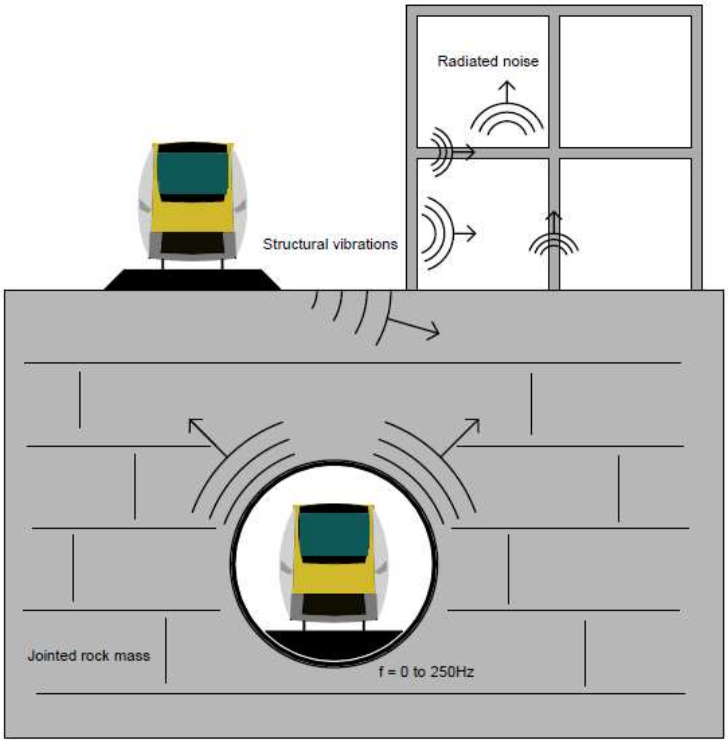

Figure 4-1 Ground vibrations from trains in jointed rock masses

While it is possible to jump straight into modelling a complex model with a tunnel, joints, and a free surface, such an approach would lose the intricacies of the transmission of stress waves through each of the individual components of the model. Instead, a more methodical approach starting with very simple models and adding complexity is adopted in this research. The simplest model of a jointed rock mass is a one-dimensional (1D) slice (Figure 4-2). As the slice is 1D the different joint angles present in the two-dimensional (2D) projection in Figure 4-2 are lost, with all the joints becoming parallel. This is a gross simplification of the problem but is a useful first step in analysing the jointed rock mass transmission pathway.

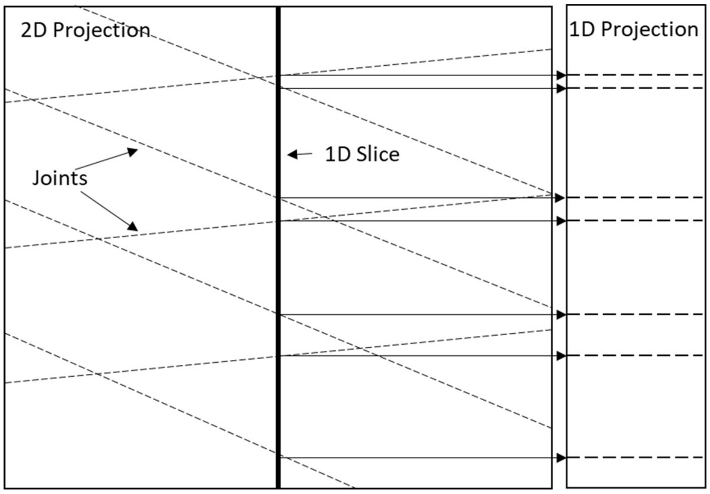

Figure 4-2 Projection of a 2D jointed rock mass onto a 1D slice showing how a relatively complex model can be simplified by reducing the number of spatial dimension

The 1D projection of the transmission pathway can be projected onto Figure 4-1, radiating out from the tunnel towards a receptor, such as a residential building. This gives a direct transmission pathway which can be analysed. By recording the waveform before and after a joint, the effect of the joint can be determined. This is undertaken using transfer functions, which are described in Section 4.3. The transfer functions are generated in the frequency domain, giving the frequency response of the model.

The work in this Chapter is undertaken using numerical models. The combined discrete element-finite difference method, solved in the time domain, is the numerical code chosen for this work. These models have been solved using the commercial software, UDEC (Itasca Consulting Group Inc., 2014). To isolate the effect of the joints on the transmission of stress waves, damping has been eliminated from the models. This is an approach adopted by previous studies into the effect of joints (Cai, 2000; Zhao et al., 2006)

This Chapter is broken down into a short recap of the background of previous work which has been undertaken in modelling of jointed rock masses, followed by a brief introduction into different input waves and transfer functions, followed by the model development using an isotropic continuum and finally modelling of jointed rock masses. The Chapter concludes with the identification of two resonance mechanisms in jointed rock masses, spring resonance and superposition resonance.

4.2. Background

Chapters 2 and 3 outlined the current work involving transmission of stress waves through jointed rock masses. However, these studies have considered transmission and reflection coefficients of rock masses and joints, as opposed to resonance (Pyrak-Nolte et al., 1990a; Pyrak-Nolte et al., 1990b; Cai and Zhao, 2000; J Zhao et al., 2006; Hildyard, 2007). When the transmission at a particular frequency is higher than surrounding frequencies, a resonant frequency for the rock mass is identified. Much previous work uses the explicit representation of joints within numerical models, such as Cai and Zhao (2000), Zhao et al. (2006) and Hildyard (2007), through the use of displacement discontinuities. This will therefore be the starting point for the research undertaken here. It could be argued that Cai and Zhao (2000) and Zhao et al. (2006) identified resonance in their models, but in terms of normalised joint spacing ($\xi=s/\lambda$). Resonance is an important consideration in many engineering studies, not least railway engineering. Resonance in buildings and the track structure are known to accentuate vibration problems (Yau, 2001; Hanson et al., 2012; Connolly et al., 2016). Resonance effects in rocks are explicitly studied by Li et al. (2019) who uses a 3D finite element model to study the resonance of different sized and shaped intact blocks using different excitation frequencies, with resonance depending on the block properties and dimensions. However, the reasons behind why such frequencies were resonant are not well defined in the study. The outcomes of the study by Li et al. (2019) and Zhao et al. (2006b) appear to differ, with the former identifying superposition at much higher frequencies than the latter. Resonance from the superposition of reflected waves is identified by Nakagawa (1998), who gives analytical Equations for resonance, terming it acoustic resonance. Acoustic resonance in natural stone blocks is a reasonably well established effect, being the subject of a British national standard (British Standard Institution, 2004). In fact, the resonances identified by Li et al. (2019) could be related to the superposition effect identified by Nakagawa (1998). The resonant frequencies of Li et al. (2019) vary in a systematic manner when the block size increases, which indicates that the resonance may be due to the superposition of the incident wave and a reflected wave from the edge of the modelled block. A standing wave could develop with the incident and reflected waves, causing wave superposition and an increase in the transmission coefficient.

There appear to be numerous effects occurring in regard to stress wave transmission through jointed rock masses that are found in literature, although up to this point full transfer functions have not been generally used in the analysis of jointed rock masses. This Chapter explores the effects that different jointed rock masses can have on a rock mass transfer function using the combined discrete element-finite difference method. Despite this numerical method being used previously (Cai and Zhao, 2000; J Zhao et al., 2006; Eitzenberger, 2012) the processing of the data using the full waveform with a transfer function provides a new lens in which to view rock mass transmission. Previous studies have studied the amplitude of the first arrival, which could miss much of the frequency content of the transmitted wave. Analysing the full waveform allows a more accurate means of determining the frequencies of waves that will be transmitted to a receptor.

4.2.1. Numerical Dispersion

Numerical dispersion is a phenomena which causes the modelled wave speed for a given medium to deviate from the elastic wave speed, and is a known to occur with the finite difference method (Hildyard, 2001). The difference between the modelled wave speed and elastic wave speed is not constant, and is greater at higher frequencies, meaning that wave speed is a function of frequency (Parastatidis, 2019). Numerical dispersion should be minimised in numerical simulations to ensure that a model matches reality as closely as possible. Hildyard (2001) showed that numerical dispersion is related to the quality of the mesh in a numerical model. When the element size is 10 times the minimum wavelength numerical dispersion is reduce. This is an effect also recognised by Kuhlemeyer and Lysmer (1973) and holds true for 2nd order wave Equations. However, the element size can be reduced to 5 times the minimum wavelength for 4th order wave Equations, such as those implemented in the WAVE2D mesh (Hildyard et al., 1995). This makes WAVE2D a particularly useful software for modelling of dynamic situations. UDEC uses 2nd order Equations, and is used extensively in this Chapter (Itasca Consulting Group Inc., 2014). While it can model dynamic scenarios, numerical dispersion will occur at lower frequencies than an equivalent WAVE2D model.

4.3. Transfer Functions

Transfer functions are used in this Chapter to analyse the transmission of stress waves through jointed rock masses. These compare the wave form which is incident upon the joint and the wave form which is transmitted through the joint. The transfer functions used in this thesis are synonymous with frequency response functions. Equation 4-1 is used to generate a transfer function using an input waveform (u_{ref}) and a transmitted waveform (u). To generate a transfer function, time series are decomposed into their harmonic components (u_{ref}' and u') using a Discrete Fourier transform and the discrete frequencies in the signal and response are compared. If the amplitude of the signal and response at a given frequency are the same, the transfer function for that frequency is equal to one. If the response has an amplitude of half the source, the transfer function for that frequency is 0.5; and if the response has an amplitude twice the source, the transfer function for that frequency is two. As transfer functions show the relative difference in the amplitude of incident and transmitted waves, the exact frequency content of the source does not matter. Therefore, the transfer function generated by a wide band impulse signal will be identical to the transfer function for a complex signal, such as railway vibrations.

$$TC = \frac{u'_{ref}}{u'} \qquad \text{Equation 4-1}$$

An example of the procedure of generating a transfer function is shown in Figure 4-3. For an undamped 1D continuum model the waveform will not be modified as it is transmitted through the material. The time series of the source and response are plotted in Figure 4-3 a, which is a 500 Hz Gaussian wave. The transfer function for these two time series is plotted in Figure 4-3 b, which is shown to be equal to one at all frequencies.

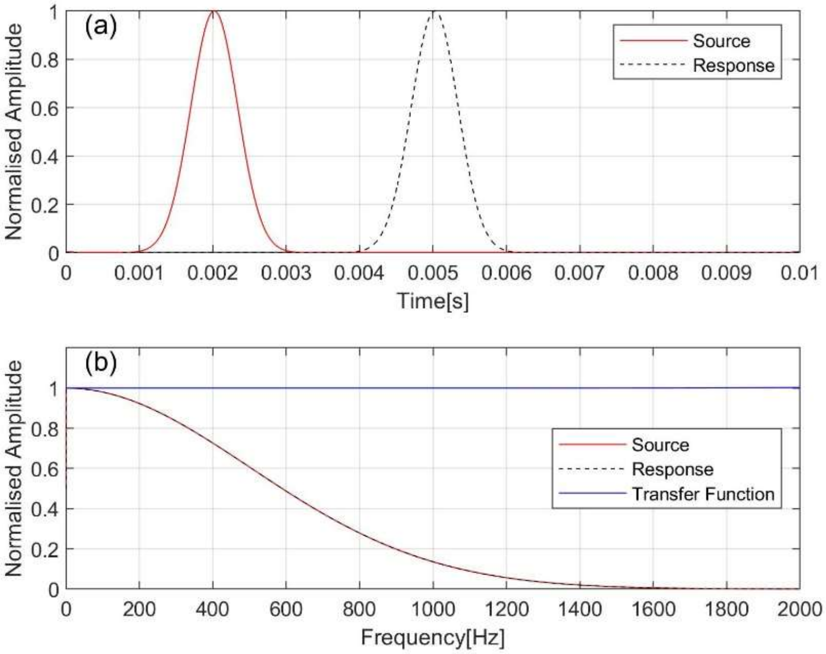

Figure 4-3 Example of a transfer function for an undamped, unjointed 1D model. a) time series of source and response, b) frequency content of source and response and transfer function. Modified from Holmes et al., (2023b) *Figure 4*

4.4. Model Development

The transfer function shown in Figure 4-3 b is a fundamental result for a 1D numerical model with no damping. This is because, a 1D continuum with no damping will not affect the transmission of any waves moving through it. However, if a model is not set up correctly waves propagating through it could be modified. Therefore, a 1D continuum model can be used as a base line to check whether a model is set up well. A model which is set up well will give accurate modelling results, which are necessary if meaningful results are to be derived from them. Inaccuracies in the transmission of the stress waves could be related to numerical dispersion (Section 4.2.1). This section deals with optimising the model set up using continuum models, which will have a transfer function equal to one at all frequencies.

As a numerical model is being used it is unlikely that the transfer function will be perfect for all possible frequencies; however, the quality of the transfer function will be influenced by the input wave properties and the model properties. A good quality model will have a transfer function equal to one across the frequency range of interest. As this work is being driven by the study of rail vibrations this will typically be up to a frequency of 250 Hz (Ouakka et al., 2022); however, a wider range will be studied in this section for a more complete and accurate model and a better indication of how rock masses transmit stress waves. The effect of various wave and modelling factors will be assessed. Wave properties which could affect the transfer functions are wave type, wave frequency content and the time step of the input wave function (4.4.4). Modelling options which could affect the transfer functions are mesh type, element size (4.4.5), model height (4.4.6), type of input function and position of the input function (4.4.7). The effect of the mesh type will be assessed in each section (4.4.4 to 4.4.7).

All models in the Model Development section of this Chapter have the same properties, giving a P-wave velocity of 3328 m/s, a S-wave velocity of 1922 m/s and a density of 2600 kg/m^3. This represents a sandstone with a high stiffness, although the selection of this rock type is arbitrary, and it could have been conducted on any material properties desired. All models in this section have adopted the large strain assumption in the UDEC set up. Although the realistic excitations induced by train vibrations are small, the excitations induced in the models are relatively large. The large strain assumption is not expected to dramatically affect the response of the models in this work.

4.4.1. Combined Discrete Element – Finite Difference Method

This section provides a very brief overview of the combined discrete element-finite difference method. For a much more complete description of the method the reader is directed to the UDEC User Manual (Itasca Consulting Group Inc., 2014). The combined discrete element-finite difference method applies a finite difference mesh to discrete blocks. Joints between blocks operate as interfaces between discrete elements. The finite difference mesh allows the blocks themselves to be deformable; however, the discrete element method can be used with rigid bodies by eliminating the internal meshing. The discrete element and explicit finite difference methods are solved numerically using a time stepping algorithm. The size of the time step is limited based on the assumption that velocities and accelerations are constant within a time step. This requires sufficiently small time steps that disturbances cannot be transmitted between two neighbouring nodal points, or discrete elements, within a single time step. In the DEM-FDM the time step is limited by the zone size and stiffness of the blocks and contacts.

The vertices of the elements in the finite difference grid are grid points. The Equations of motion for each grid point is given by Equation 4-2.

$$\ddot{u}_i = \frac{\int_b \sigma_{ij} n_j ds + F_i}{m} + g_i \qquad \text{Equation 4-2}$$

Where b is the surface enclosing the mass (m) lumped at the grid point, n_j is the unit normal to b, σ_{ij} is the stress tensor, F_i is the resultant of all external forces applied to the grid point and g_i is the gravitational acceleration.

Grid point forces are the result of the external applied loads (F_i^l), contact forces (F_i^c) and internal stresses from the adjacent zones (F_i^z), given by Equation 4-3.

$$F_i = F_i^z + F_i^c + F_i^l \qquad \text{Equation 4-3}$$

The internal stresses are calculated using Equation 4-4.

$$F_i^z = \int_c \sigma_{ij} n_j db \qquad \text{Equation 4-4}$$

All models used in this thesis do not have gravity applied; however, if it were used this would be incorporated into the solution using Equation 4-5.

$$F_i^g = g_i m_g \qquad \text{Equation 4-5}$$

Where m_g is the lumped mass at the grid point and g_i is acceleration due to gravity.

The velocity at the grid point is calculated at half time steps using Equation 4-6.

$$\dot{u}_i^{(t+\frac{\Delta t}{2})} = \dot{u}_i^{(t-\frac{\Delta t}{2})} + \sum F_i^{(t)} \frac{\Delta t}{m} \qquad \text{Equation 4-6}$$

Strains rates (ϵ_{ij}) and rotations (θ_{ij}) are related to nodal displacements using Equation 4-7 and Equation 4-8.

$$\dot{\epsilon}_{ij} = \frac{1}{2}(\dot{u}_{i,j} + \dot{u}_{j,i}) \qquad \text{Equation 4-7}$$

$$\dot{\theta}_{ij} = \frac{1}{2}(\dot{u}_{i,j} - \dot{u}_{j,i}) \qquad \text{Equation 4-8}$$

Where the comma in the nodal displacement subscript relates to the partial derivative.

4.4.2. Boundaries

Boundaries are an important part of any numerical model. Incorrect boundary conditions have the potential to affect how a model performs and the results which it yields. The boundaries used by previous researchers have been adopted for the models used here. Two different boundaries are used in different places. These are absorbing boundaries at the ends of the model (orientated perpendicular to wave propagation) and symmetrical roller boundaries on the top and bottom of the model (orientated parallel to wave propagation). These have been used for similar 1D problems by Cai & Zhao (2000) and Zhao et al. (2006), among others.

Absorbing Boundaries

Absorbing boundaries are used to reduce reflections from model boundaries. Absorbing boundaries are known as quiet boundaries in UDEC (Itasca Consulting Group Inc., 2014). UDEC uses a viscous boundary, developed by Lysmer & Kuhlemeyer (1969) and applies dashpots for the normal and shear directions at the boundaries. These are not perfect and still generate some reflected waves from the boundary; however, for incident angles of greater than 30° they work well. Therefore, for the 1D models used here, whose incidence angles are expected to be 90°, they should work.

The dashpots attached to the boundaries apply viscous normal and shear tractions given by Equation 4-9 and Equation 4-10.

$$t_n = -\rho C_p v_n \qquad \text{Equation 4-9}$$

$$t_s = -\rho C_s v_s \qquad \text{Equation 4-10}$$

Where v_n and v_s are the normal and shear components of the velocity at the boundary, ρ is the mass density and C_p and C_s are the P and S-wave velocities.

The tractions calculated by Equation 4-9 and Equation 4-10 are calculated and applied at every time step.

Symmetrical Boundaries

Symmetrical boundaries are implemented by applying a displacement constraint to a model boundary. In UDEC this is done by setting the velocity on the boundary to be zero in the vertical direction, which is opposite to the direction which the wave will be travelling. This has the effect of making the model effectively continuous in the vertical direction.

4.4.3. Mesh Type

UDEC has two different types of finite difference mesh generation functions, giving what are known in the software as edge and quad meshes. The finite difference mesh used with the discrete element method allows blocks to deform. The edge mesh uses constant strain triangular elements, which eliminates hour glassing effects found with constant-strain finite difference quadrilateral meshes (Itasca Consulting Group Inc., 2014). Examples of different sized edge meshes are shown in Figure 4-4. The quad mesh command creates diagonally opposed triangular elements, shown by Figure 4-5, which allows for improved modelling of plastic flow. Figure 4-4 and Figure 4-5 show that the two different mesh models produce different meshes, even for the same ratio of minimum edge length and model height. The quad mesh model gives a more regular finite difference mesh, compared to the edge mesh. Each mesh type has situations which they are more suitable for. The edge mesh can mesh more complex shapes and the quad mesh models plastic flow more accurately, so each mesh type will be studied in the following sections.

a) 0.5 m element length

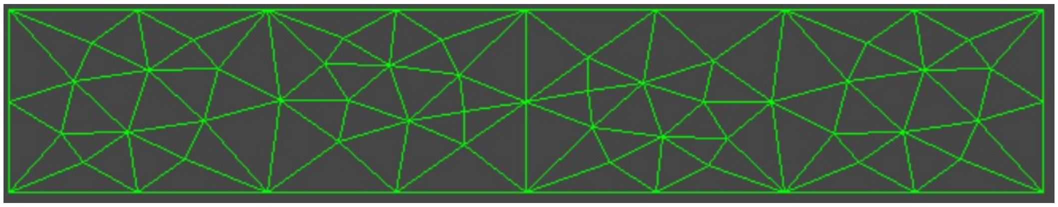

b) 0.8 m element length

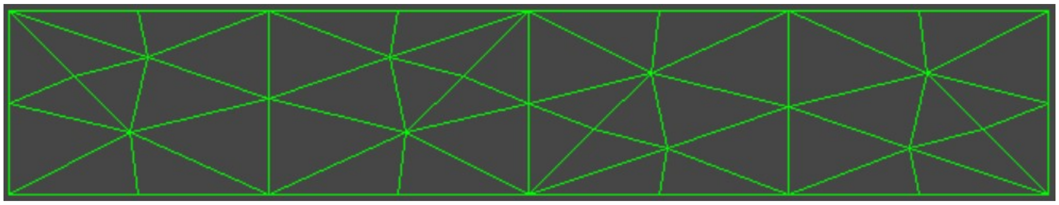

c) 1.0 m element length

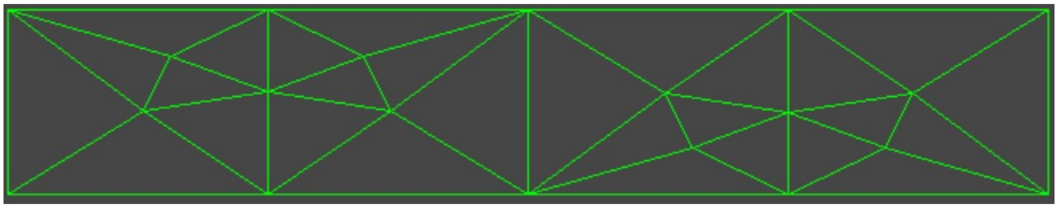

d) 1.5 m element length

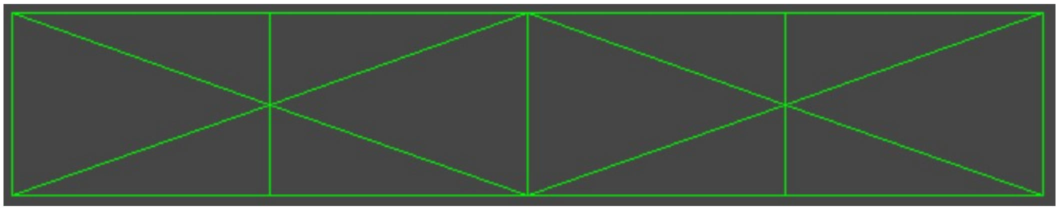

e) 2 m element length

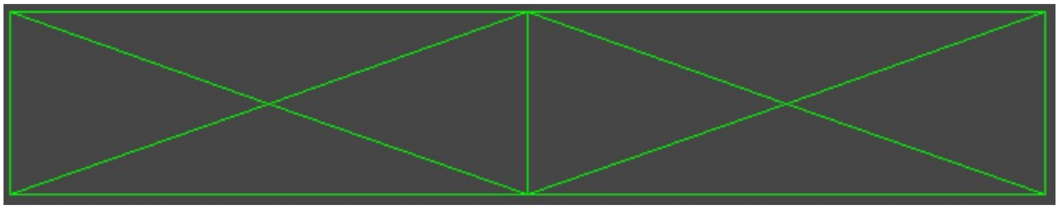

Figure 4-4 Different minimum element sizes generated using the edge mesh in a 1 m high and 5 m long model. Each intersection is a nodal point where Equations of motion are calculated

a) 0.5 m element length

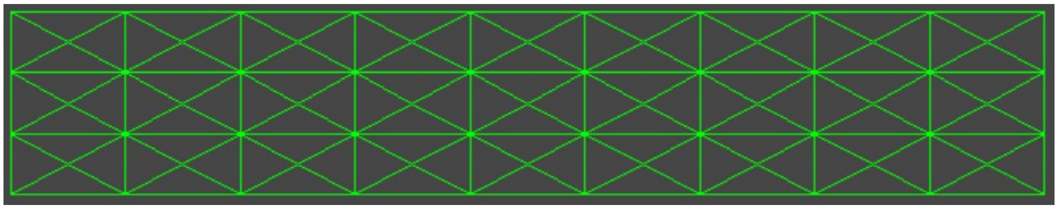

b) 0.8 m element length

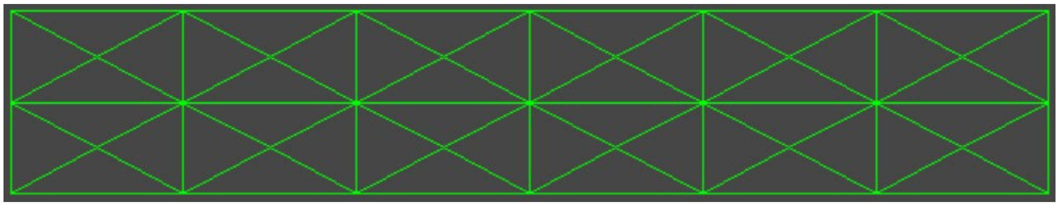

c) 1 m element length

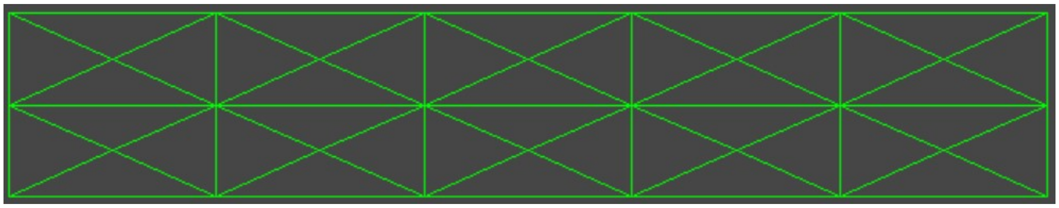

d) 1.5 m element length

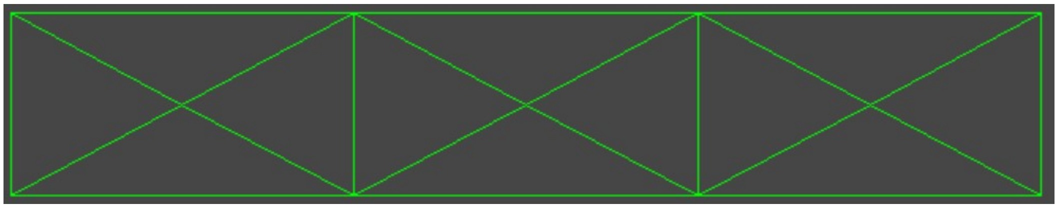

e) 2 m element length

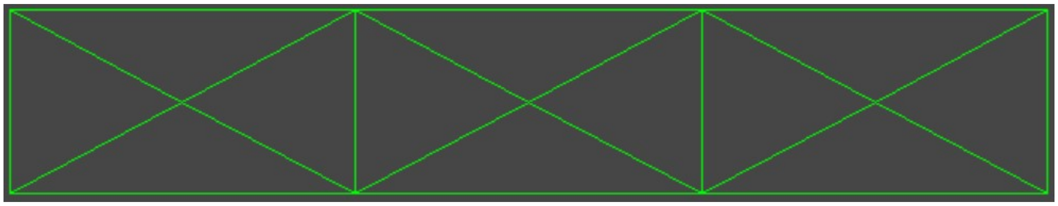

Figure 4-5 Different minimum element sizes generated using the quad mesh in a 1 m high and 5 m long model. Each intersection is a nodal point where Equations of motion are calculated

4.4.4. Effect of Input wave type, time step and frequency

This and the following sections (4.4.5 to 4.4.7) run through a sensitivity analysis to investigate how changes to the model set up and source input can affect how a model transmits waves. They are structured with an initial discussion of the aspect being investigated (i.e. wave type) with the sensitivity analysis split into the two different mesh types which can be used in UDEC, the edge mesh and the quad mesh.

Input Waves

There are numerous factors which can influence the transmission of stress waves through a numerical model. While a transfer function can handle any arbitrary wave, the quality of the transfer function is reliant on the wave itself. If the wave being used does not have a sufficient amplitude of waves over the frequency of interest, then the transfer function at these frequencies will be poor. Before any modelling is undertaken, this section will look at the frequency content of common wave sources to determine which might be most suitable for analysis.

In the time domain any input function will be composed of multiple different frequencies, but the exact function used to generate the input will dictate the relative amplitude of the frequency spectrum. Two simple functions are the Dirac delta function and the Heaviside function (Figure 4-6). The Dirac delta function is an impulse with an infinite force being applied for an infinitely short length of time, with the integral of the function equal to one. In Figure 4-6 the amplitude of the Dirac Delta function is shown to be equal to one, as it is impractical to give an infinite amplitude in a graphical form. In the time domain this function is impossible as an infinitely small modelling time step would be required; therefore, this function cannot be used. The Heaviside function applies a unit force from modelling time step zero to the end of the model run giving an equal amplitude to all frequencies. This is theoretically possible in the time domain; however, in the software being used here, UDEC, this is hard to implement as modelling time step zero is required to have no forces applied. Therefore, the Heaviside function goes from zero to 1 over the first modelling time step, leading to a shock within the model, which could lead to modelling issues. These two functions are consequently not used for modelling.

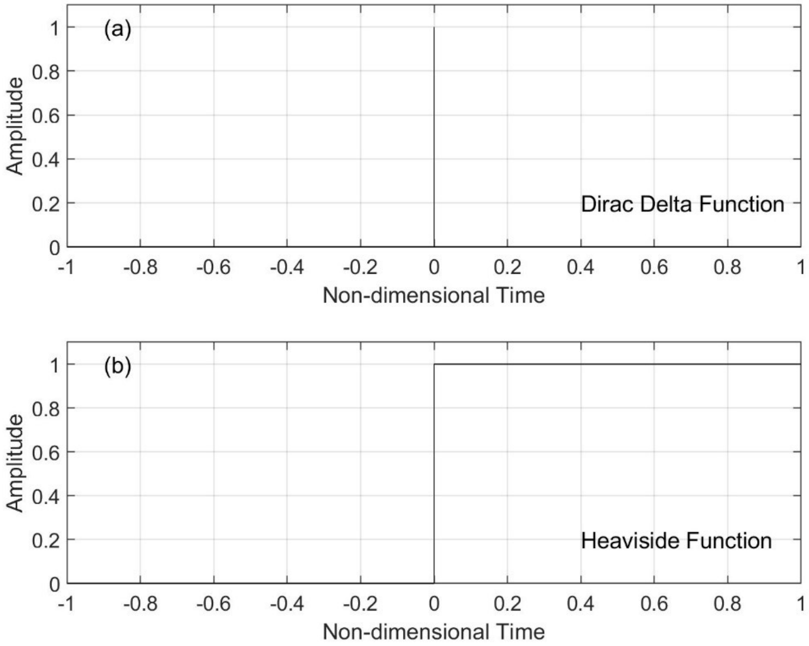

Figure 4-6 Impulse functions. a) Dirac Delta function, b) Heaviside function

Other wave functions can be used, such as the Gaussian function, and its derivatives, and the band limited cosine function.

Band Limited Cosine Function

The Equation for the band limited cosine function is included in Equation 3-1. This is similar to a cosine function, except it avoids generating high frequency content which would occur if a normal cosine function were used. The amplitude of the function at time “*t*” is given by Equation 4-11. The time series and frequency spectrum of the band limited function are shown in Figure 4-7.

$$A = 1 - \cos\left(2\pi\left(\frac{t}{T}\right)\right) \qquad \text{Equation 4-11}$$

Where *A*=amplitude of function, *T*=maximum time for signal (*T*=1/signal frequency), *t*=time from 0 to *T*.

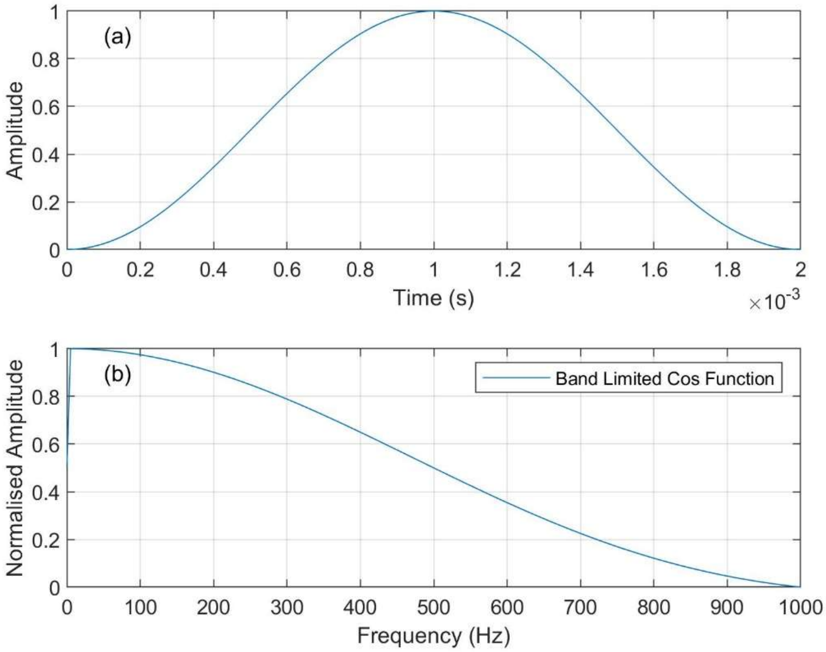

Figure 4-7 500Hz Band limited cosine function. a) Time series, b) Frequency spectrum

Gaussian Function

A Gaussian function is often used to define the probability density funciton of a normal distribution and is important in many areas of research. It can be calculated using Equation 4-12.

$$A = e^{-4\pi^2 f^2 \left(t - \frac{1}{f}\right)^2} \qquad \text{Equation 4-12}$$

Where *A*=amplitude of function, *t*=time and *f*=signal frequency.

The derivatives of the Gaussian function are smooth, with even order derivatives being even functions (symmetric about zero). The Gaussian function itself is a 0th order derivative. The odd order derivatives are odd functions, which are antisymmetric about zero. This is illustarted in Figure 4-8 a, with the frequency content of the waves shown in Figure 4-8 b. The second derivative of the Gaussian function is called a Ricker Wave and is often used as an approximation of an impulse function.

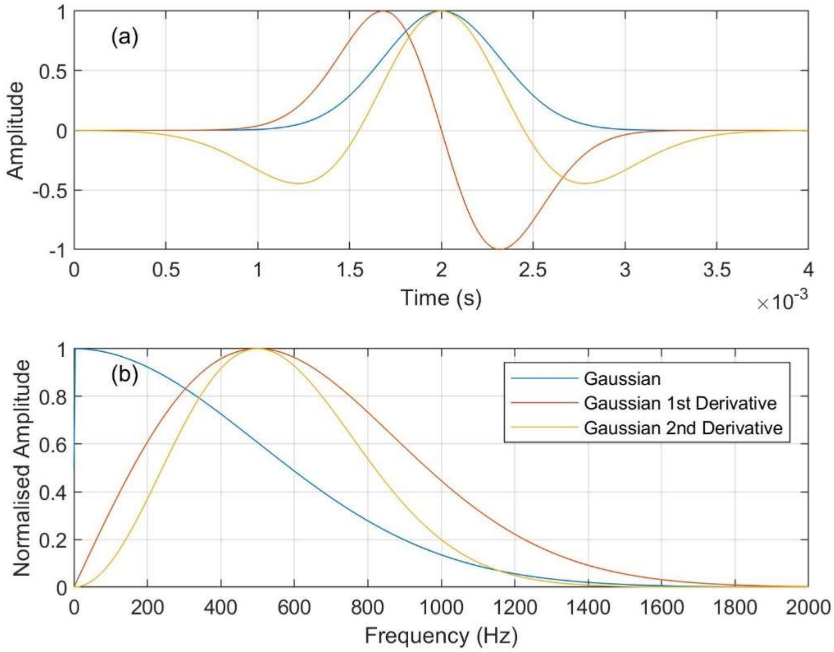

Figure 4-8 500Hz Gaussian functions. a) Time series, b) Frequency spectrum

The following section models each input wave function given above to determine which is most suitable for determining transfer functions. The input wave time step is assessed. This is the time step used as the time history of the excitation in UDEC, rather than the time step used for the UDEC solver, (1E-4, 1E-5 and 1E-6 seconds). For clarity the wave time step will be referred to as wave interval. Two different wave frequencies (100 and 200 Hz) are modelled for each wave type.

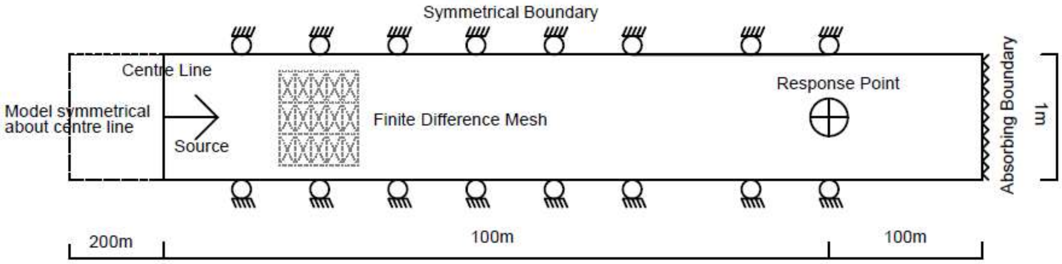

Figure 4-9 UDEC model used for sensitivity analysis

Figure 4-9 shows the model which was used for the sensitivity analysis. All analyses are run in models meshed using the edge and quad commands, introduced in the Section 4.4.3. The model is a single solid block of 400 m length, with an excitation applied in the centre of the model, 200 m from either lateral boundary. All models used have a model height of 1 m and a minimum mesh size of 0.8 m. The results of the sensitivity analysis are shown in Figure 4-10 and Figure 4-11, with the results discussed below. The results are processed using a transfer function, which shows the difference in the frequency content of the waveform at the source and at a response point 100 m from the source (Figure 4-9). This is achieved my decomposing each waveform into its frequency components using a Discrete Fourier Transform (DFT) and comparing the strength of each frequency (Equation 4-1). This procedure is illustrated in Figure 4-3 for an idealised, undamped continuum model. A plane wave travelling through an undamped 1D continuum should not be modified as it is transmitted, giving a constant transfer function at an amplitude of 1 for all frequencies. However, if the model is not set up correctly the wave could be affected during transmission, diverging the amplitude of the transfer function from 1. This provides a useful test of the performance of 1D continuum models, which will be used to determine the optimum set up of a model for transmission of stress waves through a sensitivity analysis in the following sections of this Chapter.

Edge Mesh Sensitivity Analysis

This sub-section details the performance of different waveforms in models meshed using the edge mesh. The wave interval, wave type and wave frequency are investigated in turn.

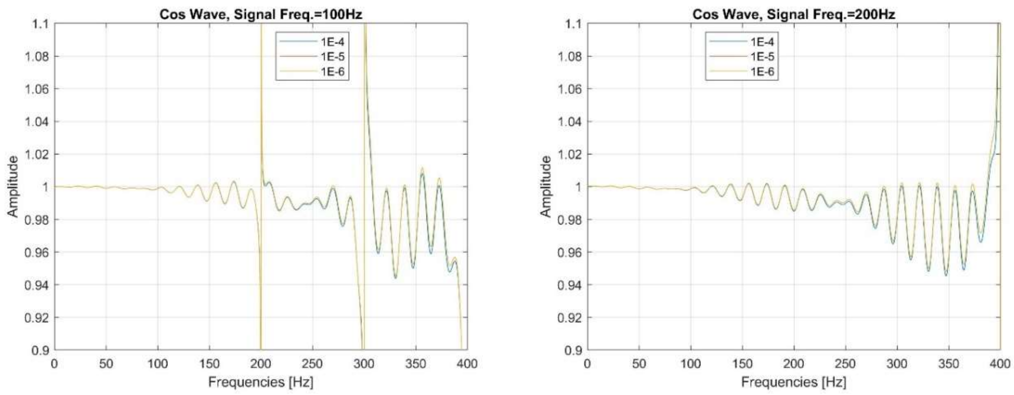
a) b)

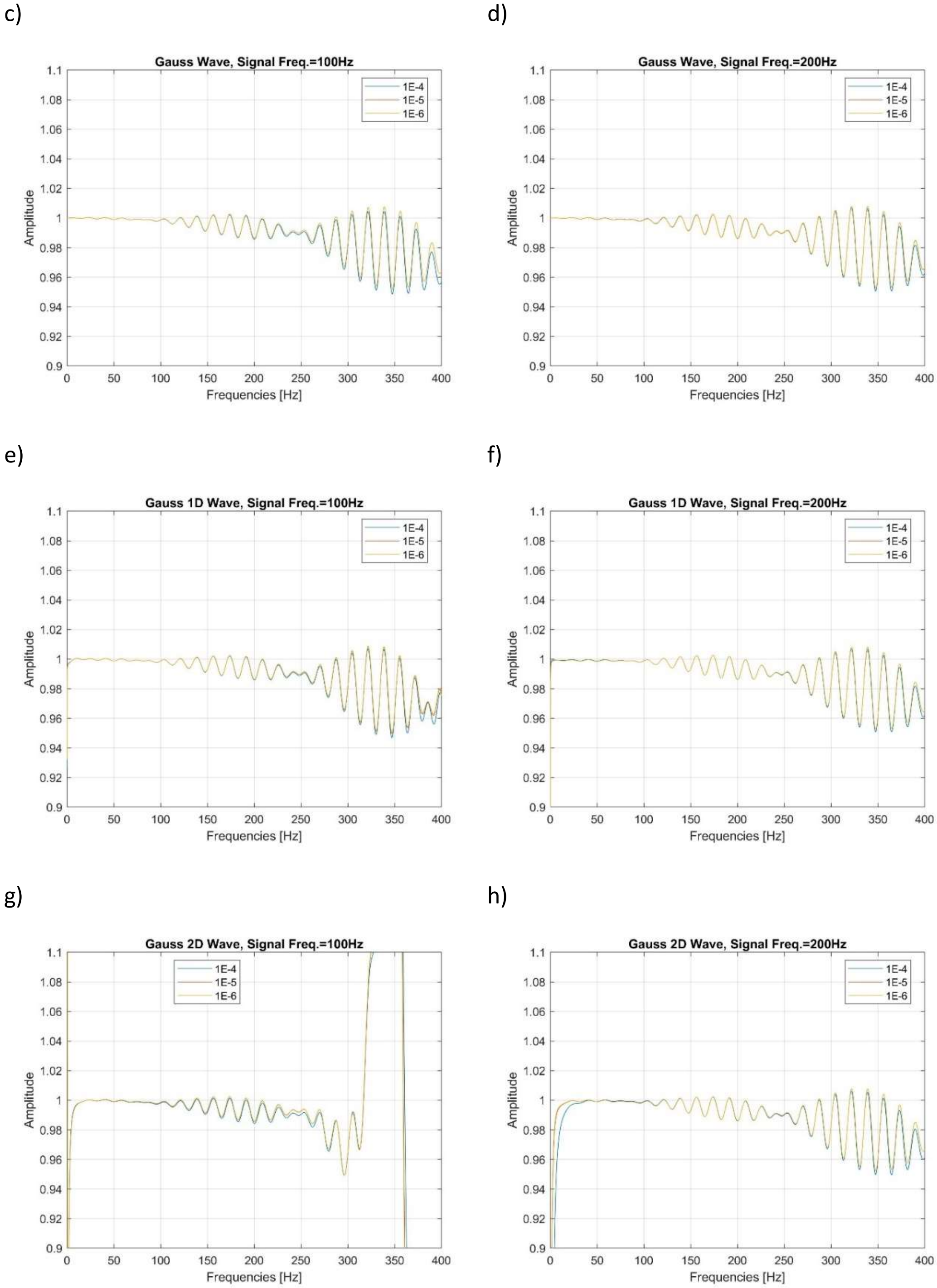

Figure 4-10 Frequency Response Function for 100 and 200 Hz waves with wave intervals of 1E-4, 1E-5, 5E-6 and 1E-6 seconds for Cosine (a-b), Gaussian (c-d), Gaussian first derivative (e-f) and Gaussian second derivative (g-h) waves for a 0.8 m element size edge mesh

Effect of Wave Interval

Figure 4-10 shows that reducing the wave interval, from 1E-4 to 1E-6 seconds, for the input function changes the frequency response function derived from the model. A smaller wave interval will allow UDEC to input the wave functions more accurately to the model; however, it is not clear exactly what the wave interval should be. Figure 4-10 shows that the wave interval of 1E-4 seconds produces a frequency response function which is clearly different from the other functions, with more noise generated in the transfer function at high frequencies, indicating that this wave interval is too long. This indicates that a wave interval of 1E-5 seconds is the maximum wave interval allowable for the input function for this particular UDEC model, with a modelling time step of 5E-6 seconds. However, the error caused by a longer wave interval is minor. Despite this, it is advantageous for the wave interval to be no more than twice the modelling time step. However, there is no computational disadvantage of having a smaller wave interval, so a wave interval as small as practicably possible should be used. For the other modelling scenarios in this section a wave interval of 1E-6 seconds is used.

Effect of Wave Type

Figure 4-10 shows four different wave functions being used as an input function: a band limited cosine function (a-b), a Gaussian function (c-d), a first derivative of the Gaussian function (e-f) and a second derivative of the Gaussian function (g-h). Each of the frequency response functions show differences when compared, although there are also some key similarities.

All four functions show a nearly constant response up to 100Hz, followed by an increase in the variability of the transfer function, centred around a value of just less than one. Figure 4-10 b, c, d, e, f, g, h show that there is then a reduction in the variability down to a variation around the amplitude of 0.99, which is followed by an increase in the variability in Figure 4-10 b, c, d, e, f, h. This shows that the model responds in similar ways when the model is excited by the same frequency of wave, even though different wave types are used. Differences are the low amplitude low frequency responses with the second derivative Gaussian function (Figure 4-10 g, h); high and low responses at double the wave frequency and following multiples of the wave frequency with the cosine function (Figure 4-10 a, b) and high responses at approximately 1.5 times the wave frequency for the second derivative of the Gaussian function (Figure 4-10 g). The Gaussian and first derivative of the Gaussian function appear to be the most stable functions to use to generate the frequency response functions, based on Figure 4-10.

Effect of Predominant Frequency

The input functions in Figure 4-10 have been generated with two different wave frequencies: 100Hz (a, c, e, g) and 200Hz (b, d, f, h). These are the central frequency of the waves, and a wide band source is generated, as shown by Figure 4-7 and Figure 4-8.

There are similarities between the frequency response functions for the two wave frequencies used, with the only differences being at multiples of the wave frequency, as previously described. The frequency used for the input signal does not appear to influence the response of the model, with exceptions being made for the cosine and second derivative of the Gaussian function, which show variable responses related to multiples of the input wave frequency, as previously described.

Quad Mesh Sensitivity Analysis

This sub-section details the performance of different waveforms in models meshed using the quad mesh. Each input to the source has been investigated in turn.

a)

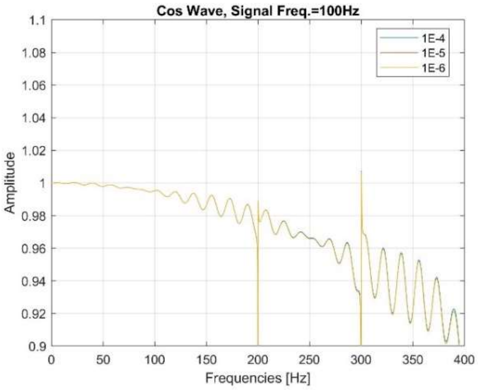

b)

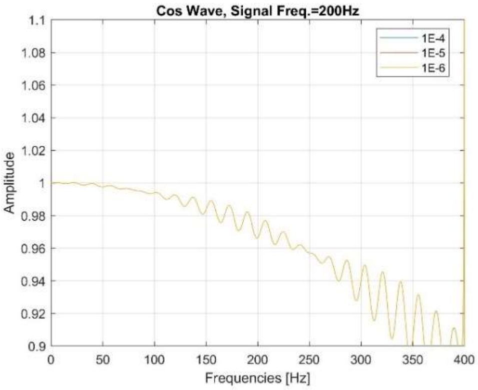

c)

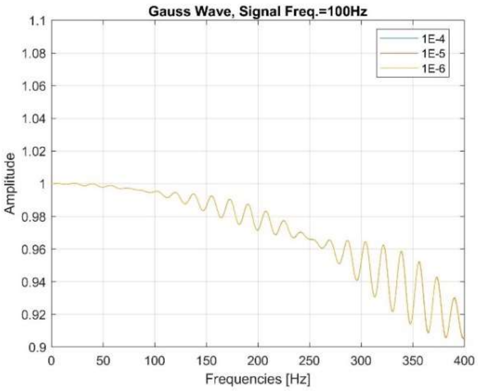

d)

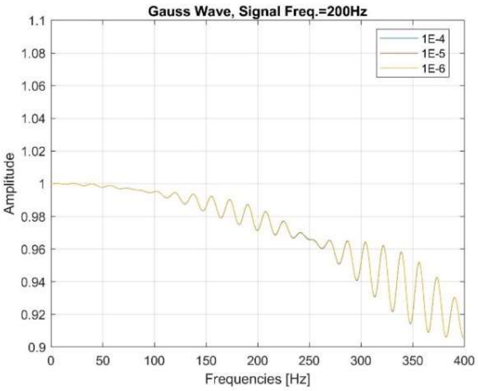

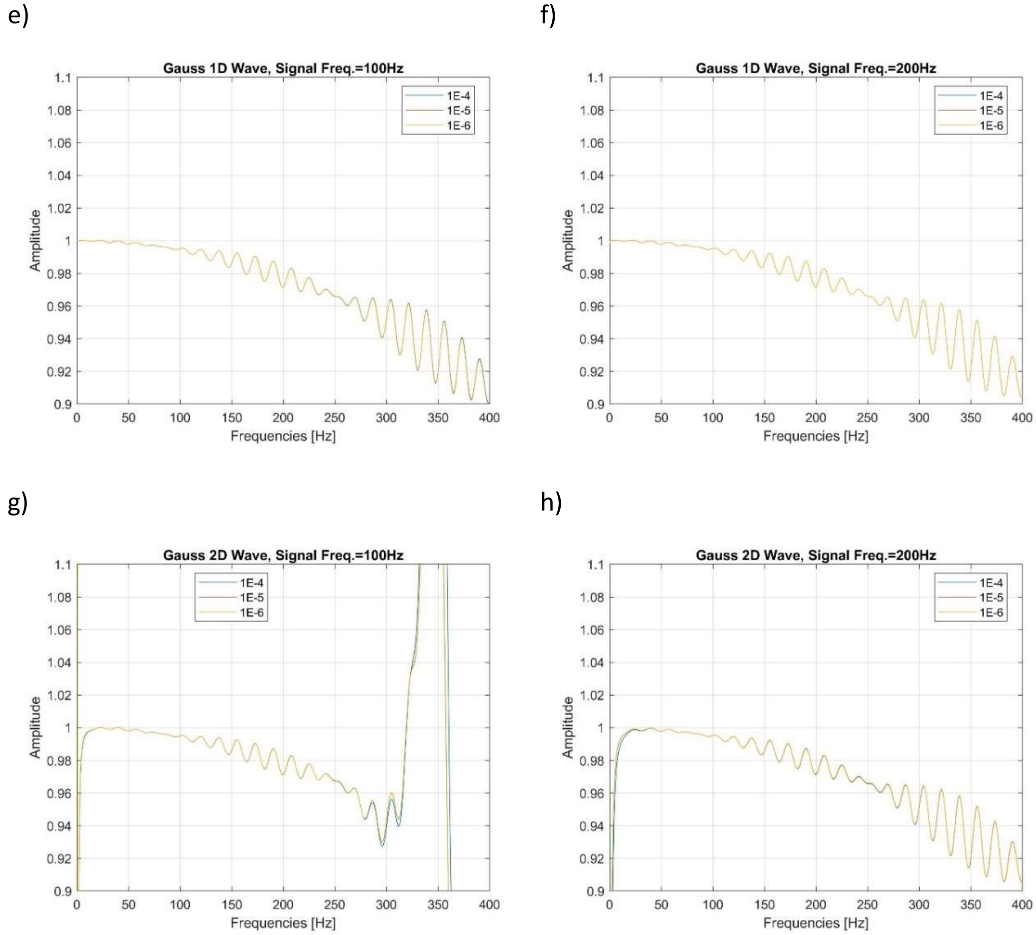

Figure 4-11 Frequency Response Function for 100 and 200 Hz waves with wave intervals of 1E-4, 1E-5, 5E-6 and 1E-6 seconds for Cosine (a-b), Gaussian (c-d), Gaussian first derivative (e-f) and Gaussian second derivative (g-h) waves for a 0.8 m element size quad mesh

Effect of Wave Interval

Figure 4-11 shows that reducing the wave interval, from 1E-4 to 1E-6 seconds, for the input function does not appreciably change the frequency response function derived from the model. At some points within the models, it is possible to discern the 1E-4 seconds wave interval; however, the 1E-5 seconds wave interval does not seem to show a significantly different response to the 1E-6 seconds wave interval. The models in Figure 4-11 have a modelling time step of 7.5E-6 seconds, so the 1E-5 seconds wave interval is not too dissimilar to the modelling time step, unlike in Figure 4-10. The minimum wave interval for these models appears to be 1E-5 seconds; however, for the other modelling scenarios in this section a wave interval of 1E-6 seconds will be used.

Effect of Wave Type

Figure 4-11, as with Figure 4-10, shows four different wave functions being used as an input function: a band limited cosine function (a-b), a Gaussian function (c-d), a first derivative of the Gaussian function (e-f) and a second derivative of the Gaussian function (g-h).

The general trend for all four functions is that the amplitude of the transfer function reduces as the frequency of the wave increases. This is divergent from the trends observed in Figure 4-10, where the amplitude of the transfer functions reduced less as the frequency increased. For example, up to 400 Hz the Gaussian waves in Figure 4-10 c and d with the edge mesh has transfer function amplitudes confined between 0.94 and 1.02, while the same wave for the quad mesh in Figure 4-11 c and d has transfer function amplitudes between 1.0 and 0.9. The spread of values for the quad mesh appears to be greater than the edge mesh and the residuals, from the idealised transfer function amplitude of one, increase too.

Between each of the quad mesh waves in Figure 4-11 the transfer functions compare similarly with those in Figure 4-10, with differences likely being caused by the differences in the input waves as described earlier in this section.

Similarly, as found with Figure 4-10, the Gaussian, Gaussian first derivative and Gaussian second derivative input wave functions appear to give the best transfer functions for further use. This is due to the erratic nature of the band limited cosine function at multiples of the signal frequency observed in Figure 4-11 a and b.

Effect of Predominant Frequency

The input functions in Figure 4-11 have been generated with two different wave frequencies: 100Hz (a, c, e, g) and 200Hz (b, d, f, h). The similarities and differences observed appear to be the same as those observed in Figure 4-10. This indicates that the model is modelling the waves in the same way, despite the different input wave functions and associated distribution of frequencies.

Although the most suitable wave to use cannot be decided upon at this stage, the band limited cosine function does not perform well. Therefore, this wave type will not be used for further analysis.

4.4.5. Effect of Element Size

Previous researchers have identified that the mesh size used in modelling is crucial in order to reduce the effects of numerical dispersion. Kuhlemeyer and Lysmer (1973) showed that an element size at least 10 times smaller than the minimum wavelength is required to prevent numerical dispersion. This has been corroborated by further studies (Hildyard, 2001). The models used in the previous section used a 0.8m mesh throughout and a P-wave velocity of 3328 m/s. This means that it is unlikely that the models will be able to accurately model a wave with a frequency greater than 416 Hz.

Another important consideration of the mesh size for a 1D model revolves around how a model, which is strictly speaking 2D, operates as a 1D model. Figure 4-4 and Figure 4-5 show the meshing of a 1m high model using elements of different sizes. In both Figures, when the mesh size is half of the model height the model shows a dense mesh. As the Equations of motion are calculated at every vertex these dense meshes with a small element size will allow a greater freedom of movement within the model. In contrast, when the element size is double the model height there is a much less dense mesh generated with less vertices within the model, giving the model a reduced ability to move in the vertical direction. This larger mesh size could potentially be considered more of a 1D scenario than the smaller mesh size, as when 1D is referred to it is the movement of waves along the long axis of the model which is of interest.

Putting the above in a different way and considering an unlimited amount of computer power, as the time step is related to the element size, the modelling software does not really care if the model is 1 Å tall or 1 pc tall, both could be considered 1D or 2D using a suitable mesh size. The intuitive concept of a small (i.e. 1 Å) model being more like a 1D scenario than a very tall model (i.e. 1 pc) is more of a projection of how we would normally view the world, not in the way a computer models a situation.

In the real world, which is limited by a finite amount of computing power, our models are limited in their maximum extents. However, to avoid dispersion a large element size is to be avoided; therefore, reducing the model height. For this reason, a 1 m model height is arbitrarily selected for use. It is not necessarily the optimum model height for a 1D analysis, or for the desired range of frequencies, but it is a useful and obvious starting point from which to explore the most suitable model height. This also conforms with the model height used by Cai & Zhao (2000), among others.

To explore the effects of the element size in a 1 m high model, with both the edge and quad meshing methods excited by the Gaussian wave and its derivatives, Figure 4-12 to Figure 4-17 were generated. Each Figure for each mesh type is discussed in turn below. The load is applied to the end of the model in this section, as opposed to being applied in the centre of the model as in the previous Figures. This is necessary as it is not possible to apply an internal load where there are no nodal points, which can occur in the centre of the model when the element size is large. Therefore, for continuity of the input loading function all loads have been applied at the end of the model.

Edge Mesh Sensitivity Analysis

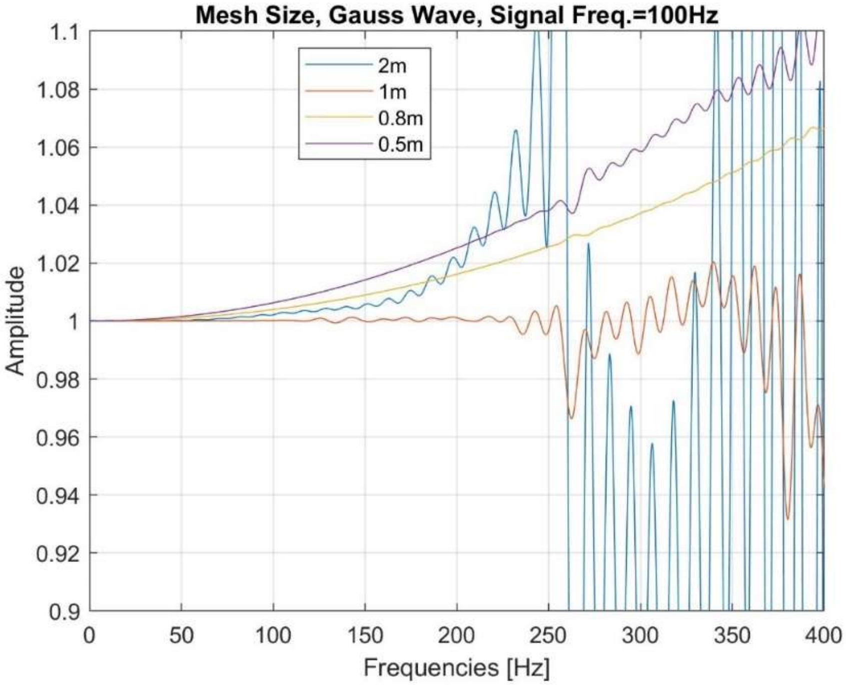

Figure 4-12 Frequency response functions for different edge mesh element sizes using a 100 Hz Gaussian wave in a model with a P-wave velocity of 3328 m/s with a load applied to the end of the model

Figure 4-12 shows the Gaussian input wave, with a 100 Hz signal frequency, in a 1 m high model with edge mesh element sizes of 0.5, 0.8, 1 and 2 m. This shows that when the element size is equal to the model height the transfer function is approximately constant at a value of 1 up to about 200 Hz. Reducing the element size gives a less accurate transfer function, even leading to amplification of the waves. This adds support to the concept of a 1D model previously discussed, as the smaller mesh size will give more mesh elements out of the plane of wave propagation. The 2 m element size is an interesting concept, as this appears to give the next best transfer function after the 1 m model up to 200 Hz. The same relative trends of the transfer functions are also observed when using the Gaussian 1st derivative and Gaussian

2nd derivative waves in Figure 4-13 and Figure 4-14, with some differences being caused by the exact input wave function.

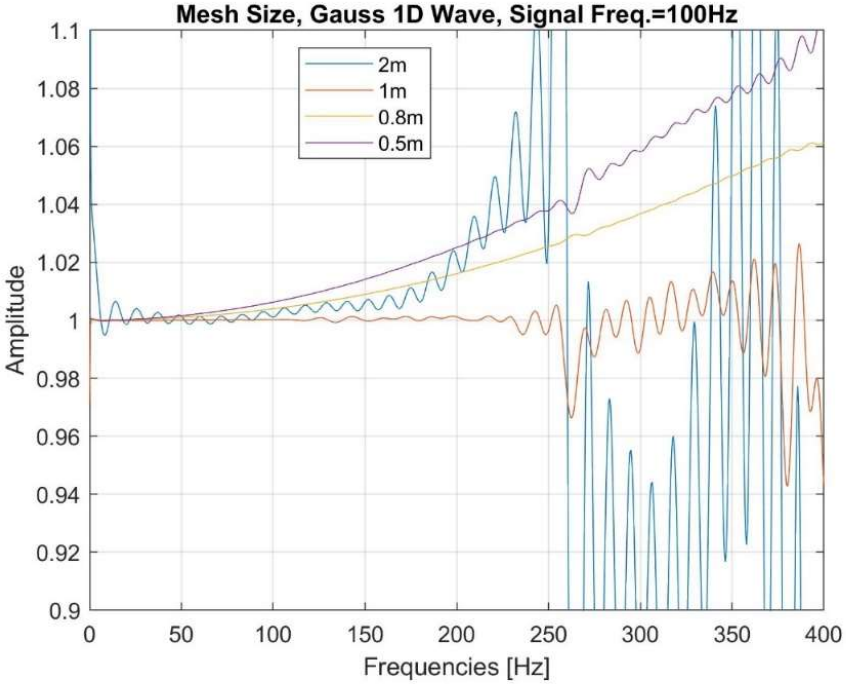

Figure 4-13 Frequency response functions for different edge mesh element sizes using a 100 Hz Gaussian first derivative wave in a model with a P-wave velocity of 3328 m/s with a load applied to the end of the model

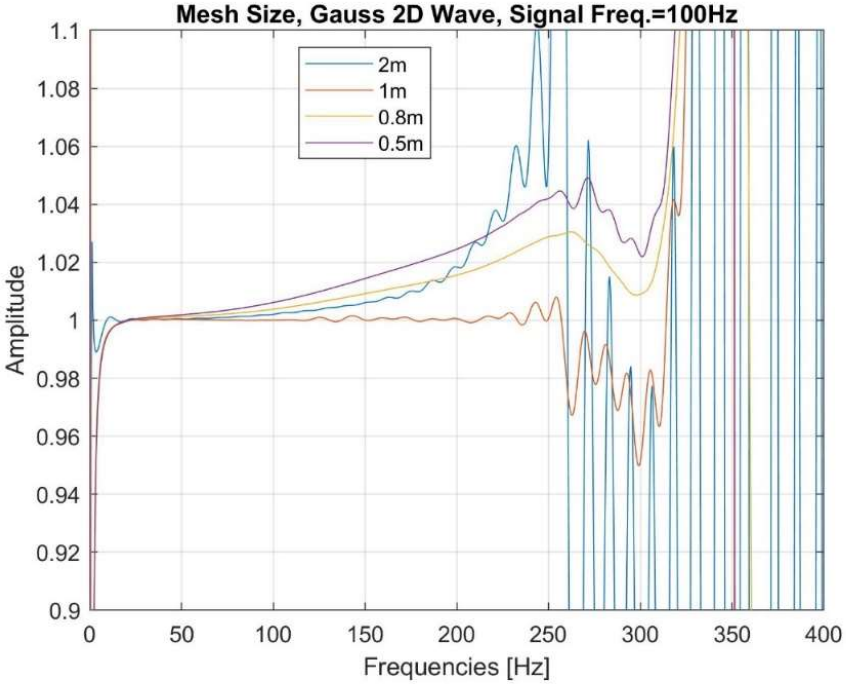

Figure 4-14 Frequency response functions for different edge mesh element sizes using a 100 Hz Gaussian second derivative wave in a model with a P-wave velocity of 3328 m/s with a load applied to the end of the model

Quad Mesh Sensitivity Analysis

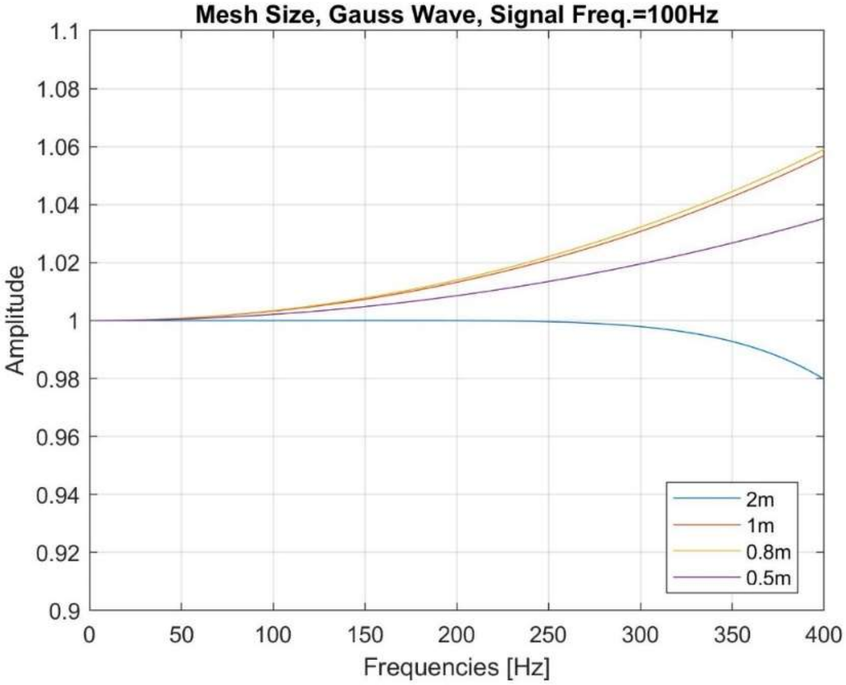

Figure 4-15 Frequency response functions for different quad mesh element sizes using a 100 Hz Gaussian wave in a model with a P-wave velocity of 3328 m/s with a load applied to the end of the model

Figure 4-15 shows the Gaussian input wave, with a 100 Hz signal frequency, in a 1 m high model with quad mesh element sizes of 0.5, 0.8, 1 and 2 m. The best transfer function is clearly derived from the 2 m element size, which is very close to one until about 250 Hz, from where it diverges. The other mesh sizes show no trend; however, when viewed in the context of Figure 4-5, indications to what could be occurring can be found. When the element size is less than or equal to the model height additional modelling nodes can be fitted into the model. Therefore, making the model diverge from being 1D. This interplay of additional modelling nodes and a smaller element size, allowing a greater accuracy of the modelling of higher frequencies, is expected to have caused the irregular pattern of the data series in Figure 4-15. However, what is clear is that when the mesh size is greater than the model height, the accuracy of the transfer function is increased.

The same trends observed in Figure 4-15 are also seen in Figure 4-16 and Figure 4-17, with exceptions for the usual differences seen in the wave inputs. When comparing Figure 4-11 with the Figures in this section it is clear that the change in the position of the loading has altered the transfer functions. The end loading seen in this section appears to be a considerable improvement on the central loading in Figure 4-11. This will be explored further in Section 4.4.7.

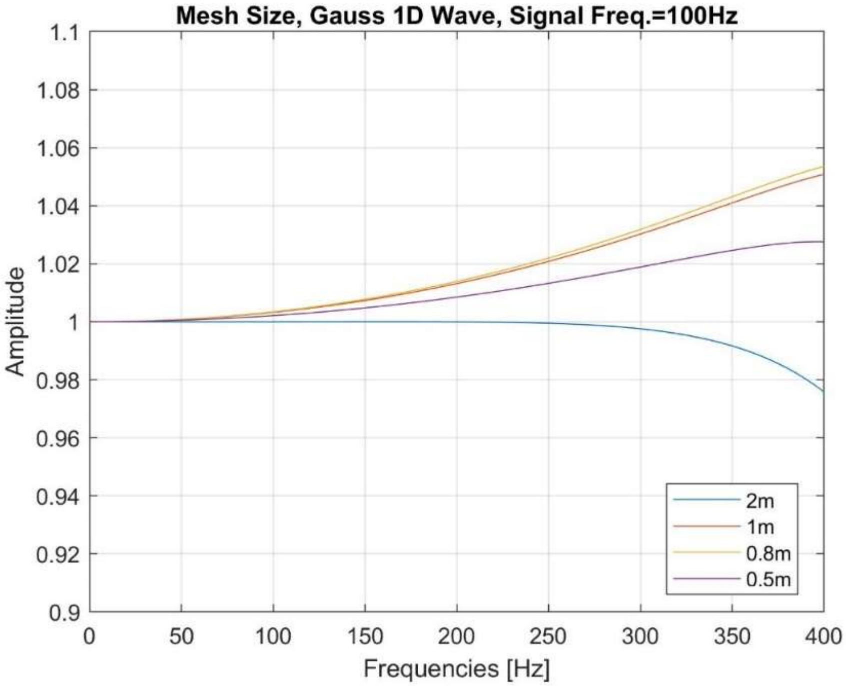

Figure 4-16 Frequency response functions for different quad mesh element sizes using a 100 Hz Gaussian first derivative wave in a model with a P-wave velocity of 3328 m/s with a load applied to the end of the model

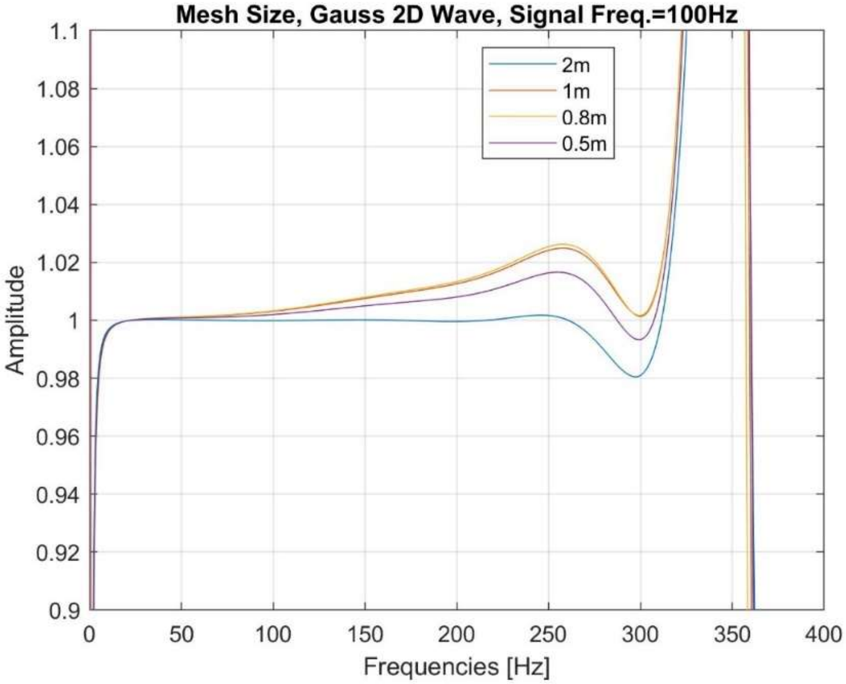

Figure 4-17 Frequency response functions for different quad mesh element sizes using a 100 Hz Gaussian second derivative wave in a model with a P-wave velocity of 3328 m/s with a load applied to the end of the model

4.4.6. Model Height

In this section the effect of the model height will be assessed. In each model a wave interval of 1E-6 seconds is used, and the mesh size is equal to the model height. End loading input functions are used, as modelled in the previous section. Both mesh types are assessed, although only a 100 Hz signal frequency Gaussian wave is modelled.

Edge Mesh Sensitivity Analysis

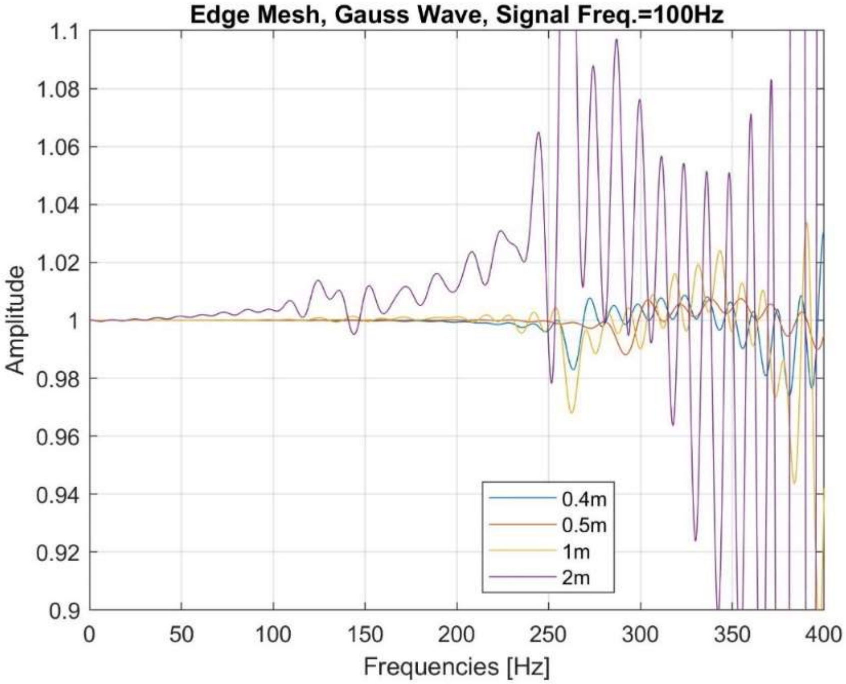

Figure 4-18 Frequency response functions for different sized models with edge mesh element sizes equal to the model height with a Gaussian wave function

Figure 4-18 shows how changing the model height, with an equal edge mesh element size, affects the transfer function. For example, a 1 m high model has a square mesh of 1 m x 1 m and a 2 m model has a square mesh of 2 m x 2 m. It is clear from the Figure that the 2 m model height / element size combination performs least well out of those modelled. This is to be expected as the large element size will not be able to model such a wide range of frequencies as the smaller element sizes. The 1 m element size appears to perform better than the 2 m element, but not as well as the 0.5 m element. When the 0.5 and 0.4 m elements are compared the 0.5 m element appears to be performing marginally better than the 0.4 m model height. The reasons behind this reversal in trend are not clear.

Quad Mesh Sensitivity Analysis

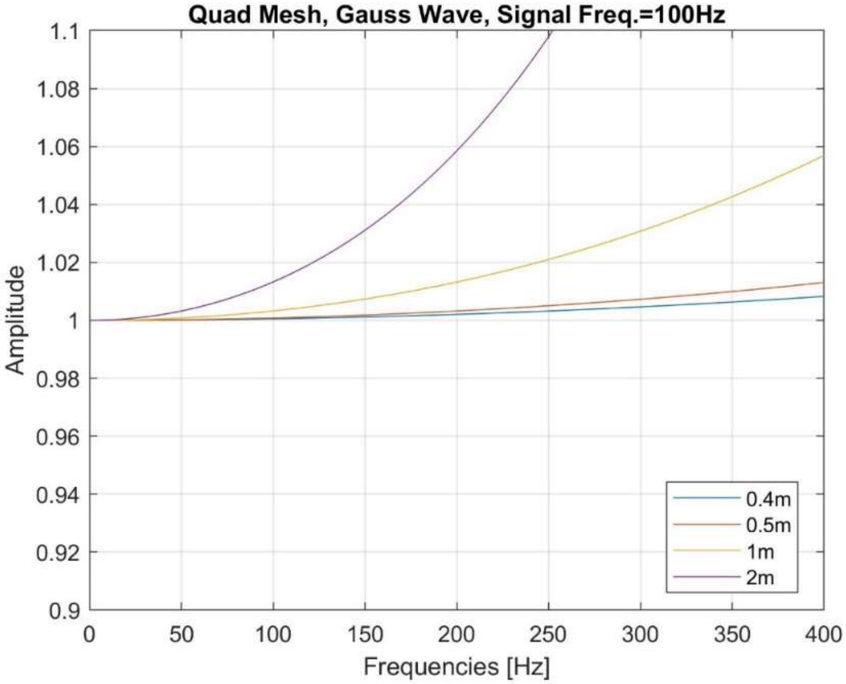

Figure 4-19 Frequency response functions for different sized models with quad mesh element sizes equal to the model height with a Gaussian wave function

Figure 4-19 shows how changing the model height, with an equal quad mesh element size, affects the transfer function. This is identical to the mesh set up as used in Figure 4-18, but with the quad mesh type. Unlike in Figure 4-18, the model height to quality of transfer function appears to be correlated. The 2 m model element size performs worst, based on its divergence form an amplitude of 1, and the 0.4 m model element size performs best. The 1 m and 0.5 m models fit between the upper and lower bounds of the 2 m and 0.4 m models.

When Figure 4-18 and Figure 4-19 are compared it is clear that the quad mesh gives better transfer functions than the edge mesh, when the model is loaded at the end. The outcome of this sensitivity analysis, showing that a small model height / element size quad mesh performs well and the outcome of the previous section, which showed that an element size larger than the model height improves the transfer function, indicates that there could be further improvements made to the transfer functions. This would be done by having a small model height with a large element size and would be expected to have the effect of not only improving the transfer function over a wide range of frequencies but also preventing over prediction of the amplitude of transfer functions past a limiting frequency.

4.4.7. Effect of Input Type and Position

The previous sections use both end loads and central loads as the input excitation. This section directly assess the effect of these changes by plotting the transfer functions beside each other. In addition to this a velocity input function is also modelled to determine the validity of using this as an input excitation to the model.

A 100 Hz signal frequency Gaussian wave is used as the input wave function in this section. All models have a height of 1 m and an element size of 0.8 m, allowing both end loading and central loading functions to be used.

Edge Mesh Sensitivity Analysis

Figure 4-20 shows that the different input functions and locations give different transfer functions with the edge mesh. The worst performing input is a centrally applied velocity function, as this gives a transfer function which is extremely divergent from an amplitude of one. The end velocity function on the other hand performs the best out of all the models. The two loading positions perform differently, with the end load increasing in amplitude along a reasonably smooth curve and the central loading function reducing in amplitude with an oscillating wave form.

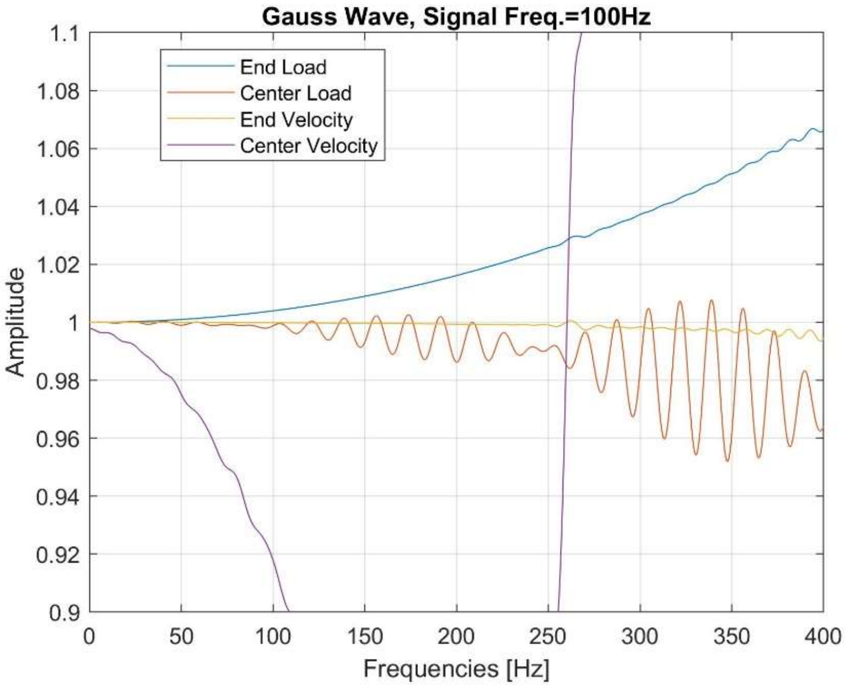

Figure 4-20 Frequency response function for an end and centre loads and velocities with a 100 Hz Gaussian wave input function and a 0.8m edge mesh element size in a model with a P-wave velocity of 3328 m/s

Quad Mesh Sensitivity Analysis

Figure 4-21 shows that the different input functions and locations give different transfer functions with the quad mesh. The trends found with the quad mesh seem to be similar with those found with the edge mesh in Figure 4-20. The worst performing function is a centrally applied velocity, and the best performing function is a velocity applied to the end of the model. The centrally applied load reduces in amplitude in an oscillatory fashion and the end load increases along a smooth curve. This supports the assumption that the inputs to the models are the same, with the differences in the transfer functions being caused by the mesh types themselves.

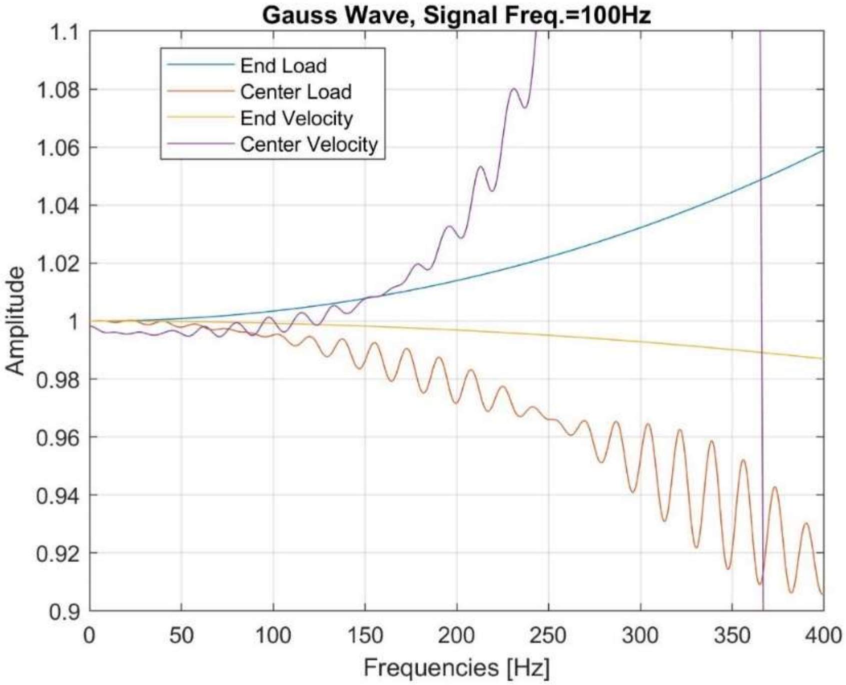

Figure 4-21 Frequency response function for an end and centre loads and velocities with a 100 Hz Gaussian wave input function and a 0.8m quad mesh element size in a model with a P-wave velocity of 3328 m/s

From this and the previous sections it is shown that the quad mesh can be used to give the smoothest transfer functions when combined with an end excitation.

4.4.8. Outcome of Parametric analysis

The parametric analysis presented can be used to determine the most appropriate combination of modelling setup options to be used to generate the most accurate transfer function possible from a 1D numerical model. The accurate transfer function is an outcome of a model which has limited numerical inaccuracies, such as numerical dispersion, which is discussed in 4.2.1. The outcome suggests the requirements detailed in Table 4-1 are needed for an accurate transfer function.

Table 4-1 Recommendations for optimum modelling of transfer functions using the finite difference method in UDEC

Modelling Option	Recommendation
Wave type	Gaussian Wave
Wave interval	Equal to or less than the modelling time step
Excitation	End load or velocity function
Element size	As small a possible
Mesh type	Quad mesh
Model height	Less than the element size (this necessitates an end loading function)

4.4.9. 1D Continuum Transfer Functions

This section applies the findings of Table 4-1 to derive a transfer function for a continuum model. The recommendations in Table 4-1 consider both the input wave and the finite difference mesh. The input wave to be used in this section is a Gaussian wave and both velocity and loading functions are modelled to determine the best transfer functions from this. A short wave interval is used, such as the 1E-6 seconds wave interval used in previous sections; however, the critical wave interval is influenced by the modelling time step, which is influenced by the element size, so this is reviewed during modelling. The models shown in this section have a minimum modelling time step of 1.6E-6 seconds, so this requirement is met in all cases.

The element size requirements given in Table 4-1 are less precise, requiring further sensitivity analysis. However, the quad mesh function is used, and the element size is greater than the model height to assure a more realistic 1D scenario, with only one finite difference mesh zone in the vertical direction. It is possible to generate non-square meshed regions using the quad mesh. This is done by specifying a different size in the vertical and horizontal directions. Up until this point, models have been run using meshes with the same vertical and horizontal element sizes.

The element size used will dictate the ability of the model to transmit waves, with a smaller element size allowing a higher wave frequency to be transmitted. Therefore, the smaller the element size the more accurate the transfer function will be over a greater range of frequencies.

A model height of 0.2 m is used for the following transfer functions and a wave frequency of 100 Hz is used as the source.

Mesh Size

Loading Function

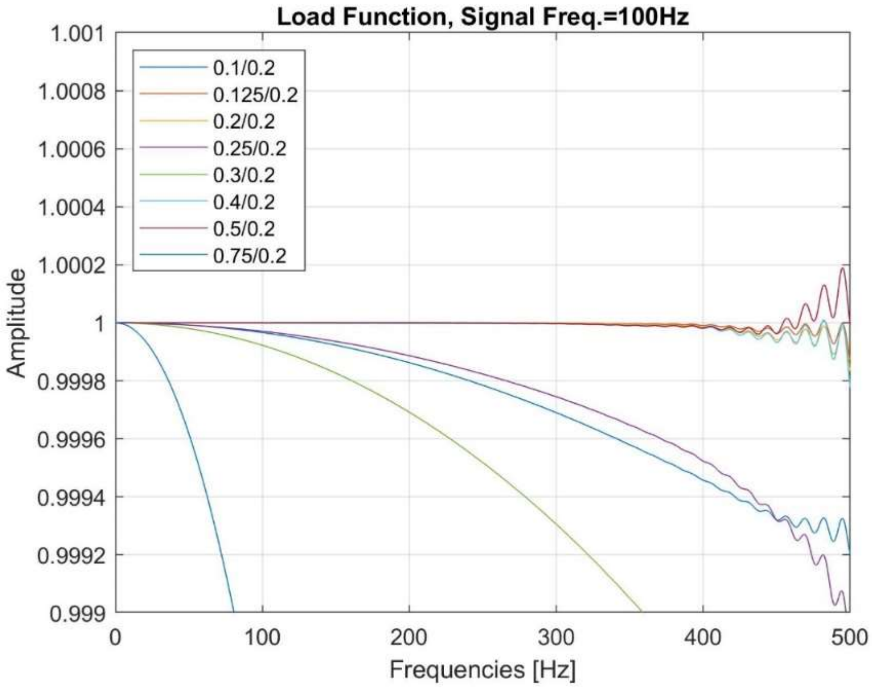

Figure 4-22 Transfer functions from 0 to 500 Hz with a 0.2 m model height and a changing horizontal element size using a loading input. Legend shows the horizontal and vertical element size (horizontal / vertical).

Figure 4-22 shows the effect on a transfer function of changing the element size in a 1D numerical model. The vertical element size is the size generated in the model, instead of the size input into the numerical code. The vertical element is limited to the model height, which is 0.2 m, with the mesh generator fitting the mesh into this limit. The actual value used for the input was 0.25 m. Figure 4-22 shows that the worst performing transfer function, defined as the transfer function which diverges most from one across the graphed range, has an element size of 0.75 m in the horizontal direction and 0.2 m in the vertical. This gives a ratio of 3.75:1 for horizontal to vertical element size. The general trend with the graphed data in this Figure is that as the horizontal element size decreases the transfer function improves. However, when interrogating the relationship of each of the data series in relation to each other there is a more complex relationship. For example, the best performing transfer function is when the horizontal element is 0.125 m, which gives a ratio of 0.625:1, but the smallest ratio of 0.5:1, from an element size of 0.1 m, performs quite poorly. The ratios of horizontal to vertical element size which perform well are 1:1, 2:1 and 2.5:1, along with 0.625:1 which has already been mentioned. This suggests that the ratio needs to be close to 1:1, although some variation is allowable.

Velocity Function

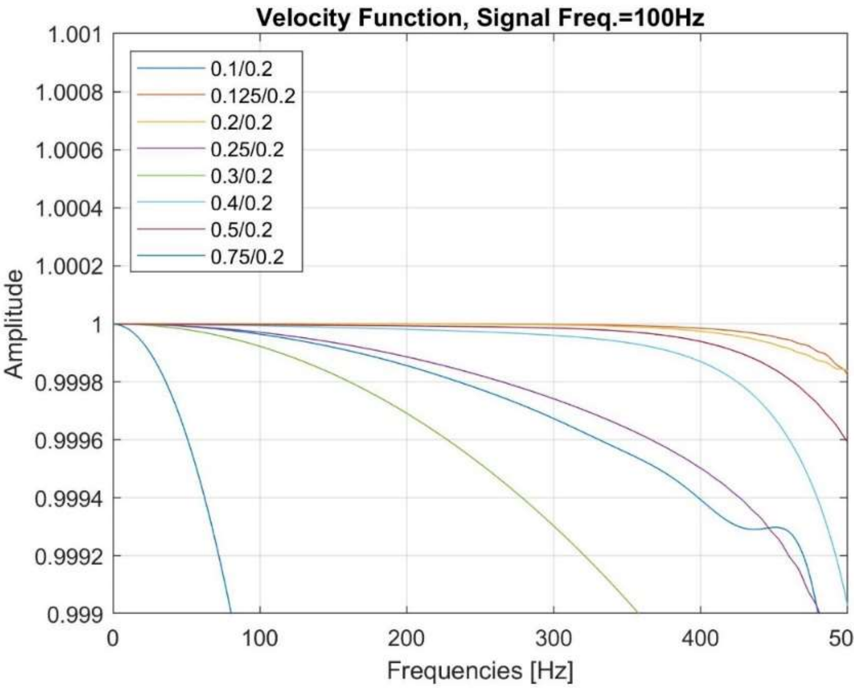

Figure 4-23 Transfer functions from 0 to 500 Hz with a 0.2 m model height and a changing horizontal element size using a velocity input. Legend shows the horizontal and vertical element size (horizontal / vertical).

Figure 4-23 shows many similar trends to Figure 4-22 for a velocity source function. These include the 0.75 m element showing the greatest divergence from 1, followed by the 0.3 m, 0.1 and 0.25 m elements. The best performing meshes are still 0.125 and 0.2 m, whereas the 0.4 and 0.5 m meshes do not perform as well as in Figure 4-22.

Vertical Mesh Size

All the models used to generate Figure 4-22 and Figure 4-23 use a vertical element height of 0.25 m. In a 0.2 m model, as used here, the model height will limit the vertical element size. Using a vertical element size greater than the model height ensures that a 1D modelling scenario is generated. To verify that this has no effect on the modelling results Figure 4-24 has been generated. In this Figure the vertical mesh height has been changed from 0.25 to 1.0 m, in a model with a 0.2 m height, using a constant horizontal element size of 0.2 m. In both cases the transfer functions for each vertical element height superimpose. Therefore, providing the vertical element size is greater than the model height, changing the vertical element size does not affect the meshing of the model, and by association the transfer function.

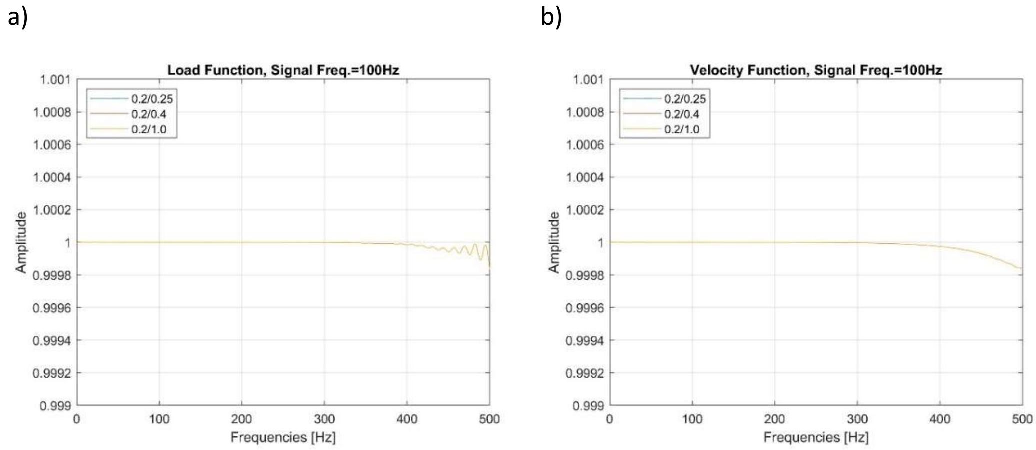

Figure 4-24 Variation in vertical mesh height with load (a) and velocity (b) excitations functions

Optimum Mesh Size

The optimum mesh size, based on the results in Figure 4-22 and Figure 4-23, is 0.125 m horizontally and 0.25 m vertically.

Optimum Wave Frequency for Optimum Mesh Size

A final sensitivity analysis has been run, where the input wave frequency is varied. Previously it was found that there was not an effect of increasing the input wave frequency from 100 to 200 Hz; however, in this section a greater range will be used.

Loading Function

Figure 4-25 shows how the transfer function varies for different signal frequencies of a Gaussian wave. This shows that both a high frequency (1000 Hz) and low frequency (100 Hz) give poor transfer functions. An optimum transfer function, over the 1000 Hz shown in the Figure, appears to be generated by a 400 or 500 Hz input wave. Over this range the error on the idealised transfer function of 1 is 0.01%. Whether this can be considered “good” depends on what the transfer function is to be used for; however, for the purpose of this study this has been considered to be reasonable.

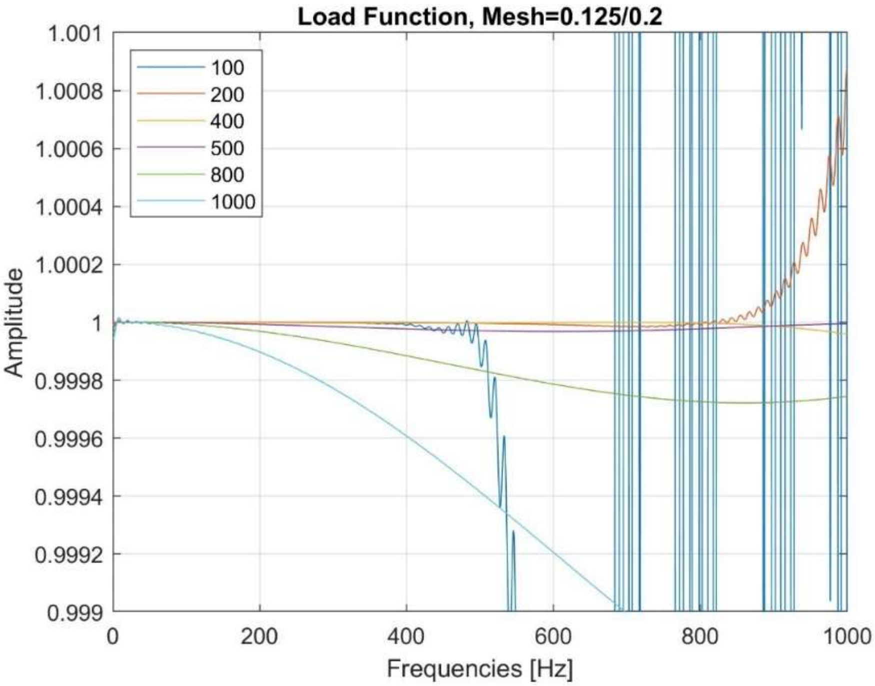

Figure 4-25 Transfer functions for varying input wave signal frequency using a 0.125/0.2 m mesh size in a 0.2 m high model with a loading function

Velocity Function

Figure 4-26 shows the transfer functions for input wave signal frequencies from 100 to 1000 Hz. Like in Figure 4-25, the low and high frequencies give poor transfer functions, with the best transfer functions being given by the 400 and 500 Hz signal frequency input waves. The 400 and 500 Hz waves also represent an error of less than 0.01% up to 1000 Hz, the same as found with the loading function.

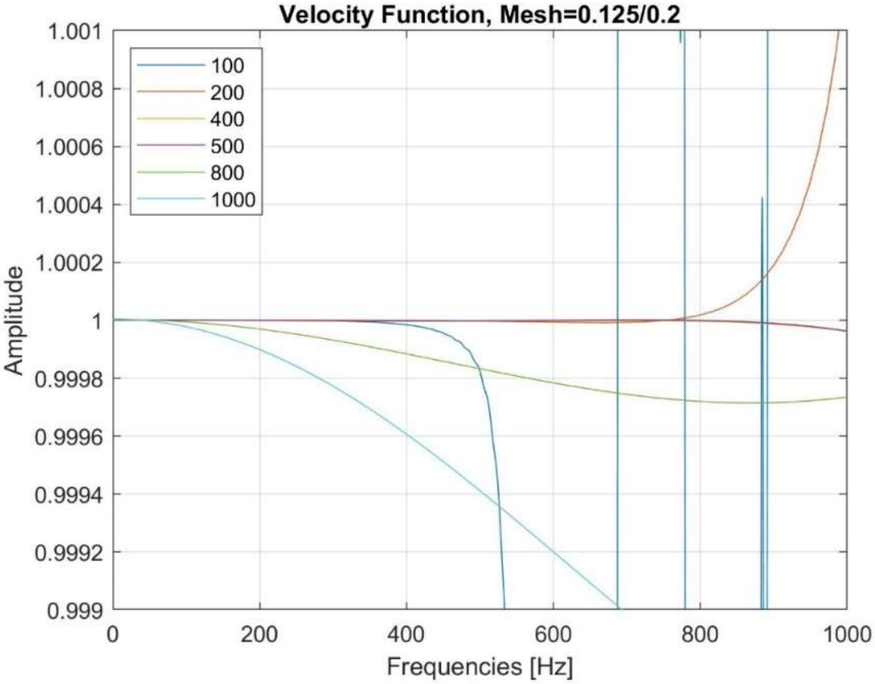

Figure 4-26 Transfer functions for varying input wave signal frequency using a 0.25/0.2 m mesh size in a 0.2 m high model with a velocity function

The frequency content of the 400 and 500 Hz waves are not the same but the results are similar. Therefore, selecting one or the other is arbitrary. Consequently, the 500 Hz wave has been selected for use in future numerical models.

4.4.10. Final Transfer Function for a 1D Continuum Model

Based on the above sensitivity analysis the transfer functions in Figure 4-27 are generated for loading and velocity inputs. This is achieved using a Gaussian wave with a 500 Hz signal frequency in a model with a horizontal element size of 0.125 m and a vertical element size equal to the model height of 0.2 m. Figure 4-27 shows a range of frequencies from 0 to 2000 Hz, which has been arbitrarily selected to show the accuracy of the transfer function over a large range of frequencies as opposed to the frequencies of interest in this thesis, which for train vibrations are typically up to 250 Hz (Ouakka et al., 2022).

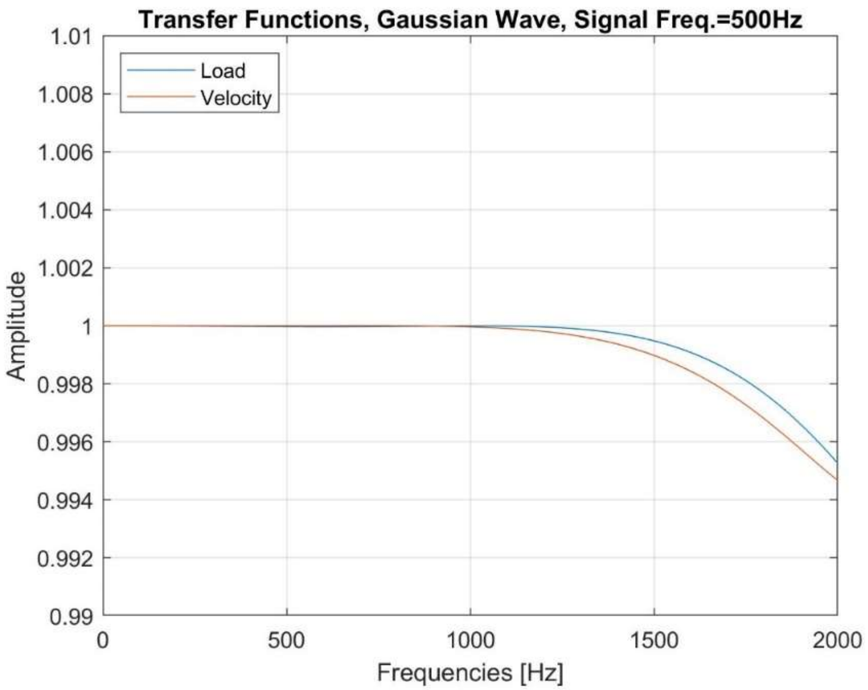

Figure 4-27 Optimum P-wave transfer functions for a 1D continuum model with a P-wave velocity of 3328 m/s

4.4.11. Transfer Functions for Other Rock Types

To test that the basic modelling assumptions found in the previous section remain valid when the model properties change, other rock types are modelled. This is necessary as different rock types will have different velocities and will be transmitted differently through a model. The rock types modelled and their properties are shown in Table 4-2, which are taken from the UDEC database of properties (Itasca Consulting Group Inc., 2014). All models are excited with a 500 Hz Gaussian wave end load function. The model setup is exactly as modelled in the previous section, so the “Original” data series shown in Figure 4-28 is the same as the “Load” series shown in Figure 4-27. “Original” refers to the hard sandstone properties used previously in Section 4.4.

Table 4-2 Properties and rock types modelled. Original is the rock used previously in this section

Rock Type	Density (kg/m^3)	Young's Modulus (GPa)	Bulk Modulus (GPa)	Shear Modulus (GPa)	S-Wave Velocity (m/s)	P-Wave Velocity (m/s)
Sandstone (Original)	2.6E3	24.0	16.0	9.6	1922	3328
Shale	2.6E3	11.1	8.8	4.3	1286	2365
Siltstone	2.6E3	3.2	15.7	1.1	1286	2568
Sandstone	2.6E3	19.2	26.8	7.0	1640	3727
Limestone	2.6E3	28.4	22.6	11.0	2057	3786
Basalt	2.6E3	34.9	32.3	13.2	2253	4381
Marble	2.6E3	55.7	37.0	22.3	2929	5066
Granite	2.6E3	73.7	44.0	30.2	3408	5693
Quartzite	2.6E3	88.3	37.7	39.8	3913	5910

Figure 4-28 shows the transfer functions for a range of rock types. The legend is shown with an ascending P-wave velocity from top to bottom. The quality of the transfer function up to 2000 Hz improves as the P-wave velocity increases, with Quartzite showing the best transfer function and Shale the worst. This would be expected as the stiffer rocks, giving a higher P-wave velocity, will increase the wavelength for any given frequency, which will allow the model to transmit a greater range of frequencies.

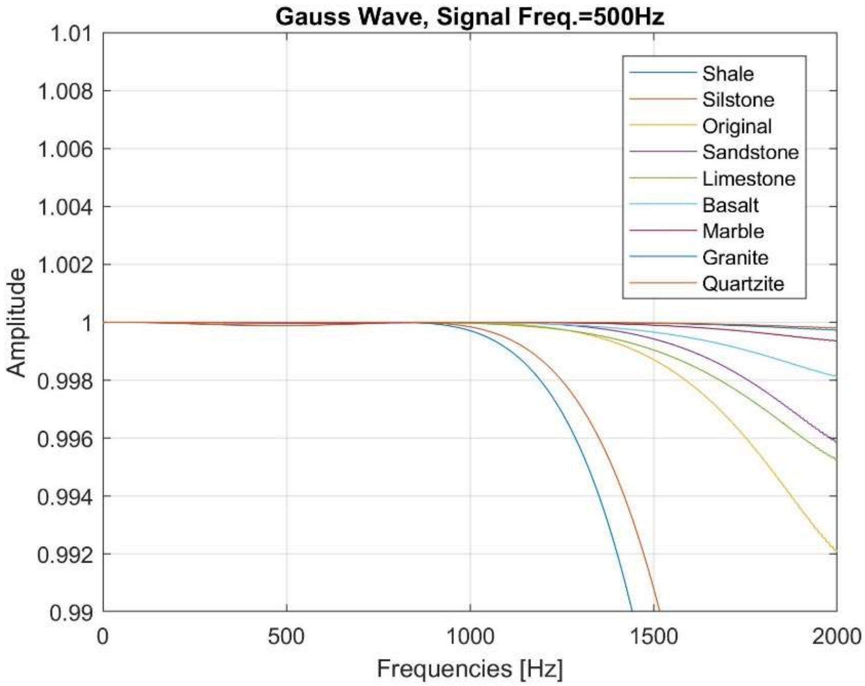

Figure 4-28 Transfer functions for other rock types modelled using a load function

To test the transfer functions quality, the frequency for each rock type when the transfer function amplitude reaches 0.9999 is recorded. The amplitude of 0.9999 is arbitrarily selected and does not necessarily represent the limit of the applicability of the transfer functions. As the ability of a model to transmit frequencies relies on the ratio of the wavelength to the element size, it is expected that as the P-wave velocity increases the frequency will also increase. It is expected that the relationship between the P-wave velocity and the frequency is linear, as these are related through the classic Equation $v=f\lambda$; where v is velocity, f is frequency and λ the wavelength. Figure 4-29 shows the results from this exercise, plotted against the P-wave velocity. This shows that there is a linear relationship between the 0.9999 cut off and the P-wave velocity with a high R-squared value, as expected. The R-squared value shows the coefficient of determination and can be used to show how data fits a bets fit equation (Holmes et al., 2019). When the same data is plotted against the S-wave velocity the R-squared value drops to 0.84, which for the data is considered low. This indicates that the waves being modelled are P-waves.

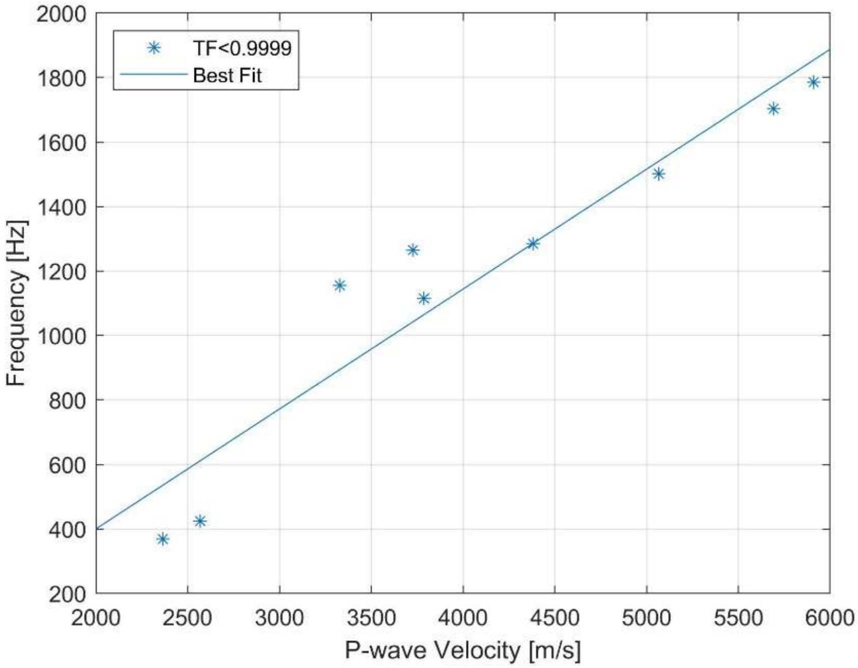

Figure 4-29 Frequency at which transfer function value drops below 0.9999 plotted against the P-wave velocity of the model. R2 value for best fit line is 0.9025

The outcome of this section is that the modelling properties perform extremely well up to about 1000 Hz, which is much greater than the 0 to 250 Hz range of typical rail vibrations. However, the applicable range of frequencies which can be modelled is extended by using a stiffer material.

4.4.12. Final Model

The final model which has been determined through the preceding sensitivity analysis is included in Figure 4-30. This will be used as the basis for future modelling of jointed rock masses using the combined discrete element-finite difference method in UDEC. The models use the large strain assumption in the UDEC set up.

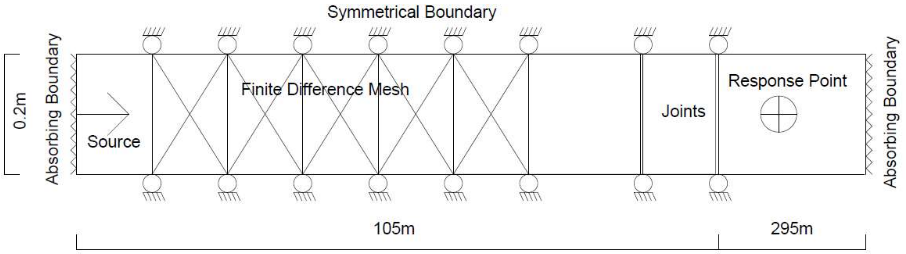

Figure 4-30 UDEC Model showing finite difference mesh. Mesh fills entire model. Not to scale. From Holmes et al., (2023b) *Figure 2*

Table 4-3 Final model setup in UDEC

Modelling Option	Recommendation
Wave type and frequency	5000 Hz Gaussian Wave
Wave interval	Equal to or less than the modelling time step
Excitation	End load
Element size	0.125 m horizontally, 0.2 m vertically
Mesh type	Quad mesh
Model height	0.2 m
Boundaries	Lateral – Absorbing Boundaries Horizontal – Roller Boundaries

4.5. Effect of Multiple Parallel Joints

"Data! Data! Data! I can't make bricks without clay." – Sherlock Holmes
(Doyle, 2014, pg. 274)

4.5.1. Joint Spacing and Number of Joints

Jointing in rock masses is common in nature. They can be found in a range of different rock types and formed in a range of different ways. These include bedding joints, formed through deposition of sedimentary rocks, to fractures in columnar basalt, formed through cooling of the molten material. Joints can form at a range of different angles; however, as shown in Figure 4-2, when projected into 1D, joints will always be parallel. This does not mean that studying a 1D projection only has theoretical relevance. Joints can form parallel to one another in reality, as shown by Figure 4-31. Multiple joints within a rock mass with the same orientation are known as joint sets.

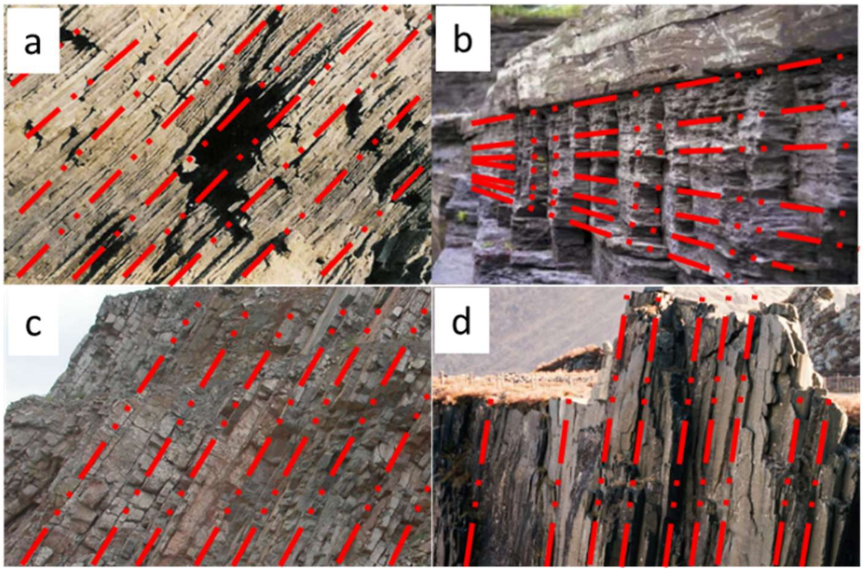

Figure 4-31 Parallel jointed rock masses which will show transverse isotropy. a) sub-vertical joints in slate-like grits, Aberystwyth, western Wales, with a sub-vertical plane of isotropy (Barton & Quadros, 2015); b) Horizontal joints in alternating siltstone and shale from Appalachian Plateau, Fingers Lakes, New York, with a vertical plane of isotropy (Germanovich & Astakhov, 2004); c) sub-vertical joints in Pembroke Limestone Group, Whatley Quarry, Mendip Hill, Somerset, England with a sub-horizontal plane of isotropy (Photograph courtesy of M. Czerewko); d) vertical joints in slate, Twll Mawr Quarry, Dinorwig Slate Quarries, North Wales with a horizontal plane of isotropy (Photo courtesy of C. Prescott, chris-prescott.com). Joints within rock masses are highlighted by dashed lines

This section considers a rock mass with a single set of joints, all separated by a constant spacing with a constant stiffness. Figure 4-32 shows the results for a rock mass with two parallel joints with a separation of 1, 2, 5 and 8 m. Three different rock types are modelled, which correspond with the properties given in Table 4-2. There is a clear structure developing in these transfer functions, with two peaks at low frequencies, followed by regular peaks at higher frequencies. The low frequency peaks appear to superimpose, regardless of the background rock mass, while the higher frequency peaks seem to increase their spacing as the background rock mass increases in stiffness. The first of the low frequency peaks is always at a frequency of 0 Hz. A 0 Hz wave is predicted to pass through a joint without being altered, as shown by the single joint transmission given by Equation 3-6 (Section 3.7). The low frequency peaks notably have transmission coefficients greater than one, with the higher stiffness rocks having a higher coefficient, while the troughs in-between the peaks have a transmission coefficient of less than one and a lower coefficient as the rock stiffness increases. Despite the transmission of these peaks being greater than one, this is over a very small range of frequencies and is not considered to be realistic. All peaks reduce their frequency spacing when the joint spacing increases.

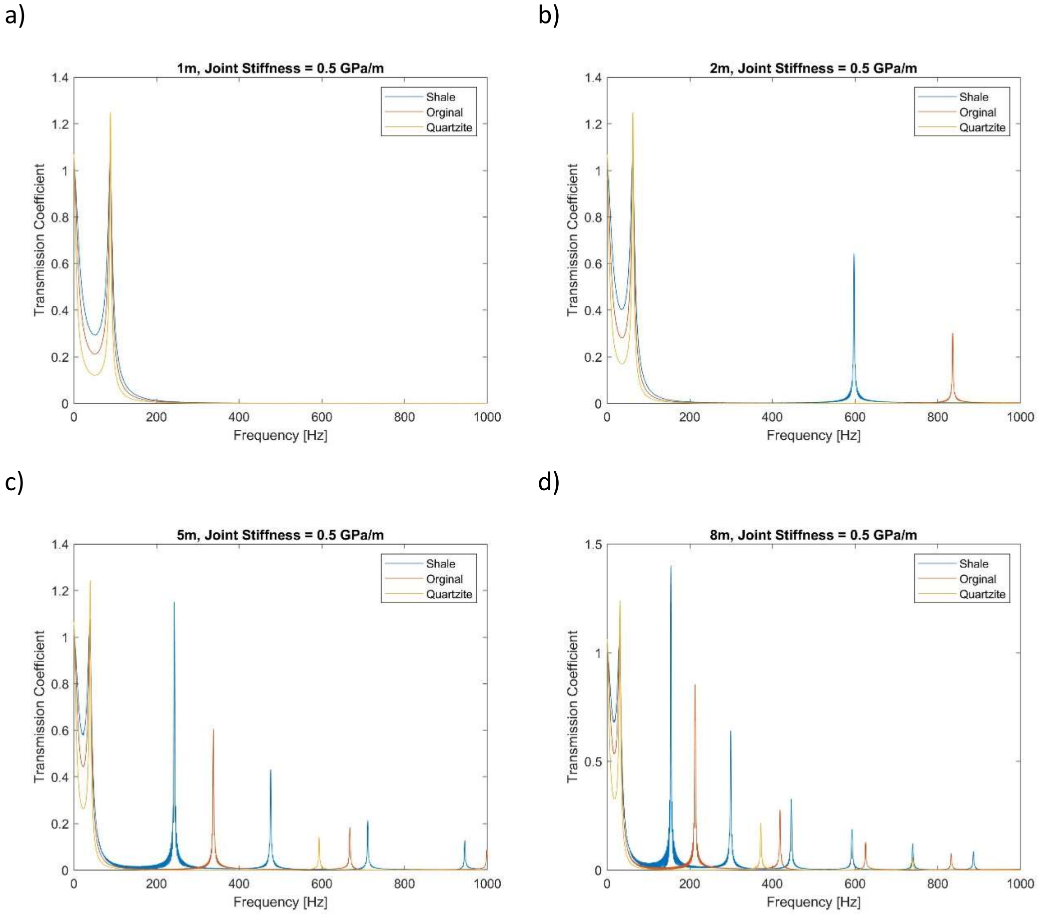

Figure 4-32 Transmission coefficient for a simple multi jointed rock mass with Jn=2 with a specific stiffness of 0.5 GPa/m separated by 1, 2, 5 and 8 m for three different rock types

Figure 4-33 shows the transfer functions for a rock mass containing four parallel joints. Similar to Figure 4-32 there are a series of peaks at low frequency, although there are now 4 peaks. The higher frequency peaks appear to be in the same location as those in the two jointed models shown in Figure 4-32. There is a clear structure here, with the number of low frequency peaks being related to the number of joints, and the higher frequency peaks being related to the rock stiffness.

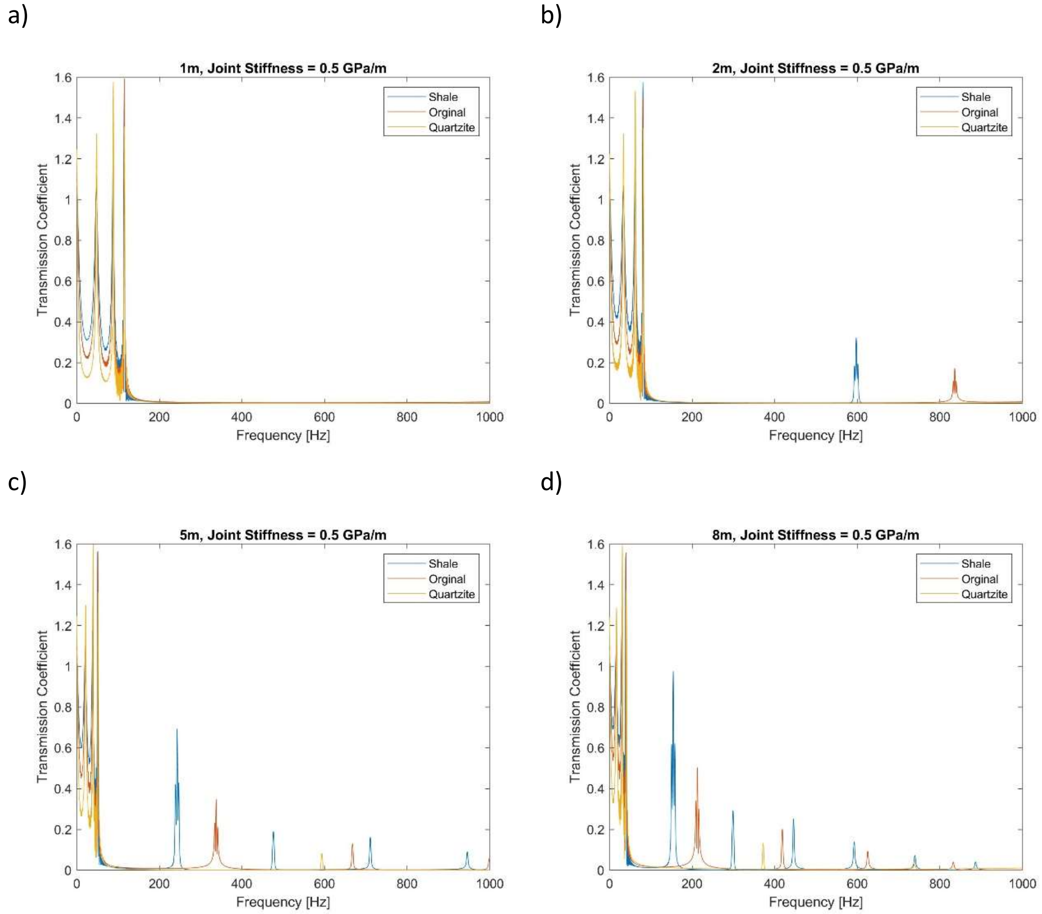

Figure 4-33 Transmission coefficient for a simple multi jointed rock mass with Jn=4 with a specific stiffness of 0.5 GPa/m separated by 1, 2, 5 and 8 m for three different rock types

Figure 4-34 shows the transfer functions for parallel jointed rock masses with 2, 3, 4 and 8 joints. This shows that there is no obvious relationship between the number of joints and the frequency of the peaks, although the maximum high transmission frequency does appear to stabilise around 120 Hz when the number of joints increases.

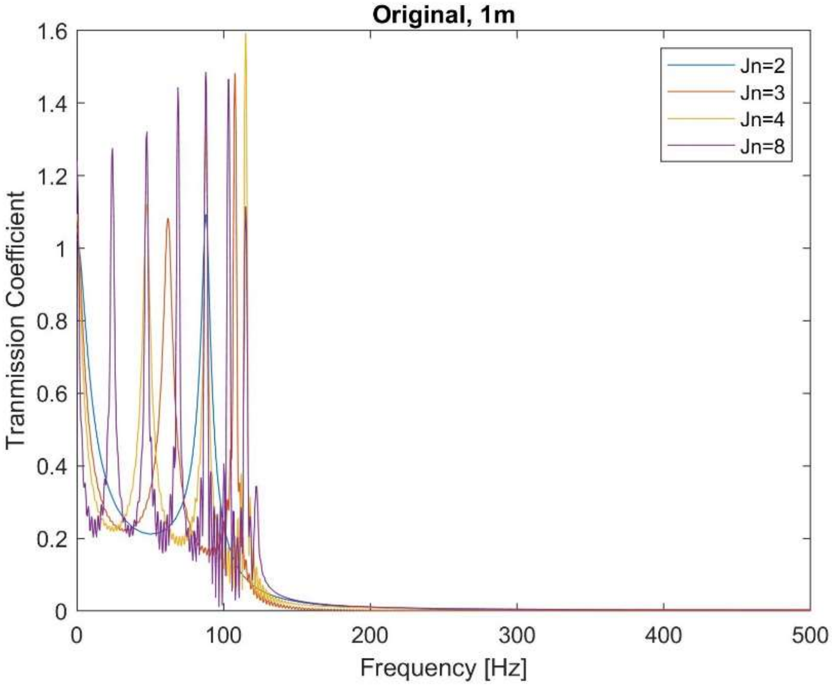

Figure 4-34 Transfer functions for multiple jointed rocks, with 2,3,4 and 8 parallel joints. All models have the same rock type Original (Sandstone) and the same joint specific stiffness of 0.5 GPa/m and joint spacing of 1 m

4.5.2. Joint Stiffness

Figure 4-35 shows how changing the stiffness of the joint affects the transfer functions for a model with two joints with the background material modelled with different properties. The Figures include transfer functions for joints of stiffnesses of 0.5, 1 and 10 GPa/m. The two peaks are still visible when the joint stiffness increases. The position of the second peak appears at higher frequencies when the joint stiffness increases, with the first peak always at a frequency of 0 Hz. The amplitude of the second peak reduces when the joint stiffness increases.

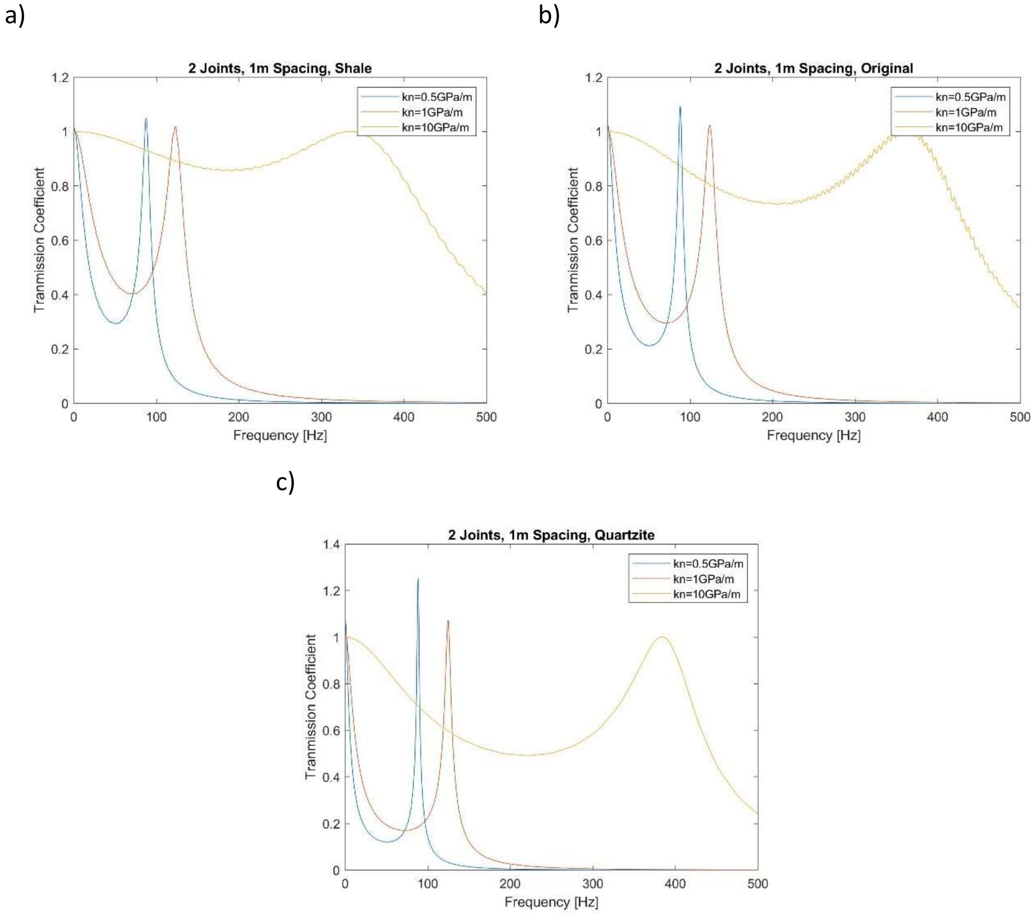

Figure 4-35 Transfer functions for multiple jointed rocks with Jn=2 at a range of joint specific stiffnesses for three different rock types

4.5.3. Sensitivity to Joint Position relative to Excitation Position

Figure 4-36 shows a sensitivity analysis of the relative position of the measurement point and joints, to the location of the excitation. This has been moved further away from the measurement point, with the joints also moved closer or further away from the excitation point. The cases shown in Figure 4-36 are not exhaustive, although they do show that the position and magnitude of the transfer function is not particularly sensitive to the relative positions of the joints, excitation, and measurement points. The cases used in Figure 4-36 are as follows:

Case 1- Joints at 104 and 105 m, measured at 200 m;

Case 2- Joints at 194 and 195 m, measured at 200 m;

Case 3- Joints at 49 and 50 m, measured at 200 m;

Case 4- Joints at 19 and 20 m, measured at 200 m;

Case 0- joints at 104 and 105 m, measured at 110 m (as used in previous Figures)

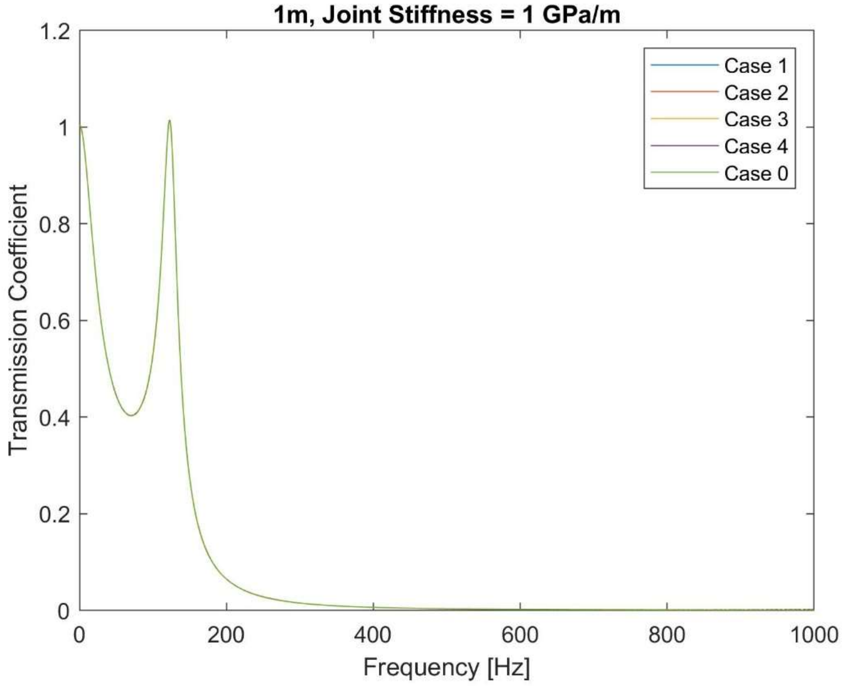

Figure 4-36 Transfer functions for multiple jointed rocks with Jn=2 for different modelling conditions with an excitation at 0m

4.6. Analytical Expressions for Resonance Mechanisms

This section looks into the physical mechanisms behind the interactions observed in the previous Figures, and introduces Equations which can be used to predict the frequencies at which these interactions occur. The Figures in the previous section show a small number of the models analysed. Many further analyses were run, with the high transmission frequencies included in Appendix A. These high transmission frequencies represent resonant frequencies of the rock masses analysed. The database shown in Appendix A was analysed by attempting to normalise the resonant frequencies using properties of the rock masses. In doing so two different mechanisms were discovered operating in the jointed rock masses, one occurring at low frequencies and the second at relatively high frequency. The low frequency resonances occur through a mass between spring like mechanism and the high frequency resonances through a superposition like mechanism. The following sections describe these mechanisms and derive Equations for the prediction of the resonant frequencies of jointed rock masses.

Readers from other engineering disciplines may have issue with using the term resonance for the phenomena highlighted in this thesis. Resonance typically causes cause amplification of a response; however, the amplitude of resonant frequencies in this work are shown as elevated compared to surrounding frequencies, which have their amplitudes reduced. The resonances have their amplitude maintained, with a transmission coefficient equal to one. Some transfer functions in this work show amplifications; however, these are thought to be caused by numerical modelling errors rather than a realistic amplification. Despite this, there are still clear maxima and minima in all the transfer functions presented here, so these artificially raised amplitudes should not detract from the presence of the mechanisms. It is not uncommon for the same terms to have slightly different applications between different scientific disciplines. While the term resonance may not be suitable from a purely engineering perspective there is a precedent in geological literature for using it for such affects, as shown by Nakagawa (1998), Li et al. (2019) and British Standard Institution (2004). As such, the term resonance is considered to be well justified.

4.6.1. Low Frequency Resonance – Spring Resonance

The low frequency resonance shows complex trends, with the number of resonant frequencies increasing when the number of joints increases (Figure 4-34) and their frequency related to the properties of the blocks and joints (Figure 4-35). To explore the trends in the data it is beneficial to be able to link these to simple physical cases with closed form solutions. To do this, initially, the simplest jointing case of two parallel joints is explored.

A model with two parallel joints is equivalent to a block between two springs, which are fixed at their ends (Figure 4-37). The block is created by the joints, with the joints operating like springs. The large blocks on either side of the joint generated block (Figure 4-30) operate to fix the springs (joints) in position. This is not strictly accurate as these end blocks can deform; however, for the purposes of a simple analogy this system suffices. In the 1D models used here, the mass can only move in a single plane. The block will oscillate at a frequency related to the stiffness of the springs and the mass of the block. Equation 4-13 gives the frequency of oscillation of a mass between two springs.

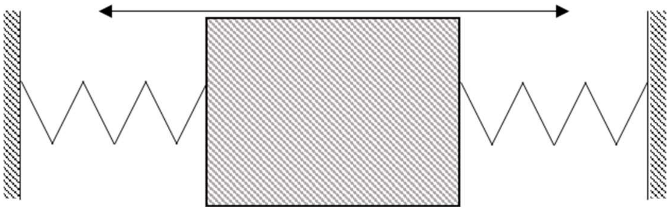

Figure 4-37 A single degree of freedom mass (block) between two springs (joints) used as an analogy for a parallel jointed rock mass. From Holmes et al., (2023b) *Figure 9*

$$\omega = \sqrt{\frac{2K}{m}} \qquad \text{Equation 4-13}$$

Where ω is the angular frequency of oscillation, m is the mass of the block and K the stiffness of the springs.

Equation 4-13 can be used with different stiffnesses on either side of the block, in which case $2K$ would become K_1+K_2, with K_1 and K_2 being the different spring stiffnesses. The m is given by the block density multiplied by the joint spacing (s) ($m=s\rho$).

To extend this analogy to more complex rock masses, additional blocks and springs can be added. When there are more blocks added, more resonant frequencies are generated, with the same number of resonant frequencies as the number of blocks. Previously it is highlighted that there is one less low frequency resonant peak than the number of joints, which is equal to the number of blocks in the model, not including the blocks in contact with the ends of the model. The ω of the resonant peaks are given by the eigenvalues (α) of Equation 4-14.

$$K_m X = \alpha M X \qquad \text{Equation 4-14}$$

K_m is the stiffness matrix (Equation 4-15) and M the mass matrix (Equation 4-16) and X is a vector that satisfies Equation 4-14.

$$K_m = \begin{bmatrix} k_1 + k_2 & -k_2 & \cdots & 0 \\ -k_2 & k_2 + k_3 & \ddots & \vdots \\ \vdots & \ddots & \ddots & k_j \\ 0 & \cdots & -k_j & k_{j-1} + k_j \end{bmatrix} \qquad \text{Equation 4-15}$$

$$M = \begin{bmatrix} m_1 & 0 & \cdots & 0 \\ 0 & m_2 & \ddots & \vdots \\ \vdots & \ddots & \ddots & 0 \\ 0 & \cdots & 0 & m_j \end{bmatrix} \qquad \text{Equation 4-16}$$

Where m_j is the j^{th} block mass, k_j is the j^{th} spring stiffness.

Equation 4-14 does not give the exact answer given by the numerical models, but the results are close, and the general trends are the same (i.e. increasing number of resonances as the number of joints increases). The difference suggests that the numerical models are not behaving like a rigid mass between two springs. The finite difference method, in its essence, attaches a number of springs in series, especially when modelled as a 1D material, as is the case here. There are springs for the intact material with one stiffness, attached to springs for the joints of another stiffness, again attached to springs for the intact material, and so on. As the blocks are able to accommodate deformations, not just the joints, the deformation of the blocks could be changing the effective stiffness of the material. The stiffness for a jointed rock mass can be calculated as the static stiffness of a series of springs, using Equation 4-17 (Ma et al., 2013), which can be incorporated into Equation 4-14 to account for the deformability of the blocks.

$$K_c = \frac{1}{\frac{1}{E_i} + \frac{1}{k_n}}$$ Equation 4-17

Where K_c is the combined spring stiffness, E_i is the intact block Young's Modulus and k_n is the joint normal specific stiffness.

Using K_c, calculated from Equation 4-14, as the spring stiffness (k_j) in Equation 4-15, the predicted resonant frequency reduces, bringing it closer to the numerical modelling results, although they are still not exactly the same.

A final Equation for the prediction of the low frequency resonant frequencies is given by Equation 4-18, and in terms of the ξ, by Equation 4-19. The term low frequency resonance is quite ambiguous, so this effect will be referred to as spring resonance.

$$f_n = \frac{1}{2\pi}\sqrt{\alpha_n}$$ Equation 4-18

$$\xi = \frac{s}{2\pi C_p}\sqrt{\alpha_n}$$ Equation 4-19

Where f_n is the n^{th} resonant frequency, α_n is the n^{th} eigenvalue for the system, and n is the peak number which has values from *1* to *Jn-1*.

Spring resonance is applicable for all rock masses which show linear elastic joint behaviour, and is not limited to the range of properties shown in Appendix A or Table 4-2.

4.6.2. High Frequency Resonance – Superposition Resonance

The wavelengths of the high frequency resonance are closely related to the joint spacing. The relationships in terms of ξ are shown in Table 4-4. The peaks are numbered following on from the resonances generated through spring resonance, of which there are *Jn-1* resonances. The frequency that gives these wavelengths can be calculated from Equation 4-20, with Equation 4-21 giving the same Equation in terms of ξ. This Equation is the same form as the classical Equation which gives the frequencies which generate a standing wave on a string fixed at its ends, of length *s*, and has been found to give rock resonance by Nakagawa (1998). Using the standing wave analogy, the string is the equivalent of a block, and the fixed ends are equivalent to the ends of the block, or joints. Multiple reflected waves, travelling in opposite directions can superimpose, amplifying the transmitted wave. Therefore, a wave of these wavelengths will have a greater transmission coefficient than a wave of a higher or lower frequency. The length of *s* has no physical limits, although in these numerical models it will be limited to a maximum of the size of the model and a minimum of 10 times the element size.

Table 4-4 Wavelengths as a multiple of joint spacing for high frequency resonance in jointed rock masses

Peak (n)	ξ
Jn	0.5
Jn+1	1
Jn+2	1.5
Jn+3	2

$$f_n = \frac{(n - Jn)C_p}{2s}$$ Equation 4-20

$$\xi = \frac{n - Jn}{2}$$ Equation 4-21

Where *n* is the peak number, including all spring resonance peaks.

Equation 4-20 does not give the exact resonant frequency and instead serves as a reasonable estimate. The reasons behind this are likely to be due to the deformation of the blocks during the analysis, therefore changing the size of the blocks and the frequencies which will form standing waves within them. This assumption is supported when viewing different block and joint stiffnesses. The stiffness of the blocks significantly affects the resonant frequency, as shown by Appendix A, with the extremely low stiffness blocks diverging significantly from the frequency predicted by Equation 4-20. The resonant frequency from modelling increases as the intact material stiffness decreases, giving a lower wavelength. A lower material stiffness will allow the block to deform more; therefore, allowing compression, reducing the size of the block. Increasing k_n also increases the frequency, further reducing the wavelength. A stiffer joint will deform less; therefore, causing all deformation to be focussed on the block, further reducing the block size, and reducing the wavelength. These effects are only evident in extremely low stiffness materials with very high stiffness joints, which are not likely in reality. In most realistic rock masses, Equation 4-20 would be expected to give a reasonable approximation of the resonant frequency. This effect will be referred to as superposition resonance.

Theoretically, there are an unlimited number of superposition resonant frequencies. However, the high frequency resonance may not be visible for low stiffness joints. This is likely to be related to the effects shown by the single joint analytical Equations, shown by Equation 3-6 and Equation 3-7 (Schoenberg, 1980; Pyrak-Nolte et al., 1990b). A combination of a very low stiffness joint and a high material stiffness will prevent energy from being transmitted. Despite this generating a large degree of reflection to allow the superposition, if energy cannot be transmitted through the joint, there will be no increase in transmission on the other side of the joints. Equation 3-6 shows that the degree of transmission also reduces as the frequency increases, so this implies that as the order of the superposition peak increases, which increases the frequency, its magnitude will decrease. Figure 4-38 shows the results of a model with a wide joint spacing, to generate a large number of superposition resonant frequencies within a confined frequency range. This clearly shows that as the frequency of the superposition resonant frequency increases, the amplitude of this peak reduces. The absolute amplitude of the resonances may be incorrect due to noise in the data, although the relative amplitude of the peaks reduces as the frequency increases.

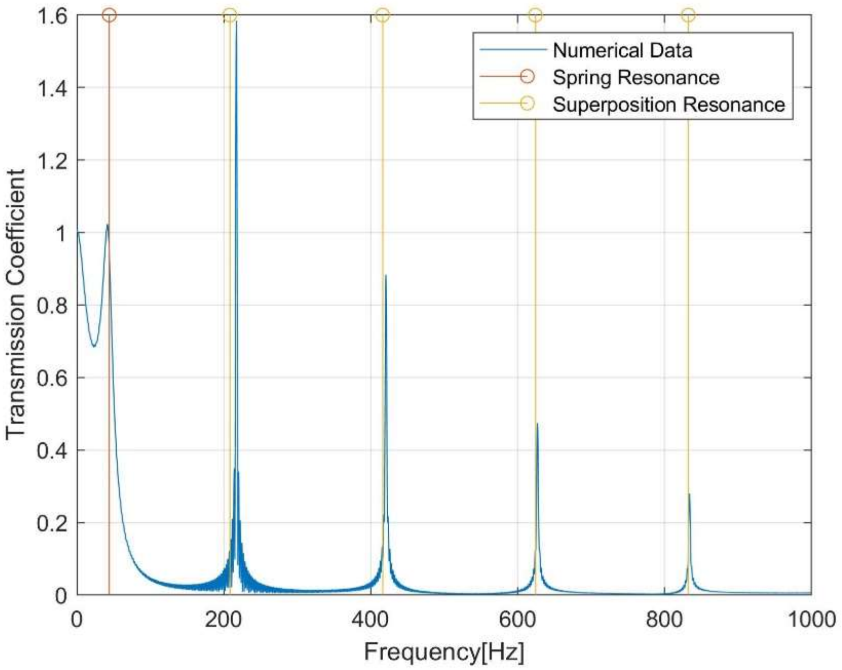

Figure 4-38 Resonance shown by a jointed rock with s=8m (Cp=3328 m/s, Cs=1922 m/s, ρ=2600 kg/m3, k_n=1 GPa/m, Jn=2). Numerical Data from a 1D UDEC model, spring resonance and superposition resonance from Equations 4-18 and 4-20, respectively

4.6.3. Application of Analytical Models

The analytical Equations for spring and superposition resonance are given in terms of frequency and ξ in Equation 4-18 to Equation 4-21. These allow a more direct comparison with previous research into wave transmission through multi-jointed rock masses (Cai and Zhao, 2000; Zhao et al., 2006), using the Equations in terms of ξ, and application of the results to other branches of engineering more easily, using the Equations in terms of frequency. For example, the results could be applied to vibration research, such as high speed rail, to determine whether a rock mass will preferentially transmit the frequencies generated by a vibrational source, a use particularly relevant to the work in this thesis. Results from such studies are typically given in terms of frequency, instead of ξ.

To test the analytical solutions a series of arbitrary test cases are modelled with the resonant frequencies compared to those predicted by the analytical functions. These cases are run in the models shown in Figure 4-30. The properties of the verification cases are shown in Table 4-5.

Table 4-5 Test cases and their properties. Multiple values indicate different properties for subsequent joints

	P (kg/m^3)	Cp (m/s)	Cs (m/s)	Jn	s (m)	k_n (GPa/m)
Case 1	2600	3328	1922	3	4, 2	3
Case 2	2600	3328	1922	2	2	0.5, 1
Case 3	2600	2364	1286	2	4	0.8, 0.4

- Case 1 contains three joints with the same stiffness, but with different joint spacing's. The first and second joints are separated by 4 m and the second and third joints by 2 m;
- Case 2 contains two joints with different joint specific stiffnesses, where the first joint has a lower stiffness than the second;
- Case 3 contains two joints with different stiffnesses, where the first joint has a higher stiffness than the second.

Table 4-6 contains the results for Cases 1 to 3, solved in UDEC, and the analytical models. The transfer functions are shown in Figure 4-39 to Figure 4-41. Only the first two superposition resonant peaks are shown in Table 4-6. The analytical superposition resonant frequencies for Case 1 are calculated using both joint spacing's, with the two lowest frequency peaks taken from this. The results in Table 4-6 seem to show a good agreement between the numerical and analytical results. Cases 2 to 3 are diverse and different from the data set used to define the analytical models, so the agreement of the results supports the hypothesis that the analytical models are performing as expected. This also adds weight to the idea that the spring and superposition mechanisms are realistic.

Table 4-6 Results of validation tests. U: UDEC, A: Analytical

Case	Spring Resonance				Superposition Resonance			
	Peak 1		Peak 2		Peak Jn		Peak Jn+1	
	U	A	U	A	U	A	U	A
Case 1	77	91	156	175	442	416	840	832
Case 2	75	84	n/a	n/a	839	832	1663	1664
Case 3	45	52	n/a	n/a	303	296	595	591

The results in this section show a good agreement between the numerically derived results and the analytical expressions in a more diverse and complex range of modelling scenarios, compared to those given in Appendix A from which the analytical models were derived. This shows a degree of robustness of the analytical expressions.

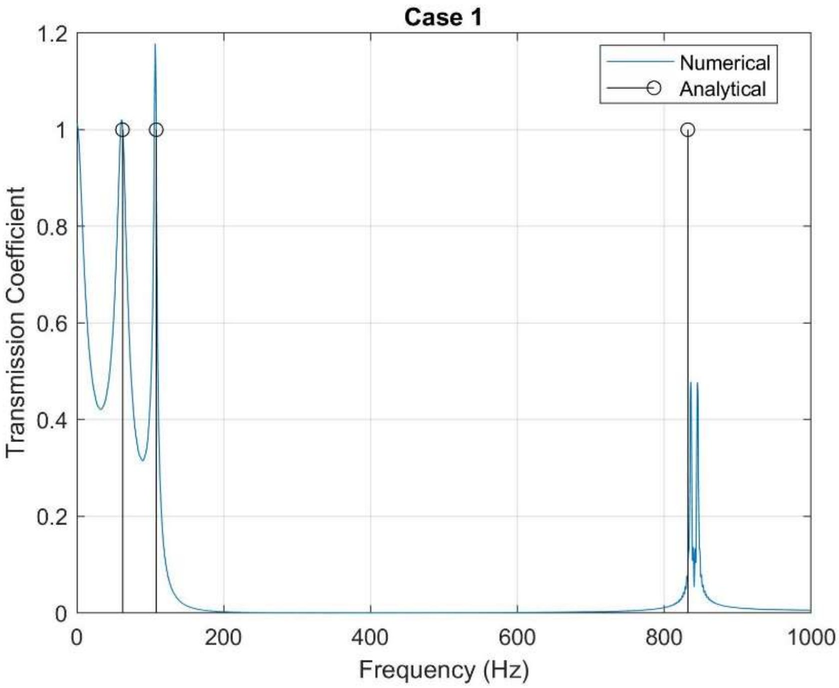

Figure 4-39 Transfer Function for Case 1

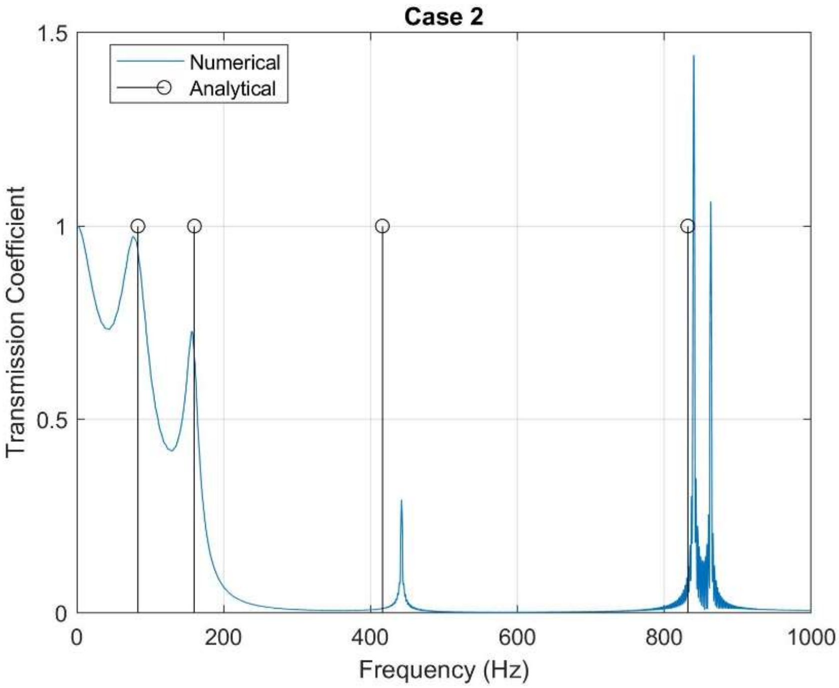

Figure 4-40 Transfer Function for Case 2

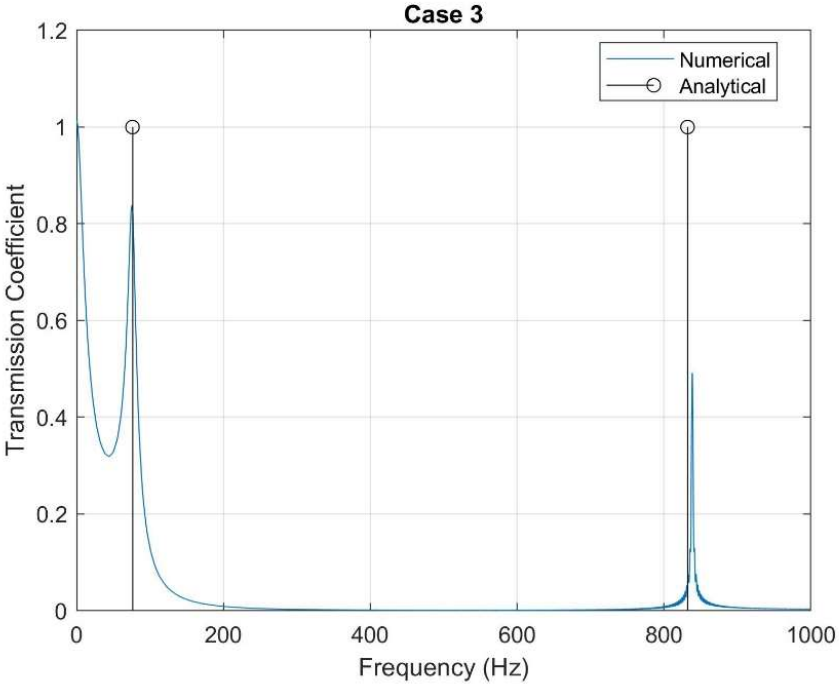

Figure 4-41 Transfer Function for Case 3

4.7. Conclusions

This Chapter has developed robust DEM-FDM models for studying jointed rock masses in 1D. This began with a model development section which outlined the important inputs to DEM-

FDM models which could affect modelling results. These modelling inputs are systematically varied in an undamped continuum model, which the transfer function is known for, and the effect on the transfer functions are determined. From this an optimised 1D model is found. This 1D model is carried forward to look at multiple jointed rock masses.

The multiple jointed rock masses are excited by a 500 Hz Gaussian function, which acts like an impulse, and the transfer functions from these are analysed. It is found that discrete high transmission zones are present in the transfer functions, which are hypothesised to be resonant frequencies for the rock mass being modelled. Evidence is presented to show that the resonances in the jointed rock mass are generated by two distinct mechanisms; spring resonance and super position resonance. Spring resonances are generated when the jointed rock mass behaves like masses between springs, with joints acting like springs and blocks acting like masses. Such systems have preferential frequencies of oscillation, which are equivalent to the resonances found in the numerical models in this Chapter. Superposition resonance is generated when waves, reflected from block edges, superimpose on one another. These resonances behave like standing waves on a string. Using classical mechanics analogues for the resonance mechanisms, analytical Equations are derived, which provide reasonable estimates for the resonance of a jointed material. This Chapter has gone some way to address the possible jointed rock mass resonances which are alluded to by Eitzenberger (2012).

"Like all Holmes's reasoning the thing seemed simplicity itself when it was once explained."
– Dr John Watson
(Doyle, 2014, pg. 313)

5. Verification of 1D Rock Mass Resonance Effects

"Further models with added complexity,
Are seen as a scientific necessity.
To verify the mechanisms presence,
Encapsulates this chapter in its essence."

© Army of Cats 2023

5.1. Introduction

Chapter 4 considers 1D jointed rock masses and identifies two resonance mechanisms which operate within them. These resonance mechanisms cause certain frequencies to be transmitted to a greater degree through a rock mass, so their identification and further study is important for a range of different real world applications which generate vibrations within a jointed rock mass, such as trains (Chua et al., 1992) and machine foundations (Gazetas, 1983).

The two resonance mechanisms identified are a mass between spring resonance (Section 4.6.1), where blocks oscillate like masses between springs, and a superposition resonance (Section 4.6.2), where resonances occur at wavelengths that allow standing waves to develop within joint bounded blocks. These are identified using highly simplified 1D models, which are a poor representation of realistic rock masses. This Chapter aims to study these effects further and validate whether these resonance effects will occur in more complicated models.

A range of different models are used in this Chapter to provide evidence of the presence of these resonance effects. These models are solved in the combined DEM-FDM, as used in Chapter 4, as well as the finite difference method (FDM). The FDM code used is called WAVE2D, developed by Hildyard et al. (1995), with the DEM-FDM code solved using UDEC (Itasca Consulting Group Inc., 2014).

To begin with, this Chapter introduces WAVE2D and the key differences between itself and UDEC. A model development section is included, which is similar to the model development followed for UDEC in the Chapter 4, although less extensive. Following this, the verification models run in WAVE2D and UDEC are shown and discussed. This Chapter also introduces anisotropic material models, which can be implemented using WAVE2D. The outcome is that the resonance mechanisms identified in jointed rock masses occur in all the modelling scenarios in this Chapter.

5.2. WAVE2D Model Description

WAVE2D is a FDM code, which handles joints as special displacement discontinuity elements within a model (Hildyard et al., 1995). The finite difference mesh in WAVE2D uses the same Equations of motion as given in Chapter 4 for the UDEC mesh (Section 4.4.1). Unlike in UDEC, which models joints as interfaces between two blocks, joints in WAVE2D are implemented in the mesh as two infinitesimally thin planes, employing fictional stresses within the joint. The two surfaces of the joint have constant stresses, with non-continuous displacements. This allows the displacements on either side of the joint to be calculated using the joint and intact block stiffnesses. A detailed derivation of these Equations are given by Hildyard et al. (1995).

WAVE2D is specifically designed to undertake dynamic analyses so it is well set up for the models which will be run here. This includes the automatic generation of a regular square finite difference mesh and a 4th order numerical scheme. The regular square mesh allows the accurate transmission of stress waves as the element size is constant throughout the model. The 4th order numerical scheme provides a more accurate approximation of the finite difference integral equations than the 2nd order numerical scheme used by UDEC. This means that instead of the wavelength of the highest frequency wave being required to be ten times the element size, this can be reduced to five times the element size, resulting in a higher maximum frequency being accurately transmitted through the model (Hildyard, 2001). This increases the frequency which causes unacceptable levels of numerical dispersion, as detailed in Section 4.2.1. A regular square mesh is found to be the optimum mesh set up for UDEC (Section 4.4.12). Despite this, there are modelling setup options such as the position of the source and the size of the mesh which can affect the results. Therefore, a brief model development section is included.

5.2.1. Position of Source

It is not possible to apply a force to an external boundary in WAVE2D, unlike the source position used in UDEC. Instead, the source needs to be located within the model. To keep this similar to the model in UDEC, which applies the excitation to the end of the model, the source will be located close to the external boundary.

5.2.2. Element Size

The element size is a key factor dictating the frequency of waves which can be transmitted through a model. If the element size is too large in relation to the wavelength of the wave which is being transmitted, numerical dispersion can introduce issues, as discussed in 4.2.1. As discussed in Chapter 4, Hildyard (2001) showed that for a 4th order numerical scheme, like adopted in WAVE2D, the element size is required to be at least 5 times the minimum wavelength in order to minimise numerical dispersion. It has been decided that an element size of 0.08 m should be used throughout the 1D WAVE2D models in this Chapter. This will allow a higher frequency of wave to be transmitted than the UDEC models in Chapter 4, which has a solver with a 2nd order numerical scheme. However, this will not affect the transfer functions below this maximum transmitted frequency. Furthermore, the slight difference between the meshes used in the two numerical codes will indicate whether this has an effect on the frequency of resonances.

5.2.3. Model Height

The model height is a parameter studied in Chapter 4 for the UDEC DEM-FDM models. This found that the model height does not have a dramatic effect on the results, so the smallest model size is used in order to reduce the computational costs. However, in WAVE2D it is not possible to implement symmetrical boundaries, like those used in UDEC to ensure that the model is effectively infinite in the short axis. Instead, plane wave boundaries are required. Therefore, a sensitivity analysis on the appropriate model height is required. A narrow model is set up with 80 grid points in the vertical direction and a wide model is set up with 2080 grid points in the vertical direction. Both models are 4800 grid points long, with a square finite difference mesh of 0.8 x 0.8 m. This sensitivity analysis is shown in Figure 5-1.

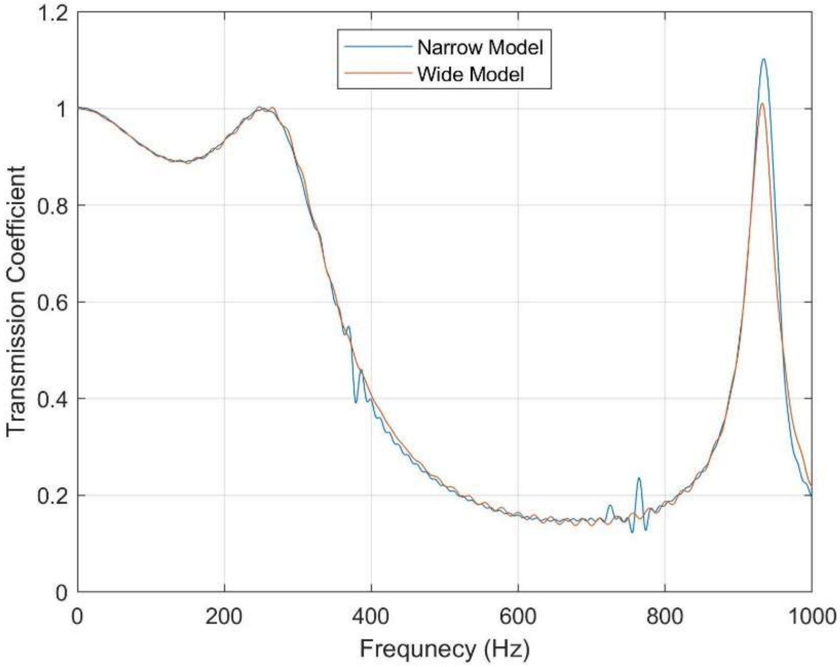

Figure 5-1 Sensitivity analysis into the model height required in WAVE2D

Figure 5-1 shows that the narrow WAVE2D model shows some instabilities, especially at 400 and 800 Hz. This is not the case in the wide model, which shows a smoother transfer function through the range shown. Despite this there is an oscillation shown in the wide model's transfer function. However, additional distinct peaks are not added to the transfer function, unlike in the narrow model. As a consequence, the wide WAVE2D model with 2080 grid points in the vertical direction appears to be a more suitable set up for future analyses.

5.2.4. WAVE2D Model

The model which is to be used for the WAVE2D analyses is shown in Figure 5-2. A plane wave is excited at the left hand boundary of the model using a horizontal velocity function. Force functions, as used for the input in UDEC, are not possible in WAVE2D. Absorbing boundaries are modelled on the vertical model boundaries, with a plane wave boundary modelled along the horizontal model boundaries. No material damping is applied, which is also assumed in the UDEC models in Chapter 4.

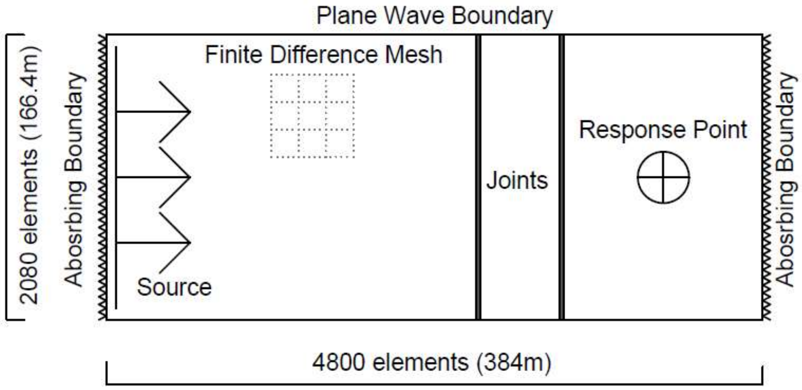

Figure 5-2 WAVE2D Model showing finite difference mesh. Mesh fills entire model. Not to scale. From Holmes et al. (2023a) *Figure 7*

The WAVE2D model is excited by a modified Ricker wave which has a central frequency of 500 Hz. This has a slightly different frequency content, when compared to the 500 Hz Gaussian wave used in UDEC, although the content of the waveforms is comparable. The time series and frequency spectrum of the UDEC and WAVE2D excitations are shown in Figure 5-3.

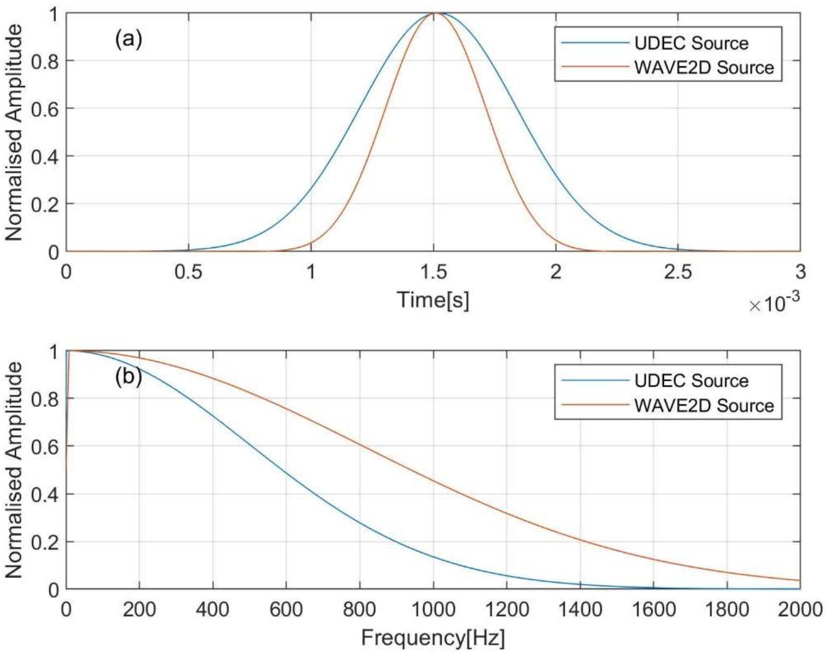

Figure 5-3 Input wave to UDEC and WAVE2D models. UDEC is a 500 Hz Gaussian wave and WAVE2D is a 500 Hz modified Ricker wave. a) time series of sources, b) frequency content of sources. From Holmes et al. (2023a) *Figure 2*

5.2.5. Comparison to UDEC Results

A series of simple models are set up to show how results from UDEC and WAVE2D compare to one another. The UDEC model is the model generated in Chapter 4, Figure 4-30. For now, the analytical prediction for the spring and superposition resonances, given by the Equations 4-18 and 4-20, are ignored. A range of different properties are used for the analysis. These have been calculated by using the same P and S-wave velocities (*Cp* and *Cs*, respectively) for all models but changing the material density from 260 to 26000 kg/m^3. This range is not intended to be representative of realistic materials, and instead show whether the resonance mechanisms can occur at extremes. Three different joint stiffnesses are used, from 1 to 10 GPa/m. The properties used and the resonant frequencies shown in UDEC and WAVE2D are given in Table 5-1 and the transfer functions given in Figure 5-4 to Figure 5-6.

Table 5-1 Models used in sensitivity analysis in UDEC and WAVE with their resonant frequencies.

ρ	Cp	Cs	E. Mod	k_n	s	Jn	Resonant Frequencies (Hz)			
(kg/m^3)	(m/s)	(m/s)	(GPa)	(GPa/m)	(m)		UDEC		WAVE2D	
26000	3328	1922	240	1	2	2	28	-	32	-
26000	3328	1922	240	4	2	2	56	835	61	830
26000	3328	1922	240	10	2	2	87	841	96	843
2600	3328	1922	24	1	2	2	87	840	96	845
2600	3328	1922	24	4	2	2	162	867	187	877
2600	3328	1922	24	10	2	2	235	914	250	932
260	3328	1922	2.4	1	2	2	237	914	250	932
260	3328	1922	2.4	4	2	2	342	1052	369	1082
260	3328	1922	2.4	10	2	2	387	1144	425	1165

The results in Figure 5-4 to Figure 5-6 and Table 5-1 show that WAVE2D and UDEC behave in a similar fashion. There is a slight difference in the exact frequency, which is shown as being resonant, although the resonant frequency is clear within the transfer functions. Therefore, it is evidence that WAVE2D and UDEC are both modelling the same problem in the same way, with similar resonance mechanisms occurring within the models.

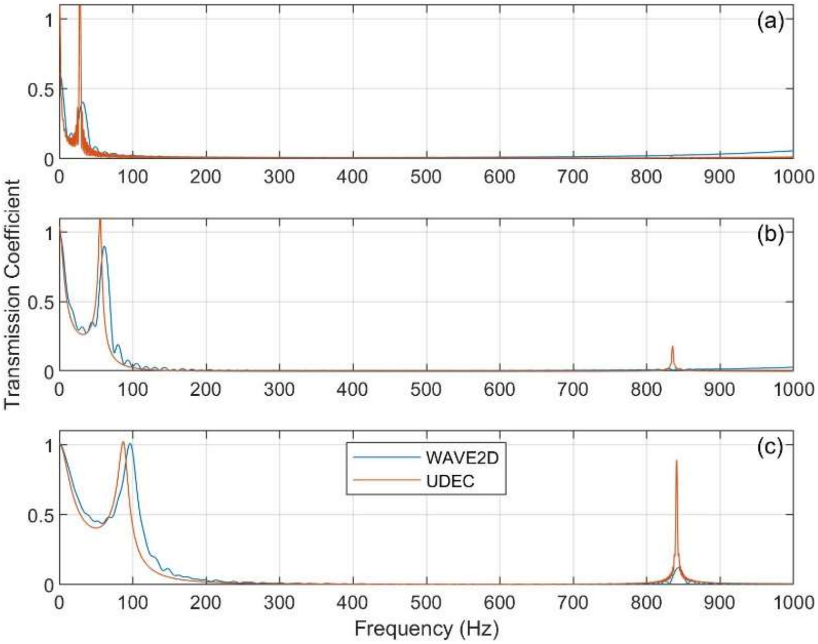

Figure 5-4 High density (26000kg/m^3) transfer functions from WAVE2D and UDEC for a material with a Cp of 3328 m/s and Cs of 1922 m/s. a) k_n=1 GPa/m, b) k_n=4 GPa/m, c) k_n=10 GPa/m. From Holmes et al., (2023b) *Figure 5*

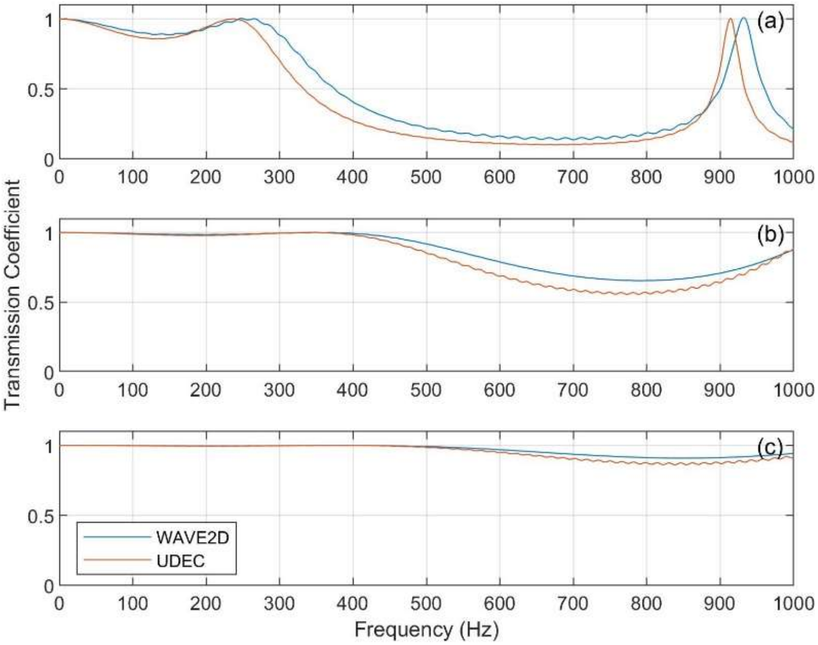

Figure 5-5 Medium density (2600kg/m^3) transfer functions from WAVE2D and UDEC for a material with a Cp of 3328 m/s and Cs of 1922 m/s. a) k_n=1 GPa/m, b) k_n=4 GPa/m, c) k_n=10 GPa/m. From Holmes et al., (2023b) *Figure 6*

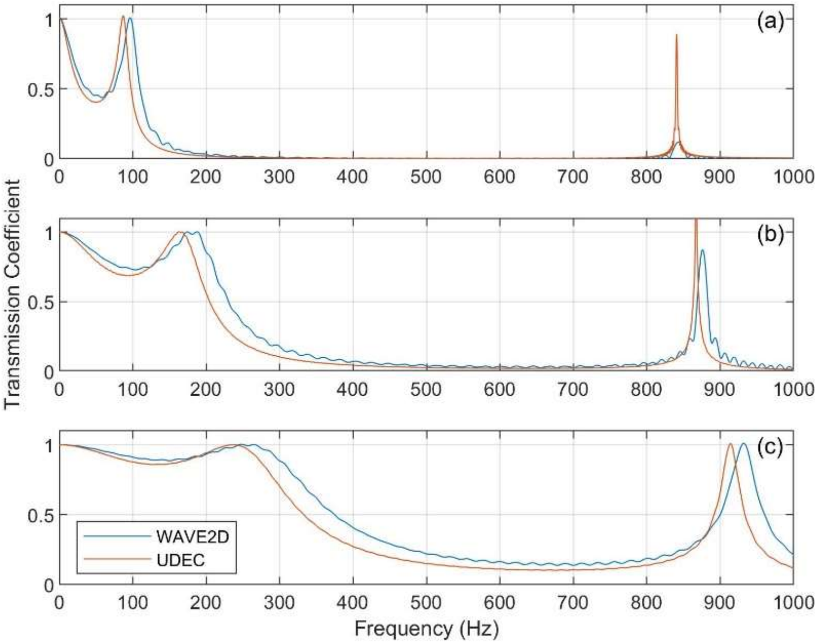

Figure 5-6 Low density (260kg/m^3) transfer functions from WAVE2D and UDEC for a material with a Cp of 3328 m/s and Cs of 1922 m/s. a) k_n=1 GPa/m, b) k_n=4 GPa/m, c) k_n=10 GPa/m. From Holmes et al., (2023b) *Figure 7*

5.3. Resonance Verification

The verification of the resonance mechanisms is undertaken using diverse numerical models to determine whether the model set up can affect whether the resonances are generated. This verification focuses on the spring resonance mechanism, as superposition resonance is known to occur within natural blocks (Nakagawa, 1998). If the resonances do not occur, then it can be assumed that their presence is a modelling artefact. The verification is undertaken in four different sections. The first two (Sections 5.3.1 and 5.3.2) model discrete joints and generates new models which break some of the modelling assumptions used in the 1D models in Chapter 4. The third (Section 5.3.3) uses equivalent material models to represent the jointed material and the fourth (Section 5.3.4) uses the 1D model from Chapter 4 using an alternative method, a frequency sweep, for exciting the model and generating a transfer function.

5.3.1. Discrete Models

This section concerns the discrete representation of joints in the jointed rock mass. The discrete representation of joints is used in all the models shown in Chapter 4. Similarly, the discrete models in this section are generated in the combined discrete element-finite difference method (DEM-FDM), in UDEC. The models are excited by the 500 Hz Gaussian wave shown in Figure 5-3.

Material damping is not applied to any model used, with linear elastic material properties applied to joints and intact blocks. The material properties used in this section are given in Table 5-2. The use of linear elastic properties is undoubtedly an assumption which requires testing; however, considering a common vibrational source, such as rail vibrations, strains within the rock mass will be low (Connolly et al., 2016). This will ensure that the response of the material is well approximated by elastic material properties. Even considering a non-linear joint stiffness model, such as the Barton-Bandis model (Bandis et al., 1983), a small portion of the stress-strain relationship for a joint will approximate a linear relationship.

Table 5-2 Modelling material properties

Joint Stiffness	1 GPa/m
Joint Spacing	2 m
Number of Joints	2
Intact Material P-Wave Velocity	3328 m/s
Intact Material S-Wave Velocity	1922 m/s
Intact Material Density	2600 kg/m^3

"I confess that I have been blind as a mole, but it is better to learn wisdom late than never to learn it at all." – Sherlock Holmes
(Doyle, 2014, pg. 200)

This section attempts to understand the spring resonance mechanism and determine the robustness of the effect to changing conditions in a numerical model. If the effect persists through using more complex numerical models than the 1D models already developed, then there is a greater certainty that the effect will occur in a physical rock mass. In order to do this, assumptions adopted by the previous Chapter are examined. The assumptions being tested are symmetrical boundary conditions and infinite joints. To achieve this, two new scenarios are modelled, solved in the DEM-FDM (Models 2 and 3). Model 1 is a 1D model, similar to the one used in Chapter 4. It is not identical, as during development of the work for the paper included in Appendix E it was found that a model with a greater number of modelling nodes orientated vertically gives a better approximation of the frequency predicted by the analytical functions given in Chapter 4 (Holmes et al., 2023a; Holmes et al., 2023b). Despite this difference to the original models used to develop the analytical functions, this model can be used as a baseline from which comparisons are made. The two new models are 1D models, one without symmetrical boundaries (Model 2) and the other with multiple blocks orientated perpendicular to the direction of wave propagation but with symmetrical boundaries (Model 3). Model 3 could be considered not to be a 1D model due to the stack of blocks perpendicular to the direction of wave propagation. Finite joints are to all intents guaranteed in nature, as joints cannot be continuous, even if they are highly persistent. Therefore, testing this assumption means the model will be more realistic. The blocky rock mass in Model 3 contains finite joints, but also tests whether the resonance mechanism occurs when an additional joint set is modelled, orientated perpendicular to the first joint set.

Model 1 – DEM-FDM

Model 1 is similar to the models used in Chapter 4, but with a 1 m out of plane dimension. An element size of 0.2 m vertically and 0.125 m horizontally is used, allowing more finite difference meshing zones to be generated in the vertical direction. This model is shown in Figure 5-7. Given this mesh set up and the properties given in Table 5-2 this model will be able to transmit frequencies up to 2662 Hz, based on the recommendations for the minimum wavelength to be at least ten times the element size for a 2nd order numerical scheme (Hildyard, 2001).

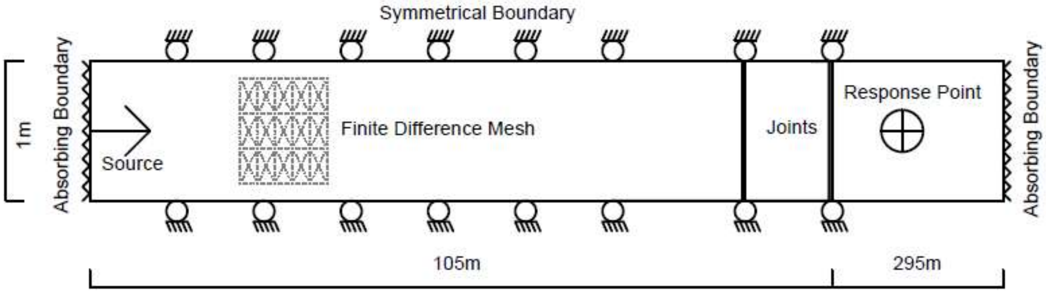

Figure 5-7 *DEM-FDM Model 1 (adapted from* Holmes et al., (2023b)*) showing finite difference mesh for finite joint verification case. Mesh fills entire model. Not to scale. From* Holmes et al. (2023a) *Figure 3*

Model 2 – DEM-FDM

Model 2 is identical to Model 1 without symmetrical horizontal boundaries. These boundaries are now modelled as being free and can move in all directions in the 2D plane of modelling. Without symmetrical boundaries this model will not contain infinite joints, allowing the assumption of infinite joints to be tested. The model setup is shown in Figure 5-8.

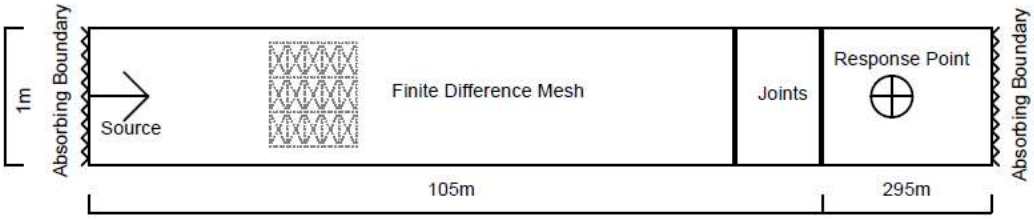

Figure 5-8 DEM-FDM Model 2 with no symmetrical boundaries showing finite difference mesh for finite joint verification case. Mesh fills entire model. Not to scale. From Holmes et al. (2023a) Figure 4

Model 3 – DEM-FDM

Model 3 is a modified version of Model 1, with multiple blocks stacked on top of each other perpendicular to the direction of wave propagation. The vertical spacing of the joints is 1 m, so the model height is increased to 3 m. The blocks represent finite joints, despite symmetrical boundaries being modelled. This gives an additional test of the infinite joints assumption, also tested in Model 2. The model set up is shown in Figure 5-9. Horizontal and vertical joints have the same properties, as those shown in Table 5-2. The element size remains as 0.2 m vertically and 0.125 m horizontally, as used in Models 1 and 2, also allowing frequencies up to 2662 Hz to be transmitted.

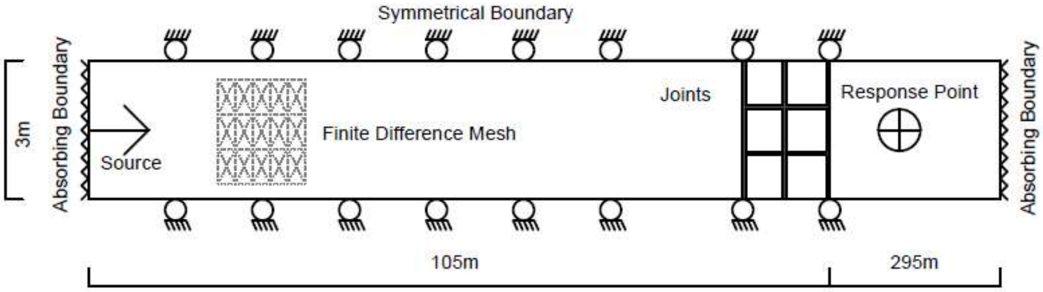

Figure 5-9 DEM-FDM Model 3 with multiple blocks showing finite difference mesh for finite joint verification case. Mesh fills entire model. Not to scale. From Holmes et al. (2023a) Figure 5

Results for Discrete Models

Figure 5-10 shows the results from Models 1 to 3, along with the analytical results, from the previous Chapter. This Figure shows that all of the models display comparable results, with maxima at similar frequencies to the resonance predicted by the analytical function (Equation 4-18), at 96 Hz.

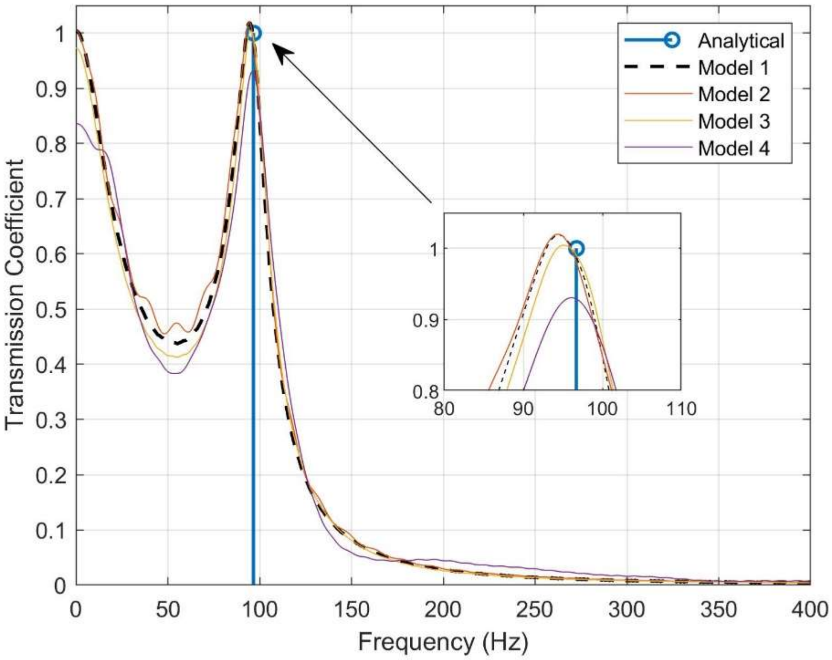

Figure 5-10 Transfer functions for Models 1 to 3 and the Analytical Function. From Holmes et al. (2023a) *Figure 9*

Despite the similarities none of the models exactly match the results of the 1D, infinite jointed, Model 1. The finite jointed Model 2 and the blocky Model 3 have similar transfer functions to Model 1, with similar high frequency content as well as similar transmission coefficients at the resonant frequency and at 0 Hz. However, there are differences at the local minima in the transfer functions at approximately 50 Hz. Model 2 shows an undulating transfer function here, with a higher transmission coefficient than Model 1. Model 3 shows a smooth transfer function, but at a lower transmission coefficient when compared to Model 1. The differences observed in the transmission coefficients of Models 2 and 3 are due to the different modelling assumptions used, as all other inputs and the signal processing are identical. Despite these differences it is clear that the spring resonance mechanism can be observed in these models, due to the clarity of the high transmission peak at the predicted frequency.

5.3.2. Boundary Types

All models used up until now in this Chapter and Chapter 4 adopt absorbing boundaries at the ends of the DEM-FDM models. This assumption should be tested, to verify how it affects results. The models in this section use the 1D model from the previous Chapter but apply different boundary types to determine their effect on the transfer functions. The boundaries applied are absorbing boundaries, which acts as a base case, as well as free and fixed boundaries. Free boundaries are allowed to move, while fixed boundaries are prevented from moving at all, with a zero velocity condition applied. Figure 5-11 shows the results of this sensitivity analysis, showing that the boundary type does not affect the amplitude of the transfer function or the frequency of the resonances. It should be noted that absorbing boundaries half the amplitude of vibrations which are transmitted into the model due to the way in which the boundary conditions are implemented in the code (Itasca Consulting Group Inc., 2014). Despite this, the transfer function does not change.

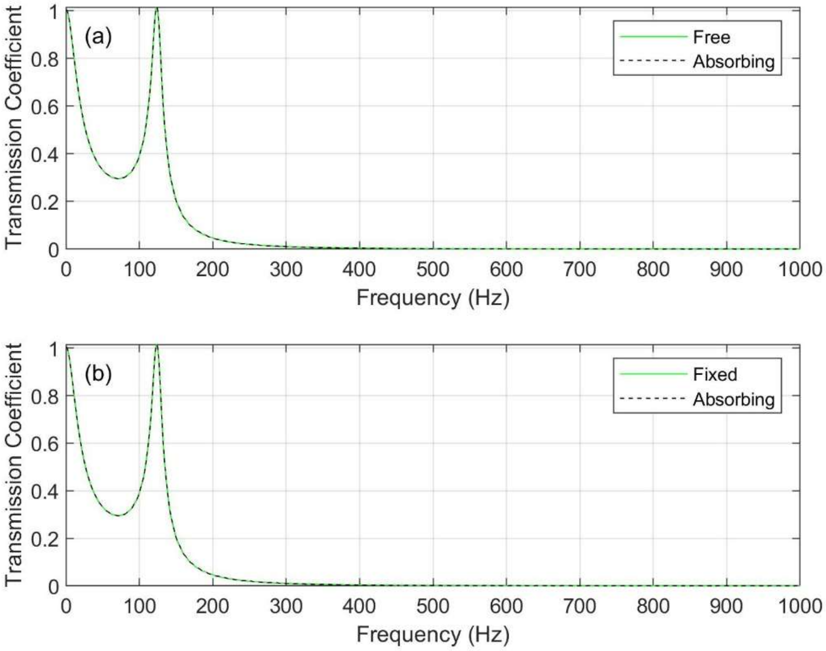

Figure 5-11 Transfer functions for different boundary types

5.3.3. Equivalent Material Models

Equivalent materials are investigated to determine whether the resonance effects are preserved when the method of representing joints is changed. The modelling is undertaken using a 1D FDM model using WAVE2D (Hildyard et al., 1995), shown in Figure 5-2, which has also been used in Section 5.2.5. This model is equivalent to Model 1 from Figure 5-10, solved in a different software. Despite being solved in a different numerical code, the model still uses a discrete representation of fractures. Figure 5-4 to Figure 5-6 show that the FDM code shows the spring resonance mechanism, so this model provides a suitable baseline to determine whether the resonance occurs in the equivalent models. The exact same set up used for this FDM model in WAVE2D is used previously in this Chapter, with dimensions of 2080 x 4800 elements. With the material properties given in Table 5-2 this model will be able to transmit frequencies up to 4160 Hz.

The models in this section follow the approach adopted by Parastatidis (2019), who models jointed materials using three different material models: a discrete representation of joints (DM), a localised equivalent medium (LEM) and a homogenous equivalent medium (HEM). Discrete joints are modelled using a special element representing joints (Hildyard et al., 1995), while the localised and homogenous equivalent mediums were modelled using equivalent transversely isotropic materials. The discrete representation of joints in the WAVE2D code is also used for the models in Section 5.2.5. The LEM applies an equivalent medium to the grid points which are represented by joints in the DM. The HEM on the other hand applies equivalent material properties to the entire model. To capture the effect of the joints, cracks per unit length (*1/s*) is used. This is calculated as the surface area of each joint divided by the volume of the equivalent material. The calculation of crack per unit length is shown in Equation 5-1, where *A* and *B* are the dimensions of the joint surface, *C* is the length of the equivalent material, *N* is the number of joints and *s* is the joint spacing. Finally, *1/s* is used to modify the elastic properties of the medium using the method of Coates & Schoenberg (1995).

$$\frac{1}{s} = \frac{ABN}{ABC} \qquad \text{Equation 5-1}$$

An additional material model using the HEM is also used in this section. This is the locally homogenous equivalent medium (LHEM). The LHEM only applies transversely isotropic material properties between the first and last joints. This will increase the *1/s* of that medium, and therefore change the material properties used in this area, when compared to the HEM. These material models are illustrated in Figure 5-12. The LHEM is introduced as joints only fill a small portion of the model shown in Figure 5-2, while they populate the entire model used by Parastatidis (2019). Due to the size of the model the effect of the joints in the HEM is diluted across the entire model, while the effect of the joints in the LHEM is contained between the first and last joint, which can be thought of as the jointed region of the model.

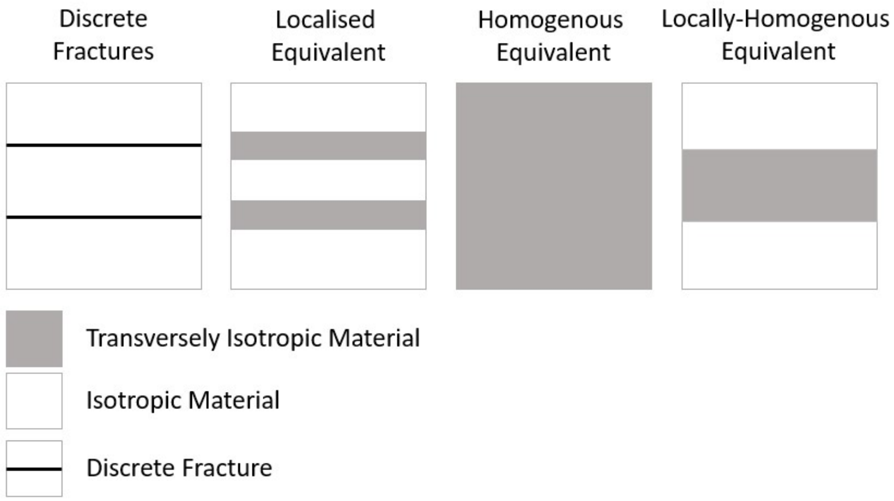

Figure 5-12 Equivalent material models used in study. From Holmes et al. (2023a) *Figure 8*

Results for Equivalent Material Models

The model presented in Figure 5-2 is modelled with the different equivalent materials shown in Figure 5-12. The results for this are shown in Figure 5-13. There is an analogous profile to the transfer functions given by the DM and LEM models, with corresponding frequencies of local maxima. In the DM this occurs at 96 Hz, while in the LEM this occurs at 92 Hz. These occur at similar frequencies to the analytical prediction of the spring resonance, occurring at 96 Hz. The LHEM and HEM models show vastly different transfer functions to the DM model. The HEM model shows a transmission coefficient equal to one at all frequencies. This is to be expected using a 1D model with no damping, as there is no potential for the wave to be modified during transmission. Up to 30 Hz the LHEM model shows similar transmission coefficients to the DM and LEM models; however, past 30 Hz the profiles of the transfer functions are quite different. The LHEM has an oscillation in the transfer function with maxima located at an even spacing of 146 Hz. This oscillating transfer function is likely to be related to the superposition of waves within the weaker, and therefore slower, block of equivalent material within the model. This is equivalent to the superposition resonance mechanism observed in jointed materials. This reduced stiffness block will not oscillate under the spring resonance mechanism as no joints, analogous to springs, are modelled.

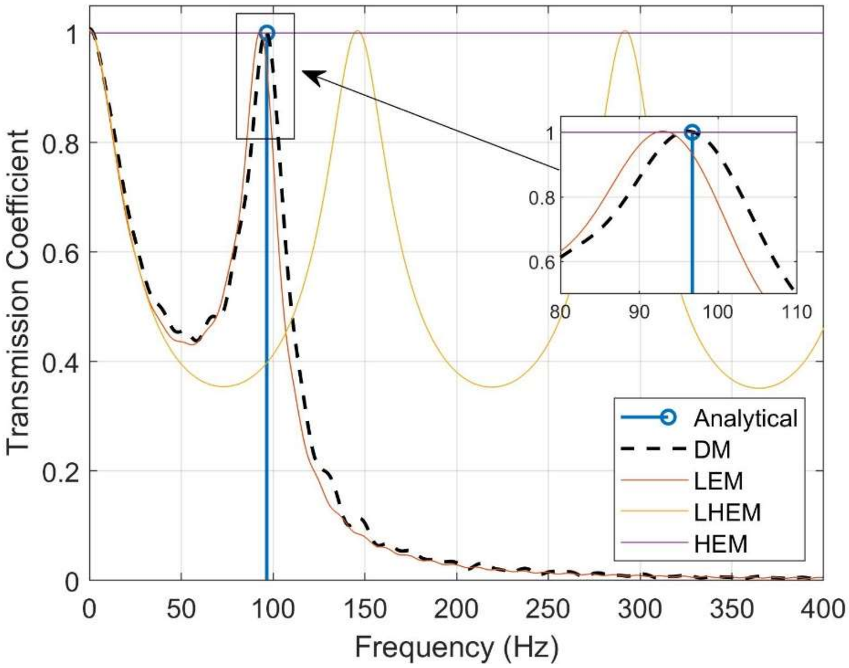

Figure 5-13 Transfer functions for equivalent material models. From Holmes et al. (2023a) *Figure 11*

It is clear from Figure 5-13 that the results for the DM and LEM models show the spring resonance, occurring at very comparable frequencies. The minor differences in the frequency of the LEM and DM resonances are likely to be due to minor differences in the properties modelled in each of these models, possibly due to the calculation of the *1/s* parameter (Equation 5-1). Despite these minor differences the spring resonance effect occurs in these models. The same cannot be said about the LHEM and the HEM models. This indicates that for the resonance effects to occur, fractures need to be modelled in their realistic locations; regardless of whether this is done using a discrete representation or an equivalent representation of the fracture properties. This doesn't mean that the fracture position needs to be a certain distance from the source, as this was tested and found to not affect the response in Figure 4-36. Instead this refers to joints needing to be modelled explicitly rather than averaged over an area using continuum techniques. Figure 4-36 Transfer functions for multiple jointed rocks with Jn=2 for different modelling conditions with an excitation at 0m

5.3.4. Frequency Sweep

Numerical Frequency Sweep

The previous verification analyses in this Chapter are conducted using numerical models and set ups which are only practical in numerical models. These includes geometrical constraints, such as exceptionally long models, and modelling assumptions, such as absorbing boundaries.

This section focuses on an analysis technique that can be adapted for use with a physical experiment.

The models in Chapter 4 and this Chapter use the same process of generating a transfer function based on a full waveform. This requires reflections to be prevented from returning from the model boundaries to be recorded at the response point. Pollution of the signal by reflections may mask any effects which the joints within the model have on the transmitted wave form. To prevent reflections in the previous models, absorbing boundaries are used and boundaries are sighted at large distances from the area of interest, giving a significant time gap between the transmitted wave and the reflected wave from the boundary. This approach is consistent with the approach of other studies, such as Cai & Zhao (2000) and Zhao et al. (2006). While these boundary conditions are possible in numerical models, they are impractical for physical experiments.

Models for physical experiments are often required to be relatively small in order to fit into experimental apparatus. The model in Figure 5-7 for instance is 400 m long, which would be impractical and expensive to produce. Smaller models will prevent reflections from being eliminated from the output, due to inevitable reflections from the ends of the sample. Therefore, a different analysis technique is required. Dynamic Mechanical Analysis (DMA) is often used for physical investigations of soft tissues (Menard and Menard, 2020); however, it has not previously been used for the investigation of jointed materials.

DMA operates by exciting a sample with a harmonic load, recording the response at the other side of the sample (Figure 5-14). As the resonance mechanisms allow transmission of resonant frequencies and does not allow the transmission of non-resonant frequencies, the response of a resonant frequency should have a greater amplitude than the response of a non-resonant frequency.

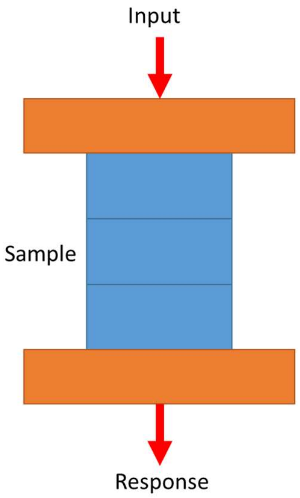

Figure 5-14 Example of a DMA experiment set up

A numerical frequency sweep experiment has been set up to test whether this approach to exciting the model, using harmonic waves, will show the resonance mechanisms identified. The model in Figure 5-7 is used, as it is known that this model works well for showing resonance using the transfer function approach and therefore should also work well for this scenario. Three joints are modelled, which have the properties shown in Table 5-2.

The experimental set up is similar to that used by Zhao et al. (2006). Zhao et al. (2006) excited a model with a harmonic wave, adjusting the model to give a constant normalised joint stiffness, given as $k_n/z\omega$ (k_n=joint stiffness, z=seismic impedance, ω=angular frequency). The numerical frequency sweep used in this section uses a harmonic wave as the input and records the PPV of the first arrival. However, the model is not changed when the frequency of the input wave changes, giving a changing normalised joint stiffness throughout the analysis.

The frequency sweep of the model is conducted between 10 and 1000 Hz. The resolution of the frequency sweep is finer in the areas where resonance is predicted, given by the resonance Equations in Chapter 4 (Equations 4-18 and 4-20), and coarser outside of these areas. The model used here is expected to have spring resonances at 62 and 107 Hz, with superposition resonance at 832 Hz. The results of this experiment are shown in Figure 5-15. A transfer function is also given as a comparison, generated from the same model excited by a 500 Hz Gaussian wave using the conventional transfer function approach adopted in previous analyses (Section 4.3).

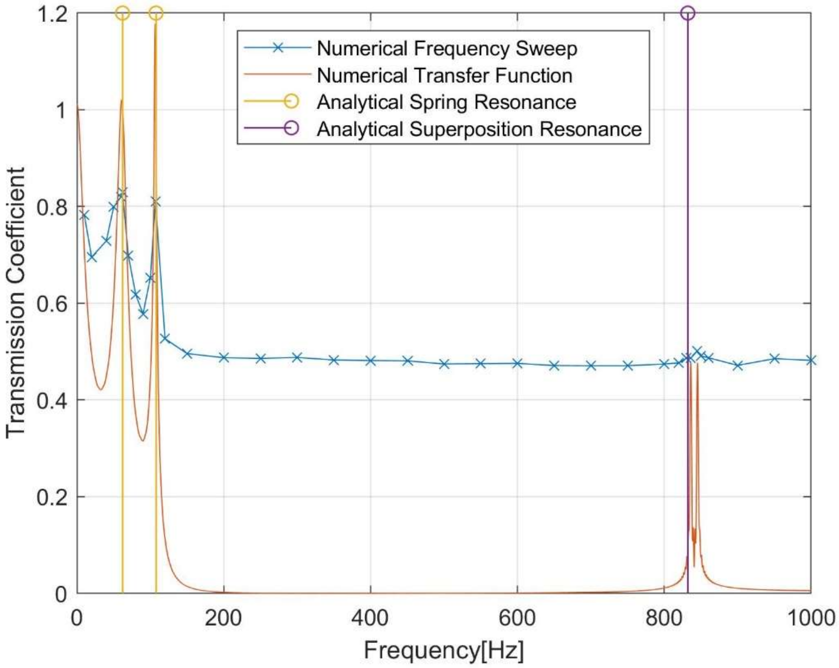

Figure 5-15 Resonance mechanism verification using a numerical frequency sweep and numerical transfer function. Resonance from analytical functions is also shown. (Jn = 3, s = 2m, k_n *= 1GPa/m, Cp = 3328m/s, Cs = 1922m/s, ρ = 2600kg/*m^3*). From* Holmes et al. (2023b) *Figure 11*

Figure 5-15 shows that the analytical resonance, numerical transfer function and numerical frequency sweep methods show the spring resonance effect at the same frequencies. These occur at the predicted frequencies of 62 and 107 Hz. The frequency sweep is targeted to find these resonances; however, the peak response of the frequency sweep is much greater than the surrounding frequencies, so this effect is unlikely to be an effect of the experiment set up.

Superposition resonance is seen at approximately 845 Hz in the numerical frequency sweep data, which is slightly greater than the analytical frequency of 832 Hz but similar to the numerical transfer function frequency, seen at 836 and 845 Hz. The peak of this has a relatively low transmission coefficient, especially compared to the transmission coefficient of the non-resonant frequencies; however, it is clearly a localised peak.

There are clear differences with the response of the two numerical experiments. The transmission coefficients of the frequency sweep data are lower for the resonant frequencies, while they are greater for non-resonant frequencies. For the non-resonant frequencies between 200 and 800Hz, the transfer function data shows a transmission coefficient of close to zero, while the frequency sweep data shows a transmission coefficient of approximately 0.5. The difference here is due to the different techniques used to measure the response of the models. The transfer function sends a single pulse of excitation and records the full waveform transmitted through the joints, while the frequency sweep method applies a constant harmonic excitation for the duration of the model run and records the PPV of the model. Despite the differences in the techniques used and the amplitude of the transmission coefficients, the presence of the resonant frequencies is clearly evident in the two different numerical experiments. This supports the hypothesis that the two resonance mechanisms of spring and superposition resonance, do exist in jointed rock masses.

Physical Frequency Sweep

With the success of the numerical frequency sweep shown above to highlight the spring and superposition resonance effects, attempts were made to run a physical experiment using the DMA apparatus located in the Faculty of Biological Sciences at the University of Leeds. The apparatus has a physical limit of 6 cm for a full sample and the equipment has a maximum loading frequency of 1 kHz. This gives a physical limit on the possible block size. In order for the sample to oscillate at a low enough frequency to be excited by the apparatus a relatively dense material is required. A sample was prepared consisting of three 2 cm tall blocks of 303-stainless steel with a diameter of 2.54 cm (Figure 5-16). This material was chosen due to its high density and because it was readily available from on-site workshops, making it cheap to prepare. The spacing of joints within a material affects the frequency by which the block will oscillate, with a smaller block oscillating at a higher frequency. Attempts were made to test the sample using clean joints; however, due to the similarity between the stiffness of the sample and the material which the apparatus is composed of. To reduce the stiffness of the sample and reduce the frequency of oscillation the joints which bound the central block were filled with a thin layer of rubber. This causes the sample to behave like a single 2 cm thick block bounded by rubber. The outer blocks will not oscillate at a low enough frequency to be recorded as the joint between the sample and the platen of the load cell has a much higher stiffness.

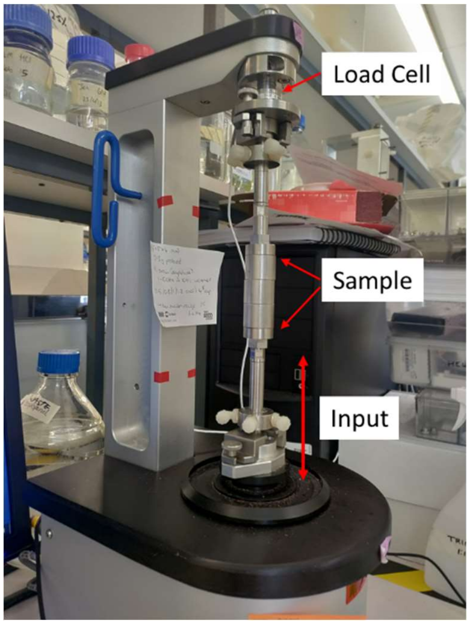

Figure 5-16 DMA apparatus in the Faculty of Biology with sample loaded

In order to test whether this sample set up will work theoretically a numerical model is generated. The model used for the numerical frequency sweep experiment is modified to have the same dimensions and properties as the physical sample. The results of this are shown in Figure 5-17. A slightly different method of determining the transmission coefficient is used for the results in Figure 5-17. Here the maximum amplitude of the source function was compared with the maximum amplitude of the response. This is necessary because the model is relatively small, at only 6cm, and it would be impossible to totally eliminate any reflected waves within the model. This set up closely matches the setup of the physical model and allows both the theoretical response of the sample to be tested as well as showing whether the model set up will work to show resonance using such a technique.

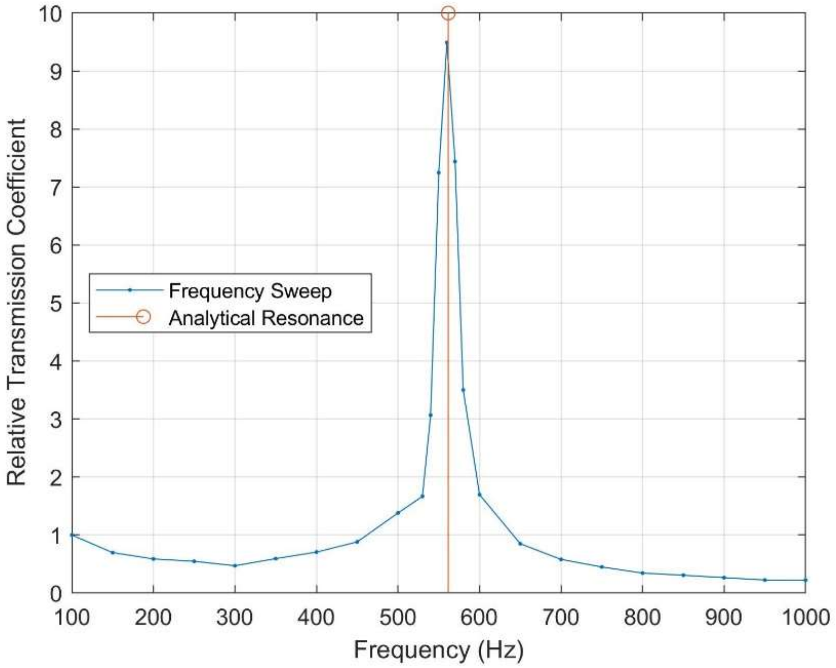

Figure 5-17 Frequency sweep experiment for 2cm wide steel block with rubber filled joints

Figure 5-17 shows that the sample has a resonant frequency of 560 Hz, identified by Equation 4-18 and the experiment. This is within the range of excitations which can be generated by the DMA apparatus. Unfortunately, this experiment was never successfully run. The steel sample, even with rubber filled joints, has an extremely high stiffness which the load cell struggles to respond to. This causes the apparatus to indicate an error and shut down before results are given.

5.4. Discussion

The two jointed rock mass resonance mechanisms are identified in numerous different scenarios in this thesis. These are spring and superposition resonance. These mechanisms are shown to occur for materials with a wide range of different properties and joint spacing's. Therefore, the analytical models in this study can be confidently applied to all jointed media; including natural jointed materials from the weakest of Sandstones through to the strongest of Granites, as well as synthetic jointed materials, such as metamaterials (Witarto et al., 2018; Huang et al., 2021), aligned metallic or mortar blocks (Pyrak-Nolte et al., 1990a; J. Zhao et al., 2006) and masonry structures.

While the superposition mechanism is described by Nakagawa (1998), the spring resonance mechanism has not previously been isolated, despite being based on the simple system of masses between springs. Superposition effects are a common theme in relation to the transmission coefficient from jointed rock masses. Cai and Zhao (2000) and Zhao et al. (2006b, 2008) identify an increased transmission zone occurring when the ξ $(=s/\lambda)$ of the rock mass is very low, which is explained as a superposition effect of multiple reflected waves. Cai and Zhao (2000) found that the greatest transmission coefficient occurred with a ξ of 0.075, and an increased transmission zone between ξ of 0.05 and 0.3, with no increase in transmission at 0.5. Comparable results were found by Zhao et al. (2006b, 2008). The values of ξ found by these studies are much lower than what is expected to generate superposition resonance, which occurs at a value of 0.5. The previous studies give analytical Equations for the first arrivals of a sine wave which is transmitted through joints based on superposition of transmitted and reflected waves. These are found to perform well against numerical results. Therefore, while the values of ξ given in the previous studies are too low to be superposition effects based on Equation 4-18, it is considered that the mechanism proposed previously is still correct for first arrivals.

Despite this, it is curious that this research found that values of ξ smaller than 0.5 tend to be associated with spring resonance as opposed to superposition resonance. The reason behind this is due to the way in which this thesis and previous studies approach the calculation of the transmission coefficient. Previous studies (Cai and Zhao, 2000; J Zhao et al., 2006) take the amplitude of the first arrival after the joint and divide this by the amplitude of the wave before the joint, with the rest of the transmitted waveform ignored. However, this study takes the full waveforms before and after the joint and calculates a transfer function from these, by decomposing these into their harmonic components using Discrete Fourier transforms (Section 4.3). These represent two methods of characterising the transmission of stress waves through joints, being a first arrival method, as used in previous studies, and a full waveform method, as used in this thesis. While it can be considered that for a first arrival the superposition mechanism of Zhao et al. (2006b) is correct, any receptor will experience the full waveform. Therefore, for practical applications, Equations 4-18 and 4-20 are of value.

To test that the models considered in the current study are simulating the same problem as Zhao et al. (2006b), a set of their results have been replicated in Figure 5-18. The results of Cai and Zhao (2000) and Zhao et al. (2006b) are normalised for joint stiffness, so cannot be directly compared to the results in this thesis. Therefore, a bespoke analysis is undertaken to replicate their results. Figure 5-18 shows the results from Zhao et al. (2006b) for a model with two joints with a normalised joint stiffness ($k_n/z\omega$) of 0.494. A new model is generated to match this normalised joint stiffness and two sets of modelling results are collected. The first set modells a single period of a 40Hz sine wave, with the amplitude of the first arrival recorded. The second set modelled a 500Hz Gaussian wave, with a transfer function generated based on the full waveform and the response at 40Hz recorded. The first arrival of data is synonymous with the approach of Zhao et al. (2006b) and the full waveform synonymous with the transfer function method in this study.

The First Arrival data, shown in Figure 5-18, shows that the 1D models used in Chapter 4 agree with the results from Zhao et al. (2006b). However, when the full waveform is analysed to generate a transfer function and the response at 40 Hz is taken from this, shown by the Full Waveform data, the results of this thesis reveal something different to the Zhao et al. (2006b) study. The peak of the full waveform is at a different ξ and with a greater transmission coefficient than the peak of the first arrival data. There is a low transmission portion of the full waveform data series approaching a ξ of 0.4; however, it is at a lower transmission than the First Arrival data. The differences exhibited highlight that different mechanisms are occurring in the rock mass when a first arrival is considered in isolation and the full transmitted waveform is analysed. In the full waveform it is not just superposition, which is occurring, and such superposition only occurs at much higher frequencies. This implies that the spring resonance mechanism is not contained within the first arrival. The spring resonance requires the blocks to oscillate, with a period given by $1/f(n)$ from Equation 4-18, so it is unlikely that these resonance mechanisms will be realised in a first arrival.

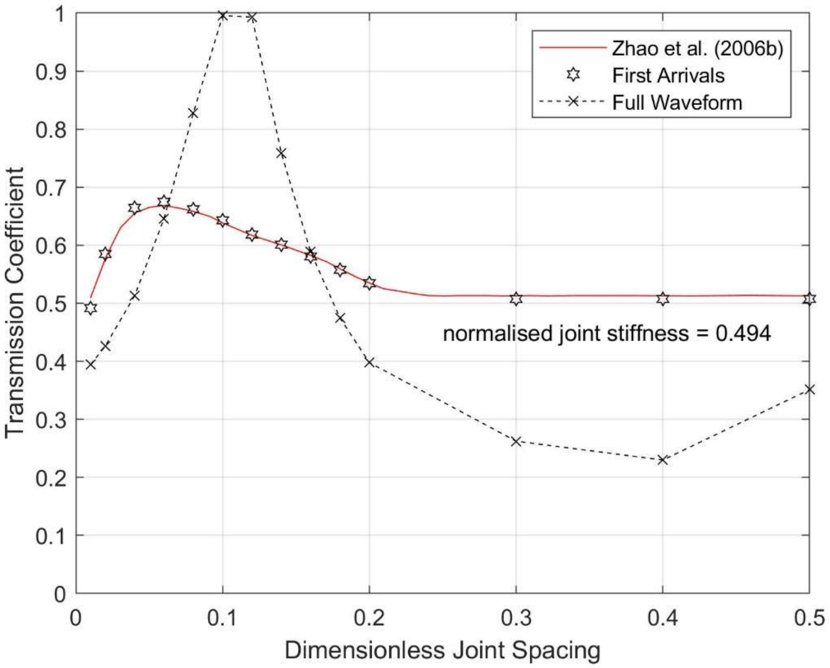

Figure 5-18 Transmission coefficients for jointed rocks with Jn of 2, plotted against dimensionless joint spacing (ξ) with results from Zhao et al. (2006b) *and from the current study generated using the first arrival and the full waveform. From* Holmes et al. (2023b) *Figure 12*

Figure 5-18 shows that the results of Zhao et al. (2006b) appear to be appropriate for first arrivals; although, as highlighted by the newly identified jointed rock mass excitation mechanism of spring resonance presented in this study, only studying first arrivals will miss the nuances of transmission of the full waveform. This could lead to a miss-identification of the frequencies of a wave that are preferentially transmitted through a jointed rock mass.

It is clear from Figure 5-18 that any resonance effects in the full waveform method are not clear. This is brought about using the normalised joint stiffness. Instead of considering a range of frequencies from a single model with a constant joint spacing, each data point represents a new model with the same wave frequency and a different joint spacing. As a consequence, the clear resonant peaks identified in this study are not apparent. This is not to say that resonance cannot be shown in dimensionless terms. For instance, Figure 5-19 shows the resonance of a numerical model with 8 joints modelled in UDEC, along with the analytical resonances. This model does not have a constant normalised joint stiffness but represents a transfer function for a range of frequencies for the same rock mass.

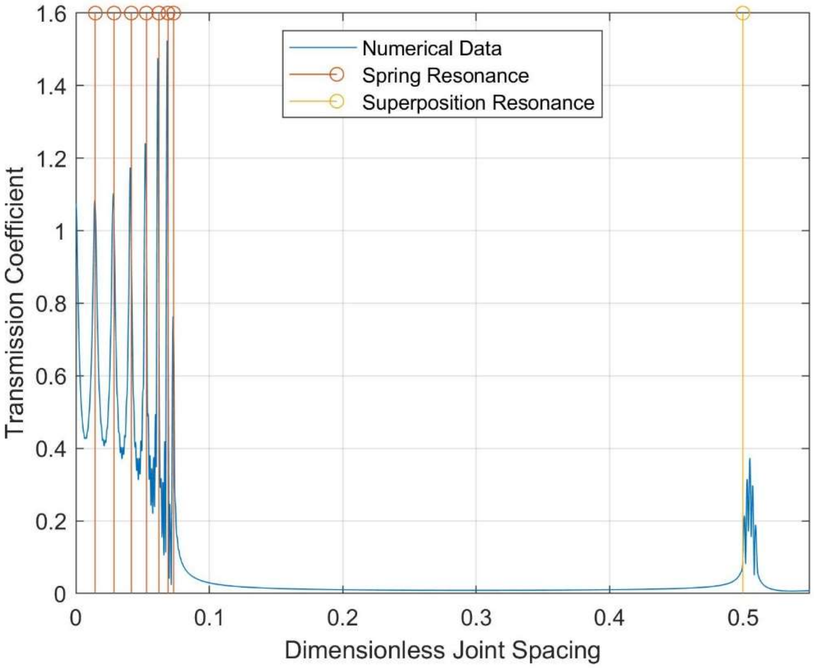

Figure 5-19 Jointed rock resonance shown by a model with 8 joints (7 blocks) along with the analytical spring and superposition resonance, plotted against dimensionless joint spacing (ξ). Cp = 3328 m/s, Cs = 1922 m/s, ρ = 2600 kg/m^3*,* k_n *= 1GPa/m, s = 2m, Jn = 8. From* Holmes et al. (2023b) *Figure 13*

The apparent agreement of the models of Zhao et al. (2006b) and this study implies that if the full waveform were analysed then the resonance effects found here would be identified in the previous study as well. Zhao et al. (2006b) do not give clear time series for the full waveform; however, these are given by Cai and Zhao (2000) and are reproduced here in Figure 5-20. These are given in dimensionless terms for time, joint spacing and joint stiffness, so it is not possible to directly calculate the resonances from the full waveform. Despite this, there are clear oscillations occurring in the transmitted wave in the plots given. Figure 5-20 shows the initial wave in each of the plots followed by oscillations. These are most clearly shown by Figure 5-20 b and c, although they are evident in all of the plots. The dimensionless period of the oscillations seems to reduce as the relative joint spacing reduces, with the largest relative joint spacing in Figure 5-20 a, and the smallest in Figure 5-20 d. As the joint spacing reduces, assuming all other properties of the model are the same, resonance of the models will occur at a higher frequency. With two joints there will be a single spring resonance, although there will also be additional superposition resonant frequencies. The superposition resonance will be at a high frequency when the joint spacing is small, but this will reduce as the joint spacing increases. This will lead to the spring and superposition resonances overprinting on each other in the transmitted waveform, which is evident in the complex time series given in Figure 5-20 a for the largest joint spacing.

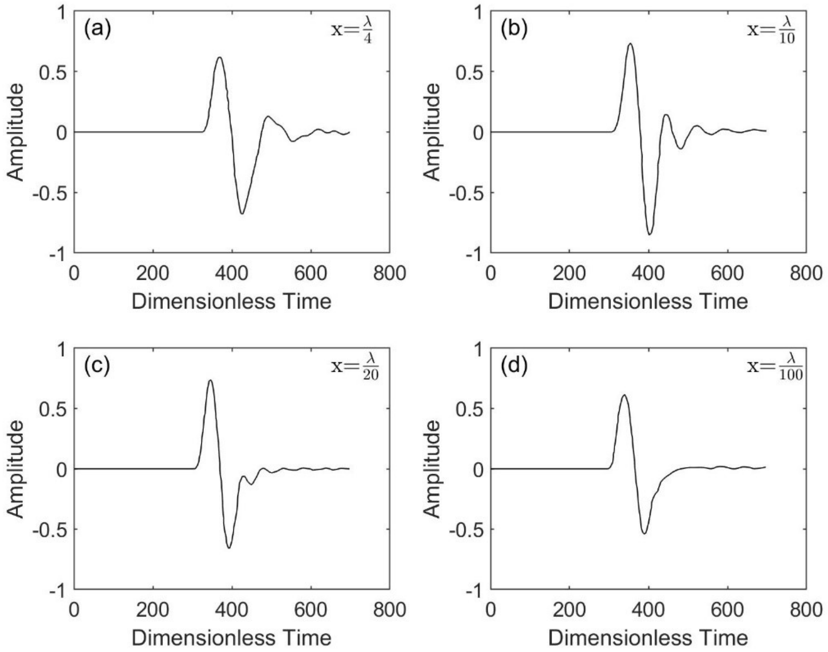

Figure 5-20 Transmitted waveforms from numerical model with two joints. X represents joint spacing relative to wavelength (λ) of incident sine wave. Modified from Cai and Zhao (2000) *Figure 6*

5.5. Conclusion

This Chapter has undertaken further investigations into the resonance effects observed in jointed rock masses in Chapter 4, with most work conducted into the spring resonance effect, which operates at relatively low frequencies. This low frequency resonance is most likely to occur within the frequency range of rail vibrations, so is of most relevance to this research.

Verifications are undertaken in the combined DEM-FDM (as used in Chapter 4) as well as using the FDM. The modelling in this Chapter is split into four sections; an initial comparison of the two methods, discrete joints, and equivalent material models. The initial analysis was run to compare the two methods used in this Chapter, to show that the FDM can model the same problems as the DEM-FDM. Following this the DEM-FDM model from Chapter 4 is modified to change modelling assumptions used previously, including symmetrical, absorbing, and fixed boundaries as well as infinite joints. All models run show the spring resonance effect at the predicted frequency. Finally equivalent material models are used and compared to a discrete jointing representation. These are run to indicate whether continuum methods can be used to accurately model the response of a jointed rock mass. It is found that a localised equivalent medium gives a similar response to a model with discrete joints; however, a homogenous equivalent medium does not. This is because the homogenous equivalent medium averages out the effect of joints over a wide area, while for the spring and superposition resonance to occur the joint needs to be modelled in position. A potential physical experiment is presented using the technique of dynamic mechanical analysis with a frequency sweep to excite a physical sample. Numerical simulations of this experiment are shown to have high transmissions at the resonant frequencies of a jointed material. However, it was not possible to run the experiment physically.

The Chapter finishes by looking at why the resonance mechanisms have not previously been identified in literature. This is done by comparing the analyses in previous similar studies to the work conducted here. It is shown that the resonance mechanisms identified in this study are generated by analysing the full waveform, while previous studies only use data from first arrivals. An analysis is run which shows that the models in the current study can replicate previous researcher’s results, indicating that they are modelling the same problem. Evidence is finally presented showing that, if a full waveform were used to generate transfer functions in previous studies, the resonance mechanisms would have been identified.

6. Resonance in 2D Rock Masses

"An extra dimension is introduced,
To see if the effects can be reproduced.
Models containing a cavity,
Give this chapter a realistic gravity."

© Army of Cats 2023

6.1. Introduction

This chapter discusses the modelling of vibrations in 2D jointed rock masses and adds an additional layer of complexity following on from the 1D work covered in Chapters 4 and 5. It aims to identify whether the trends observed in 1D occur in 2D models, as well as attempting to identify whether there are any additional effects generated in 2D models. In 2D it is possible to also model tunnels and cavities, making this Chapter much more applicable to real situations in which vibrations could be generated. The 2D models in this Chapter only consider non-moving point loads, with moving loads being the subject of Chapter 8.

Much research has been undertaken looking into the effects of 2D and 3D models, which is reviewed in Chapter 2, so will not be revisited in detail here. In summary, a 2D model will not give a realistic magnitude to the vibrations from tunnels, so cannot be used to accurately predict vibration levels; however, 2D models can be used for the qualitative assessment of vibrations (Andersen and Jones, 2006). The use of 2D models in this section represents a gross simplification of the real-world problem but does provide a reasonable initial step in a poorly understood field, with regards to vibrations from tunnels in jointed rock masses. They are also be used as an additional verification, in addition to those presented in Chapter 5, for the presence of the 1D rock mass resonance mechanisms.

The models in this section consider 2D plane strain rock masses, with a load applied at a point in the centre of the model. Transfer functions for the velocity response of the rock mass at points in the model are derived. These are used to highlight how changes to a model affect the transmission of stress waves in a rock mass. The changes which are made to models here include the addition of joints and a tunnel as well as changing the material model used. Therefore, this section examines not only the transmission of stress waves in jointed rock masses but also different ways of modelling equivalent rock masses, by using an equivalent continuum and a discontinuum. The use of equivalent materials follows on from similar work in Chapter 5.

6.2. Methodology

Models are created in the FDM and solved in the software WAVE2D, which is used in Chapter 5. WAVE2D is used, as opposed to UDEC, as the solver is much more efficient for larger 2D models, such as those used in this chapter. In addition to this, due to the method used to generate the transfer functions in this Chapter the ability to manually define the modelling time step is advantageous. The modelling time step can be set manually I both WAVE2D and UDEC; however, this is much easier to do in WAVE2D.

There are some key differences between the previous 1D models and the 2D models presented in this Chapter, as all the previous models are physically 2D, despite representing a 1D scenario. In order to ensure that the models in this Chapter are modelling a 2D scenario a non-plane wave is excited from a single node of the finite difference mesh in the centre of the model (Figure 6-1). This gives a wave front that spreads out in all directions. Even if there is no material damping in the model, the non-planar wave causes geometrical damping to occur. If the previous method for generating the transfer functions are used, by comparing the frequency response before the joints and after the joints (Section 4.3), the geometrical damping will influence the results. While geometrical damping is a natural consequence of the transmission of stress waves, it could obscure any frequency dependent transmission effects. To mitigate the effects of geometrical damping, the transfer functions are generated between a test model and a reference model, with the input signal being generated by the reference with the response at position x_i,y_i and the response from the test model also at position x_i,y_i. As both the input and response are taken at the same point, with identical loading inputs, the effects of geometrical damping is removed. This is illustrated in Figure 6-2. The model outputs ($u[ref]$ and u) are equivalent to u_{ref}' and u' which are shown Equation 4-1, after they have been transformed into the frequency domain using a Discrete Fourier Transform, for the calculation of transmission coefficients. This is an identical process to the generation of insertion losses, typically used with the study of wave barriers (Ouakka et al., 2022). The technique of comparing a reference model and a test case has the flexibility to be able to assess the frequency response of the model to changing model inputs. For example, a continuum model can be used as the reference model and a continuum with a tunnel for the test model. If the velocity time-history is taken from both models at a point 10m above the source, the effect of adding a tunnel to the model at this point is determined.

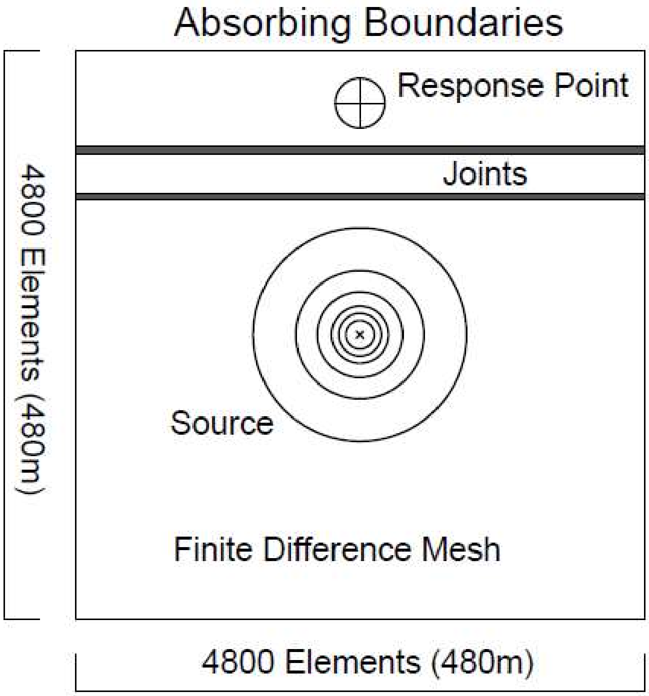

Figure 6-1 2D FDM Model 4 showing finite difference mesh for finite joint verification case. Mesh fills entire model. Not to scale. Modified from Holmes et al. (2023a) *Figure 6*

The model shown in Figure 6-1 uses a similar set up to the 1D FDM models used in Chapter 5 but increases the small axis from the models in that Chapter to be equal to the long axis.

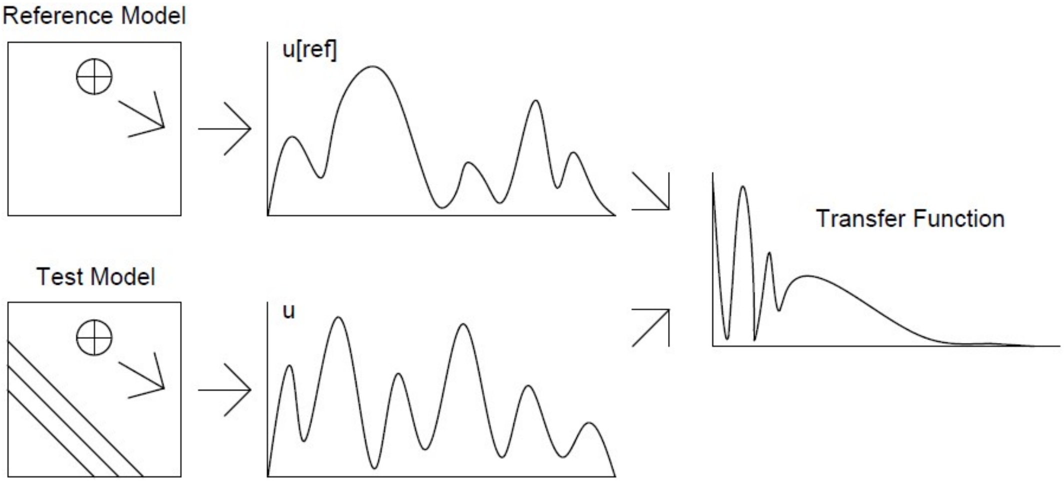

Figure 6-2 Process of generating insertion loss transfer functions from two models giving u[ref] and u response of the models which are used with Equation 4-1 and the methodology outlined in Section 4.3. The example in this figure will show the effect of the diagonal featured aligned in the bottom left of the Test Model

6.3. Verification of Numerical Models

Due to a new 2D model being generated some verification work is undertaken to determine whether the models are behaving as expected. This is undertaken using simple numerical models which approximate an isotropic full space. Much of the work in this Chapter is undertaken using the FDM; however, results from DEM-FDM models are also included. Verification is also undertaken using Green's Functions for an isotropic full space.

6.3.1. Green's Functions for a Full Space

Green's functions, sometimes referred to as fundamental solutions, are partial differential Equations which give the response of a material to an applied load. Their derivation is beyond the scope of this thesis and is a distinct area of applied mathematics in its own right. The previously published Green's Functions, given by Tadeu and Kausel (2000) and Dominguez (1993), are used here.

Green's Functions can be used for static and dynamic responses, although their formulation differs for these two cases. They are the used as the basis of the boundary element method (Crouch et al., 1983). The work in this section is not as in depth as the boundary element method and only requires a single point load in the centre of a full space, with the response recorded at various places within the full space. The Equations required for this are shown below, taken from Tadeu and Kausel (2000).

$$\epsilon_{yy}^{l} = A(\left(\frac{2}{r}B_2 - k_s^2 k_\beta H_{1\beta}\right)\delta_{yl} + \frac{1}{2}B_2 - {\gamma_y}^3 B_3) \qquad \text{Equation 6-1}$$

$$\gamma_i = \frac{x_i}{r} \quad [i{=}x{,}y] \qquad \text{Equation 6-2}$$

$$B_n = k_\beta^n H_n^{(2)}(k_\beta r) - k_\beta^n H_n^{(2)}(k_\alpha r) \qquad \text{Equation 6-3}$$

$$A = \frac{1}{4i\rho\omega^2} \qquad \text{Equation 6-4}$$

$$r = \sqrt{x^2 + y^2} \qquad \text{Equation 6-5}$$

Where x,y are the coordinates of the measurement point, relative to the source; ω is the angular frequency of the source, ρ is the density of the material, ${H^{(2)}}_n$ is the Hankel function of the second kind, $H_{1\beta}$ is the Hankel function of the first kind, ${k^n}_\beta$ is the S-wave wavenumber, ${k^n}_\alpha$ is the P-wave wavenumber, δ_{yl} is the direct delta function and i is $\sqrt{-1}$. A full explanation of the Green's Functions are given in Appendix B.

Equation 6-1 gives the response in the y-direction of a full space at a distance r from an impulse acting in direction l. Equation 6-2 to Equation 6-5 are auxiliary functions which are used with Equation 6-1.

Tadeu and Kausel (2000) are not the only published Green's Functions given in literature. Dominguez (1993) also provides Green's Functions. These can be used to verify that the Green's Functions of Tadeu and Kausel (2000) are working as intended, much like how Hussein

(2004) used the Green’s Functions of Dominguez (1993) to verify that the Pipe-in-Pipe model was working correctly. The results of this verifications are replicated for Dominguez (1993) in Figure 6-3. This Figure also shows the results for the same problem calculated using Equation 6-1. The properties used for this verification are taken directly from Hussein (2004) and are included in Table 6-1.

Table 6-1 Properties for verification of Green’s Functions

Property	**Value**
Density	2000 kg/m^3
Complex P-Wave Velocity	94.983 + 1.085i m/s
Complex S-Wave Velocity	50.79 + 1.522i m/s

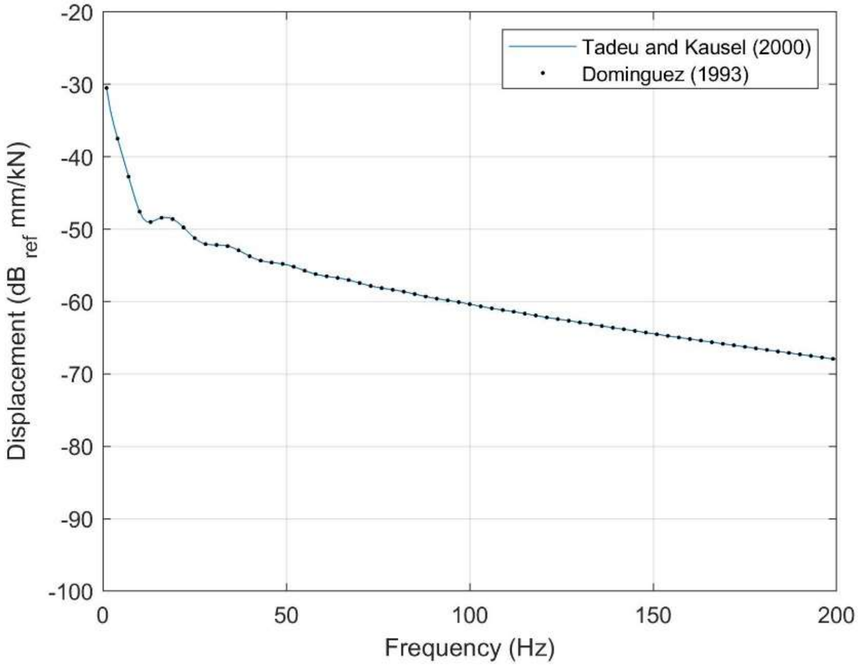

Figure 6-3 Results for Green's functions for displacement from Tadeu and Kausel (2000) and Dominguez (1993) for a response 7 m from an applied load

Figure 6-3 shows that the Green’s Functions of Tadeu and Kausel (2000) are working as expected, so can be used in the verification of the numerical models in this Chapter.

6.3.2. Homogenous Continuum

The Green’s Functions which are discussed in the previous section are now used to verify that a homogenous isotropic WAVE2D model appropriately approximates a full space. In addition to this an equivalent UDEC model is used.

A continuum 2D plane strain model is generated in WAVE2D and UDEC with a vertical load applied at the centre of the model. The WAVE2D model used is equivalent to that shown in Figure 6-1, with the joints removed, with a similar UDEC model also used. These models are compared to the analytical response of an equivalent model, calculated using the closed form solutions for full space Green's functions given by Tadeu and Kausel (2000), shown in Equation 6-1.

Green's functions are a powerful tool for determining the response of elastic materials due to impulses; however, when evaluating these integrals at the source a singularity occurs. This is because of the fraction *1/r* in Equation 6-1. As the value of *r* approaches zero the result of Equation 6-1 approaches infinity. The green's function in Equation 6-1 can be used to determine the response of a full space any point, expect for at the origin. Therefore, transfer functions are recorded between points within the model. Responses for each model are recorded at 5, 15 and 25 m above the load. The transfer functions for the wave travelling between 5 and 15 m and 15 and 25 m are shown in Figure 6-4. This process is identical to the generation of transfer functions from numerical models, as outlined in Section 4.3, except without the need to use a Discrete Fourier transform, as the Green's functions are already solved in the frequency domains. There are some minor differences in the numerical results from the analytical; however, the results appear broadly similar. This shows that the numerical models are performing as intended and can be used for further study into 2D rock masses.

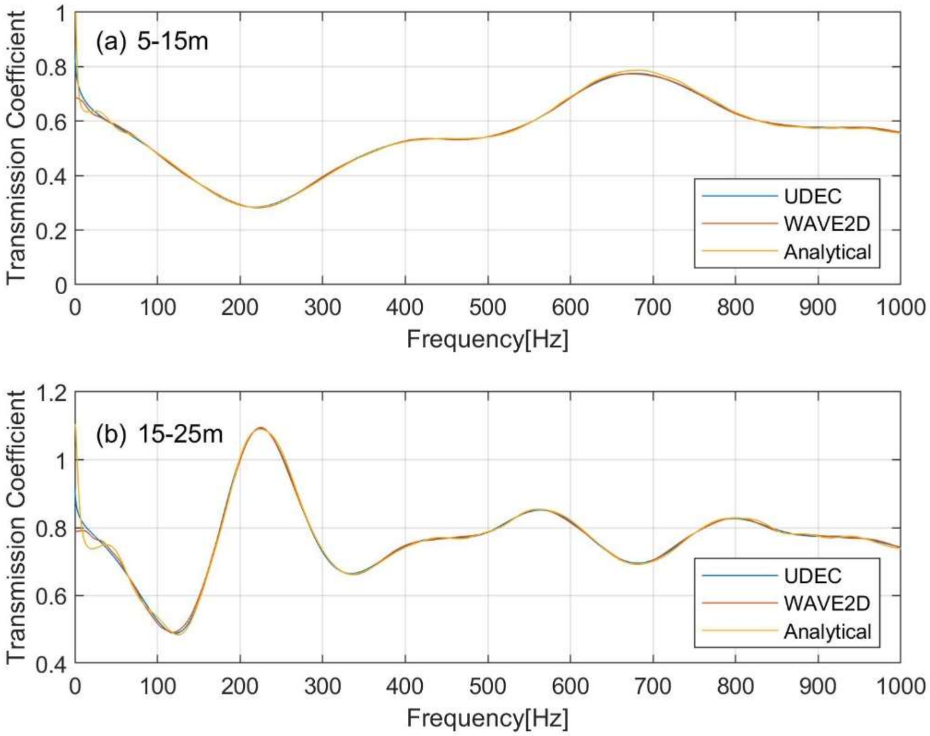

Figure 6-4 Numerical modelling transfer functions for a line load in a 2D plane strain model compared against analytical transfer function. Measurement positions were 5, 15 and 25 m from the source, with transfer function calculated for 5-15 m and 15-25 m. The intact material in all models have a P-wave velocity of 3328 m/s

6.3.3. Cavity in a Full Space

This section attempts to verify whether WAVE2D is accurately modelling the dynamic response of an unfilled cavity in a full space by comparing the response of a WAVE2D model to that of an equivalent UDEC model. There is no closed form solution to the dynamic response of a cavity in full space. This requires a boundary element model using numerical integration techniques.

WAVE2D and UDEC model cavities in different ways. Both models rely on fractures which trace the cavity shape to be generated during the model set up. It is possible to remove the material within the cavity in UDEC; however, in WAVE2D, material cannot be deleted from the model. Instead, a zero stiffness fracture is specified. This has the effect of causing the fractures which define the cavity to become free surfaces, with the material within the cavity not being affected by forces applied outside the cavity. The formulation of the cavities in the models is different, although both have the same effect of generating a free surface within the modelling domain.

Another difference in the way which WAVE2D and UDEC generate cavities is that in WAVE2D fractures are required to be aligned with the finite difference grid, which is generated prior to any fractures being specified. A square grid is used in WAVE2D, meaning that fractures have to be either horizontal or vertical. In UDEC fractures are generated before the finite difference mesh, meaning that fractures can be generated at any arbitrary angle. The mesh is then generated around these surfaces. Despite this, UDEC can still only approximate a curved surface, as the surface is still required to be discretised into line segments. If a square cavity is generated the models will be similar. However, the shape of a circular cavity in WAVE2D can be significantly different to that of a circular cavity in UDEC. Figure 6-5 shows the approximation of a circular cavity in WAVE2D and UDEC. These differences in modelling of the cavity raise the possibility that errors in the transmission of waves could arise due to the boundaries.

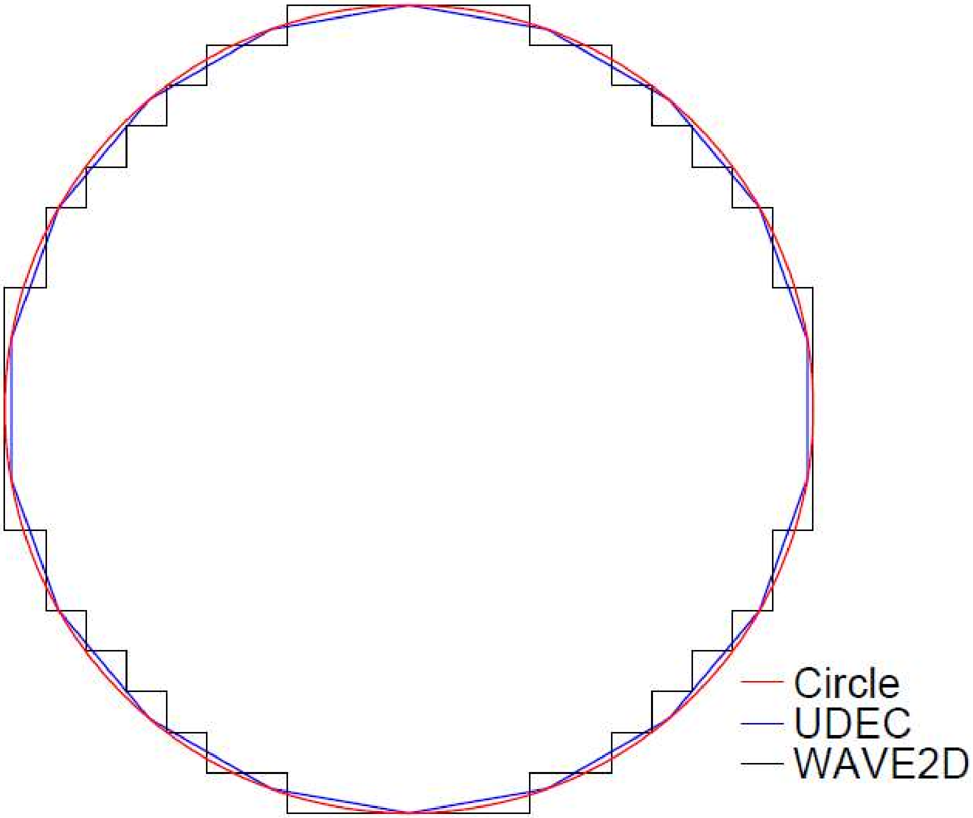

Figure 6-5 Different approximations of a circular tunnel in UDEC and WAVE2D, compared to a realistic circle

To test the validity of the cavity boundaries in WAVE2D results for a series of simple cases are compared with results from UDEC. The simplest case of a cavity in a continuum is a square cavity. The transfer functions for this are calculated in the same way as those for the continuum (Figure 6-4) and are shown in Figure 6-6. This shows that there are some differences in the UDEC and WAVE2D results, although the results are similar.

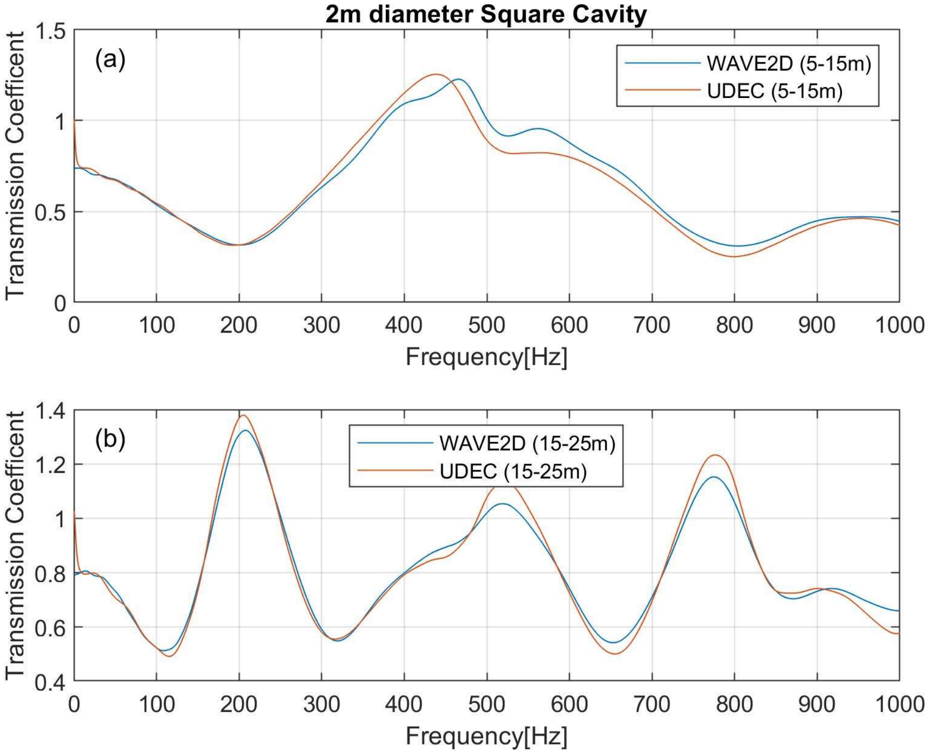

Figure 6-6 Numerical modelling transfer functions for a line load in a 2D plane strain model with a 2 m diameter square cavity. Measurement positions are 5, 15 and 25 m from the source, with transfer function calculated for 5-15 m and 15-25 m. The intact material in all models have a P-wave velocity of 3328 m/s

A more complex case, and the case which has motivated this validation, is the case of a circular cavity. The pseudo-circular cavity shown in Figure 6-5 has been modelled against a discretised circular cavity in UDEC. The transfer functions for this case are shown in Figure 6-7. These show that the models give a similar frequency response up to about 800Hz.

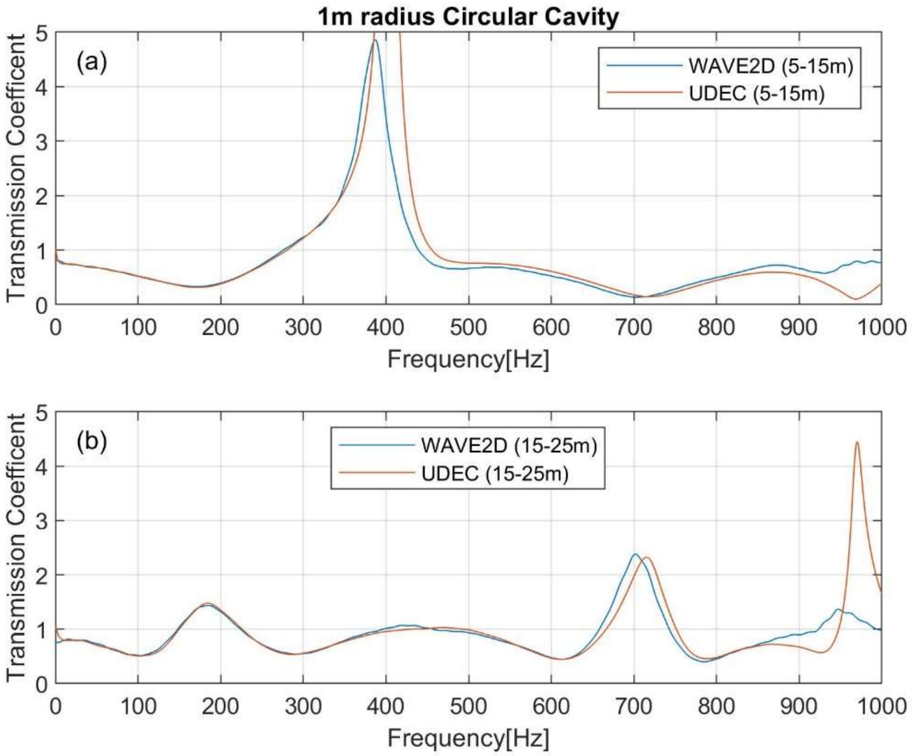

Figure 6-7 Numerical modelling transfer functions for a line load in a 2D plane strain model with a 1 m radius circular cavity. Measurement positions are 5, 15 and 25 m from the source, with transfer function calculated for 5-15 m and 15-25 m. The intact material in all models have a P-wave velocity of 3328 m/s

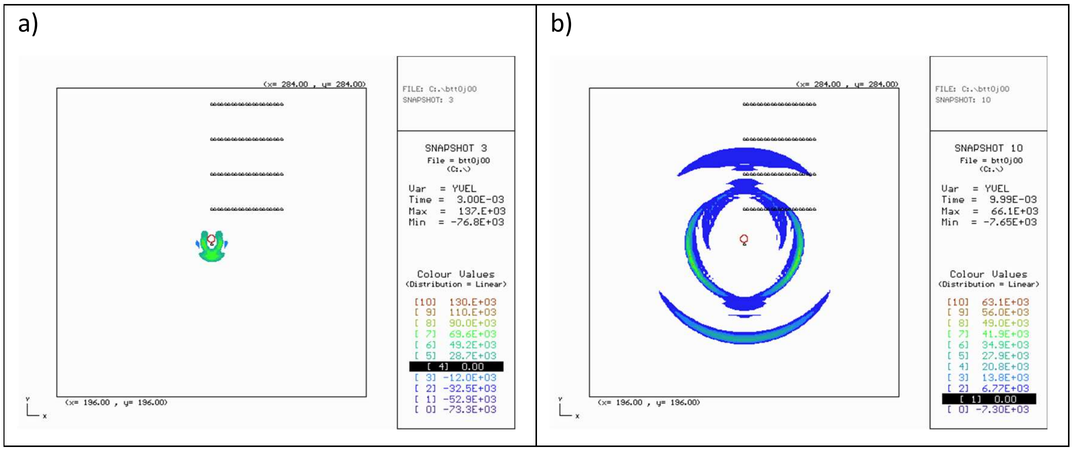

Figure 6-8 Y-velocity contours showing the wave excited from a circular cavity in WAVE2D. a) after 3E-3 s b) after 9.99E-3 s. The intact material in all models have a P-wave velocity of 3328 m/s

Figure 6-8 shows the y-velocity contours for a wave, excited at the invert of a circular cavity. This shows how the wave move out from the cavity, located in the centre of the model with a transmission shadow located directly above the cavity, especially evident in Figure 6-8 a.

Figure 6-9 shows the comparison of a 2 m square cavity, also shown in Figure 6-6, and a 2 m diameter circular tunnel, also shown in Figure 6-7. The results here are shown for WAVE2D only. This shows that a similar diameter square cavity is not a reasonable approximation of a circular cavity, especially at small distances from the cavity boundary. At greater distances, as shown by Figure 6-9 b, the responses of each model become more similar, as found by Jones et al. (2012). Despite this, the response also appears to be affected by the wave frequency. For small distances, shown by Figure 6-9 a the responses are similar up to about 200 Hz, while in the lower plot the responses are similar up to about 600 Hz.

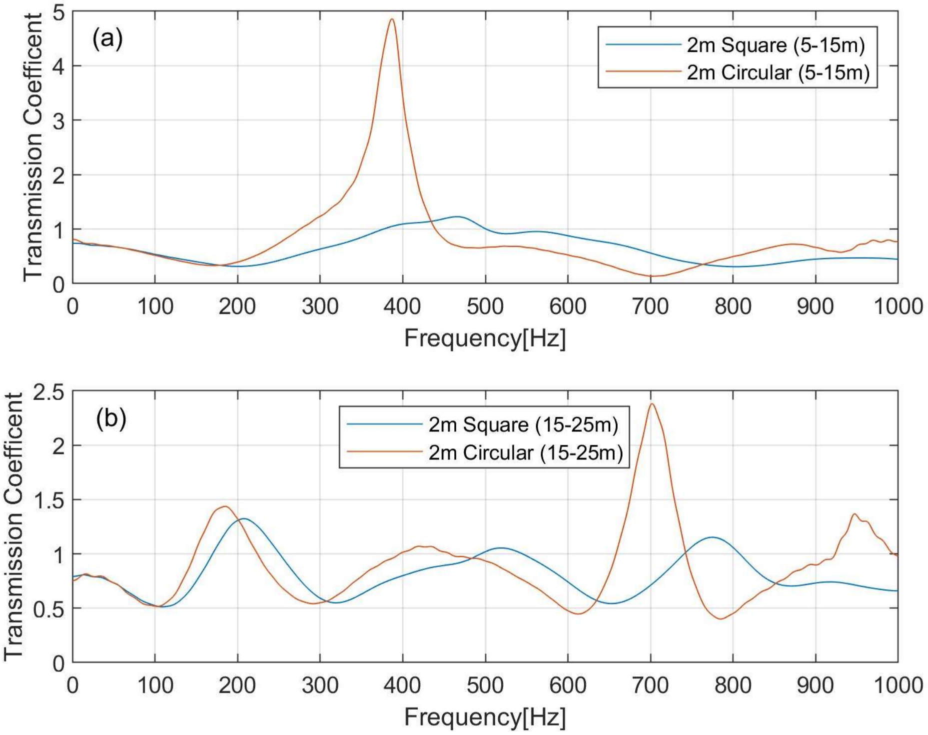

Figure 6-9 Square versus Circular cavity in WAVE2D. Numerical modelling transfer functions for a line load in a 2D plane strain model with a 2 m diameter square and circular cavity. Measurement positions are 5, 15 and 25m from the source, with transfer function calculated for 5-15 m and 15-25 m. The intact material in all models have a P-wave velocity of 3328 m/s

Figure 6-4, Figure 6-6 and Figure 6-7 show that WAVE2D and UDEC give similar responses. This shows that the use of the grid aligned circular cavity in WAVE2D does not significantly affect the response of the models and can be used for analysis of circular cavities without significant deviation from reality. Figure 6-9 shows that it may not be appropriate to model a circular tunnel by approximating it as a square tunnel, except for in the far field and / or for a limited range of frequencies. Although it has been stated that the circular cavity in UDEC and WAVE2D give similar responses up to about 800 Hz, it is likely that this is also related to the tunnel size and background material properties.

6.4. Verification of Resonance Mechanisms

This section focuses on the verification of the 1D rock mass resonance mechanisms studied in the previous Chapters using a 2D numerical model. Following the verification of the validity of the numerical models in Figure 6-4, it is a reasonable next step to add joints into the model. A model with two joints is studied here, using the set up shown in Figure 6-1. This work serves as a further verification of the resonance mechanisms, as carried out in Chapter 5, as it is a test of the plane wave assumption. The results of the comparison of the 1D and 2D models are shown in Figure 6-10. The 1D model set up used here is shown in Figure 5-7. The transfer functions contain similar elements, with the high transmission at 0 Hz, followed by a high transmission that is at the spring resonance frequency. There is also another high transmission zone at the superposition resonant frequency, although this is a broader and lower peak, than that shown by the 1D model. This is likely to be due to additional internal refractions and reflections within the model. The low transmission zone between the spring and superposition resonances shows more variability in the 2D model. The reasons behind this are unclear; however, it could be caused by superposition of P and S-waves within the model. In previous analyses, only P-waves are considered as only P-waves are generated by the plane wave source. However, in a 2D model with a point source both P and S-waves are generated. Therefore, there is potential for these waves to superimpose, which can cause relative peaks and troughs in the transfer functions. These effects are studied in subsequent sections in this Chapter.

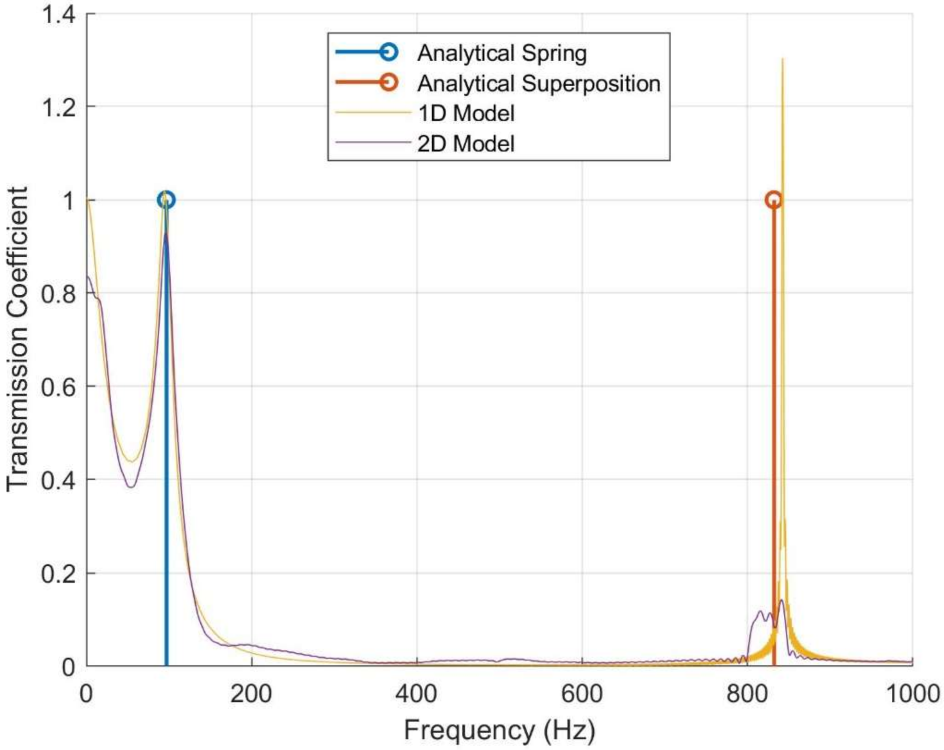

Figure 6-10 Comparison of transfer functions from a 1D model and a 2D model

This verification of the spring resonance mechanism occurring in a 2D model has been quite brief; however, it is clear from Figure 6-10 that both the spring and superposition resonances occur in a 2D plane strain model excited with a non-planar wave. It is not deemed necessary to include further plots confirming the existence of the jointed rock mass resonance effects, as the results in Figure 6-10 closely match the frequencies predicted by Equations 4-18 and 4-20.

6.5. 2D Transfer Functions

This section studies how joints and cavities can affect the relative transmission coefficients of stress waves in a 2D plane strain model. This work is an extension of the results shown in Figure 6-10, with additional models used to study the resonances and interactions observed there. In addition to this, transfer functions are generated over a 1D surface within the models. The transfer functions are displayed as a surface plot in a frequency-offset domain, with the vertical dimension being the transmission coefficient.

The model used is similar to that shown in Figure 6-1, but with a tunnel and additional points used for recording the models response. Figure 6-11 shows a schematic of the model and Table 6-2 gives the details of the models used in this section. The properties of the models are identical to those in Table 5-2. In all models, measurements are recorded at 1 m lateral intervals. The height at which the response points are located are given in the Figures as distance above the point at which the load is applied. In models with a tunnel the load is applied at the tunnel invert.

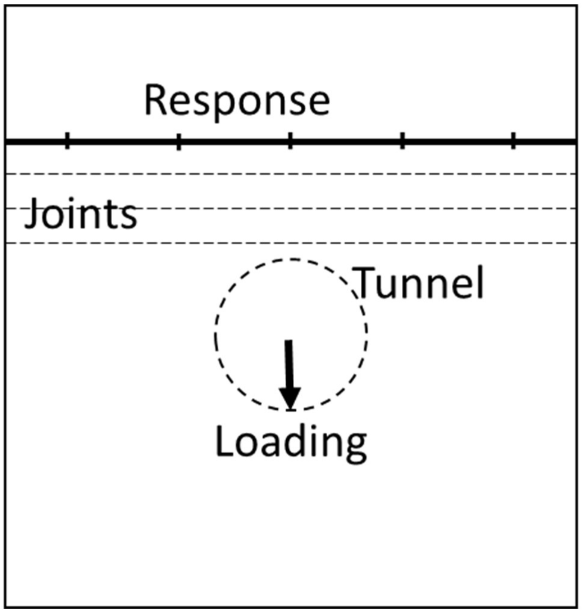

Figure 6-11 Schematic of model used for 2D transfer functions. Dashed lines represent features which are not included in all models. More joints can be modelled than are shown.

For ease of conveying what the model inputs are, each model is given a six digit code referring to its properties. The first two digits relate to whether there is a tunnel (nt – no tunnel, tt – tunnel); the third and fourth to the number of joints (joint number followed by j, m refers to the model being entirely populated by joints, e refers to an equivalent medium); and the final two to the position and orientation of the joints (a or b for above or below loading, h or v for horizontal or vertical, or 00 if there are no joints, m refers to the model being entirely populated by joints, e refers to an equivalent medium).

Table 6-2 2D plane strain models used to derive transfer functions

Tunnel (yes/no)	Number of Joints (location/orientation)	Descriptions (code)
No	0	Continuum Model (nt0j00)
Yes	0	Continuum with a tunnel (tt0j00)
No	1 (above/horizontal)	Single jointed model (nt1jah)
Yes	1 (above/horizontal)	Single joint with a tunnel (tt1jah)
No	2 (above/horizontal)	Twin jointed model (nt2jah)
Yes	2 (above/horizontal)	Twin jointed model with tunnel (tt2jah)
No	1 (below/horizontal)	Single jointed model (nt1jbh)
Yes	1 (below/horizontal)	Single joint with a tunnel (tt1jbh)
No	2 (below/horizontal)	Twin jointed model (nt2jbh)
Yes	2 (below/horizontal)	Twin jointed model with tunnel (tt2jbh)
No	Maximum (throughout/horizontal)	Fully jointed model without tunnel (ntmjmh)
Yes	Maximum (throughout/horizontal)	Fully jointed model with tunnel (ttmjmh)
No	0 (equivalent transversely isotropic)	Equivalent to ntmjmh – no tunnel (ntejeh)
Yes	0 (equivalent transversely isotropic)	Equivalent to ttmjmh – tunnel (ttejeh)

6.5.1. Effect of a Tunnel

The effect of a tunnel is investigated in this section. Table 6-3 shows the combination of models which show the effect of adding a tunnel to a model, with all tunnels having a radius of 1 m. The tunnel is modelled as shown in Figure 6-5 for WAVE2D. Despite this only one of these cases will be considered, nt0j00 versus tt0j00. There is undoubtedly an effect of tunnel size on the transmission of stress waves, although this has already been well investigated by numerous authors and is discussed in Chapter 2, so is not investigated further here.

Table 6-3 Cases giving the effect of a tunnel

Reference Case	Test Case
nt0j00	tt0j00
nt1jah	tt1jah
nt2jah	tt2jah
nt1jbh	tt1jbh
nt2jbh	tt2jbh

Figure 6-12 shows nt0j00 versus tt0j00, giving the effect of adding a 1 m radius tunnel to a continuum. If the tunnel has no effect on the transmission of stress waves, then the transfer function will have a transmission coefficient of one at all frequencies. This is clearly not the case, so the tunnel is having some effect. There are clear interactions occurring with regular peaks in the transfer functions, which occur at different frequencies depending on the offset of the measurement point.

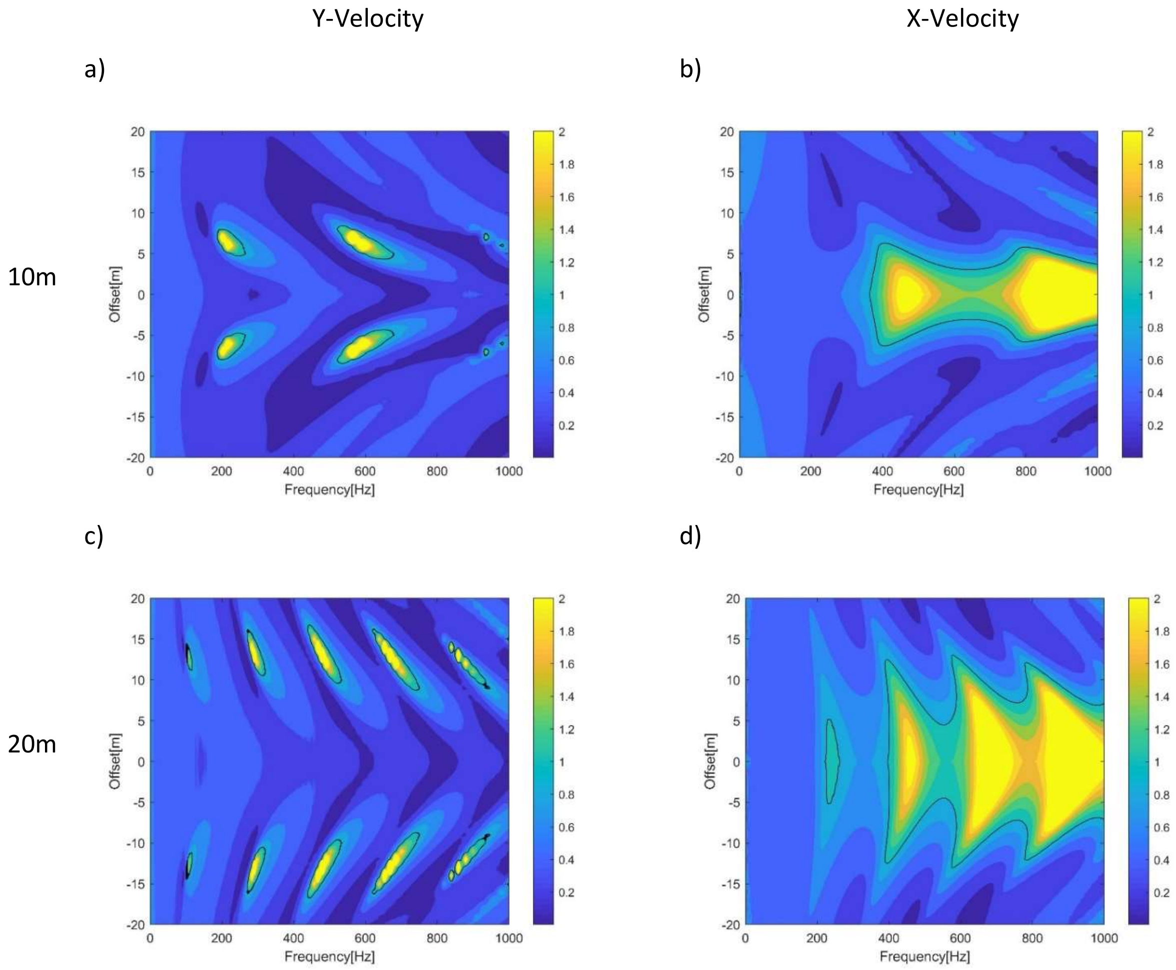

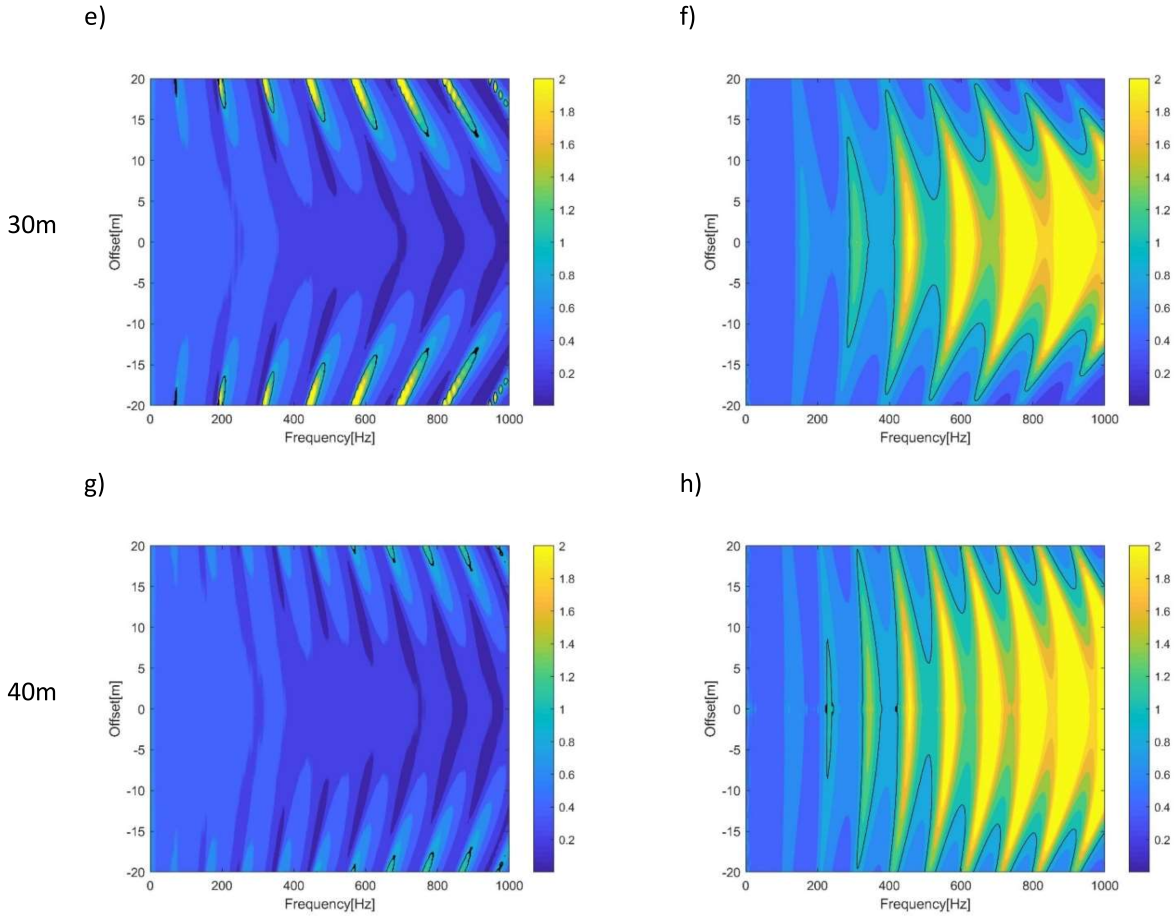

Figure 6-12 Effect of adding a tunnel to continuum mode (nt0j00 vs tt0j00). a) 10 m vertical response, b) 10 m horizontal response, c) 20 m vertical response, d) 20 m horizontal response, e) 30 m vertical response, f) 30 m horizontal response, g) 40 m vertical response, h) 40 m horizontal response. Black isocline indicates transmission coefficient = 1

Figure 6-12 shows the distribution of velocity changes for different elevations above the load at 10 m intervals between 10 and 40 m. A clear pattern has developed with high y-velocities spreading out as the elevation above the tunnel increases, with low transmission coefficients directly above the tunnel. The low transmission zone directly above the tunnel has been found by previous studies and is referred to as a vibration shadow (Gupta et al., 2009). This shadow is also shown in Figure 6-8. This is formed as the tunnel itself prevents vibrations from being transmitted through it.

The x-velocity transmission coefficients are always highest directly above the tunnel but, much like the y-velocity component of vibrations, also show a degree of spreading out as the elevation increases. If the edges of the area with a transmission coefficient of 1 are looked at for the x-velocities it is seen that this occurs at approximately the same offset as the maximum in the y-velocity transmission for the same elevation. These zones spread out at an angle of approximately 30 degrees.

There is a clear frequency dependent maximum occurring in both y and x-velocities. Despite an apparent similarity for the position of peaks along the frequency axis, between y and x-velocities, upon further interrogation these positions do not appear to be in the same place. For instance, the 40 m elevation plots in Figure 6-12 g and h have ten peaks in the y-velocity plot and only nine in the x-velocity plot. The nine peaks for the y-velocity plot do not fit in between the ten peaks for the x-velocity plot either.

The interactions shown in the x and y-velocities in Figure 6-12 appear to be closely related, due to the spatial similarity in the velocity responses, rising at an angle of 30 degrees from the tunnel invert, despite the differing number of peaks in the different directions. It is likely that similar processes bring about both interactions, with the tunnel acting to guide waves in different directions. In the models shown here, this shadow spreads out at an angle of 30 degrees. Within 30 degrees from the vertical axis above the tunnel there will be low vertical vibrations, in relation to the continuum case. However, due to the method which these transfer functions are generated this does not mean that there are no vibrations here. As these transfer functions calculate the difference between a case with and without a tunnel, this shows a relative reduction between the two cases. Therefore, this does not mean there will be no vibrations, as the highest y-vibrations in the continuum case would be directly above the loading point, although they have been significantly reduced. The clear maxima, which are located in a narrow band around the 30 degree line, are likely to be the location where waves interact through superposition.

Similar processes are likely to be occurring with the x-velocities; however, there is no vibration shadow. Directly above the tunnel there are greater transmission coefficients, showing that there are greater x-vibrations here than in the continuum case. Again, this does not imply high vibrations occurring in the tunnel case, as there are extremely low vibrations in the x-direction directly above the loading in the continuum case. For instance, Green's Functions predict zero displacements at this position for a homogenous full space, as shown by Figure 6-13. Regardless of the potentially low vibrations, there is still an increase in x-vibrations in the y-vibration shadow caused by the tunnel, although in absolute terms these are likely to be small.

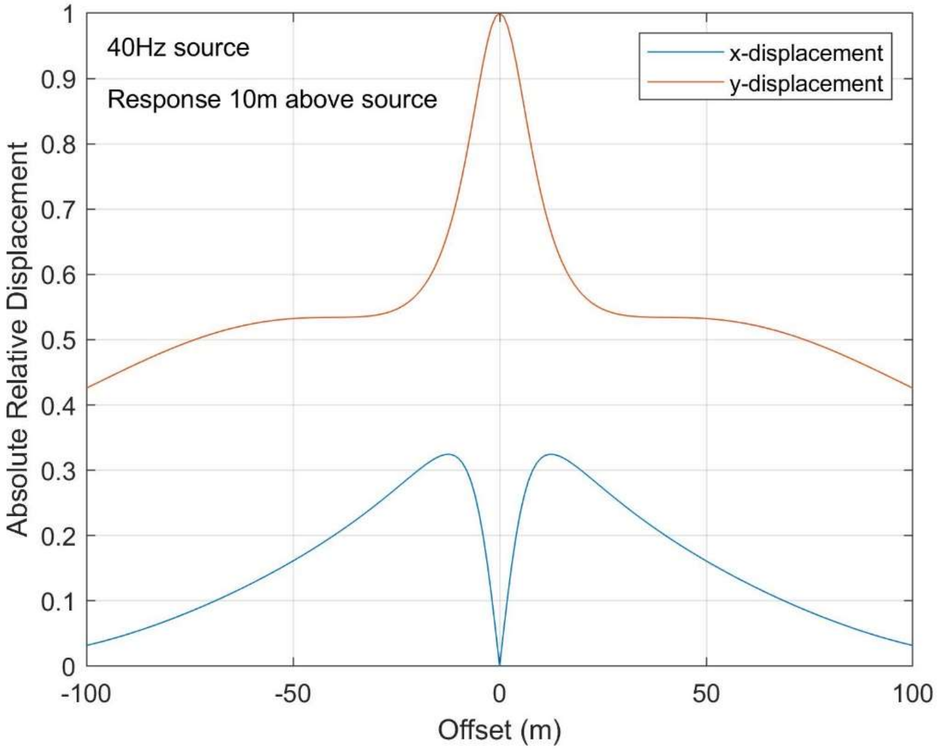

Figure 6-13 Relative amplitude of x and y-displacements due to vertical point source within an isotropic full space. Absolute relative displacement for both x and y directions take from the maximum displacement in either direction

Both the shadow and associated maxima in the y-vibrations and maxima in the x-vibrations are generated by the presence of the tunnel. The mechanism behind this is likely to be superposition of stress waves, caused by refraction around the tunnel surface.

6.5.2. Effect of Joints

The effects of joints are investigated in the same way as the effect of the tunnel, by comparing cases where a joint is added with an otherwise identical case without joints. The comparisons to do this are shown in Table 6-4.

Table 6-4 Cases to give the effect of joints

Reference Case	Test Case
Joints Above Tunnel	
nt0j00	nt1jah
nt0j00	nt2jah
Joints Below Tunnel	
nt0j00	nt1jbh
nt0j00	nt2jbh

Figure 6-14 shows the effect on the transmission of stress waves of adding joints above the loading location in a model when there is no tunnel. Figure 6-14 a and b show the effect of adding a single joint to a continuum model. This gives a general decrease in the transmission, although there are clear effects of the P / S-wave interaction occurring with a similar form (30 degree offset) to those found when a tunnel is added. Despite this, the clear peaks observed in Figure 6-12 are much less obvious here. This is likely to be because there is no tunnel. As the interaction effects are generated by the presence of the tunnel, these will not occur. However, they are still clear; therefore, the interactions here must be generated during the stress wave passage through the joints. It cannot merely be a consequence of the passage of waves through the continuum, otherwise the effect would not show up in the transfer function as it would be expected to be equal in both models. An incident stress wave on a joint will be partly transmitted and partly reflected. The transmitted wave will be refracted and, unless it is normally incident, will be transformed to some degree. This effect is well known and related to Snell's Law.

When there are two joints, shown by Figure 6-14 c and d, the 30 degree interaction effects are much less obvious. The 1D-interaction effects of the masses between springs, operating at 96Hz, and superposition of waves, occurring at approximately 832 Hz, are still apparent, although the spring resonance effect is quite weak. The zero offset for Figure 6-14 c is identical to the transfer function shown in Figure 6-10. The two resonance mechanisms are shown by the black crosses in Figure 6-14 c and d.

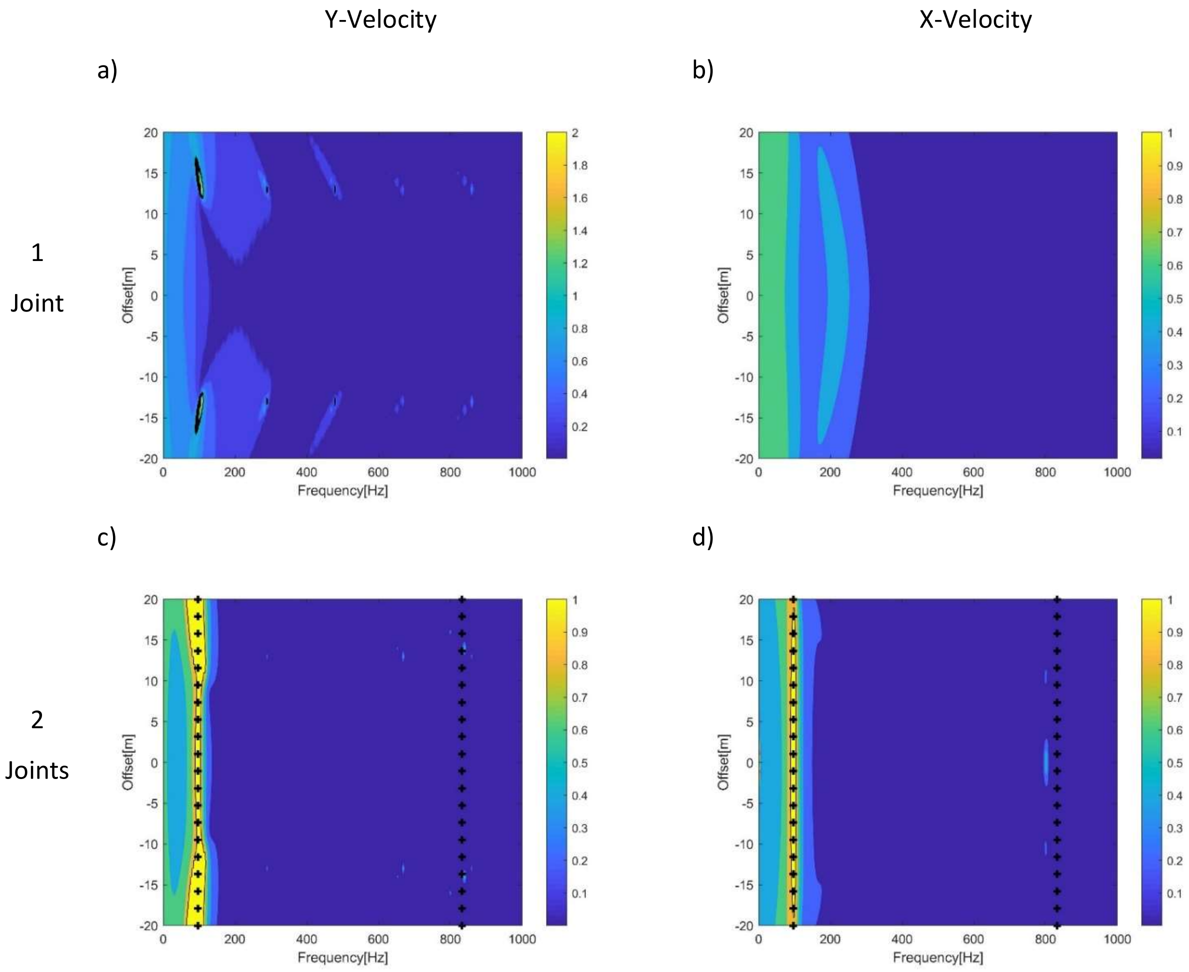

Figure 6-14 Effect of adding joint to a model above the loading location (nt0j00 vs nt1jah, nt0j00 vs nt2jah). a) single joint vertical response, b) single joint horizontal response, c) twin joints vertical response, d) twin joints horizontal response. Isocline indicates transmission coefficient = 1. Black crosses indicate resonances.

The similarity with the transfer functions in Figure 6-14 c and d shows that the spring resonance effect operates even when vibrations are not polarised to be acting normal to the plane of the joints. As the joints in the models used are horizontal, the y-vibrations are normal to this. This is the same orientation of vibrations and joints as was used in the Chapters 4 and 5 which uses plane waves. However, in Figure 6-14 d the vibrations are horizontal as well as the fractures. With the vibration being in the opposite direction to the direction of travel of the wave, which is still vertical, the waves captured in Figure 6-14 d must be a S-wave. The peak transmission occurs at the same frequency in both Figure 6-14 c and d, and as the specific shear and normal stiffnesses of the joints is modelled as being the same, it suggests that the spring resonance effect also occurs with S-waves.

Figure 6-15 shows how adding a joint below a loading location changes the transmission coefficient of a velocity response point above the loading location. This scenario has no joints between the load and the measurement point. Figure 6-15 shows that the transmission coefficients are mostly equal to or greater than one. This increase in transmission is caused by reflection from the joint below the load, causing the stress waves to be transmitted upwards instead of down. Similar effects have previously been identified by Eitzenberger (2012) in jointed materials. There are interactions occurring with minima at regular intervals in the frequency spectrum. With the lack of any other surfaces in the model, these interactions are likely to be generated by the superposition of reflected P and S-waves. When there are two joints, as shown by Figure 6-15 c and d, there is little difference to the single joint case shown in Figure 6-15 a and b. The spring resonance is also evident, although as a minima. This suggests that the mass between spring effects of the joints is occurring but causing out of phase waves of the resonant frequency to be transmitted into the model, therefore cancelling out the vibrations in the model.

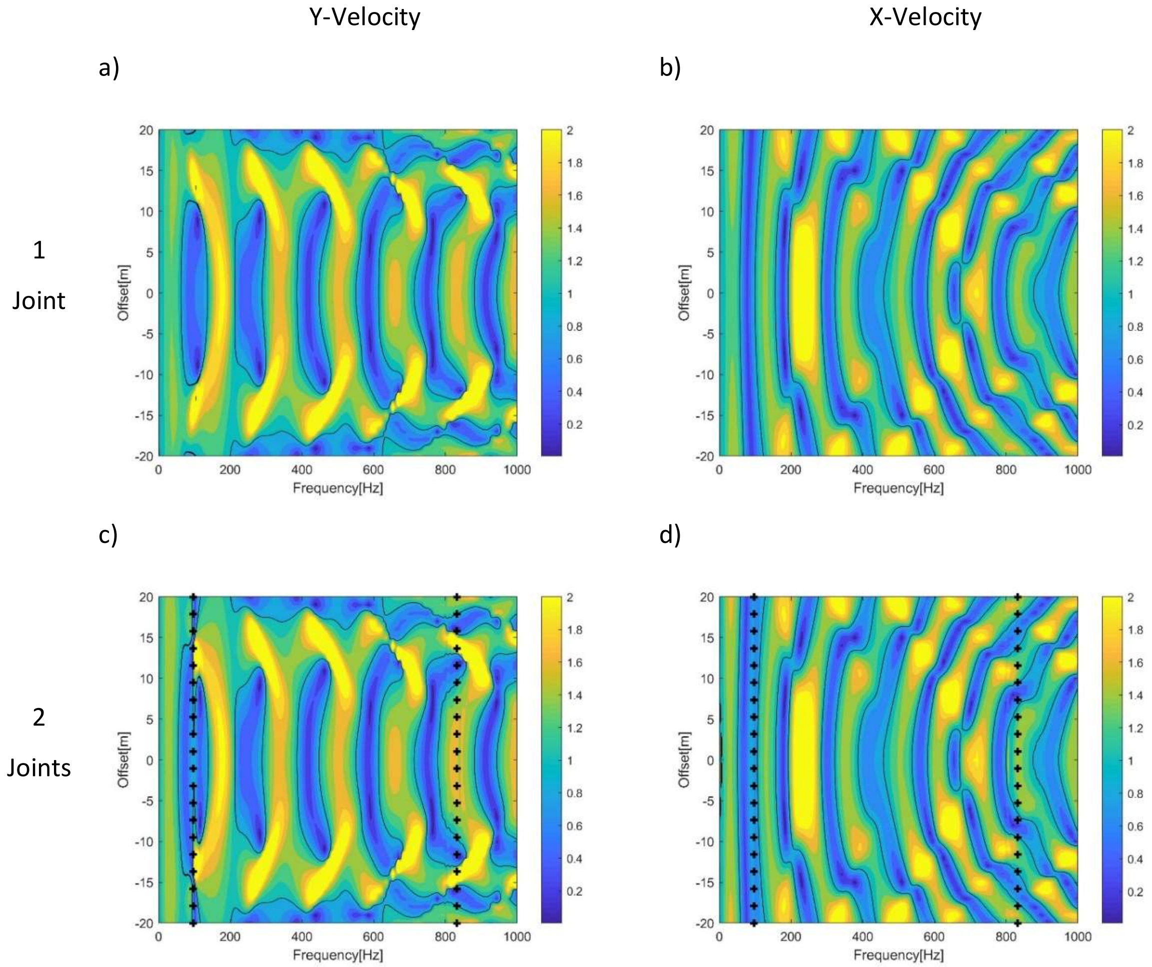

Figure 6-15 Effect of adding joint to a model below the loading location (nt0j00 vs nt1jbh, nt0j00 vs nt2jbh). a) single joint vertical response, b) single joint horizontal response, c) twin joints vertical response, d) twin joints horizontal response. Isocline indicates transmission coefficient = 1. Black crosses indicate resonances.

6.5.3. Effect of Adding Joints and a Tunnel

This section combines the two previous sections adding both joints and a tunnel to a model. It would be expected that these transfer functions would be a combination of the two interaction effects observed, with reflection and superposition of waves from the tunnel surface giving the periodic maxima and minima, as well as resonance effects when there are multiple joints. The various combinations of models discussed in this section are given in Table 6-5.

Table 6-5 Cases to give the effects of a tunnel and joints

Reference Case	Test Case
Joints Above Tunnel	
nt0j00	tt1jah
nt0j00	tt2jah
Joints Below Tunnel	
nt0j00	tt1jbh
nt0j00	tt2jbh

Figure 6-16 shows the effect of adding a tunnel and joints to a continuum model. For the single joint case, the maxima in the y-vibrations at the 30 degree angle are clearly shown for a single joint (Figure 6-16 a). These occur at an offset of approximately 14 m for a recording at 20 m above the loading, as shown in the Figure. These are also present for the case with two joints, although only at the spring resonant frequency (Figure 6-16 c). Despite the maxima being present, they do not exceed the vibrations from the continuum case. This is in opposition to the findings of the tunnel in a continuum, where these areas showed greater levels of vibration. The reasons behind this are due to the addition of the joints. This shows that the spring resonance mechanism in the rock mass effectively cuts out waves with frequencies greater than the spring resonant frequency for the rock mass. This appears to be more effective than the single joint, as although it ideally acts as a low pass filter some energy is still transmitted at high frequencies. This allows the interaction effects which are observed at the 30 degree offset in Figure 6-16 a. The spring resonant frequency is still visible in the x-vibrations in Figure 6-16 d. The increase in x-vibrations above the tunnel are evident in Figure 6-16 b, with a similar pattern to that observed for the addition of a tunnel in Figure 6-12.

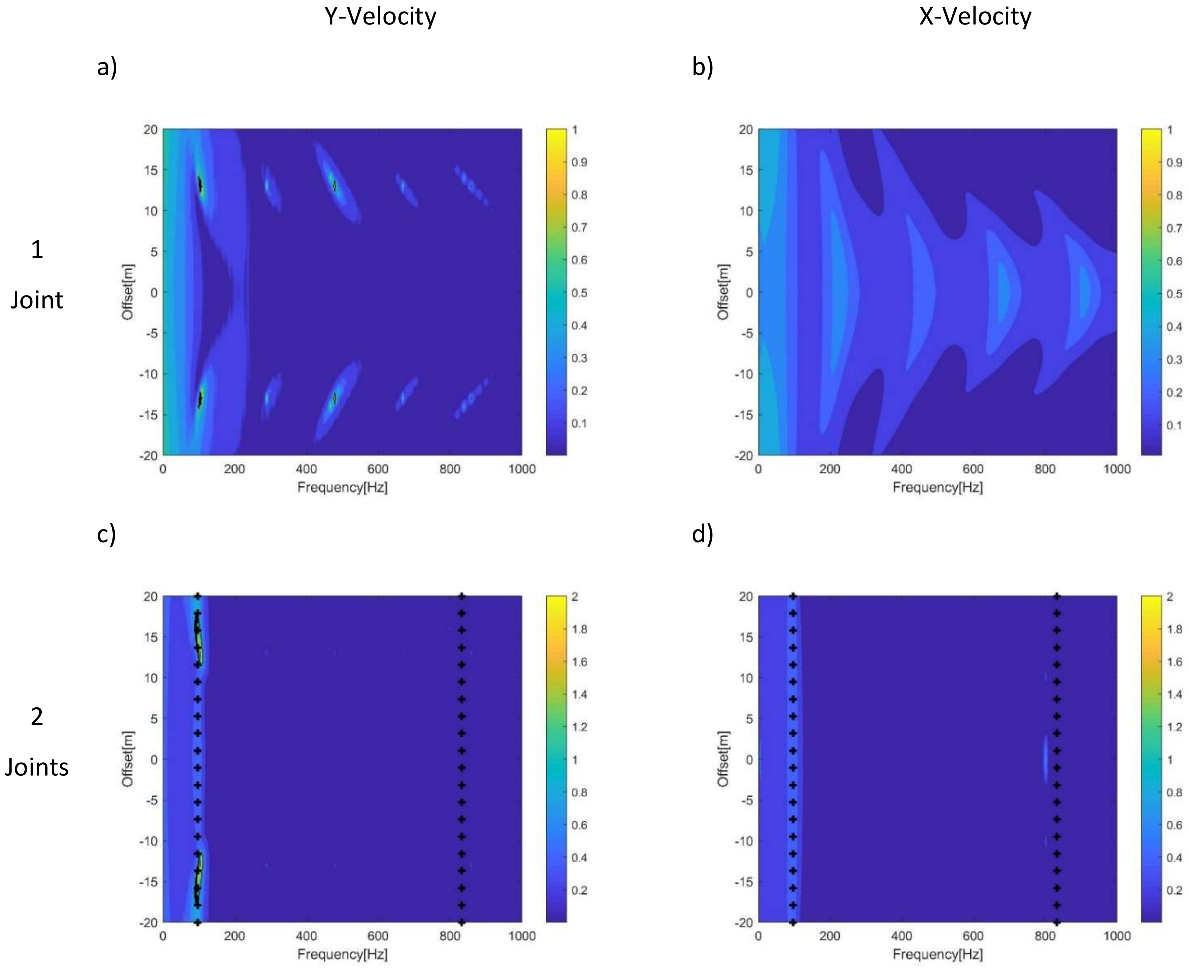

Figure 6-16 Effect of adding a joint to a model above a tunnel / loading location (nt0j00 vs tt1jah, nt0j00 vs tt2jah). a) single joint vertical response, b) single joint horizontal response, c) twin joints vertical response, d) twin joints horizontal response. Isocline indicates transmission coefficient = 1. Black crosses indicate resonances.

Figure 6-17 shows the effect of one and two joints below the tunnel. The x and y-vibration plots for the single and double joint cases look remarkably similar. The double joint case does show a weak effect of the spring resonance effect for the joints, but excluding this the interaction effects appear to be almost identical. This suggests that the first joint that is encountered does most of the reflecting work, with the effect of the second joint only being felt with the spring resonance. This is much like the case without a tunnel, as shown by Figure 6-15, although there appears to be a bit of a vibration shadow caused by the tunnel. This effect is not as significant when compared to the shadow when the joints are only above the tunnel. A pattern has developed with high transmission zones in the y-vibrations occurring at an offset of 10 m, and high vibrations in the x-direction occurring at 10 m either side of the tunnel centre line. These occur at a more acute angle than the 30 degree angle found for a tunnel on its own. This shows that the vibrations excited at the base of the tunnel are transmitted downwards and then reflected from the joint upwards. This will narrow the angular shadow cast by the tunnel, allowing high transmissions at smaller offset distances.

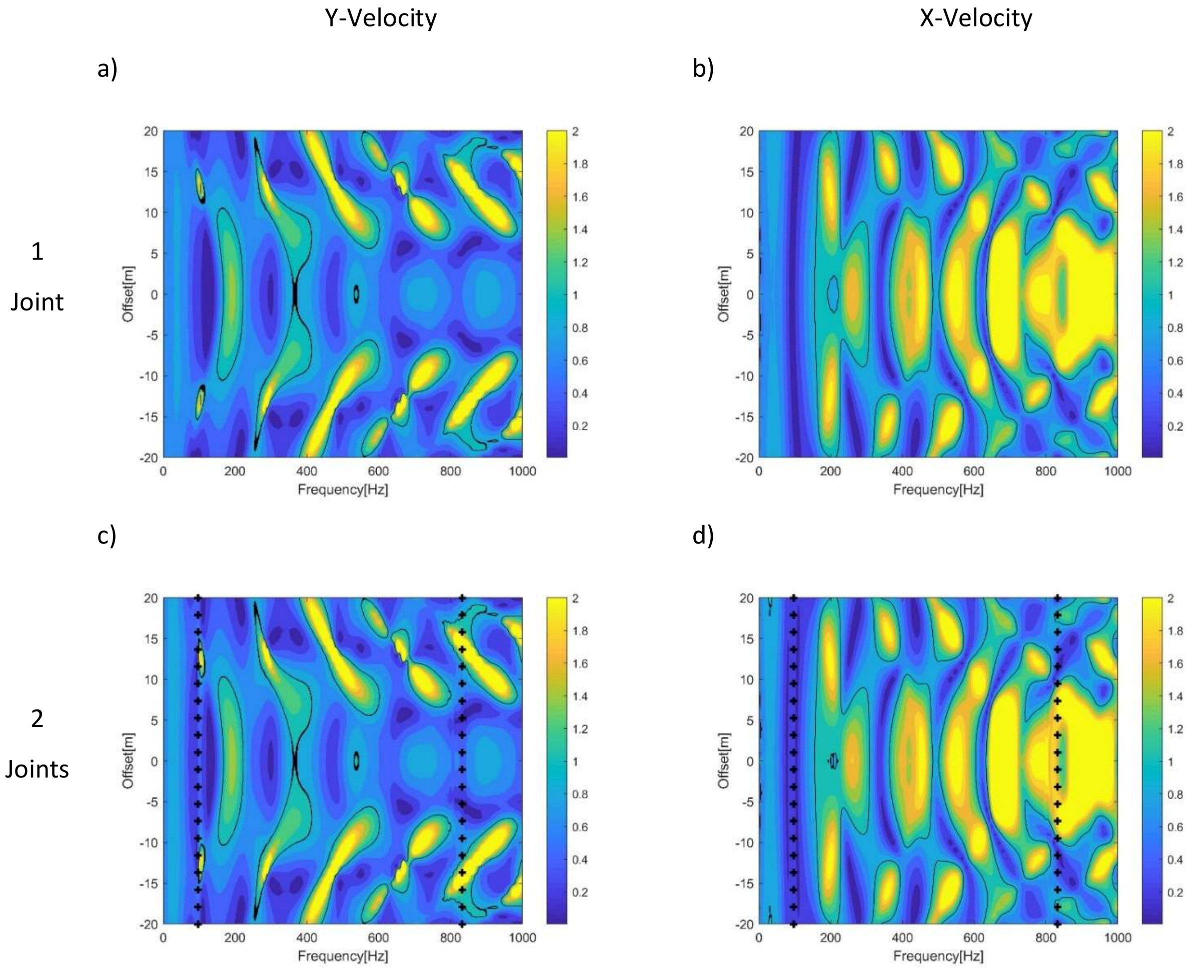

Figure 6-17 Effect of adding a joint to a model below a tunnel / loading location (nt0j00 vs tt1jbh, nt0j00 vs tt2jbh). a) single joint vertical response, b) single joint horizontal response, c) twin joints vertical response, d) twin joints horizontal response. Isocline indicates transmission coefficient = 1. Black crosses indicate resonances.

This section has shown that joints beneath a tunnel will increase the transmission above the tunnel and joints above the tunnel will reduce transmission, effects which have already been observed by previous researchers. As shown in the previous section, when two joints are used the 1D resonance effects observed also operate in 2D models with a tunnel.

6.5.4. Effect of Continuously Jointed Discontinua

This section will consider the effect of continuously jointed materials on stress wave transmission. Here, continuously jointed materials refer to a model which has a large number of joints. To reduce the run time the entire model will not be populated with joints, and just the area of interest surrounding the loading and tunnel. A single horizontal joint set is used.

Horizontal joints are common in sedimentary rocks, such as bedding joints created during deposition.

This section will compare different equivalent continuously jointed models. These will have a range of different joint spacing's with the joint stiffness altered to give the same overall rock mass stiffness. As all these rock masses have the same equivalent stiffness it will be possible to compare them using a single equivalent continuum, which has transversely isotropic properties due to the single set of joints. Equivalent continua will be investigated in Section 6.5.5.

Figure 6-18 shows the effect of continuous jointing without a tunnel (Figure 6-18 a and b) and with a tunnel (Figure 6-18 c and d). Included in these plots are black crosses indicating the maximum spring resonant and the first superposition resonant frequencies. These Figures show that the spring resonance presents as a wide zone of high transmission in the y-vibration plots. The superposition resonance shows a clear zone of high transmission at the predicted frequency in the y-vibration plots. The x-vibrations also show the effect of the spring resonance, and the superposition resonance is also apparent, albeit this now shows a reduction in the transmission rather than an increase. For both y and x-vibrations there is a zone of localised high transmission either side of the predicted resonant frequency. When compared to Figure 6-16 and Figure 6-17, where there is continuous jointing, the transmission coefficients have increased. This could be thought of as being different from what would be expected. Adding more joints would be expected to cause more energy to be reflected and cut out, with the joints acting as low pass filters. This is especially the case if the Equation $|T_N|=|T_1|^N$, introduced in Chapter 3, is correct. Instead, a spring resonance high transmission zone has developed, and the superposition resonance zone is much more distinct. The high transmissions at intermediate frequencies are harder to explain, although they do seem to be synonymous with the 30 degree effects identified in other models. When there is no tunnel the high transmission effects seem to develop at 30 degrees in the y-vibrations (Figure 6-18 a). When there is a tunnel, these effects are still visible but much less clear (Figure 6-18 c). These effects are outside the range for the spring resonance effect and not at the correct frequency for superposition, according to Equations 4-18 and 4-20. However, owing to the greater number of degrees of freedom in the 2D scenario, there will be a greater number of different transmission pathways allowing a greater range of frequencies to have constructive interference through superposition. Equally, as indicated in previous sections, the presence of S-waves will also generate other interactions with a model without a plane wave.

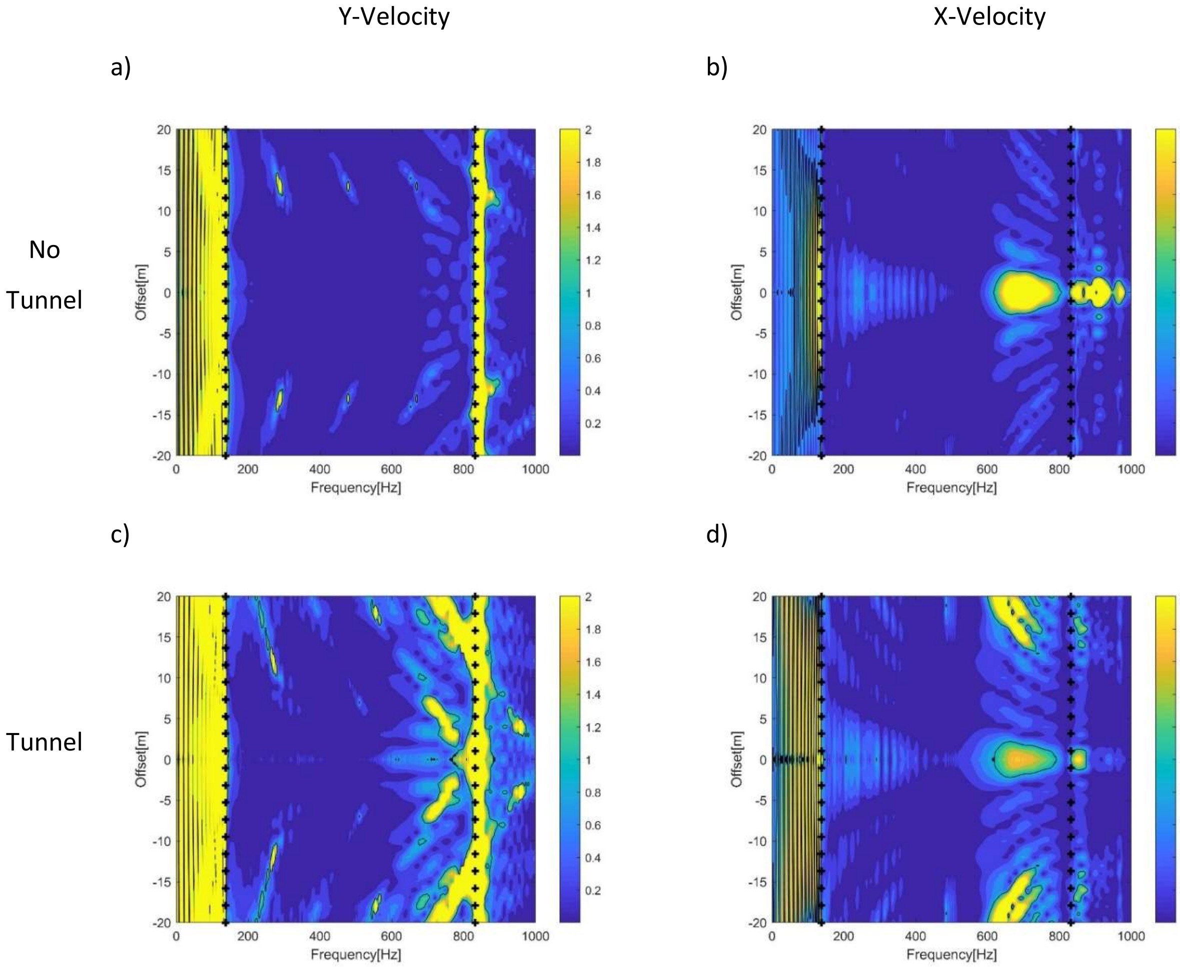

Figure 6-18 Effect of adding continuous jointing to a model (nt0j00 vs ntmjmh, tt0j00 vs ttmjmh). a) single joint vertical response, b) single joint horizontal response, c) twin joints vertical response, d) twin joints horizontal response. Isocline indicates transmission coefficient = 1. Black crosses indicate resonances.

Figure 6-18 shows the difference between an isotropic medium and a jointed medium with the intact blocks having the same properties as the isotropic material. The joints modelled for Figure 6-18 in models ntmjmh and ttmjmh have a spacing of 2 m and a specific stiffness of 1 GPa/m for both normal and shear stiffnesses, which have been used for all previous jointed models. Using Equation 3-2 the rock mass stiffness can be determined based on the intact block stiffness, joint stiffness and joint spacing. This shows that it is possible to derive the same rock mass stiffness from a combination of different properties of a discontinuous rock mass. Keeping E_m and E_r constant, the joint spacing can be changed and the joint stiffness altered to compensate, giving the same rock mass stiffness. The relationship is inverse, with a doubling of the joint spacing requiring a halving of the joint stiffness to give the same rock mass stiffness. Based on this, if the joints are at a spacing of 4 m a 0.5 GPa/m specific joint stiffness will be required (models ntmjmh4 and ttmjmh4) and if they are separated by 8 m a 0.25 GPa/m specific joint stiffness will be required (models ntmjmh8 and ttmjmh8). These equivalent cases, compared to the original 2 m joint spacing used in Figure 6-18, are shown in Figure 6-19 and Figure 6-20.

Figure 6-19 shows that the 4 m jointed model has higher vibrations at low frequencies, due to the lowering of the spring resonance maximum frequency. Both frequencies are shown by the left hand of the two dashed lines. Due to the lowering of the maximum spring resonant frequency, there is also a reduced transmission zone between the 4 m joint spacing resonance and the 2 m joint spacing resonance. There is a high transmission zone from the 2 m spring resonance up to the 2 m superposition resonance, shown at just over 800 Hz. The intermediate cross dashed line is the first 4 m superposition resonance, which is not distinct.

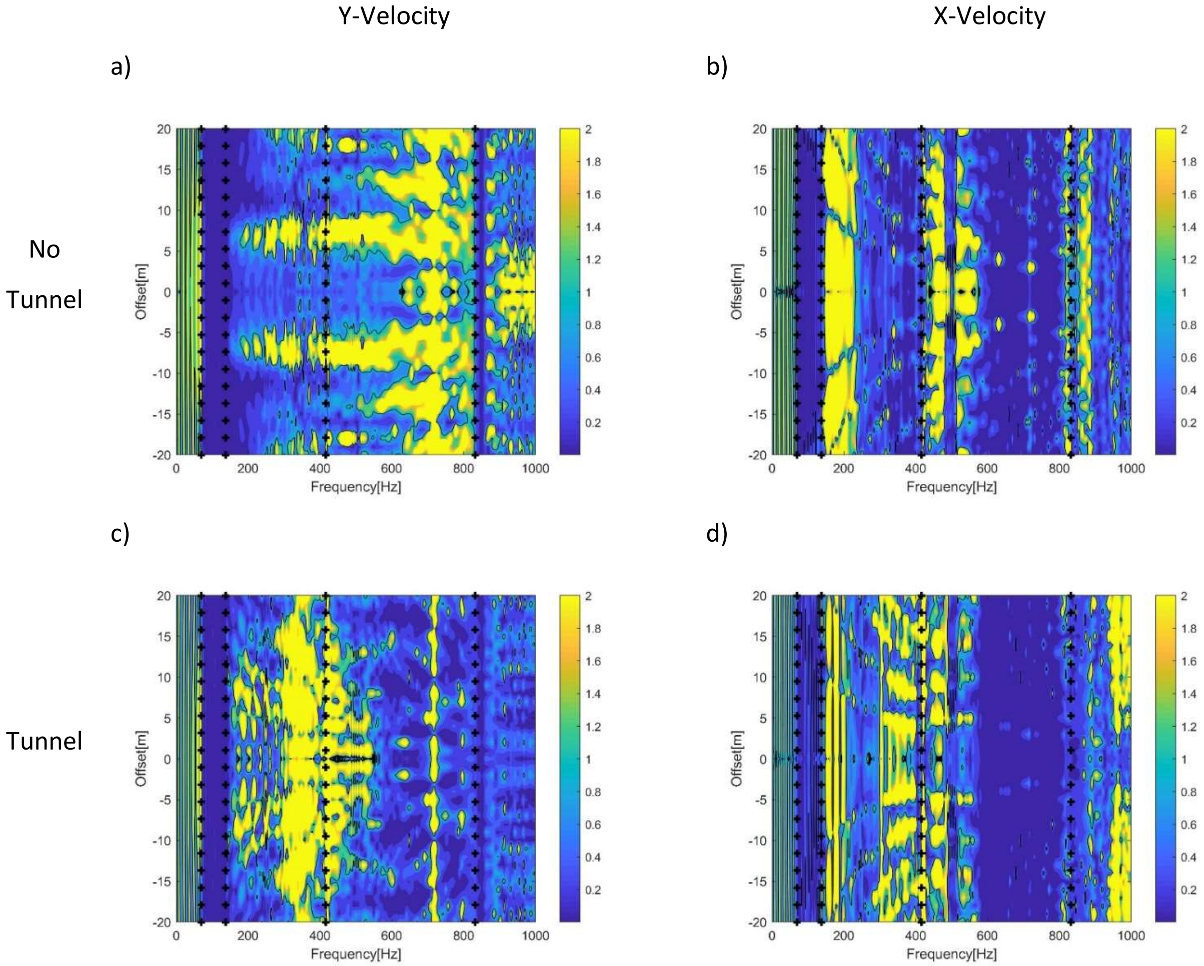

Figure 6-19 Effect of changing the joint spacing in a model with the same equivalent continuum stiffness (ntmjmh vs ntmjmh4, ttmjmh vs ttmjmh4). a) single joint vertical response, b) single joint horizontal response, c) twin joints vertical response, d) twin joints horizontal response. Isocline indicates transmission coefficient = 1. Black crosses indicate resonances.

Figure 6-20 shows the 8 m joint spacing model. Similarly, with Figure 6-19 there is a high transmission zone at low frequencies, synonymous with the spring resonance. This is followed by a low transmission zone, which is followed by a further high transmission zone.

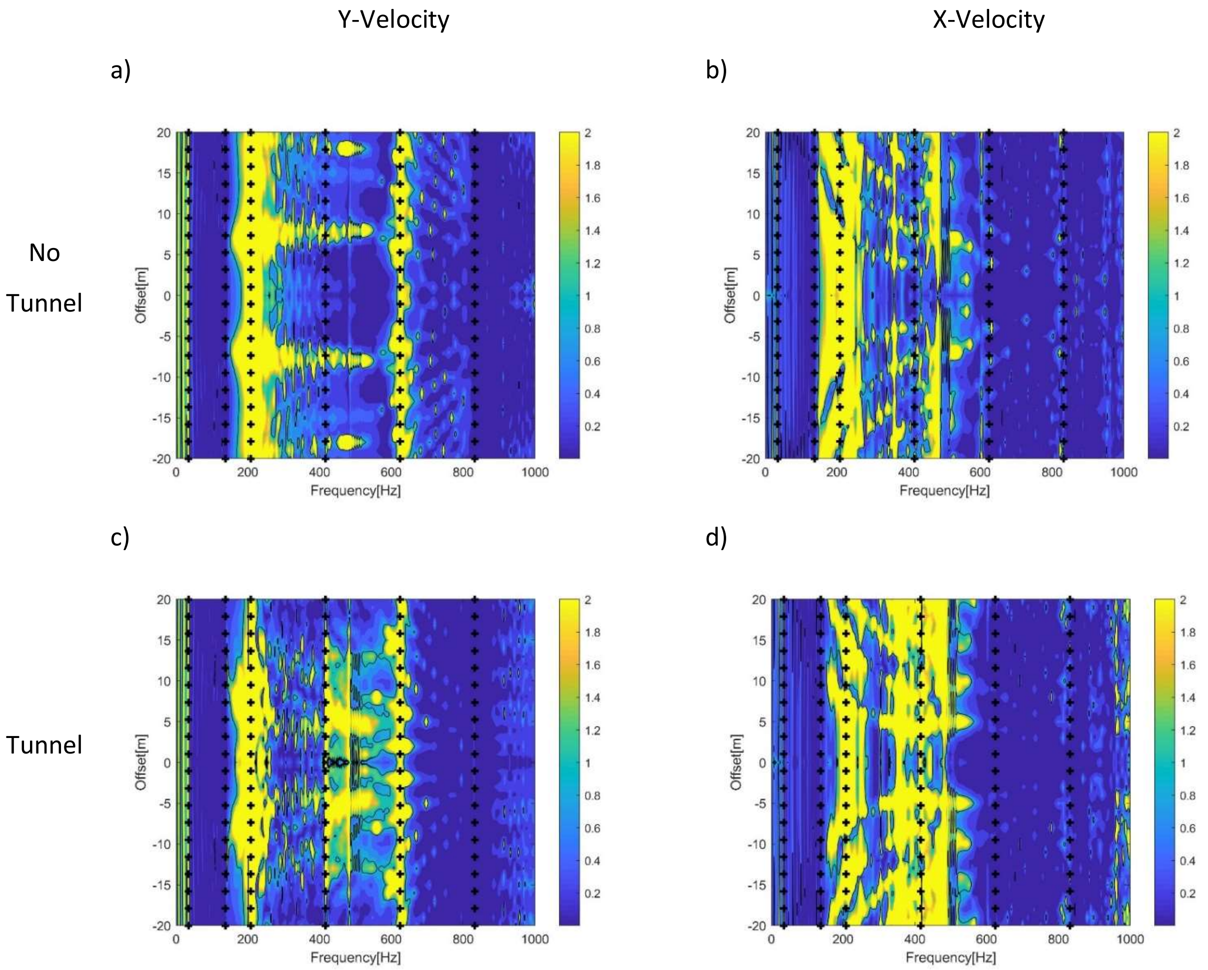

Figure 6-20 Effect of changing the joint spacing in a model with the same equivalent continuum stiffness (ntmjmh vs ntmjmh8, ttmjmh vs ttmjmh8). a) single joint vertical response, b) single joint horizontal response, c) twin joints vertical response, d) twin joints horizontal response. Isocline indicates transmission coefficient = 1. Black crosses indicate resonances.

6.5.5. Effect of Equivalent Continua and Discontinua

Section 6.5.4 shows how different equivalent discontinuum models give different results. These models show that the effects of the jointed rock resonance mechanisms prevail causing areas of high and low transmission within the models to change. This section studies equivalent continuum models and how their results differ from the discontinuum, which they are derived from. Modelling as a continuum is a desirable trait for models as they often require a lower amount of computing power than discontinuum models. The models used here adopt the HEM and DM material models, as shown in Figure 5-12.

Figure 6-21 shows the transfer functions for the comparison of an equivalent continuum and discontinuum. This shows the effects of the spring and superposition resonances for horizontal and vertical vibrations. The spring resonance zone gives a higher transmission in the discontinuum model than the equivalent continuum for both vibration directions. The superposition resonance is only clearly visible in the vertical vibration plots (y-velocity). This indicates, as found in Figure 5-13, that the HEM does not exhibit the spring or superposition resonance effects.

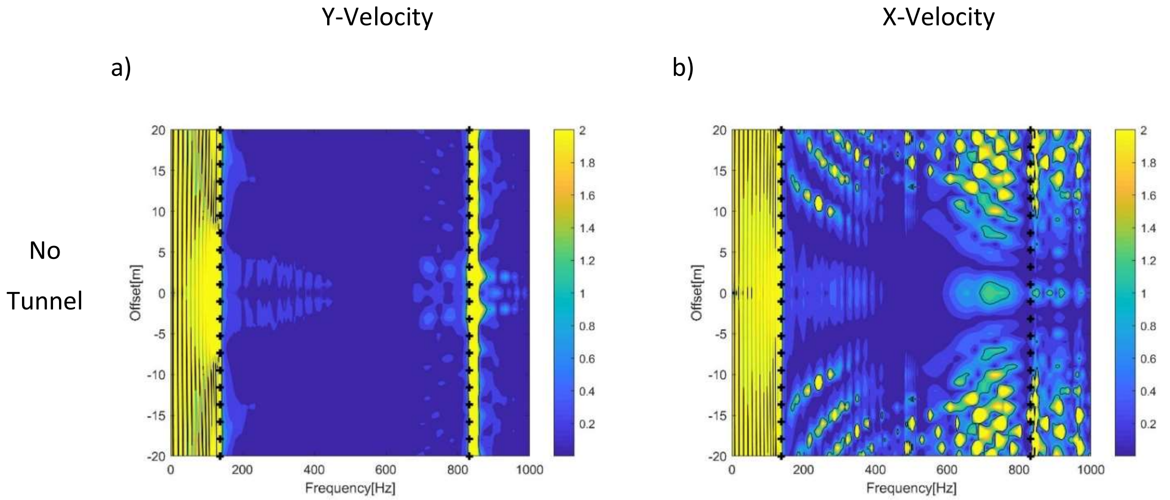

Figure 6-21 Effect of modelling a discontinuum as an equivalent continuum (ntejeh vs ntmjmh). a) no tunnel vertical response, b) no tunnel horizontal response. Isocline indicates transmission coefficient = 1. Black crosses indicate resonances.

6.6. Discussion

Figure 6-22 shows high transmission coefficients at typical frequencies for train excitation, from car body and bogie bounce, and bogie, axel, and wheel passage, as well as track excitation, from wheel out of roundness, rail bending and wheel-ballast and rail / sleeper-ballast resonance. These show that there are a range of different excitation mechanisms which can cause sources at the frequencies shown by the wide spring resonance zone. The consequence of this could be that, if an equivalent continuum were used in the vibration assessment of a new tunnel there could be significant errors introduced for these frequencies. This is because equivalent material models, such as the HEM material model, do not exhibit the rock mass resonances identified in this work, as shown by Figure 6-21.

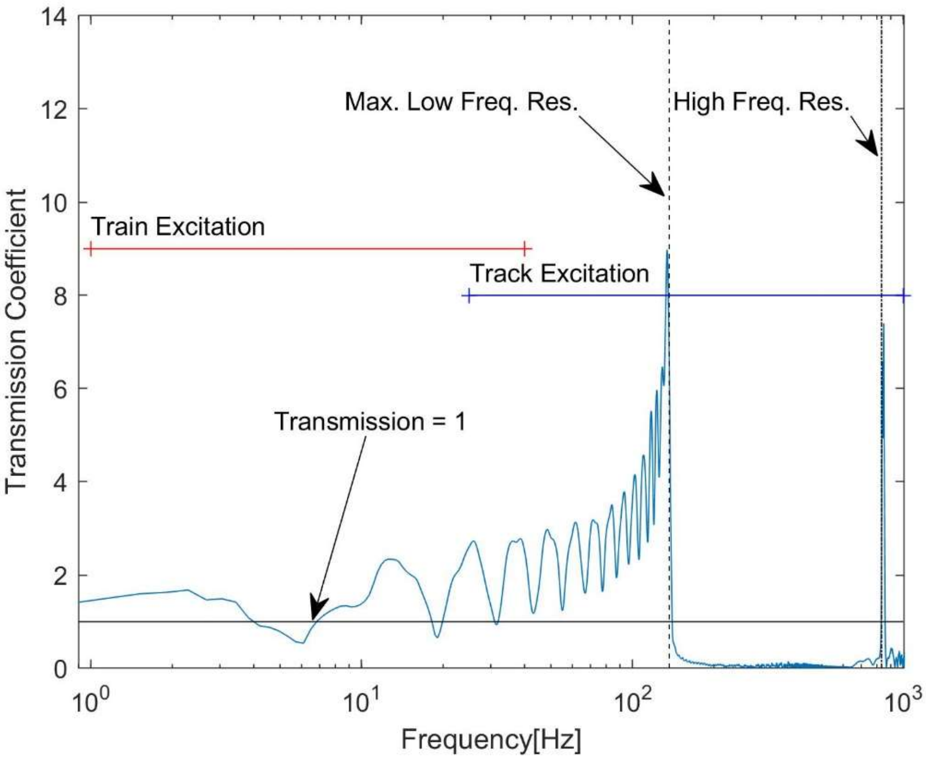

Figure 6-22 Vertical transfer function directly above loading for equivalent continuum versus discontinuum model with no tunnel (ntejeh vs ntmjmh). Range of frequencies for train and track excitation from Connolly et al. (2014)

The results shown above are a consequence of the rock mass being modelled as a discontinuum or an equivalent continuum. A different rock mass with different joint spacings and block and joint stiffnesses would generate different rock mass resonant frequencies. Despite this, at least some of the train excitations will always fall in the spring resonance zone as it occurs at low frequencies, which dominate a train vibration spectrum. The calculation of these resonances is simplified with the analytical models derived for 1D rock masses (Equation 4-18). This exercise has been performed for a range of different rock masses to generate Figure 6-23. This shows the likely maximum resonant frequencies for a selection of common rock types. It is assumed that there are a large number of joints with an equal spacing and stiffness. Figure 6-23 shows different probabilities of vibrations being transmitted through a rock mass. The probabilities are determined qualitatively based on the likely maximum spring resonant frequency of a jointed rock mass with the properties in Table 6-6. All rock and joint properties in Table 6-6 are taken from Bandis et al. (1983) or based on the engineering judgement of the author. In Figure 6-23, the likely transmission zone represents the portion of the vibration spectrum which will be transmitted in a rock mass which has small blocks and strong joints. The possible transmission zone represents the cut off frequency of the spring resonance high transmission zone for a rock mass with large blocks and weak joints. This represents a zone in which transmission could occur given the appropriate rock mass conditions, although it isn't as likely to occur as the likely transmission zone. At higher frequencies rock mass conditions are unlikely to be met to allow the spring resonance effect to form a high transmission zone, therefore transmission is unlikely. Also plotted on this graph are the range of frequencies which are generated from track and train excitations given by Connolly et al. (2014).

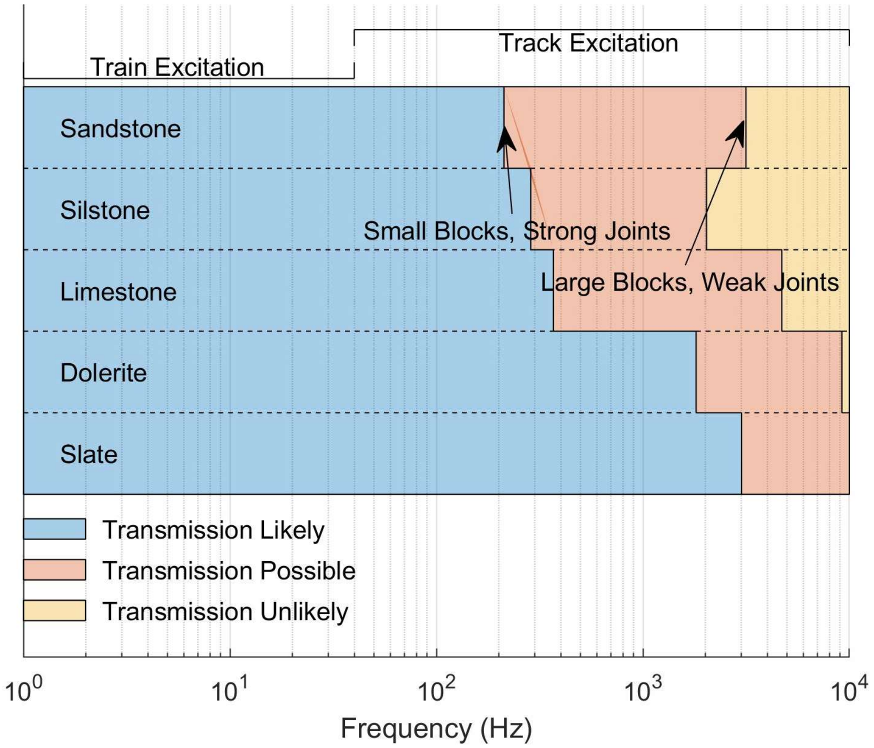

Figure 6-23 Spring resonance high transmission zones for different rock masses plotted with ranges of train and track excitation frequencies from Connolly et al. (2014). *The coloured boxes refer to the cut off frequencies of the spring resonance mechanism for different rock mass conditions, resulting in different probabilities of transmission through a rock mass. From* Holmes et al. (2023a) *Figure 14*

Figure 6-23 shows that train excitations are likely to be transmitted without modification of the amplitude of vibrations due to the presence of joints, regardless of the rock mass and its conditions. However, the higher frequency vibrations generated by the track may not be transmitted. Slate, for instance, is likely to have a high transmittance zone which spans much of the range of frequencies which can be excited from a rail track, while Siltstone shows a much smaller range. This suggests that, depending on the geological conditions in which a rail tunnel is excavated, mitigation measures can be targeted at certain excitation sources to use resources most economically.

Table 6-6 Properties used for resonance ranges in Figure 6-23. All properties from Bandis et al. (1983)*, except joint spacing which were based on engineering judgement from BS EN ISO 14689 Part 1*

Rock Type	Block Stiffness (GPa)	Fresh Joint Stiffness (GPa/m)	Weathered Joint Stiffness (GPa/m)	Density (Mg/m^3)	Max. Joint Spacing (m)	Min. Joint Spacing (m)
Sandstone	24.0	34.9	8.8	2.41	6	0.06
Siltstone	28.5	64.2	20.0	2.42	6	0.2
Limestone	49.0	133.5	39.8	2.73	6	0.06
Dolerite	78.0	75.3	24.7	2.90	0.2	0.006
Slate	66.0	344.3	19.1	2.77	0.06	0.006

6.7. Conclusions

This Chapter builds upon the work in Chapters 4 and 5 to further investigate the jointed rock mass resonance mechanisms identified in this research.

2D plane strain models are used throughout, which are verified using fundamental solutions. The fundamental solutions are analytical Equations which provide a way of checking that the models are behaving as expected. Following this, the response of WAVE2D and UDEC are compared for a square and circular cavity. This is a crucial step, as WAVE2D can only approximate a circular cavity, while UDEC can do this much more accurately. The models were found to be sufficiently similar for WAVE2D to be used for further analysis.

WAVE2D is used to verify the presence of the rock mass resonance mechanisms in a 2D model, excited by a non-planar wave. The resonant frequency of the rock mass is found to match the predictions from the analytical Equations given in Chapter 4, for both spring and superposition resonance. When a large number of joints are modelled it is shown that a high transmission zone at low frequencies is generated. This occurs up to the highest spring resonance frequency, so the extent of the high transmission zone can be easily evaluated using the Equation 4-18 in Chapter 4.

The 2D models used in this Chapter allow a tunnel to be modelled. When a tunnel is modelled it is found that a high transmission zone occurs at an offset of 30 degrees from the loading in the vertical direction, with a transmission shadow within this region. In the horizontal direction vibrations are shown to increase within this zone.

Finally, the rock mass resonance characteristics are put into the context of train vibrations. It is shown that the high transmission zone which can develop at low frequencies, due to spring resonance, is likely to encompass all excitations which are generated by trains for a range of common rock masses. Some track related excitation sources could fall outside this high transmission zone, although this is highly dependent upon the weathering condition of the rock mass. This indicates that, given a large number of joints, the presence of the spring resonance mechanism is not likely to lead to any significant reduction in vibrations from railways.

7. Jointed Rock Masses as Metamaterials

"A jointed rocks frequency response,
Is shown to be a metamaterial in nuance.
Matching experimental results shows validity,
Of the resonance's physical applicability."

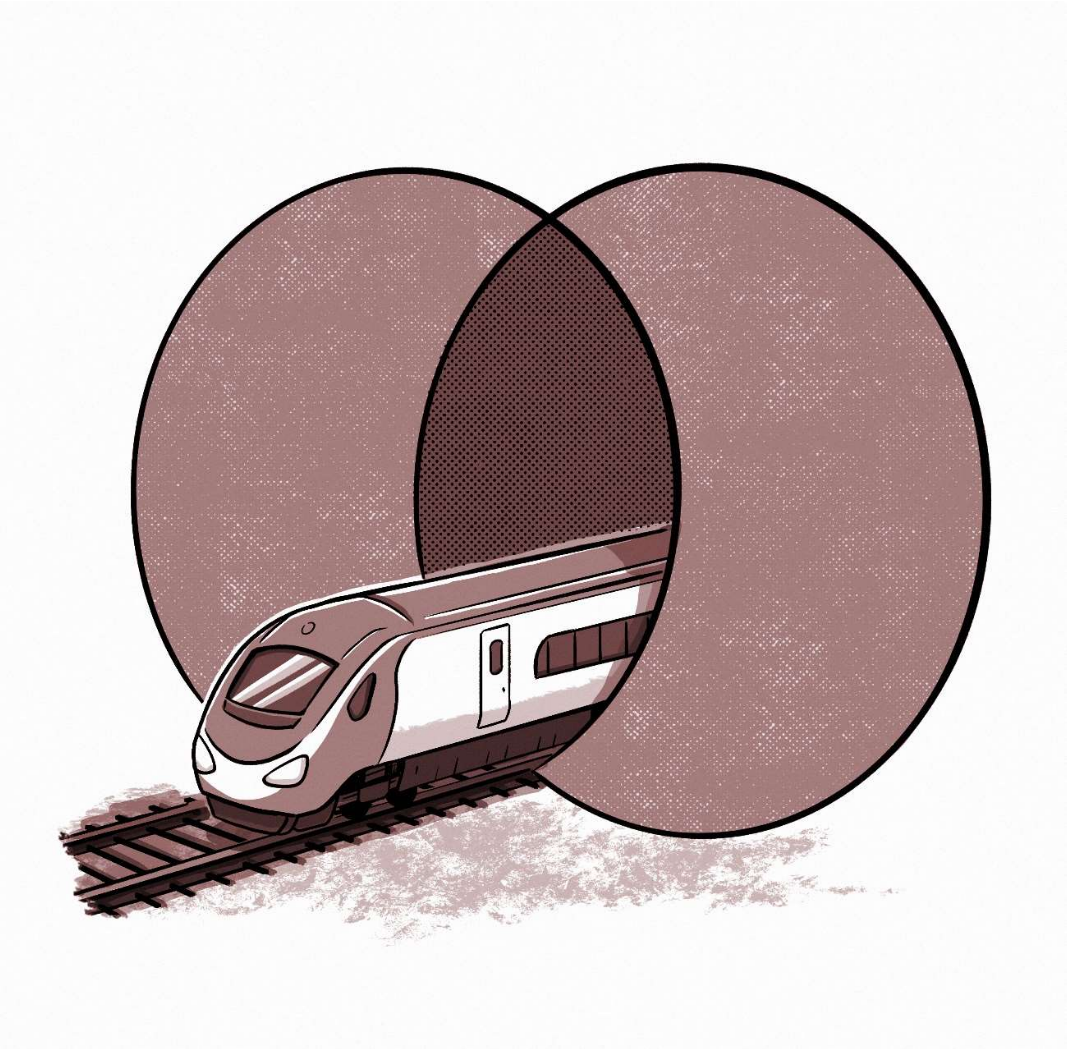

© Army of Cats 2023

7.1. Introduction

This Chapter builds upon Chapters 4 to 6 and investigates the implications of their findings. The idea that jointed rock masses can be redefined as being a natural type of metamaterial is explored and their frequency characteristics viewed in this context. Applications of this type of metamaterial for the mitigation of vibrations from railway lines are appraised. This Chapter diverges somewhat from the approach adopted by the other chapters in this thesis, drawing together abstract concepts and presenting a thought experiment.

> *"How often have I said to you that when you have eliminated the impossible, whatever remains, however improbable, must be the truth?" – Sherlock Holmes*
> *(Doyle, 2014, pg. 89)*

7.2. Recap of Rock Mass Resonances

Chapters 4 to 6 have investigated the transmission of stress waves through jointed materials using numerical models. The key findings of these Chapters are summarised below.

Jointed rock masses show two resonance mechanisms:

1. Spring resonance - occurs at low frequencies;
    - An analytical Equation is given which can accurately predict resonant frequencies (Equation 4-18),
    - The blocks within the rock mass oscillate like masses between springs, with the springs being analogous with joints and the masses as the blocks,
    - There are an equal number of resonant frequencies as there are blocks,
    - Spring resonance reaches a maximum frequency for the given rock mass, so when there are a large number of blocks the resonances merge to give a high transmission zone at low frequencies,
    - This effect is shown to occur with both P and S-waves.
2. Super position resonance - occurs at high frequencies;
    - An analytical Equation is given which can accurately predict resonant frequencies (Equation 4-20),
    - Waves reflected from joints can constructively interfere giving high transmission of these frequencies through joints,
    - Superposition resonance is related to the velocity of the block material and the joint spacing.

The rock mass resonance effects have been shown to occur in different numerical models with different assumptions.

- Initial work was undertaken using the combined discrete element-finite difference method (DEM-FDM) with a second code using the finite difference method used to validate this,
- The resonance effects are not affected by the type of excitation source used,
- The resonance effects still occur when different boundary conditions are used, a blocky rock mass is modelled, and a non-planar wave is used.

The work carried out into the transmission of stress waves through jointed rock masses shows that the resonance mechanisms observed in Chapter 4 appear to be quite robust to changes in numerical modelling set up, as illustrated in Chapters 5 and 6.

7.3. Physical Verification

While the superposition resonance mechanism is a well-known phenomenon in rock blocks (Nakagawa, 1998) there has been no physical evidence of the spring resonance effect presented before Holmes et al. (2023b). If the jointed materials previously considered are viewed as a succession of stiff material (the blocks) and weaker material (the joints), which is what the analogy of the spring resonance mechanism assumes, then these materials can be considered to be periodic metamaterials. If it were so desired, an artificial rock mass could be constructed to have a particular set of frequency related properties, which is a similar concept to those used for the design and manufacture of periodic metamaterials (Cummer et al., 2016; Witarto et al., 2018; Huang et al., 2021). In acoustics, the parallel jointed rock mass studied in Chapter 4 can be considered a 1D phononic crystal. Like a phononic crystal, a jointed rock mass can absorb or transmit different frequencies. The transmission of frequencies occurs in pass bands, which are coincident with the resonant frequencies of the rock mass, and absorption occurs in band gaps. This is illustrated in Figure 7-1 with the aid of a transfer function from a rock mass with a single block. With a small number of blocks, this will act as a band-pass filter prohibiting wave frequencies that do not fall within the pass bands. As the number of joints increases the rock mass will transition to an effectively low-pass filter as the resonances begin to overlap one another at low frequencies, as shown in Chapter 6. Defining jointed rock masses in such a way puts them in the context of current research into metamaterials, a current and fast evolving field of research. Hussein et al. (2014) investigated the mass between spring resonance shown by periodic metamaterials, showing these do exist in 1D lattices.

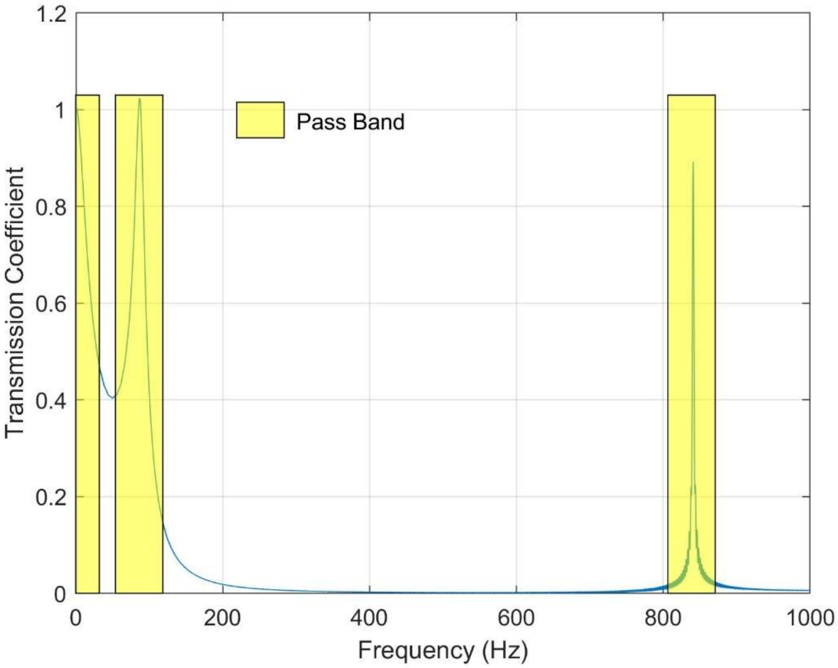

Figure 7-1 Pass bands in a rock mass with a single block with a width of 2 m. Pass band indicators are of an arbitrary width

Examples can be found in studies relating to periodic metamaterials that show high transmission zones within frequency response functions, which are synonymous with the transfer functions presented in this thesis. Witarto et al. (2018) presented a simple periodic metamaterial and analysed its performance using a frequency sweep on a shake table (Figure 7-2). This is equivalent to the attempted dynamic mechanical analysis experiment in Chapter 5. Later, Huang et al. (2021) modelled the same material using the finite-element method. The material being analysed was a concrete layer, sandwiched between polyurethane. A concrete cap is also present, as shown by Figure 7-2, which was surcharged with an equivalent structural loading. Due to the relative stiffness of the materials, the less stiff polyurethane acts like a joint, while the stiffer concrete acts like a block. The properties of the materials used in the test are shown in Table 7-1. Assuming that the top concrete block will not act as a block, due to the loading from the structural surcharge, the spring resonance of the single block system is 8 Hz. Figure 7-3 shows the frequency response function from the studies of Witarto et al. (2018) and Huang et al. (2021), along with the spring resonance frequency generated using the analytical Equations from this thesis. This shows that the amplified frequencies found by the previous studies closely match the resonant frequency predicted by Equation 4-18 for spring resonance, giving convincing evidence that the resonance effect can be isolated in physical models, and that it is a realistic phenomenon.

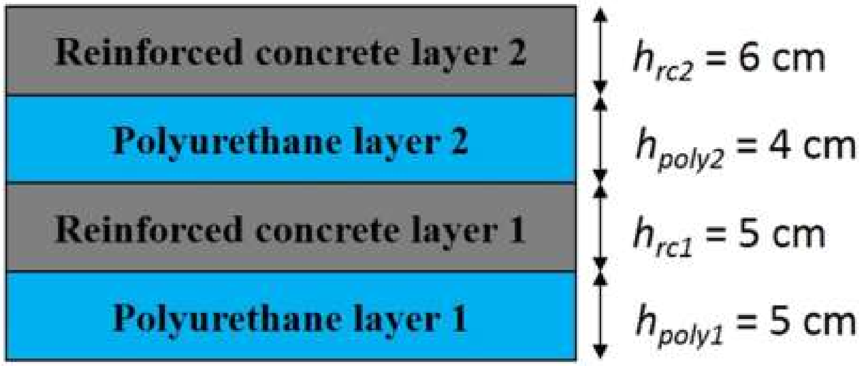

Figure 7-2 Periodic metamaterial as used in the experiment of Witarto et al. (2018)*, Figure 5a*

Table 7-1 Material properties of the periodic metamaterial (Witarto et al., 2018)

Material	Property
Concrete	
Density	2300 kg/m^3
Elastic Stiffness	31400 MPa
Poisson’s Ratio	0.2
Thickness	0.05 m
Polyurethane	
Stiffness	0.1586 MPa

Huang et al. (2021) and Witarto et al. (2018) show amplification of waves travelling through the metamaterial, which has a value of up to 4 if plotted as transmission coefficients, as used extensively in this study. The amplification of the 8 Hz waves is something which is not predicted by the spring resonance effect. This could be due to the low stiffness of the polyurethane layers, allowing greater displacement of the overlying concrete layers, than the displacement allowed in the shake table. Therefore, the upper blocks can displace more than the block attached to the shake table, giving the appearance of an amplification of the vibrations. Despite this, the clear match between the spring resonant frequency for the material and the peak transmission in the transfer functions shown in Figure 7-3 is compelling evidence of the presence of the spring resonance mechanism in a physical sample.

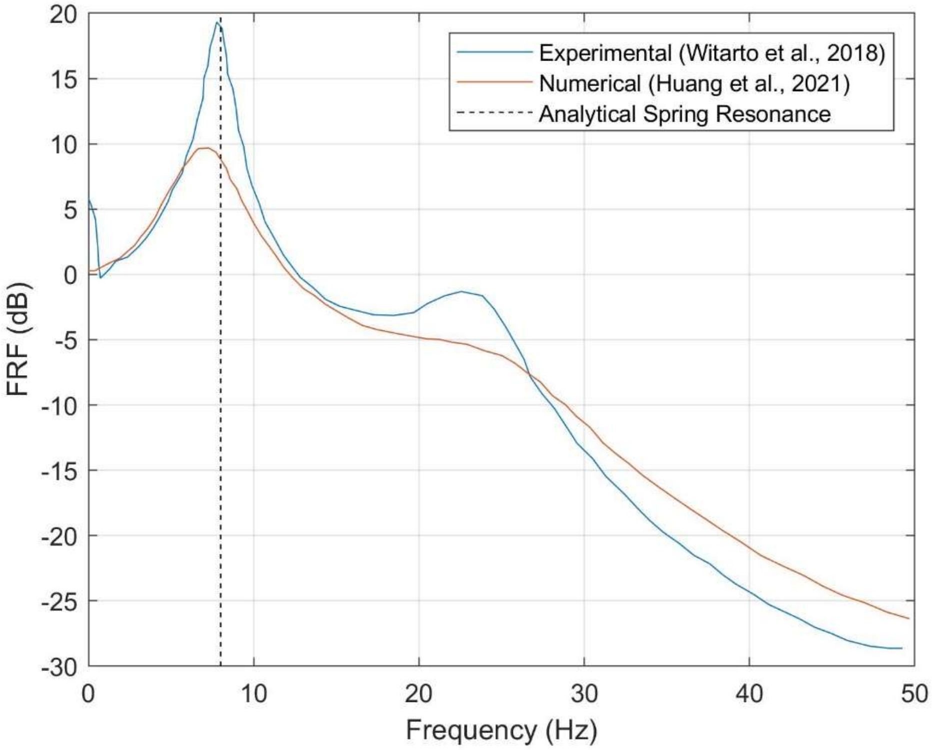

Figure 7-3 Frequency response function for single block metamaterial from the laboratory experiment (Witarto et al., 2018) *and corresponding numerical experiment of* (Huang et al., 2021)*. Analytical spring resonance Equation 4-18. From* (Holmes et al., 2023a) *Figure 13*

The study of Witarto et al. (2018) serves as a useful verification of the presence of the spring resonance effect in a physical material. This suggests that, if it is set up successfully, the experiment outlined in Section 5.3.4 will show the spring resonance effect.

7.4. Jointed Rock masses as Natural Metamaterials

The previous section shows that the spring resonance mechanism found in jointed rock masses is evident in a periodic metamaterial. This suggests that the effect is likely to persist in other periodic metamaterials. The consequence of this is that jointed rock masses could be considered to be a periodic metamaterials themselves. This section appraises this concept, and determines whether defining jointed rock masses as periodic metamaterials is a reasonable and useful approach.

Metamaterials are composite materials which exhibit properties not usually found in natural materials. The word itself is a composite the Greek and Latin terms. The first element “meta” is Greek and has the meaning “beyond”. The second element is the Latin “material”, meaning “a substance”. Therefore, metamaterials are materials which have properties beyond those of a normal material. Rock masses are one of the most common materials on earth, with much of the earth being composed of them. Therefore, their inherent properties, which includes the spring resonance effect, are very normal. As far as the strict definition goes, rock masses are not metamaterials. However, definitions regularly change through time.

As described above, metamaterials are composite materials. Therefore, they must be composed of more than one element. A very simple jointed rock mass is composed of blocks and joints. There are also other potential elements, such as mineralised veins and intrusions, but for simplicity these can be ignored. In these simple terms the two elements (blocks and joints) present a composite material (Figure 7-4). However, if any joint infilling is ignored, joints are merely where two blocks meet and are not really a thing in themselves. If a rock mass were deconstructed into its elements, there would be a pile of blocks and nothing else. The joints need the blocks to exist, otherwise there are no properties to define this element in the composite material. This is unlike the elements in the periodic metamaterial of Witarto et al. (2018). In this, there are concrete blocks and rubber blocks, each with their own clear properties, which exist without the presence of the other element. This again suggests that the rock mass is not really a metamaterial; however, when considered in terms of differing properties throughout the rock mass, the joints have different stiffnesses to the blocks, and therefore do show a composite of different properties.

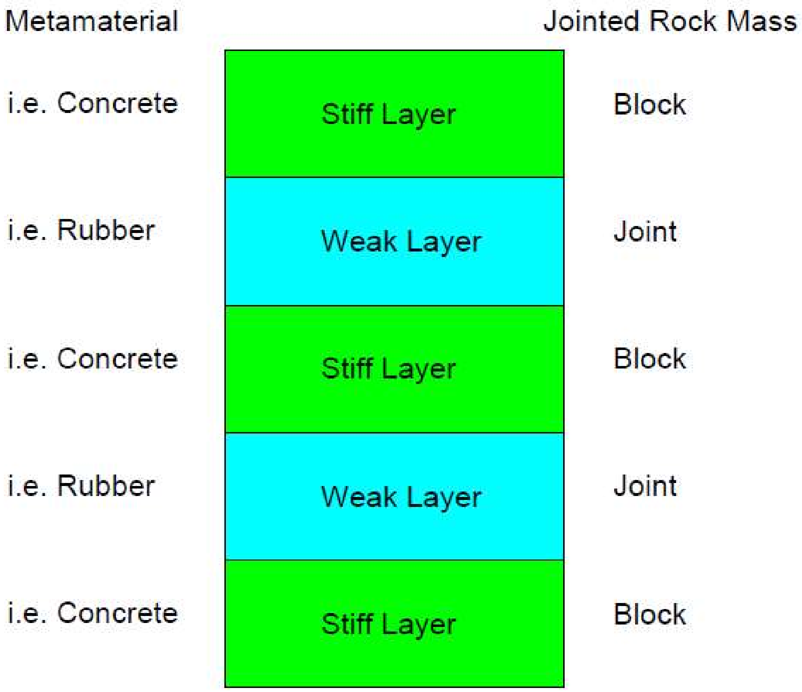

Figure 7-4 Schematic comparing metamaterials and Jointed Rock Masses

A periodic metamaterial is not merely composed of a repeatable sequence of different layers but these layers will also have repeating thickness and properties. While this can occur over small scales within jointed rock masses it is unlikely to persist over large distances, with the way a rock mass will have evolved over time. As such taking the concept of periodicity at face value a jointed rock mass is not a periodic material. However, if a rock mass is thought of more conceptually as a sequence of joint and blocks and ignoring the exact thickness of each layer and their properties the periodicity returns.

Another desirable property of metamaterials is that they can be designed to give certain characteristics. The design element of metamaterials is possible because they are man-made. This is not the case for natural materials. Natural materials are a product of the geological settings in which they were created and modified through time.

Based on the conventional view of metamaterials, jointed rock masses are not actually metamaterials in their truest form. Despite this, they do exhibit properties similar to metamaterials, namely the spring resonance effect as shown by Figure 7-3. However, this could be phrased differently to say that metamaterials exhibit properties similar to jointed rock masses. Therefore, it can be said that jointed rock masses are a class of periodic materials, namely natural periodic materials. Periodic metamaterials are also a type of periodic material; however, these should be classed as synthetic periodic materials.

7.5. Wave Barriers

While it has been shown that jointed rock masses are not periodic metamaterials, the resonance effects are shown to occur in periodic metamaterials. Therefore, it is useful to think about what these materials can be used for, and how the resonance effects can be used to our advantage. Specifically, and on the theme of the work which has motivated this research, this section is concerned with the use of the periodic materials to suppress train vibrations.

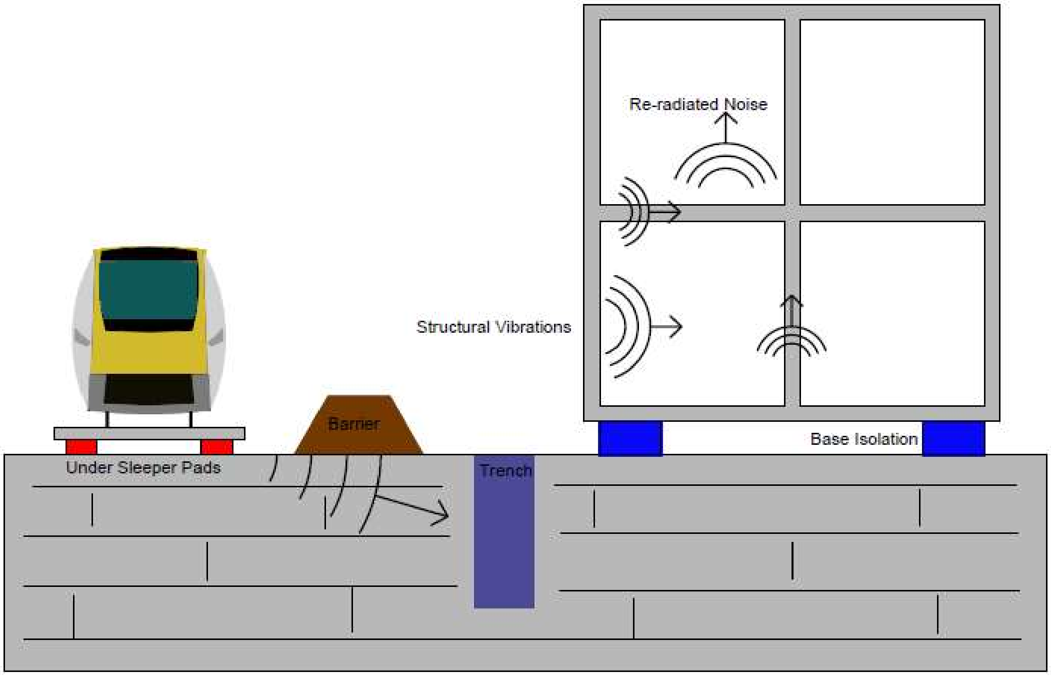

Figure 7-5 Train vibration mitigation measures

Solutions to reduce vibrations are grouped into those near the source (i.e. under sleeper pads, ballast mats), at the receiver changing its dynamic behaviour (i.e. building base isolation) and those in the propagation pathway (i.e. trenches and barriers) (Castanheira-Pinto et al., 2018). These vibration reduction measures are shown in Figure 7-5. Periodic metamaterials can be used in any of these places; however, this section is focussed on the fill of wave barriers.

Wave barriers introduce a geometry to the propagation pathway which can be with or without a material fill. These are placed between the source and receiver and act to deviate or dampen waves (Ouakka et al., 2022). Unfilled wave barriers do not allow any transmission through the barrier, acting as a zero stiffness discontinuity, instead diffracting waves around the barrier. The success of such barriers relies on their depth, which is limited due to the potential instability of an unfilled void. Good results are obtained when the depth of the barrier is at least half the Rayleigh wavelength, with reductions of up to 12 dB being reported in some cases.

Soft and stiff filled wave barriers are other alternatives to trenches. The designation of barriers as being soft or stiff is related to the stiffness of the fill material, in relation to the stiffness of the surrounding ground. Soft barriers can be filled with gas cushions, rubber chips, polystyrene, and water, among others. These act as a weakened discontinuity within the ground, allowing waves to be either dampened as they propagate through the low stiffness barrier or diffracted around them. Reductions depend on the type of barrier used and the frequency, with reductions of 3 to 12 dB expressed in literature. Stiff barriers work in a similar way to soft barriers, with waves diffracted around them and reflected off them. Steel or concrete piles, sheet piles and jet grouting have been used in the past for such structures. Insertion losses of 3 dB are quoted in literature. Heavy masses are another option, which are placed directly on the surface of the ground. These have been found to reduce transmission by up to 10 dB.

Phononic crystal barriers, consisting of a periodic metamaterial, are a promising alternative to conventional wave barriers. Insertion losses of up to 18 dB have been shown in literature (Ouakka et al., 2022). Hussein et al. (2014) appraised phononic crystals, showing that when a layered material is subject to a vibrational source, they exhibit a response synonymous with the spring resonance effect. This superposition effect is also identified by Van Hoorickx et al. (2017) between twin wave barriers. Double wave barriers have been investigated by numerous researchers (Castanheira-Pinto et al., 2018; Albino et al., 2019). Albino et al. (2019) found that improvement is registered when a second buried wall is added to a wave barrier system, although resonances occurring between walls may decrease the efficiency for specific frequencies.

Periodic barriers are proposed, which consist of a low stiffness core sandwiched between a stiffer material (Huang et al., 2021). A common material for these is polyurethane, for the low stiffness core, and concrete for the stiffer material.

Cheng and Shi (2014), Krödel et al. (2015) and Dertimanis et al. (2016) propose other periodic barriers, which display locally resonant characteristics. These types of wave barriers are shown in Figure 7-6. These are termed phononic crystal barriers and are composed of a high density mass encased in a lower stiffness medium, such as rubber. This isolation of the high density mass within the low stiffness medium allows the mass to oscillate and resonate like a mass between springs.

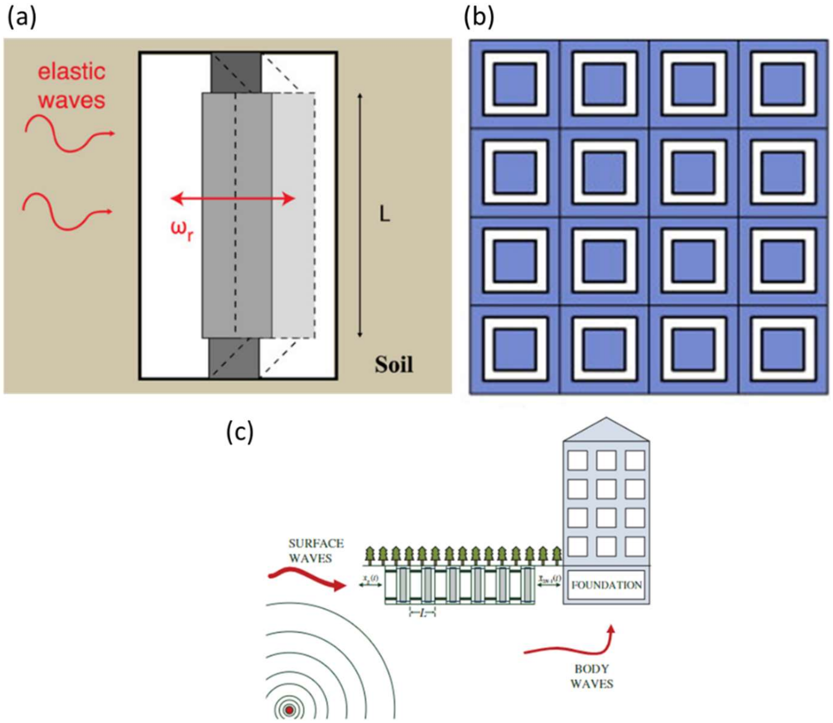

Figure 7-6 Periodic metamaterials used in wave barriers. a) Krödel et al. (2015) *Figure 1c, b)* Cheng & Shi (2014) *Figure 15b, c)* Dertimanis et al. (2016) *Figure 7*

The wave barriers proposed by Cheng and Shi (2014), Krödel et al. (2015) and Dertimanis et al. (2016) all adopt a standardised makeup of phononic crystal, with all the crystals in these barriers having the same geometry and properties. As such, all of the cells within the wave barrier will either have the same resonance characteristics if the cells are isolated from each other or will operate as a long series of masses and springs, like the jointed rock masses modelled in this thesis.

7.5.1. Proposed Wave Barriers

An alternative to the arrangement adopted in previous research is suggested, with the intention of improving the efficiency of the wave barrier. It is proposed that the standard crystal set up, shown in Figure 7-6, may not be optimal for vibration reduction. A series of coupled phononic cells would operate like a low pass filter, allowing much of the low frequency content to be transmitted, while the high frequency content is eliminated. A set of isolated cells, whose oscillations are decoupled from one another, will reduce the vibrations transmitted through the material, but will allow the resonant frequency of the cell to be transmitted unopposed. Cells can be engineered so that the transmitted frequency does not correspond with a frequency that will significantly adversely affect a receiver. However, this may not be the most optimum set up. A more efficient wave barrier could be generated by using two different unit cells, with different resonant characteristics, isolated from one another and installed in series. The proposed cells and current consistent cells (standard cells) are illustrated in Figure 7-7. The resonant frequency of the cell will represent the pass band, while non-resonant frequencies will be the band gaps. If the unit cells are designed appropriately, it would be possible to have the pass band of one unit cell fall within the band gap of the other unit cell. Therefore, the energy which is passed through the first cell is eliminated by the second cell. All other frequencies will fall within band gaps and be significantly reduced during transmission.

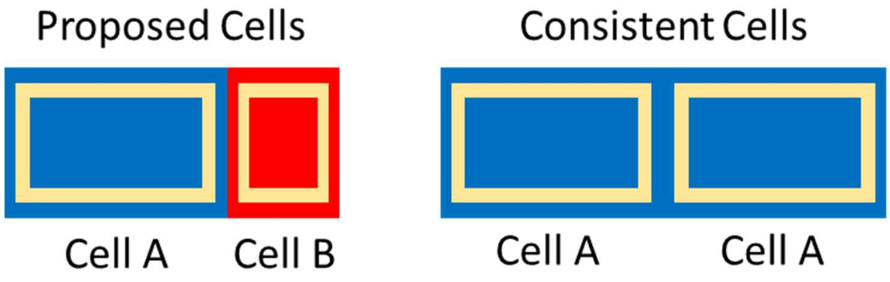

Figure 7-7 Proposed phononic cells for wave barriers and current consistent cells used in wave barriers. Each cell consists of a stiff block surrounded in a less stiff material (i.e. rubber) encases in a stiff cell

7.5.2. Semi-Analytical Modelling of Wave Barriers

To simply investigate the efficiency of the proposed phononic cell set up a semi-analytical approach is adopted. The semi-analytical approach takes the numerically derived transfer functions from models of each cell and multiplies these together. This approach is reasonable as transfer function represents the proportion of the frequency content of an incident wave which is transmitted through a medium. The transmission through each cell is given by their respective transfer functions. So, knowing the wave input to the first cell, the transmission through the barrier is calculated by multiplying these transfer functions together, as shown by Figure 7-8 and Equation 7-1. This is an idealised assumption of the transmission of vibrations through the barrier, ignoring any waves which may bypass the barrier and those which are transmitted directly though the stiff outer material of each cell.

The theory behind this is that, assuming all waves entering the first cell are transmitted to the next one, with no extra energy being input from the environment, the transfer function for the first cell will give the energy which is transmitted to the second cell. If the input wave is known, then the wave which enters the second cell is given by the input wave multiplied by the transfer function for the first cell. And therefore, the wave which is transmitted through the full system in the frequency domain is given by Equation 7-1.

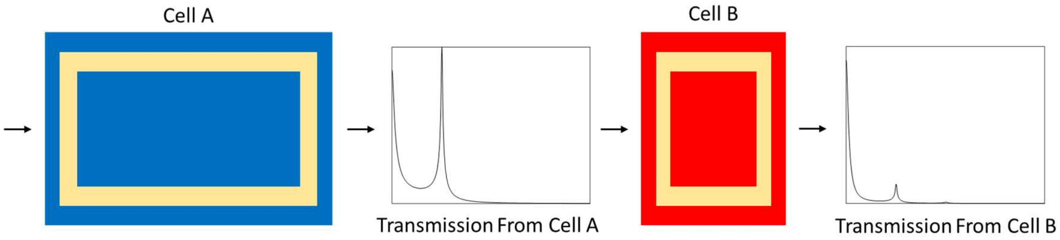

Figure 7-8 Transmission pathway for uncoupled cells

$$f(out) = (t_1 t_2 \dots . t_i) f(in) \qquad \text{Equation 7-1}$$

Where t_i is the transfer function, *f(in)* is the input wave in the frequency domain, *f(out)* is the output wave in the frequency domain.

Equation 7-1 shows that the order in which the cells are placed in the barrier does not affect the transmission coefficient of the full system. It also shows that there can be an unlimited number of different cells in the barrier. Equation 7-1 works for the semi-analytical calculation of the proposed cells and the consistent cells.

The process described in Figure 7-8 and Equation 7-1 is carried out in non-dimensional terms for two Cells “A” and “B”. These cells have arbitrary properties, although Cell A has a spring resonant frequency half that of Cell B. The proposed barrier is composed of Cell A followed by Cell B, while the consistent barrier is composed of two of Cell A. The transfer functions for these barriers are shown in Figure 7-9.

Figure 7-9a shows the proposed wave barrier set up. There is a clear peak in the transmission at the resonant frequency of Cell A; however, this is significantly lower than the transmission of the single cell. There is also a minor peak at the resonant frequency of Cell B, although this is not visible on the linear scale shown in this Figure. With two cells, the peak in the transmission coefficient will coincide with the cell with the lowest resonant frequency. This is because the transmission coefficient between 0 Hz and the resonant frequency is always greater for this type of cell than the transmission coefficient greater than the resonant frequency. Therefore, the higher frequency resonant peak will be multiplied by a smaller number than the lower frequency resonant peak, giving a smaller overall resultant peak. Figure 7-9b shows the transfer function for a wave barrier composed of a single geometry of cell. The combined transmission coefficient at the resonant frequency is equal to that of the single cell, while the amplitude of all other frequencies are reduced.

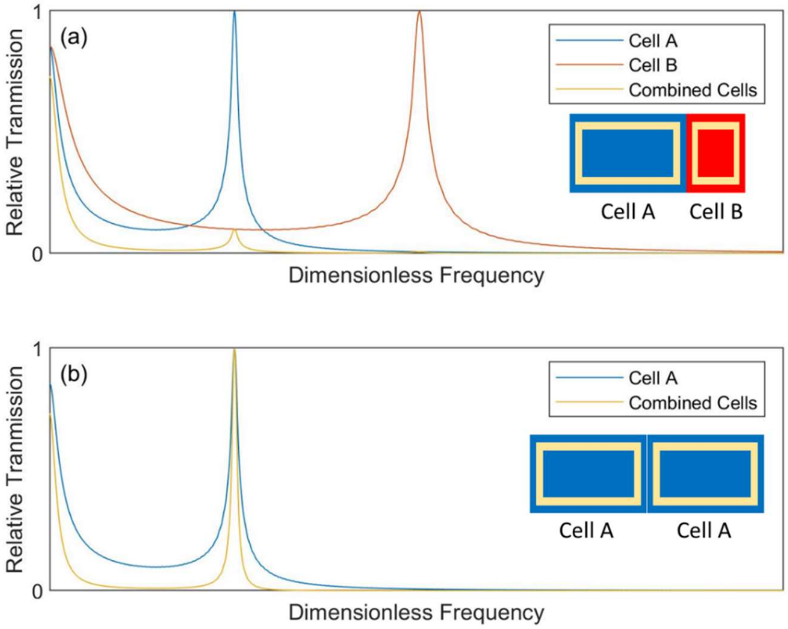

Figure 7-9 Example of transfer functions for two isolated cells installed in series. (a) Two cells of different geometries, (b) two cells of the same geometry

Figure 7-10 shows the combined cells transfer functions from Figure 7-9. The “Proposed Cells” are the two different geometry cells in Figure 7-9a, and the “Consistent Cells” are the cells with the same geometry in Figure 7-9b. The x-axis scale on this Figure is given in dB as insertion losses, which are a common way of displaying the effect of proposed wave barriers (Castanheira-Pinto et al., 2018). Insertion losses indicate the reduction in amplitude of vibrations which would be expected if the wave barrier were installed between the source and a receiver. The greater the decibels the greater the vibration content which is removed by the barrier. Figure 7-10 indicates that both wave barrier setups have the potential to significantly reduce vibrations; however, reductions are greatest in the barrier with the consistently sized cells. This is with the exception of the resonant frequency of the cells in the consistent barrier, whose transmission is higher than in the proposed barrier.

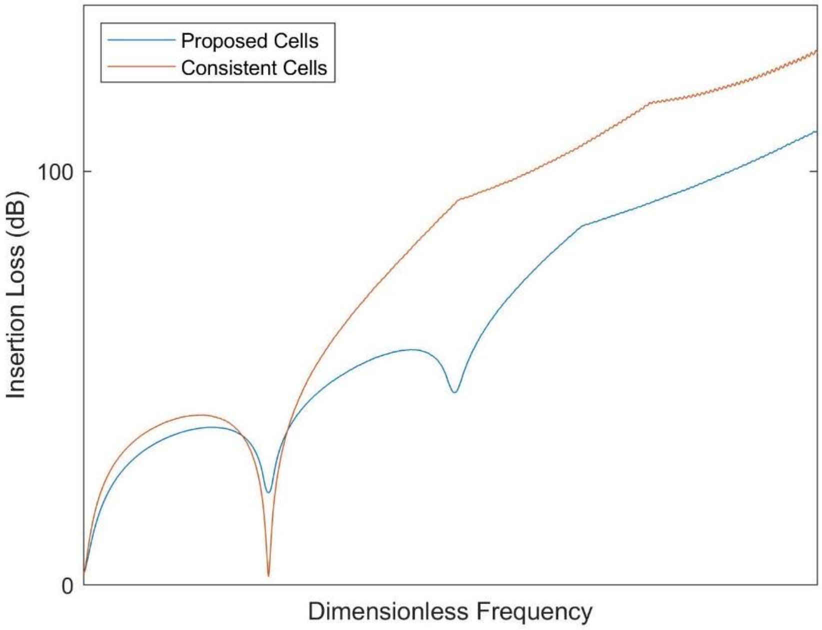

Figure 7-10 Insertion Losses of different phononic cell arrangements in wave barriers

It is clear from Figure 7-10 that the proposed cells in the barrier are not as effective as the consistent cells, as given by Cheng & Shi (2014), among others. It could be argued that because a sensitivity analysis is not conducted an optimum arrangement has not been found for the different cells to reduce the vibrations further. While this is undoubtedly true, one of the two cells used would have a lower resonant frequency than the other. It would then be more beneficial to use two of these lower resonant frequency cells in a consistent barrier than use two different cells in the proposed barrier arrangement. If the frequency spectrum of the source is known, the high transmission shown by the “Consistent Cells” could be designed to fit into this gap.

7.6. Conclusions

Chapter 7 attempts to use the findings of the previous Chapters work into resonance in jointed rock masses for the practical application of mitigating vibrations. To begin with, jointed rock masses are compared to periodic metamaterials. An example is presented from literature of a periodic metamaterial which is used in a physical experiment involving a frequency sweep on a vibration table. It is found that the frequency which exhibited a high transmission in the frequency response function from literature is at the same frequency as the spring resonance as predicted by the Equation 4-18. This not only shows physical verification of the spring resonance mechanism, but also indicates that jointed rock masses could be considered to be periodic metamaterials. Subsequently the concept of rock masses being periodic metamaterials is investigated; however, it is determined that jointed rock masses are natural periodic materials, with periodic metamaterials being synthetic periodic materials.

Finally, a concept wave barrier is proposed which takes the resonance mechanisms from periodic materials and applies them to vibration mitigation techniques. The concept barrier proposed consists of two cells of a different geometry which are combined in a wave barrier. The approach currently used consists of multiple cells of a single geometry. The proposed barrier arrangement of two different cells with different frequencies theoretically works well in reducing vibrations at all frequencies. This arrangement will also be able to remove the potentially high transmission at the resonant frequency of the cells. However, it is found that this arrangement is not as effective as using a single geometry of cell, all with identical transfer functions. Therefore, the proposed arrangement of using two different cells is not an improvement on the current approach of using consistent cells.

While the insertion loss of the proposed barrier is greater than the consistent barrier at the resonant frequency of the cells, this is not replicated at other frequencies. Using a sufficiently robust scoping study of the potentially adverse vibration frequencies from a source, a barrier could be designed so that the resonant frequency of the barrier falls within a range of frequencies that are not generated to a significant degree by the source. This will eliminate the need to reduce the transmission of the resonant frequency, which the proposed barrier would achieve.

8. Moving Loads

“Viewing the model from the side,
A moving load is applied.
Transfer functions provide the evidence,
Of frequencies which have precedence.”

© Army of Cats 2023

8.1. Introduction

Chapters 4 to 7 concern non-moving point loads, which are a reasonable simplification, and in some scenarios can be considered to be realistic, such as machine foundations. The research presented up to this point has been useful as it has allowed the effect of vibrations on joints to be assessed without the complication of the load speed or direction. However, as this thesis is motivated by studies of train vibrations, moving loads are an essential further step. The outcome of the non-moving point load studies can be used as a basis for understanding the more complex reaction of such models.

Moving loads are studied in the context of train vibration studies be previous researchers, with the literature covered in depth in Chapter 2, so will only be briefly recapped here. Moving loads can be modelled in 2D, 2.5D and 3D and various effects have been looked at, including the speed of the train (Yuan et al., 2017), pore water pressures (Di et al., 2016) and stiffness of the track (Forrest and Hunt, 2006b), to name a few. However, the effects of joints in moving load studies are investigated, which is a common them in train vibration studies. There are in fact no studies on the effects of joints on vibrations from moving loads published, even generalised ones which are not related to train vibrations, so this work reflects a new avenue of rock mechanics research.

This Chapter will use 2D models to study the effect of joints with moving loads. This represents a sensible first step for studying moving loads in jointed materials. A 1D model can model a moving load moving along the model; however, it was shown in Section 4.5.3 that the location of a load in relation to the measurement point in a 1D model does not affect the transfer function which is produced. Therefore, movement of a load perpendicular to joints will not cause a different response. Therefore, a 2D model is the minimum number of dimensions which needs to be used. A 3D model will represent the response better than a 2D model, although this adds additional complexity which should be avoided at this early stage of an investigation.

The literature review identifies a study by Yuan et al. (2015), who applies a moving load to a beam element in a 2D model. The train loading was approximated as a uniform moving point load traversing the beam element. Yuan et al. (2015) described the beam element as a tunnel, although there is no associated void modelled. This study presents a highly simplified approximation of the real-world problem, and its results are only of use qualitatively. Despite this, the approach adopted is applicable to the 2D models used in this Chapter. The results in this Chapter are only likely to have qualitative significance; however, general trends in the data can be identified and used to assist the design of more complex investigations.

The work in this section is undertaken using the two numerical codes which have been used throughout this project. Section 8.2 uses the combined discrete element-finite difference method, in UDEC, to assess the response of parallel jointed rock masses to a moving load. During this investigation, properties of joints are changed, including for the first time in this thesis the joint angle. Discrete jointed models and equivalent continuum models are studied. Section 8.3 uses the finite difference method, in WAVE2D. This uses the transfer function approach which has been extensively used in this research to determine the effect joints have on vibrations in the frequency domain. Specifically, this will attempt to determine whether the resonance mechanisms previously described prevail when the excitation comes from a moving load.

8.2. UDEC Modelling

This section aims to numerically investigate the role of jointing and transversely isotropic materials in the near and far field through the excitation of a rock mass, subject to a moving point load, using the combined DEM-FDM in UDEC (Itasca Consulting Group Inc., 2014). The moving point load is applied within a full space, with a horizontal loading path, after Yuan et al. (2015). Displacement histories are recorded in the centre of the loading path (the near field) and at 10 m above this (the far field). The near field is defined as the response close to the loading and the far field as the response away from the loading, which is a similar approach to that used by Jones & Hunt (2011). The actual position of the near and far field in this research are arbitrary and should not be confused with near and far field in seismology which have a specific meaning (Chen, 2021). The naming convention for near and far field in this research is a matter of convenience, and has a scale with engineering relevance. The far field results indicate the potential vibration levels reaching receptors, while near field results give indications as to the dynamic interaction of the tunnel and surrounding ground. The 10 m distance used in this study is used as it is half the length of the loading path (Figure 8-2) and is likely to give the most representative impression of how the response of a point in the rock mass is affected by the passage of the load towards and away from it. Displacements are recorded to allow direct comparisons with the results of Rieckh et al. (2012) and Ba et al. (2019). UDEC is suited to modelling blocky materials as it allows realistic deformations along the interface between blocks and has been widely used for studying dynamic interactions of jointed rock masses and stress waves, with modelling confirming the similarity between numerical and analytical results for simple cases (Cai and Zhao, 2000; Zhao et al., 2008; Deng et al., 2012; Eitzenberger, 2012). A 2D plane strain model is used for the analysis with no free surface and a linear load travel path is modelled longitudinally in accordance with the concept adopted by Yuan et al. (2015). The results from the jointed rock mass are compared to equivalent transversely isotropic continua as well as an isotropic continuum. The isotropic continuum is not strictly equivalent to the other models analysed; however, it does represent a common assumption in railway vibration modelling. Therefore, its inclusion allows the effects of making this assumption to be assessed. The effects of joint properties are assessed and mechanisms for the displacement response of the models suggested.

The models considered here are intended to analyse the relative effect of joints and transversely isotropic material properties when subject to a moving point load, instead of a realistic ground response. Therefore, instead of a beam, as modelled by Yuan et al. (2015), the path which the load traverses is modelled as a string of internal modelling nodes with no unique model properties. No void is modelled, as in the study of Yuan et al. (2015); however, the previous study referred to this path as a tunnel, so this is the terminology which will be used here. The beam element in the study of Yuan et al. (2015) was used to simulate the increase in stiffness of the material due to the presence of a tunnel liner, so the omission of the beam element in this research can be thought of as an unsupported tunnel. Although the point load cannot be considered a realistic train loading, this study is an important contribution to the train vibration field as it considers how a rock mass will respond to the movement of a loading source relative to joints, like the movement of a train along a track. This movement will change the angle of incidence of waves from the load interacting with joints and could alter their transmission through the rock mass.

Several models are created which allow the sensitivity of displacement to different modelling assumptions to be analysed. The methodology outlined below describes how the time domain, combined DEM-FDM model is created, the material properties used, and specifics related to the application of the load and initial modelling conditions.

8.2.1. Model Setup

Figure 8-1 shows a schematic of a tunnel in a 3D block. A load can travel along the long axis of the tunnel, which would appear to be either not moving, if the tunnel is viewed end on, or moving, if the tunnel is viewed along its long axis. In either of these perspectives the model will look 2D to an observer. As such, the modelling conducted in this section is undertaken in 2D plane strain. As the non-moving point load case is studied in the previous Chapters, the model used in this section analyses the long profile of a tunnel, with the short axis of the tunnel running in the out of plane direction (Figure 8-1). This gives the tunnel the appearance of being a line within the model. Therefore, the tunnel can be represented by a horizontal line in the centre of the model. The horizontal loading path has no unique properties so this model simulates an unsupported tunnel based on the reasoning of a beam element representing a lined tunnel as set out by Yuan et al. (2015). For situations where loads are moving in a tunnel, like the movement of a train, the assumption that the load path is linear is a reasonable approximation of the 3D load, as it will only realistically move in a single dimension (i.e. left to right, backwards and forwards, up and down). However, the propagation of stress waves induced by the load in the ground will propagate in 3D, so this assumption will affect the ground response. Andersen & Jones (2006) found that a 2D model of a tunnel excited by train vibrations can give comparative qualitative results to a 3D model. Therefore, as only the qualitative trends of how joints affect wave propagation from a moving source are of interest, the assumption of 2D plane strain is a reasonable simplification.

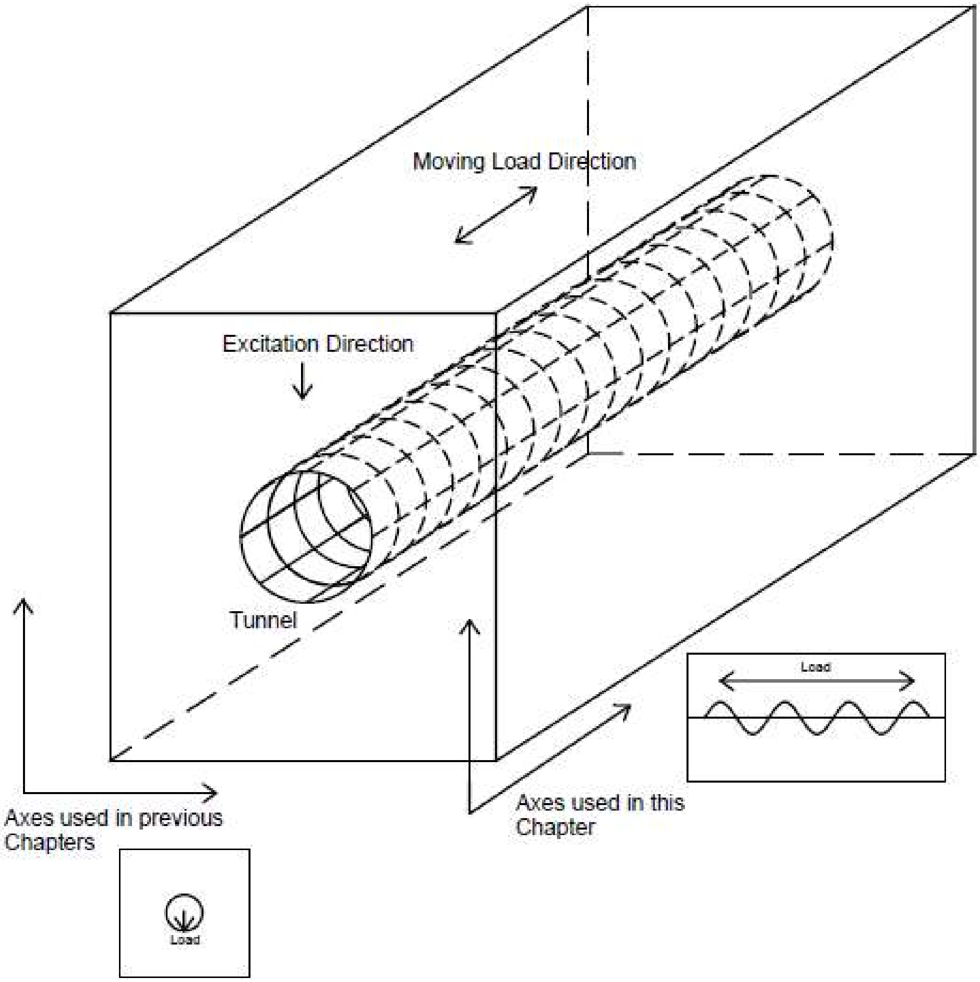

Figure 8-1 Block model showing modelling orientations

A time domain model is created in UDEC which is used for all analyses in this section by changing the presence, orientation and spacing of the joints and the model properties. The basic model is shown in Figure 8-2. Discontinuum analyses are conducted with joint angles of 0^o, 45^o, 90^o and 135^o (Figure 8-3a). Joint angles are measured anti-clockwise from horizontal; therefore, a 0^o joint is horizontal and a 90^o joint is vertical. Symmetry dictates that the results for 180^o joints will be identical to the 0^o joint. Joints are only modelled in the centre of the model (Figure 8-2), with the region surrounding this modelled as a continuum. This allows the boundaries to be sufficiently far to reduce reflections from boundaries without unnecessarily increasing the model run times, which would occur if the entire modelling domain contained joints. The presence of the continuum surrounding the model will affect the results, although this is not expected to be significant. Equally, as the continuum region is used in all models the effect of this region will give a standard error in all the results, so should not affect any conclusions as only the qualitative results are of interest.

Two different types of continuum analysis are run as unjointed comparisons: i) an isotropic model using the intact block properties used in the discontinuum analysis for the entire model; and ii) a transversely isotropic continuum using equivalent properties based on the discontinuum model, equivalent to the HEM used in Chapters 5 and 6. Continuum models have the same properties applied throughout the entire model. The isotropic continuum model represents a common assumption adopted in railway vibration analysis (Connolly et al., 2019), specifically that the ground has isotropic properties. Chapter 3 has shown that this is not the case in reality, so its inclusion here is important, despite not accurately giving the properties of a jointed rock mass. The transversely isotropic continuum represents a continuum with equivalent elastic properties in each direction to the discontinuum models, which more accurately represents a jointed rock mass.

Absorbing boundary conditions are modelled in order to prevent reflections from the model boundaries. Absorbing boundaries prevent prominent reflections in history data, which are not recorded when absorbing boundaries are modelled. The absorbing boundaries are located 100m horizontally and vertically from the centre of the loading path. The boundaries are sited at this distance to prevent them from interacting with the load in the centre of the model. There is likely to be some effect of the boundaries on the results from the model as this will always occur with a model which is not of infinite extent. However, as the boundaries are in the same position in all the models and only the relative results between the models are of interest, this should not affect the outcome. A graded mesh is modelled, with an element length of 0.2 m within 10 m of the loading location, doubling every 20 m away from this

(Figure 8-2). This increasing of the element length could affect modelling results; however, as this model is only intended to give indicative results, rather than fully realistic magnitudes of displacements, this will create a systematic error which will not affect the relative results. The mesh is generated using UDEC's quad mesh command (Figure 8-3 b and d), which is consistent with the findings in Chapter 4 which showed that this meshing command gives more accurate results for dynamic modelling.

No in-situ stresses or gravity are modelled, consistent with the approach used in previous Chapters. This is considered appropriate as only the interaction between the moving load and the model is of interest. In addition to this, the discontinuum analyses adopt a joint model where the joint stiffness properties do not change due to a change in stress.

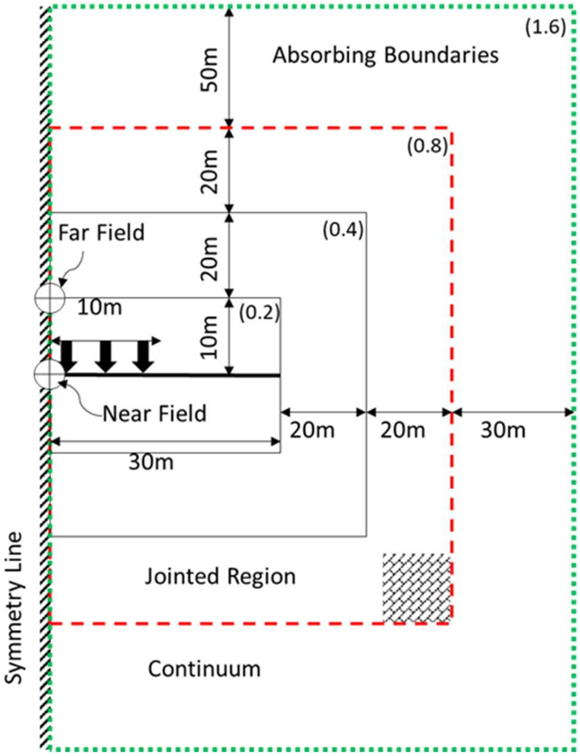

Figure 8-2 Right hand side of model used for analysis (not to scale). Model is symmetrical about centreline and is shown to reduce the size of the Figure with the model used for the analysis being a full space (see Figure 8-3). Crossed circles = measurement points, solid vertical arrows = loading locations, values in parentheses = mesh size, dashed box shows jointed region

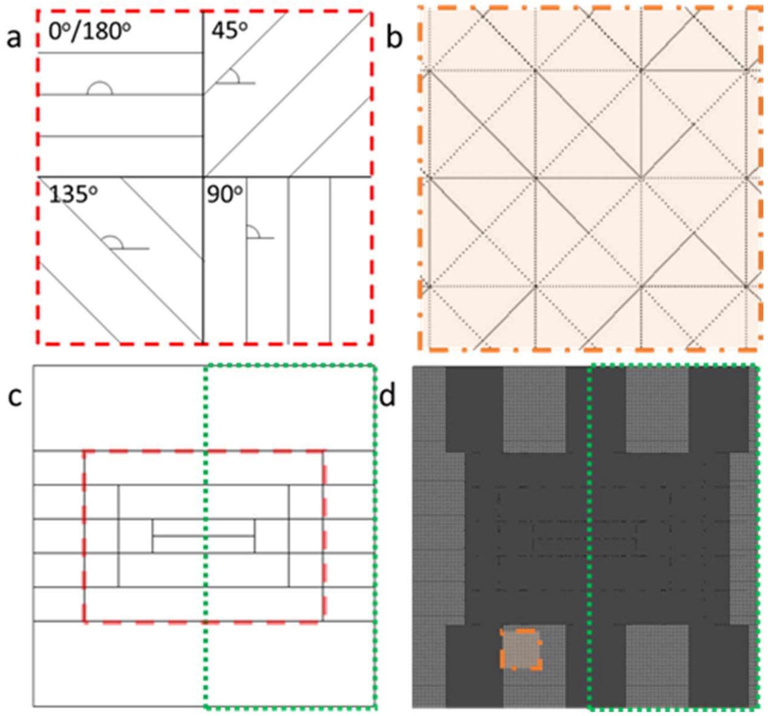

Figure 8-3 a) Joint orientations; b) Quadrilateral mesh setup; c) Screenshot of model from UDEC, dotted box shows location of schematic in Figure 8-2, dashed box shows jointed region; d) Screenshot of model mesh from UDEC, dotted box shows location of schematic in Figure 8-2, dash-dotted box shows location of mesh setup in 8-3 b (box not to scale)

A moving point load is modelled travelling from left to right in the model at 100 m/s along the line marked with solid vertical arrows in Figure 8-2, the “Loading Line”. The “Loading Line” is modelled as a construction line in the model. There is no inbuilt function in UDEC which can induce a moving load, so instead a FISH function is defined which allows the point of excitation to move along a linear path at a pre-defined speed through the model (Appendix C). A point load is approximated using a band-limited cosine pulse to avoid generating very high frequencies, as would be created if the load increased from zero to its maximum over a single time step. The amplitude of the function at time “*t*” is given by Equation 4-11 introduced in Chapter 4 (Figure 4-7). While Chapter 4 shows that this source waveform is not optimum for transfer functions, its simplicity is advantageous here for use with the moving point load FISH function. A peak load of 1 N is applied. The 1 N force is not related to any realistic train loading and the construction line does not behave like a realistic tunnel; however, for a comparative study such as this, this set up is sufficient to achieve useful results. A signal frequency of 500Hz is used with Equation 4-11 for the point load. The time-series of the variation of the loading is shown in Figure 8-4 a, with Figure 8-4 b showing the frequency spectrum of the waves generated. Figure 8-4 c shows the loading of three nodes spaced at 0.4 m intervals, showing that the force varies according to Equation 4-11 in all nodes. Figure 8-4 b shows that frequencies of 0 to 1000 Hz are generated. These have a ratio of greater than 1:10 between the maximum mesh size and the minimum wavelength for a 1000 Hz wave, which is necessary to allow the model to accurately model the transmission of waves and reduce numerical dispersion for a 2nd order numerical scheme such as that used by UDEC. Figure 8-4 d shows the frequency spectrum of the stresses in a UDEC model induced due to the loading in Figure 8-4 a. This shows that the displacement response has a similar distribution of frequencies as the input load, given by Figure 8-4 b, meaning that the model is seeing the correct distribution of frequencies.

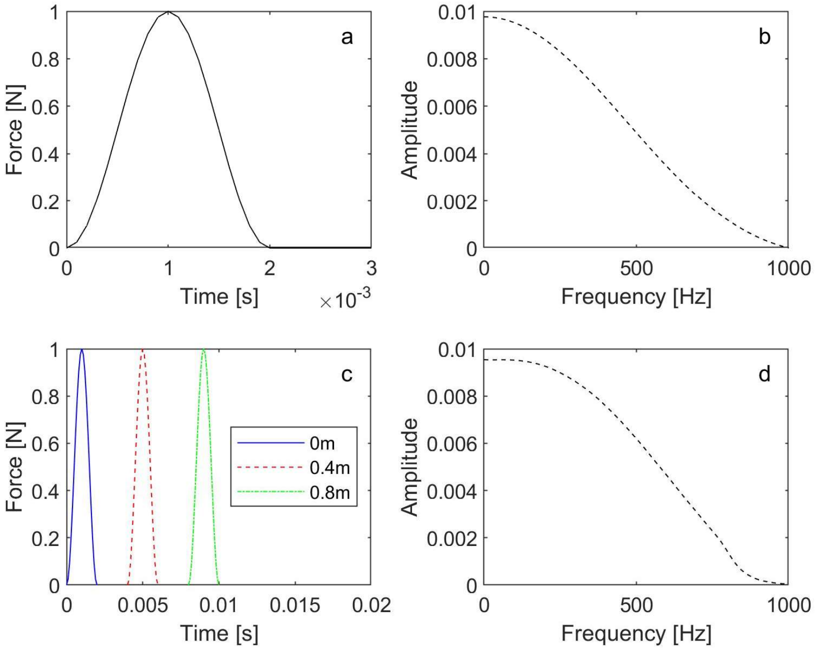

Figure 8-4 a) Time series of force input function at a single node; b) Frequency spectrum of force input function in 4 a; c) Time series of force input function at nodes located at 0, 0.4 and 0.8 m; d) Frequency spectrum of UDEC stress response to loading in 4 a

Vertical displacement histories are recorded at the same location in each model, which are indicated in Figure 8-2 with crosses within circles on the symmetry line. Near field displacements are recorded at the centre of the "Loading Line", with the far field displacements being recorded 10 m above this. These monitoring points are located so that they record the load both moving towards and away from them. The maximum absolute displacement recorded at any time in the model at the measurement point is taken as the displacement. Where possible, joints are generated so that the measurement points are not placed on joints. This is because this section is concerned with the movement of blocks and not the opening and closing of joints, which may show a different displacement to that of the intact blocks. All displacements therefore refer to the displacement of the block and any reference to joints in connection with the displacement are the displacement of the blocks between the joints. This is not to be confused with the opening and closing on the joints themselves, although in reality this will be connected.

8.2.2. Model Properties

The models used are linear elastic, preventing failure from occurring. In all the discontinuum models a single joint set is modelled; therefore, all discontinuum models behave as transversely isotropic materials. These are characterised as having two different stiffnesses, with the out of plane stiffness equal to the stiffness in one of the in-plane directions. Joints reduce the stiffness of the model normal to the joint plane; therefore, the plane of isotropy in the transversely isotropic material runs parallel to the joints (Figure 8-5). For the joint orientations given in Figure 8-3 a, the plane of isotropy is equal to the joint angle.

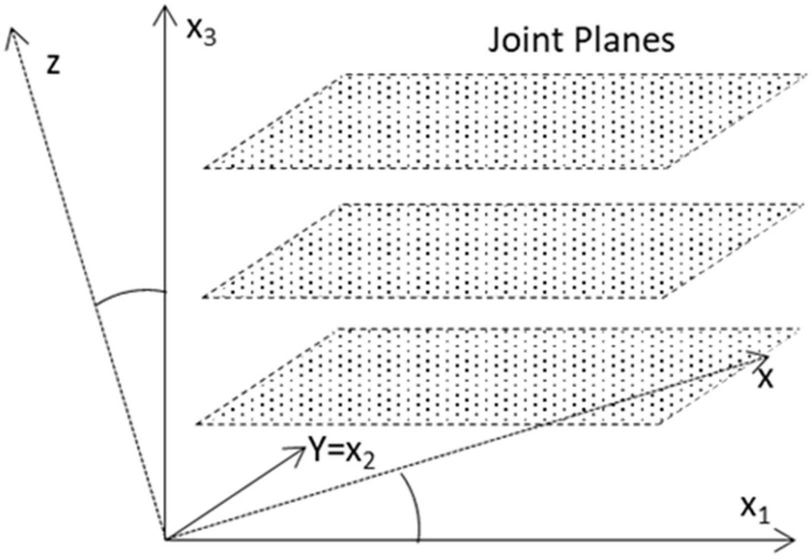

Figure 8-5 Axes notation for transversely isotropic axes (x_i, i=1,2,3) with relation to joints and modelling axes (x, y, z). Plane of isotropy in i=1,2

The different coordinate directions are given by Figure 8-5. The plane of isotropy is in *i*=1,2. Transversely isotropic axes do not need to align with the model axes; however, the joint orientations rotate around the y-axis, so in all cases in this section y=x_2.

The difference in stiffness is brought about by the parallel jointing which acts to reduce the elastic stiffness perpendicular to the plane of isotropy (E_3) and the cross shear modulus between plane of isotropy and anisotropic plane (G_{13}), given by Equation 8-1 and Equation 8-2. These are identical to Equations 3-2 and 3-3, with terms altered to be related to the axes in Figure 8-5.

$$\frac{1}{E_3} = \frac{1}{E_1} + \frac{1}{sk_n}$$ Equation 8-1

$$\frac{1}{G_{13}} = \frac{1}{G_{12}} + \frac{1}{sk_s}$$ Equation 8-2

Where E_3=stiffness perpendicular to plane of isotropy, E_1=stiffness in plane of isotropy, s=joint spacing, k_n=joint normal stiffness, k_s=joint shear stiffness.

A transversely isotropic model is characterised as having five independent elastic material constants which are calculated from the discontinuum properties using Equation 8-1 and Equation 8-2 (Itasca Consulting Group Inc., 2014). Further assumptions considered in the elastic constants are given by Equation 8-3 to Equation 8-6.

$$E_1 = E_3$$ Equation 8-3

$$v_{13} = v_{31} \frac{E_1}{E_3}$$ Equation 8-4

$$v_{12} = v_{21}$$ Equation 8-5

$$v_{13} = v_{23}$$ Equation 8-6

Where v_{13}=Poisson's ratio between x_1 and x_3, v_{12}=Poisson's ratio in plane of isotropy.

All of the analyses are run as being elastic and do not assess failure of the rock mass. The intact blocks in the discontinuum models and the entire isotropic continuum model use the same properties, shown in Table 8-1. Table 8-2 gives the transversely isotropic continuum properties of the rock mass composed of the intact block and joint properties in Table 8-1, derived using Equation 8-1 and Equation 8-2. All models in this study are analysed as perfectly elastic, which is a reasonable assumption for the small degrees of strain which occur due to the loads applied in the model, and indeed realistic strains induced by railway vibrations (Connolly et al., 2014; Ruiz et al., 2019). The properties for the intact blocks are Basalt from UDEC's inbuilt property database. These are chosen as they have a high stiffness which will give large wavelengths for even high frequency waves, allowing a less dense mesh to be modelled and still allowing accurate modelling of the possible waves generated in the model.

Table 8-1 Intact block and joint properties (unless stated on Figures) used in discontinuum and isotropic continuum models

Property	Value
Block Elastic Stiffness – (E_1)	34.9 GPa
Block Shear Modulus – (G_{12})	13.2 GPa
Poisson's Ratio – (ν_{12})	0.320
Block Density	2700 kg/m^3
Damping Factor	5%
Joint spacing	2 m
Joint normal stiffness (k_n)	1 GPa/m
Joint shear stiffness (k_s)	1 GPa/m

Table 8-2 Transversely isotropic continuum models

Property	Value
Elastic Stiffness – (E_1)	34.9 GPa
Elastic Stiffness – (E_3)	1.9 GPa
Shear Modulus – (G_{13})	1.7 GPa
Poisson's Ratio – (ν_{12})	0.320
Poisson's Ratio – (ν_{13})	0.017
Density – Block	2700 kg/m^3
Damping Factor	5%

Material damping in all models is set to 5% and implemented using the local damping option in UDEC (Itasca Consulting Group Inc., 2014). Local damping provides a reasonable estimate of the damping of a dynamic problem and gives a shorter computation time than the more realistic Rayleigh damping. The systematic error, which this assumption will introduce, will not affect the comparison between the results. A 5% damping factor is modelled following the approach of Eitzenberger (2012). This is a different approach to those used in the previous 2D Chapters in this thesis. This is justified as in this case a transfer function is not being generated, and instead the distribution of the wave front is of concern.

A parametric analysis is undertaken which alters individual properties of the joints in the discontinuum to study their effects on the displacement results. The models which are run are detailed in Table 8-3. All anisotropic models are run using both discontinuum and equivalent transversely isotropic continuum methods. This list is not a continuation of the case numbers in Section 4.6.3.

Table 8-3 Models analysed in study. Equivalent stiffness properties shows the combined effect of joints and intact block properties in the discontinuum analyses, with the intact block stiffness properties being shown in Table 8-1. Cont. = continuum; Discont. = discontinuum

Case	**Model Type**	**Material Type**	**Joint/Plane of Isotropy Angles**	**Joint Stiffness**	**Joint Spacing**	**Equivalent Stiffness Properties**			**Figures**
						E_1	**E_2**	**E_3**	
1	Discont.	Anisotropic	0,45,90,135,180°	1GPa/m	10m	34.9GPa	34.9GPa	7.8GPa	13-14
2	Cont.	Anisotropic	0,45,90,135,180°	-	-	34.9GPa	34.9GPa	7.8GPa	13-14
3	Discont.	Anisotropic	0,45,90,135,180°	1GPa/m	4m	34.9GPa	34.9GPa	3.6GPa	13-14
4	Cont.	Anisotropic	0,45,90,135,180°	-	-	34.9GPa	34.9GPa	3.6GPa	13-14
5	Discont.	Anisotropic	0,45,90,135,180°	1GPa/m	2m	34.9GPa	34.9GPa	1.9GPa	6-8, 10-18
6	Cont.	Anisotropic	0,45,90,135,180°	-	-	34.9GPa	34.9GPa	1.9GPa	6-8, 10-18
7	Discont.	Anisotropic	0,45,90,135,180°	0.5GPa/m	4m	34.9GPa	34.9GPa	1.9GPa	10-12
8	Discont.	Anisotropic	0,45,90,135,180°	0.2GPa/m	10m	34.9GPa	34.9GPa	1.9GPa	10-12
9	Discont.	Anisotropic	0,45,90,135,180°	0.5GPa/m	2m	34.9GPa	34.9GPa	0.9GPa	16-18
10	Cont.	Anisotropic	0,45,90,135,180°	-	-	34.9GPa	34.9GPa	0.9GPa	16-18
11	Discont.	Anisotropic	0,45,90,135,180°	0.2GPa/m	2m	34.9GPa	34.9GPa	0.4GPa	16-18
12	Cont.	Anisotropic	0,45,90,135,180°	-	-	34.9GPa	34.9GPa	0.4GPa	16-18
13	Cont.	Isotropic	-	-	-	34.9GPa	34.9GPa	34.9GPa	6-9
14	Cont.	Anisotropic	0,180°	-	-	1.9GPa	1.9GPa	34.9GPa	9

8.2.3. Results

This section presents the detailed results for all modelling scenarios given in Table 8-3. The analysis is split into: the comparison between different model types (Cases 5, 6, 13, 14); the comparison between different discontinuum and continuum models which have the same equivalent stiffness properties (Cases 5, 6, 7, 8); a parametric analysis of the effect of joint spacing on discontinuum displacement (Cases 1, 2, 3, 4, 5, 6); and a parametric analysis of the effect of joint stiffness on discontinuum displacement (Cases 5, 6, 9, 10, 11, 12).

8.2.3.1. Comparison of Equivalent Anisotropic Models and an Isotropic Continuum Models

The modelling results in this subsection describe how the different material models perform in relation to each other. The models include a discontinuum model and a transversely isotropic continuum model with the same equivalent stiffness, as well as an isotropic continuum model with the properties used in the intact blocks of the discontinuum model. Figure 8-6 shows the near field displacement results, recorded in the centre of the "Loading Line" (Figure 8-2). The key observations from Figure 8-6 are:

- The discontinuum has a greater displacement response than the continuum models;
- The discontinuum has a minimum when joints are vertical (90°);
- In the discontinuum the 135° model shows more displacement than the 45° model, with the horizontal (0/180°) model being at an intermediate value between these;
- The transversely isotropic continuum is symmetrical about a vertical plane of isotropy (90°), which represents its maximum value, with minima when the plane of isotropy is horizontal (0/180°);
- The isotropic continuum has a lower displacement than the transversely isotropic continuum model except when the plane of isotropy is horizontal (0/180°), where the isotropic continuum has a greater displacement.

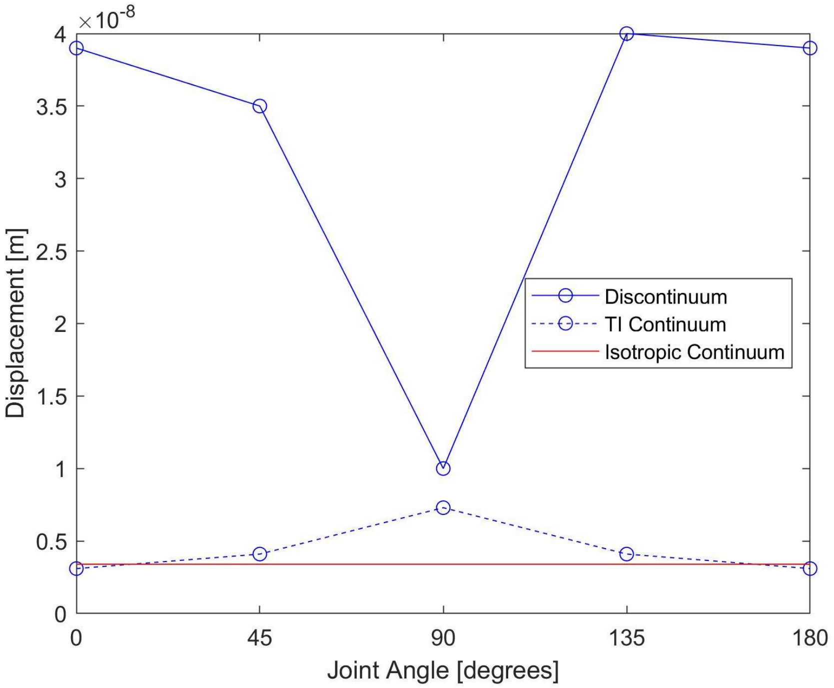

Figure 8-6 Near field vertical displacement of model due to moving point load modelled in a discontinuum (Case 5), equivalent transversely isotropic (TI) continuum (Case 6) and isotropic continuum (Case 13) models. Joint angle ≡ angle of plane of isotropy. Measured at a vertical offset of 0 m from "Loading Line"

Figure 8-7 shows the far field displacement results, recorded 10 m above the "Loading Line" (Figure 8-2). The key observations from Figure 8-7 are:

- The discontinuum has a greater displacement response than the continuum models, like in the near field;
- The discontinuum has a maximum when joints are vertical (90°), unlike in the near field;
- In the discontinuum the 135° model shows more displacement than the 45° model, like in the near field;
- The discontinuum has a minimum when joints are horizontal (0/180°), unlike in the near field;

- The transversely isotropic continuum is symmetrical about a vertical plane of isotropy (90°), which represents its maximum value, with minima when the plane of isotropy is horizontal (0/180°), like in the near field;
- The isotropic continuum has a lower displacement than the transversely isotropic continuum model except when the plane of isotropy is horizontal (0/180°), where both models have the same response, like in the near field.

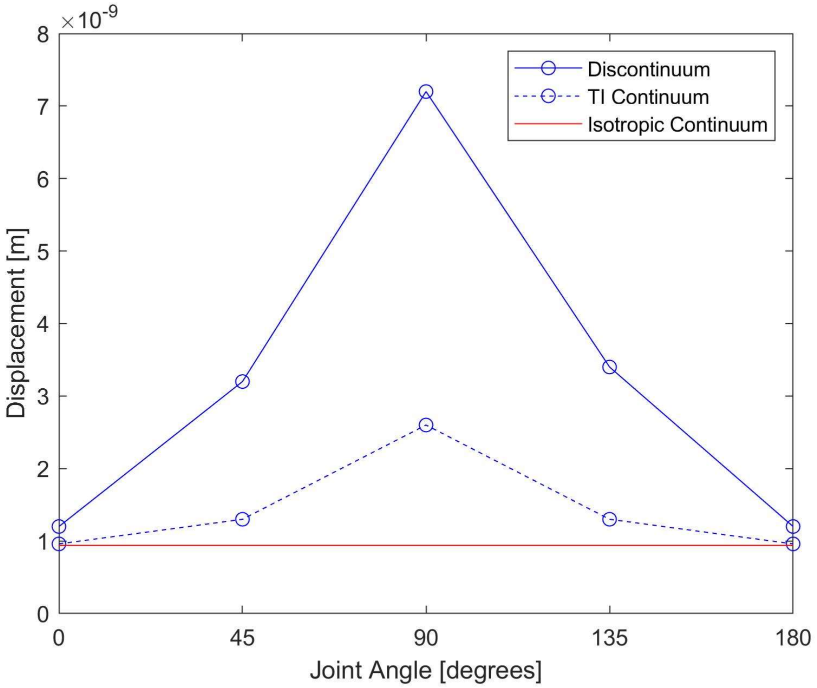

Figure 8-7 Far field vertical displacement of model due to moving point load modelled in a discontinuum (Case 5), equivalent transversely isotropic (TI) continuum (Case 6) and isotropic continuum (Case 13) models. Joint angle ≡ angle of plane of isotropy. Measured at a vertical offset of 10 m from "Loading Line"

Figure 8-8 shows the displacement contours for the models shown in this section after 0.2 s, which is when the moving load had reached the end of the "Loading Line". The displacement at the measurement locations shown may not be the same as the displacements shown in Figure 8-6 and Figure 8-7, as Figure 8-8 only shows a snapshot of the displacement of the model and the previous Figures show the maximum displacement recorded at the measurement locations at any time during modelling. As the models are elastic, there is a linear relationship between stress and displacement. Therefore, the displacements in Figure 8-8 can be thought of as a proxy for the stresses in the model. The key observations from Figure 8-8 are:

- The continuum models, whether they are transversely isotropic or isotropic, give displacement patterns which are symmetrical about the "Loading Line";
- In the transversely isotropic continuum models, the zone of peak displacement becomes elongated vertically when the plane of isotropy is orientated vertically (90°), while a horizontal plane of isotropy does not affect the horizontal spread of the displacement;

- When the plane of isotropy is orientated horizontally the displacement pattern is almost identical to the isotropic case, shown by Figure 8-8 j;
- The discontinuum models show greater displacement being concentrated underneath the "Loading Line", in comparison to the continuum models. This is with the exception of vertical (90°) joints which have more energy transferred upwards. Energy is being transferred downwards in most of these models due to the loading being applied vertically downwards to the model;
- The dipped joints (45 and 135°) show that energy is transferred along intact blocks, with 45° joints transferring energy downwards opposite the direction of travel of the load and upwards in the direction of travel of the load. The opposite pattern occurs with the 135° joints in Figure 8-8 f. The same trends are not observed in their equivalent continuum models, shown by Figure 8-8 c and Figure 8-8 e, which show identical displacement patterns for both 45 and 135° planes of isotropy.

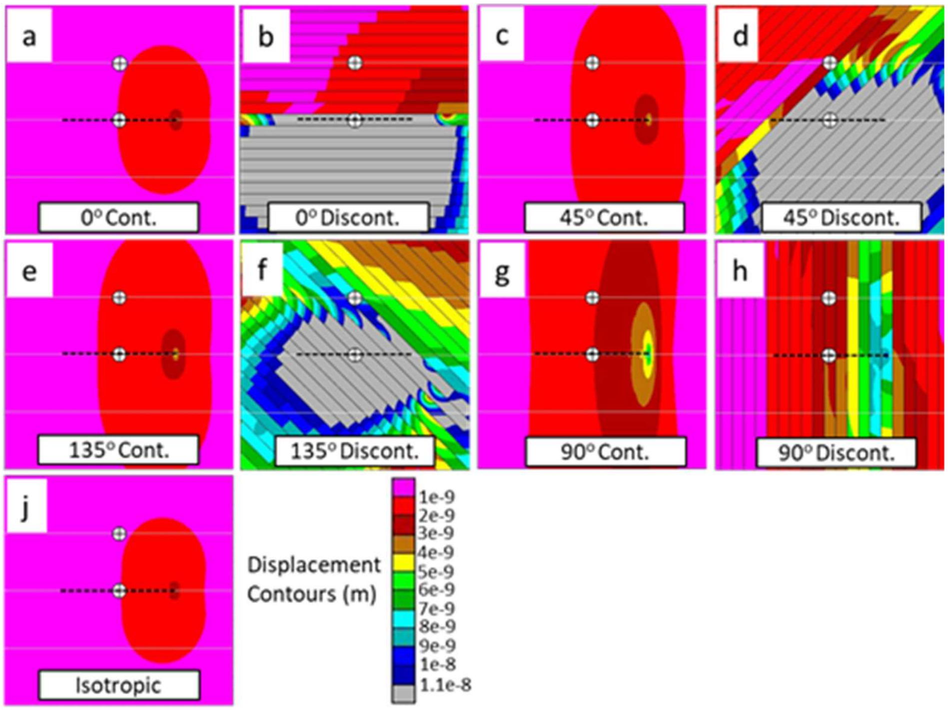

Figure 8-8 Contours of vertical displacement (m) of model after 0.2 s. a,c,e,g = transversely isotropic continuum; b, d, f, h = discontinuum; j = isotropic continuum; black lines = joints; white lines = construction lines for mesh; crossed circles = measurement locations; black dashed line = Loading Line (20 m)

When the transversely isotropic continuum models are considered in isolation Figure 8-6 and Figure 8-7 show that as the vertical stiffness of the model increases the vertical displacement increases. This is a different outcome to the studies of Rieckh et al. (2012) and Ba et al. (2019) where they found that increasing the vertical stiffness results in a reduction in the vertical displacement. The model used in this study is fundamentally different from those of Rieckh et al. (2012) and Ba et al. (2019). Firstly, in the previously mentioned studies the angle of the plane of isotropy is always horizontal (0 or 180°). The ratio of horizontal (E_h) to vertical stiffness (E_v) is altered by changing the properties of the relative directions, while in this study the in-plane stiffness is varied by changing the angle of the plane of isotropy. This has the result that the out of plane horizontal stiffness is always high. Secondly, previous studies model the transversely isotropic material as being located directly below a free surface. Finally, the tunnel loading in Rieckh et al. (2012) is applied to an isotropic layer, with transversely isotropic properties applied to a layer above this. Any of these effects could cause the differences observed. To eliminate one possible cause, the E_h:E_v ratio, Figure 8-9 is generated. The stiffnesses used in the models for Figure 8-9 are implemented in the same way as Rieckh et al. (2012) and Ba et al. (2019), with the angle of the plane of isotropy kept at 0°. Case 14 is generated for this sensitivity analysis. Figure 8-9 shows the same trend of results as Figure 8-6 and Figure 8-7, with an increasing vertical stiffness leading to a reduction in the vertical displacement. This implies that the differing relationship between E_h:E_v found in this study and in literature is due to the model confinement and the position of the load, rather than effects relating to the out of plane material stiffness.

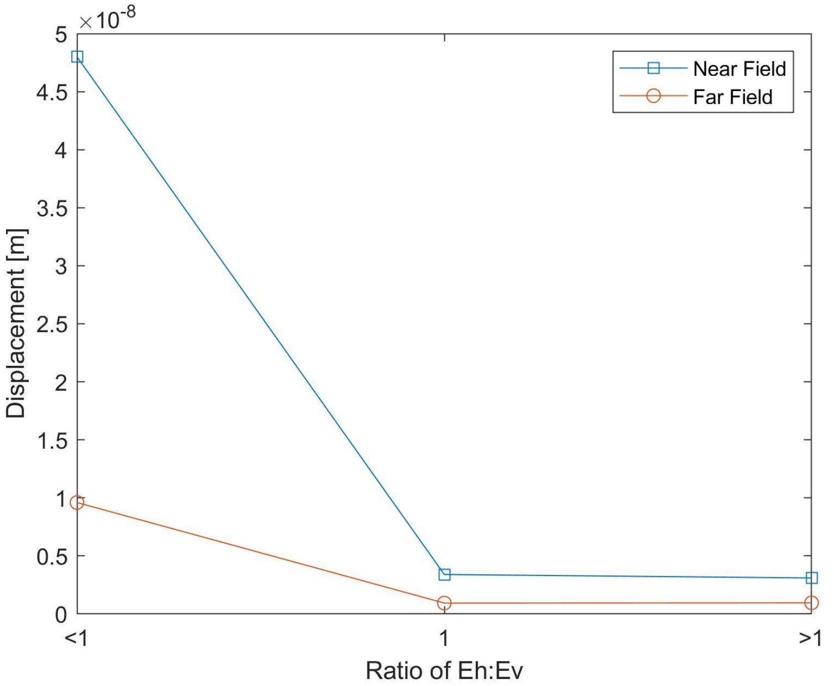

Figure 8-9 Vertical displacement of model due to moving point load modelled in a Transversely Isotropic continuum with a changing vertical (E_h) to horizontal (E_v) stiffness ratio (E_h:E_h). Angle of plane of isotropy = 0°

8.2.3.2. Equivalent Discontinuum Models

The modelling results in this section show different discontinuum models, which have the same overall transversely isotropic properties. Using Equation 8-1 and Equation 8-2 the joint spacing is changed and the joint stiffness modified to compensate. The combinations of joint spacing and stiffness modelled in this section are: i) 2 m / 1 GPa/m (Case 5), as modelled in section 4.1; ii) 4 m / 0.5 GPa/m (Case 7), and iii) 10 m / 0.2 GPa/m (Case 8). The transversely isotropic results shown in Figure 8-10 and Figure 8-11 are the same as those shown in Figure 8-6 and Figure 8-7 (Case 6). Figure 8-10 shows the near field displacement results, recorded in the centre of the "Loading Line" (Figure 8-2). The key observations from Figure 8-10 are:

- All discontinuum models have a minimum when joints are vertical (90^o), as also observed in Figure 8-6;
- Increasing the joint spacing / decreasing the joint stiffness leads to a reduction in displacement;
- Increasing the joint spacing / decreasing the joint stiffness reduces the effect of the joint angle on modifying displacements, with a smaller difference between the minimum displacement and maximum displacement;
- The difference between the 45 and 135^o joints reduces as the joint spacing increases / joint stiffness decreases;
- When the plane of isotropy is vertical (90^o) the transversely isotropic continuum shows a greater displacement than the 10 m spacing discontinuum and equal displacement as the 4 m spacing discontinuum when joints are orientated vertically.

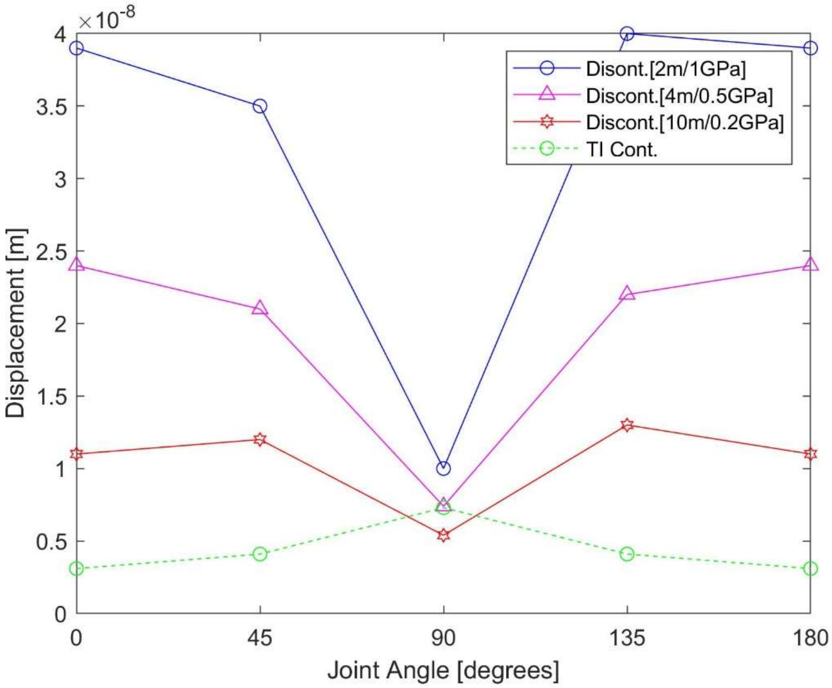

Figure 8-10 Near field vertical displacement of model due to moving point load in discontinuum models of the same rock mass stiffness but different joint spacing and stiffness (Cases 5, 7, 8). Legend shows joint spacing (m) and joint stiffness (GPa/m). Equivalent transversely isotropic continuum results are included (TI Cont.) (Case 6). Measured at a vertical offset of 0 m from "Loading Line"

Figure 8-11 shows the far field displacement results, recorded in the centre of the "Loading Line" (Figure 8-2). The key observations from Figure 8-11 are:

- Vertical joints (90°) do not always represent maximum displacements, unlike in Figure 8-7;
- For vertical (90°) and horizontal (0/180°) joints, increasing the joint spacing / decreasing the joint stiffness leads to a reduction in displacement, like in Figure 8-10;
- For 45° joints increasing the joint spacing / decreasing the joint stiffness leads to an increase in displacement, the opposite of the trend in the near field (Figure 8-10);
- For 135° joints increasing the joint spacing / decreasing the joint stiffness has a non-linear relationship with displacement, with 2 m spacing being the minimum, 4 m spacing the maximum and 10 m spacing an intermediate value. This is different to the 45° joints;
- When the plane of isotropy is horizontal (0/180°) the transversely isotropic continuum displacement is greater than the 4 m spacing and 10 m spacing discontinuum models.

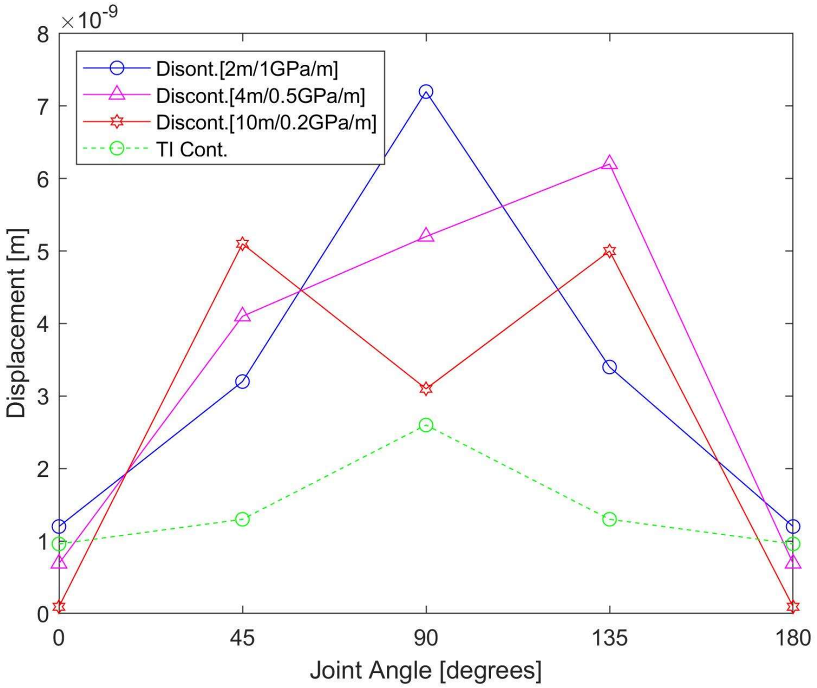

Figure 8-11 Far field vertical displacement of model due to moving point load in discontinuum models of the same rock mass stiffness but different joint spacing and stiffness (Cases 5, 7, 8). Legend shows joint spacing (m) and joint stiffness (GPa/m). Equivalent transversely isotropic continuum results are included (TI Cont.) (Case 6). Measured at a vertical offset of 10 m from "Loading Line"

Figure 8-12 shows the displacement contours for the models shown in this section after 0.2 s, which is when the moving load had reached the end of the "Loading Line". The results in the third column for the 2 m spacing / 1 GPa/m model are identical to those in Figure 8-8. The equivalent transversely isotropic continuum results for all models are shown in Figure 8-8. Figure 8-12 confirms the results found in Figure 8-10 and Figure 8-11, although it does not indicate mechanisms for the unexpected trends in the far field for 45 and 135° joints. The key observations from Figure 8-12 are:

- Reducing the joint stiffness reduces the amount of energy which can be transmitted away from blocks which are not directly influenced by the loading. For example, Figure

8-12 a shows little displacement above the joint directly above the “Loading Line”, with Figure 8-12 b showing more displacement above the equivalent joint and Figure 8-12 c more again;

- The displacement pattern of each discontinuum model is quite different, despite all being equivalent.

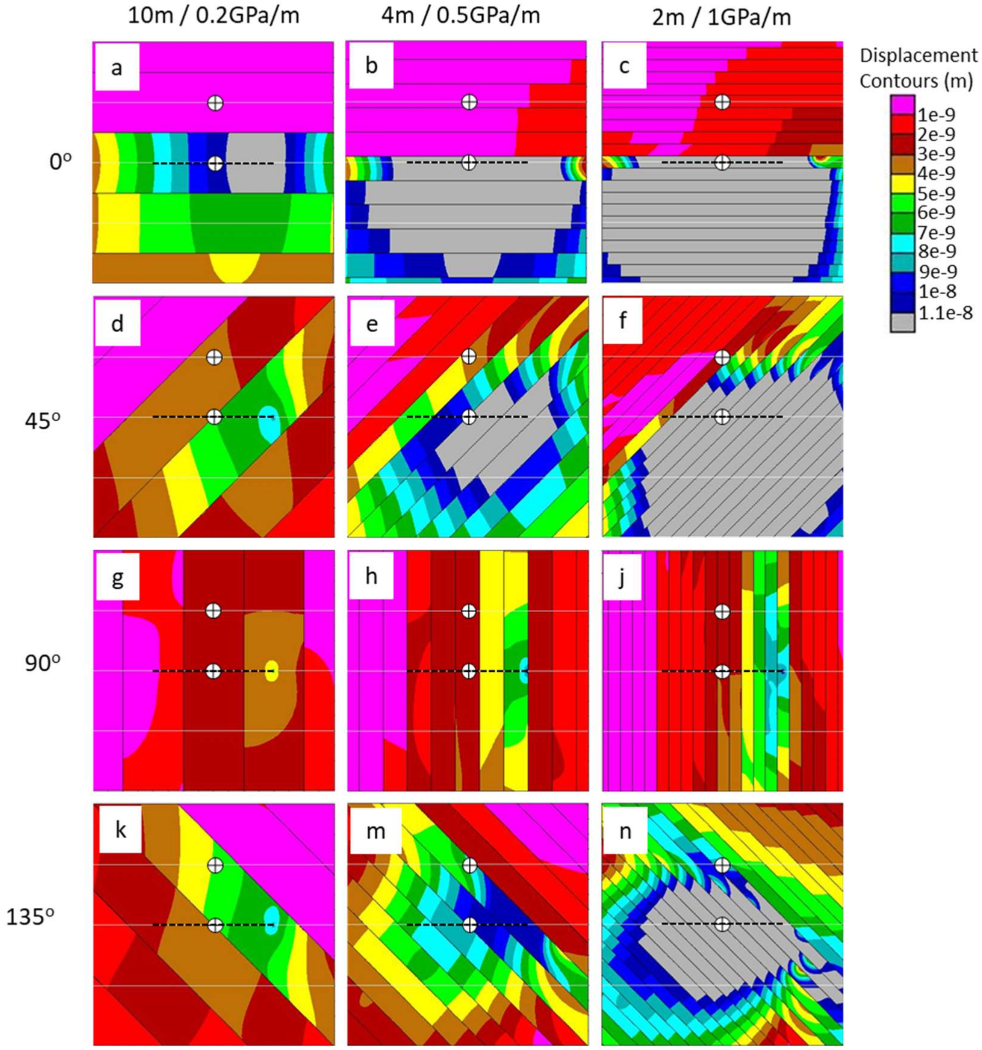

Figure 8-12 Contours of vertical displacement (m) of equivalent discontinuum models after 0.2 s. Black lines = joints; white lines = construction lines for mesh; crossed circles = measurement locations (lower = near field, upper = far field); black dashed line = Loading Line (20 m). Joint spacing (m) and joint stiffness (GPa/m) for columns, joint angle shown for rows

8.2.3.3. *Effect of Changing Joint Spacing*

The modelling results in this section show the effect of changing the joint spacing on the displacement response of discontinuum and transversely isotropic continuum models. All models in Figure 8-13 to Figure 8-15 have the same joint stiffness, so changing the joint spacing leads to different equivalent transversely isotropic continuum properties, which are also modelled. The joint spacings modelled are 2, 4 and 10 m, as modelled in the previous subsection, with a constant joint stiffness of 1 GPa/m, as modelled in the subsection previous to that (Cases 1, 3, 5). Bespoke modelling properties for each transversely isotropic continuum are calculated using Equation 8-1 and Equation 8-2 (Cases 2, 4, 6). Figure 8-13 shows the near field displacement results, recorded in the centre of the "Loading Line" (Figure 8-2). The key observations from Figure 8-13 are:

- All discontinuum models have a minimum when joints are vertical (90°), like observed in Figure 8-6 and Figure 8-10;
- Increasing the joint spacing leads to a reduction in displacement, like in Figure 8-10;
- Increasing the joint spacing reduces the effect of the joint angle on modifying displacements, with a smaller difference between the minimum displacement and maximum displacement, like observed in Figure 8-10;
- The difference between 45 and 135° joints reduces as the joint spacing increases, like observed in Figure 8-10;
- The transversely isotropic continuum always shows less displacement than their equivalent discontinuum models, which is different to the observations in Figure 8-10;
- When the plane of isotropy is horizontal (0/180°) all transversely isotropic continua show the same displacement.

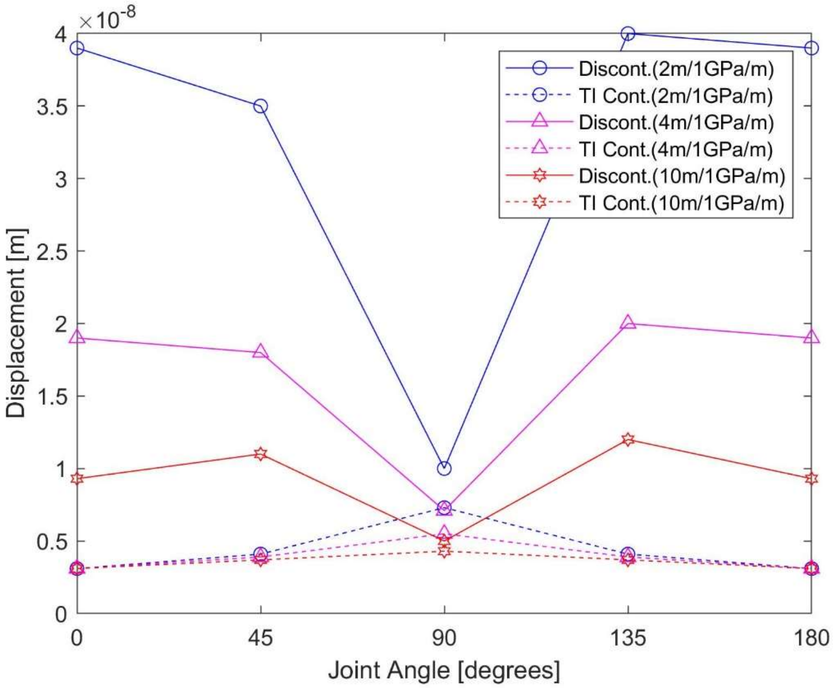

Figure 8-13 Near field vertical displacement of model due to moving point load with different joint spacing modelled as a discontinuum (Cases 1, 3, 5). Legend shows joint spacing (m) and joint stiffness (GPa/m). Equivalent transversely isotropic continuum results are included (TI Cont.) (Cases 2, 4, 6). Measured at a vertical offset of 0 m from "Loading Line"

Figure 8-14 shows the far field displacement results, recorded in the centre of the "Loading Line" (Figure 8-2). The key observations from Figure 8-14 are:

- Vertical joints (90°) do not always represent maximum displacements, like in Figure 8-11;
- For vertical (90°) and horizontal (0/180°) joints, increasing the joint spacing leads to a reduction in displacement, like in Figure 8-11;
- For 45° joints, increasing the joint spacing leads to an increase in displacement, like in Figure 8-11;
- For 135° joints, increasing the joint spacing has a non-linear relationship with displacement, as observed in Figure 8-11;
- When the plane of isotropy is horizontal (0/180°) the transversely isotropic continuum displacement is greater than the 4 m spacing and 10 m spacing discontinuum models;
- When the plane of isotropy is horizontal (0/180°) all transversely isotropic continua show the same displacement, like in Figure 8-13.

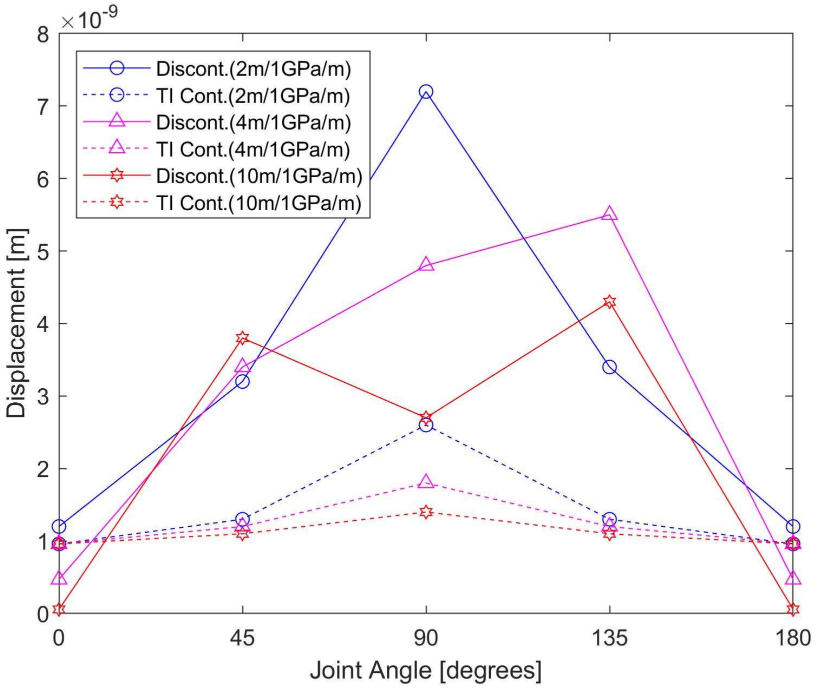

Figure 8-14 Far field vertical displacement of model due to moving point load with different joint spacing modelled as a discontinuum (Cases 1, 3, 5). Legend shows joint spacing (m) and joint stiffness (GPa/m). Equivalent transversely isotropic continuum results are included (TI Cont.) (Cases 2, 4, 6). Measured at a vertical offset of 10 m from "Loading Line"

Figure 8-15 shows the displacement contours for the models shown in this section after 0.2 s, which is when the moving load had reached the end of the "Loading Line". The results in the third column for the 2 m spacing / 1 GPa/m model are identical to those in Figure 8-8. The key observations from Figure 8-15 are:

- The displacements in the first two columns are lower than in the first two columns of Figure 8-12;

- There is less displacement above the first joint above the "Loading Line" in Figure 8-15 b than in Figure 8-12 b;
- Comparing the 45° joint results in Figure 8-12 and Figure 8-15 indicate that the higher joint stiffnesses in Figure 8-15 allow less energy to be transmitted into blocks which are not directly loaded by the loading source. This can be seen by comparing the top left of Figure 8-12 e and Figure 8-15 e. However, at 135° the opposite appears to be true, which can be seen by comparing in Figure 8-12 m and Figure 8-15 m;
- When comparing the vertical (90°) joints in in Figure 8-12 and Figure 8-15 the results seem to be similar.

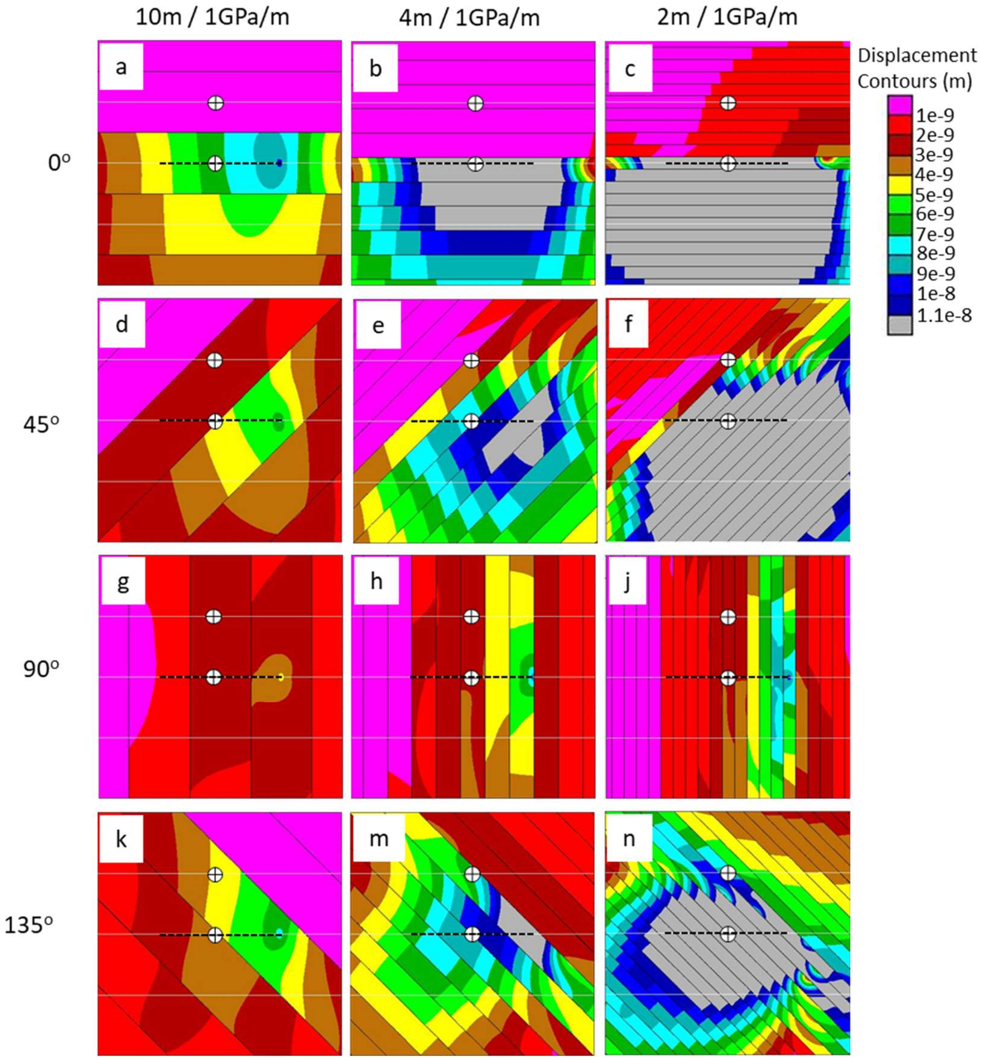

Figure 8-15 Contours of vertical displacement (m) of changing joint spacing in discontinuum models after 0.2 s. Black lines = joints; white lines = construction lines for mesh; crossed circles = measurement locations (lower = near field, upper = far field); black dashed line = Loading Line (20 m). Joint spacing (m) and joint stiffness (GPa/m) for columns, joint angle shown for rows

8.2.3.4. *Effect of Changing Joint Stiffness*

The modelling results in this section show the effect of changing the joint stiffness on the displacement response of discontinuum and transversely isotropic continuum models. All models in Figure 8-16 to Figure 8-18 have the same joint spacing, so changing the joint stiffness leads to different equivalent transversely isotropic continuum properties, which are also modelled. The joint stiffnesses modelled are 0.2, 0.5 and 1 GPa/m, as modelled in section 4.2, with a constant joint spacing of 2 m, as modelled in section 4.1 (Cases 5, 9, 11). Bespoke modelling properties for each transversely isotropic continuum are calculated using Equations 8-1 to 8-3 (Cases 6, 10, 12). Figure 8-16 shows the near field displacement results, recorded in the centre of the "Loading Line" (Figure 8-2). The key observations from Figure 8-16 are:

- All discontinuum models have a minimum when joints are vertical (90^o), as observed in Figure 8-6, Figure 8-10 and Figure 8-13;
- Decreasing the joint stiffness leads to an increase in displacement, the opposite of Figure 8-10;
- Decreasing the joint stiffness causes the relative displacement magnitude of the 45^o and 135^o joints to change. At a joint stiffness of 0.2 GPa/m the 45^o joint shows more displacement than the 135^o joint. At a joint stiffness of 1 GPa/m the 135^o joint shows more displacement than the 45^o joint, while for the intermediate joint stiffness of 0.5 GPa/m the two joint angles are similar. This effect is not observed in Figure 8-10;
- When the plane of isotropy is vertical (90^o) the transversely isotropic continuum shows greater displacement than the equivalent discontinuum when the joint stiffness is low (0.2 GPa/m), with similar results at 0.5 GPa/m and less displacement at 1 GPa/m. The same trend can be observed in Figure 8-10;
- When the plane of isotropy is horizontal (0/180^o) all transversely isotropic continua show the same displacement, like in Figure 8-13 and Figure 8-14.

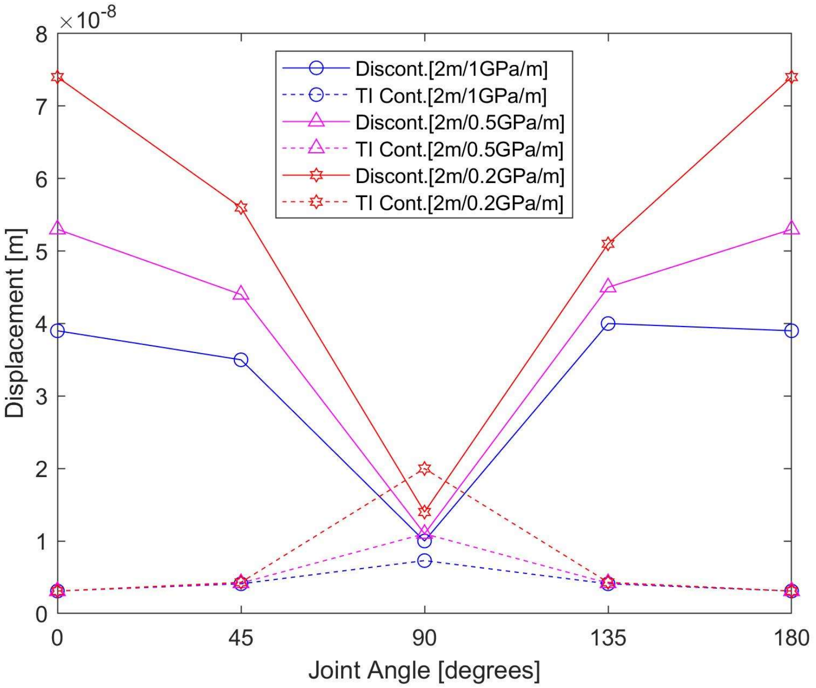

Figure 8-16 Near field vertical displacement of model due to moving point load with different joint stiffness modelled as a discontinuum (Cases 5, 9, 11). Legend shows joint spacing (m) and joint stiffness (GPa/m). Equivalent transversely isotropic continuum results are included (TI Cont.) (Cases 6, 10, 12). Measured at a vertical offset of 0 m from "Loading Line"

Figure 8-17 shows the far field displacement results, recorded in the centre of the "Loading Line" (Figure 8-2). The key observations from Figure 8-17 are:

- Vertical joints (90^o) always represent maximum displacements, unlike in Figure 8-11;
- For vertical (90^o), horizontal (0/180^o) and 45^o joints increasing the joint stiffness leads to a reduction in displacement. This is the same trend as observed in Figure 8-11 for vertical and horizontal joints, but not for the 45^o joints;
- For 135^o joints increasing the joint stiffness increases displacement, while the same angle in Figure 8-11 had a non-linear relationship with displacement;
- The displacement of the transversely isotropic continuum is always less than the displacement of the equivalent discontinuum;
- When the plane of isotropy is horizontal (0/180^o) all transversely isotropic continua show the same displacement, like in Figure 8-13, Figure 8-14 and Figure 8-16.

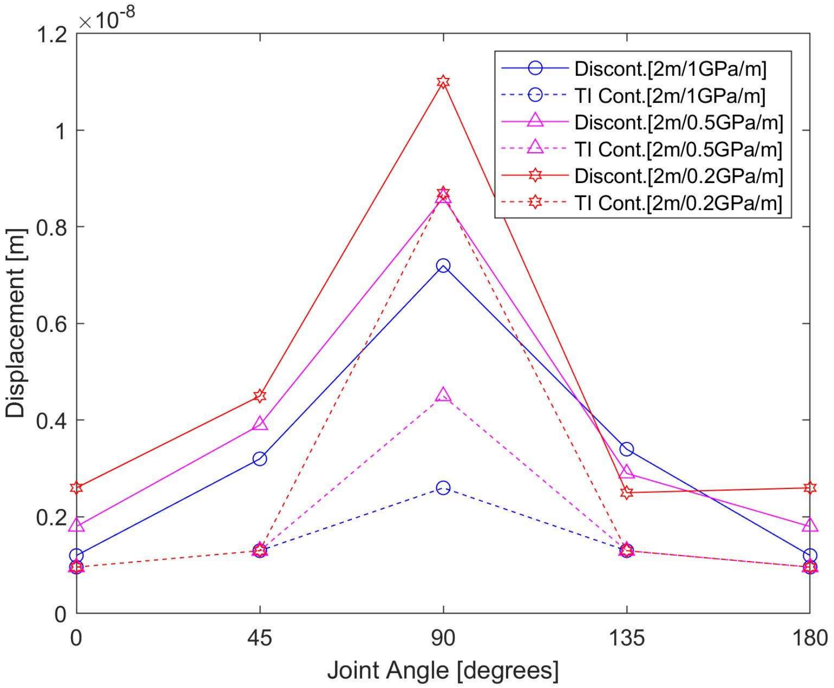

Figure 8-17 Far field vertical displacement of model due to moving point load with different joint stiffness modelled as a discontinuum (Cases 5, 9, 11). Legend shows joint spacing (m) and joint stiffness (GPa/m). Equivalent transversely isotropic continuum results are included (TI Cont.) (Cases 6, 10, 12). Measured at a vertical offset of 10 m from "Loading Line"

Figure 8-18 shows the displacement contours for the models shown in this section after 0.2 s, which is when the moving load had reached the end of the "Loading Line". The results in the third column for the 2 m spacing / 1 GPa/m model are identical to those in Figure 8-8. The key observations from Figure 8-18 are:

- The displacements in the first two columns are greater than in the first two columns of Figure 8-12 and Figure 8-15;
- When the joint stiffness is reduced there is a greater displacement above the joint directly above the "Loading Line", for the horizontal joints shown by Figure 8-18 a to c.
- When comparing the vertical (90^o) joints in Figure 8-12 and Figure 8-18 the results are hugely different, with the low joint stiffness leading to much greater displacements.

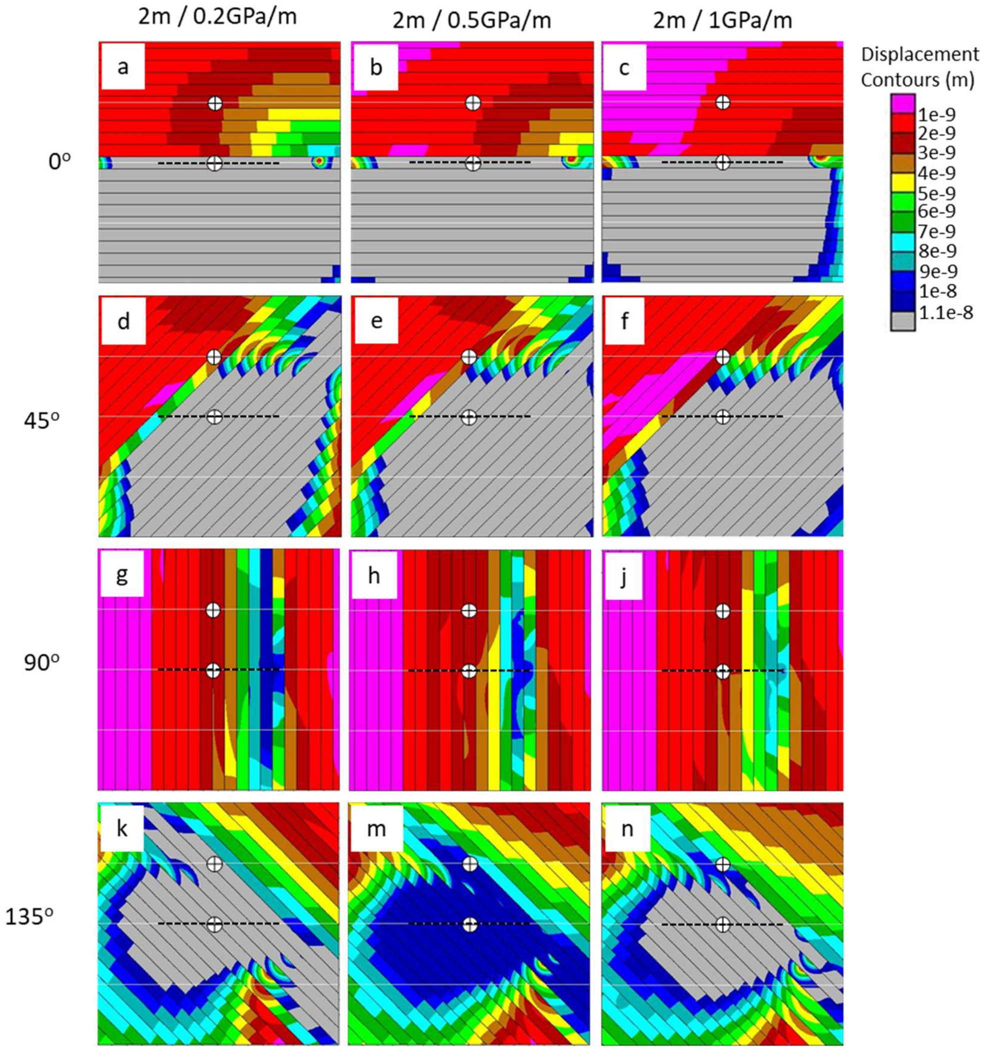

Figure 8-18 Contours of vertical displacement (m) of changing joint stiffness in discontinuum models after 0.2 s. Black lines = joints; white lines = construction lines for mesh; crossed circles = measurement locations (lower = near field, upper = far field); black dashed line = Loading Line (20 m). Joint spacing (m) and joint stiffness (GPa/m) for columns, joint angle shown for rows

8.2.4. Discussion of UDEC Modelling Results

The displacement results shown in Figure 8-6 to Figure 8-18 indicate that minor changes to a model can have significant impacts in the near field and far field displacement response. Even when models are equivalent in terms of overall stiffness, small changes to joint properties or changing the material model can cause significant differences in displacement. These differences are not brought about by inelastic or non-linear behaviour in the discontinuum models, as all models are modelled as linear-elastic, and instead are brought about by localised differences in stiffness around explicit fractures. This is in opposition to the conclusion of Eitzenberger (2012), who suggests that jointed rock masses can be modelled as an equivalent continuum when the joint spacing is small, as this study found that the response in the near and far field is different to a changing joint spacing. This agrees with other findings in this thesis, as the spring resonance effect tends to occur when the joint spacing is smaller than the wavelength of an incident wave.

8.2.4.1. Material Model of Equivalent Rock Masses

Figure 8-6, 8-7, 8-8, 8-10, 8-11 and 8-12 address the effect of analysing equivalent situations using different material models; namely a discontinuum, equivalent transversely isotropic continuum and an isotropic continuum. These Figures show that the discontinuum results typically show greater displacement than continuum results. However, when the joint spacing is large and joint stiffness is low, the near field displacement can reduce sufficiently to be lower in the discontinuum model than the transversely isotropic continuum model. The transversely isotropic continuum results are very similar to the isotropic continuum results when the plane of isotropy is orientated horizontally (0 and 180°), with the difference between the results increasing as the angle of the plane of isotropy approaches a vertical orientation (90°).

Figure 8-12 indicates that the mechanism behind the differences between the discontinuum and continuum models is due to the presence of joints in the discontinuum. When a stress wave, induced by the moving load, is incident upon a joint, some of the energy from this will be transmitted through the joint to the next block while some is reflected. In the near field reflected energy is trapped between joints, which leads to the general increase in displacement across all joint angles. Horizontal joints (0 and 180°) reflect more energy back to the near field, while vertical joints (90°) reflect more energy away from the near field. This can be seen in Figure 8-6 and Figure 8-10 where the horizontal joints show greater displacement than the vertical joints. The intermediate joint angles of 45 and 135° are expected to show less displacement than the horizontal joints as some energy will be reflected away from the near field while some is reflected towards it. This is the case of 45° joints; however, 135° joints show more displacement than the horizontal joints. This is likely to be due to the joint dip angle in relation to the direction of the moving load and represents a physical reason for the difference than a numerical one related to the model set up.

The same effects which cause the difference in displacement in the near field also appears to occur in the far field, albeit with the effect reversed. In Figure 8-7 the horizontal joints (0 and 180°) show the least displacement, with the vertical joints (90°) showing the most. As the horizontal joints trap energy in the near field, energy will be prevented from entering the far field, while vertical joints do not trap as much energy in the near field allowing it to "leak away" into the far field. The intermediate joint angles of 45 and 135° show very similar results in the far field, indicating that they both transmit energy away from the near field to a similar degree.

All the transversely isotropic continuum results, regardless of if they are measured in the near field or far field, show the same trend, with a maximum displacement at 90°. This is in opposition to the trends observed by Ba et al. (2019) and Rieckh et al. (2012), where a high horizontal stiffness leads to a high vertical displacement. Figure 8-9 shows that this is not due to the different out of plane stiffnesses modelled in this research and the previous studies. Therefore, for a deep tunnel the trends identified in this study are expected to be found in practice, where a tunnel is embedded in a transversely isotropic material. When considered in this context the difference in displacement response between the different angles of isotropy can be explained by the different stiffnesses in different directions. When the plane of isotropy is orientated vertically (90°), energy is preferentially transferred vertically, giving a greater displacement in the vertical direction, as shown by Figure 8-8. When the plane of isotropy is horizontal (0 and 180°), the horizontal stiffness is higher than the vertical stiffness, giving a greater horizontal velocity, which prevents energy from being transmitted vertically. It would be expected that the energy will spread out horizontally although Figure 8-8 indicates that this is not the case.

8.2.4.2. Near Field Response of Changing Joint Properties

Figure 8-10, 8-13 and 8-16 show how the near field response is affected by the joint properties and joint angle. The relationships found in the near field are quite clear with increasing stiffness or joint spacing leading to a reduction in displacement. The effect of joint spacing appears to be more significant than joint stiffness. For example, in the case of the equivalent models in Figure 8-10, the increase in spacing, despite a reduction in stiffness, still causes a reduction in displacement. The mechanism behind this is that increasing either the joint stiffness or joint spacing leads to a reduction in the ability of the model to reflect energy back into the near field. This allows energy to escape and reduce the near field displacement response. The same is evident in the different responses of the joint angles, with horizontal joints reflecting more energy back into the near field and giving a greater displacement, while vertical joints allow more energy to escape the near field reducing the displacement.

When near field discontinuum displacements are compared to their equivalent transversely isotropic continuum displacements, a large joint spacing or a low joint stiffness can lead to a discontinuum showing less displacement than the continuum, when the plane of isotropy is orientated vertically (90°). For all other angles of the plane of isotropy the discontinuum shows a greater displacement than its equivalent transversely isotropic continuum.

8.2.4.3. Far field response of changing joint properties

Figure 8-11, Figure 8-14 and Figure 8-17 show how the far field response is affected by the joint properties and joint angle. The relationships between these properties in the far field is more complicated than the near field, with different responses depending on the joint angle. Generally, increasing either the spacing or stiffness of joints causes a reduction in far field displacements. This is only a general trend as there are different trends depending on the joint angle. These are somewhat contradictory if thought of in terms of a static load. With less joints, brought about by a higher joint spacing, less energy will be reflected, while an increase in joint stiffness will also lead to less energy being reflected. It would be expected that this would mean more energy present in the far field to increase the displacement response, although this appears not to be the case. Therefore, it seems likely that the process causing the change in displacement is not a simple case of energy being able to escape the near field. There could be some degree of superposition of incident and reflected waves occurring in the low joint stiffness and low joint spacing models. With more reflective surfaces the possibility of superposition of these waves will increase, which may then lead to greater amplitude waves and an associated greater displacement. This process is similar to the superposition resonance effects observed in 2D models Chapter 6.

A reversal of the previously described trends is observed at 45° when joint spacing is altered (Figure 8-11 and 8-14) and at 135° when only joint stiffness is altered (Figure 8-17). When joint spacing is also altered the trend at 135° becomes non-linear. The mechanism causing this to occur is unclear, although it is likely to be a complex interaction between joint stiffness and joint spacing as well as the joint angle, with some effect of wave superposition.

The transversely isotropic continuum results are not always lower than their equivalent discontinuum. When the plane of isotropy is horizontal (0/180°) large joint spacings can lead to the continuum showing a greater displacement than the equivalent discontinuum. Whereas, in Figure 8-17, altering the joint stiffness does not have the same effect, with discontinuum results always being greater than the equivalent continuum.

8.2.4.4. Effect of moving load direction

The discontinuum results presented in Figure 8-6 to Figure 8-18 show that there is often a difference in the displacement response at 45° and 135° in the same model. These two joint angles are mirror images of each other (Figure 8-3 a), with a 45° jointed model with a left to right moving load being the same geometrically as a 135° jointed model with a right to left moving load. The difference in the responses of the same model for these different joint angles implies that the direction of the moving load can affect the response of a model. It is not always the case that one joint angle shows greater displacement than the other, with the relative magnitude of the displacements being affected by the joint stiffness and joint spacing. However, a general trend is that the 135° jointed model has a greater displacement if joint spacing is modified, with the 45° jointed model showing a greater displacement if the joint stiffness is modified. The same movement direction effects are not observed in any of the continuum models, indicating that this only occurs due to the presence of joints. This suggests that if a train tunnel is constructed in a jointed rock mass it is necessary to model the train loading moving in both directions along the tunnel to ensure the maximum vibration levels are recorded during modelling.

8.2.4.5. Comment on results

This section has examined the effect of joint spacing and stiffness, although there are expected to be some combinations of measurement location, joint spacing and stiffness which will change the trends found. For example, a very high joint stiffness, where no joint is present between the loading location and the tunnel, would be expected to perform very similarly to an isotropic model as there will be a limited influence of joints on the results. Therefore, the stress waves will only have travelled through an isotropic continuum on their way to the measurement point. This rock mass would be considered as massive, so it should be modelled as a continuum, although the presence of a single major fracture, such as a fault, could influence transmission in certain places surrounding a tunnel, as found by Eitzenberger (2012). Engineering judgement should be exercised in such situations and a sensitivity analysis carried out to investigate whether the presence of a joint affects results.

The results presented above do not show any great degree of equivalence between the discontinuum and equivalent transversely isotropic continuum models, with the exception of the near field results for the 2 m spacing, 0.5 GPa/m model in Figure 8-16 at 90°. However, this individual result should not be considered significant. The observed effect of the moving load direction will further obscure any equivalence. Equivalence between the discontinuum and equivalent continuum results is expected when the wavelength is much greater than the joint spacing, following the work of Schoenberg & Sayers (1995), so it can be assumed that the models studied here do not reach that limit. However, the previous Chapters in this thesis suggest that a large wavelength in comparison to the joint spacing can bring about resonance through the spring resonance effect. Despite this, with a sufficient number of joints, the spring resonances will merge giving the possibility of a low frequency equivalence. The equivalence will therefore be a function of the position of the measurement point, with the greater distance between the excitation and measurement allowing more potential blocks to be formed and therefore more spring resonance frequencies.

Although this study only considers relatively stiff rock, specifically basalt, there are some suggestions as to the expected results of modelling soft ground tunnels in materials which behave as a continuum. Natural soft ground tunnelling materials, such as London Clay, which show E_h:E_v ratios of greater than 1 and with a plane of isotropy orientated close to horizontal, could be modelled as an isotropic continuum with minimal error introduced in the results. This is shown by the similarity between the results for the horizontal (0^{o}) plane of isotropy in the transversely isotropic continuum and the isotropic continuum. This approach represents a more simplistic approach to modelling transversely isotropic continuum materials. This would only be applicable to deep tunnels, where the influence of a free surface is not felt, embedded in a material which can be considered as a continuum, such as soft ground deposits (i.e. London Clay) or a disintegrated (i.e. flysch) or massive (i.e. granitic batholith) rock masses.

8.2.5. Summary of results

This section provides a comparison of the results in the near field and far field for a moving load source in a transversely isotropic material, modelled as either a parallel jointed discontinuum or a transversely isotropic continuum. All cases studied are modelled as jointed basalt, although it should not be considered that the outcomes of this study only apply to igneous or other very stiff rocks. Although the exact results presented here will only be applicable to a rock mass composed of basalt, the qualitative trends which are identified, and which are considered to be the main outcome of this analysis, can be applied to any rock mass which can be considered as a discontinuum. Table 8-4 provides a summary of the key trends observed in modelling from Section 8.2.

Table 8-4 Summary of modelling results

Model	**Near Field Effect**	**Far Field Effect**
Discontinuum	Least displacement in vertical (90°) joints. Greatest displacement in dipped (45 or 135°) or horizontal (0 or 180°) joints. Displacement with 45° joints are not necessarily equal to 135° joints.	Least displacement in horizontal (0 or 180°) joints. Greatest displacement depends on joint spacing and stiffness. Displacement with 45° joints are not necessarily equal to 135° joints.
Transversely Isotropic Continuum	Greatest displacement with vertical (90°) plane of isotropy. Least displacement with horizontal (0 or 180°) plane of isotropy. Equal to isotropic continuum results. Displacement with 45 and 135° plane of isotropy is equal.	Greatest displacement with vertical (90°) plane of isotropy. Least displacement with horizontal (0 or 180°) plane of isotropy. Equal to isotropic continuum results. Displacement with 45 and 135° plane of isotropy is equal.
Effects of Material Model (Equivalent discontinuum, transversely isotropic continuum and isotropic continuum)	Discontinuum has greater displacement than continuum models. Isotropic continuum has greater displacement than transversely isotropic continuum when plane of isotropy is horizontal (0 or 180°). At all other angles isotropic continuum displacement is less than transversely isotropic continuum.	Discontinuum has greater displacement than continuum models. Isotropic continuum has equal displacement to transversely isotropic continuum when plane of isotropy is horizontal (0 or 180°). At all other angles isotropic continuum displacement is less than transversely isotropic continuum.
Effects of Equivalent Discontinuum (Joint spacing increased and joint stiffness decreased to give same overall stiffness)	Increasing joint spacing and decreasing joint stiffness leads to reduced displacement.	Increasing joint spacing and decreasing joint stiffness leads to reduced displacement at 0, 90 and 180° joints and increased displacement at 45° joints. Effect at 135° joints is non-linear.
Effects of Joint Spacing (Consistent joint stiffness)	Increasing joint spacing reduces displacement.	Increasing joint spacing leads to reduced displacement at 0, 90 and 180° joints and increased displacement at 45° joints. Effect at 135° joints is non-linear. Joint spacing has a greater effect than joint stiffness.
Effects of Joint Stiffness (Consistent joint spacing)	Increasing joint stiffness reduces displacement.	Increasing joint stiffness leads to reduced displacement at 0, 45, 90 and 180° joints and increased displacement at 135°.

8.3. Transfer Functions for Moving Loads

The previous section uses a slightly different approach to previous Chapters, by not determining the effect of joints on wave transmission in the frequency domain. This section analyses results of models using transfer functions, with the insertion loss concept being adopted, as used with the 2D analyses in Chapter 6 (Figure 6-2). The goal of this section is to determine whether the previously identified resonance effects persist with moving loads, instead of the distribution of the displacement pattern, as investigated in the previous section in this Chapter.

The finite difference method, using WAVE2D, is used in this section. This simplifies the application of the source as a moving load as WAVE2D has a built-in moving load function.

8.3.1. Model setup

The rock masses considered in this section are modelled in 2D plane strain, similar to those modelled in the Chapters which focus on non-moving point loads. The loads in this section are modelled following the same reasoning as the previous section in this Chapter, based on the study of Yuan et al. (2015), with a source modelled moving along a linear path within the model.

All models used in this section have the same material properties and use the same joint stiffness. The effect of these parameters has been extensively studied in previous Chapters, so their effect is known.

All models used have a square grid with an element size of 0.1 m, composed of 2400 x 2400 elements. This gives a model size of 240 x 240 m. The model is shown in Figure 8-19.

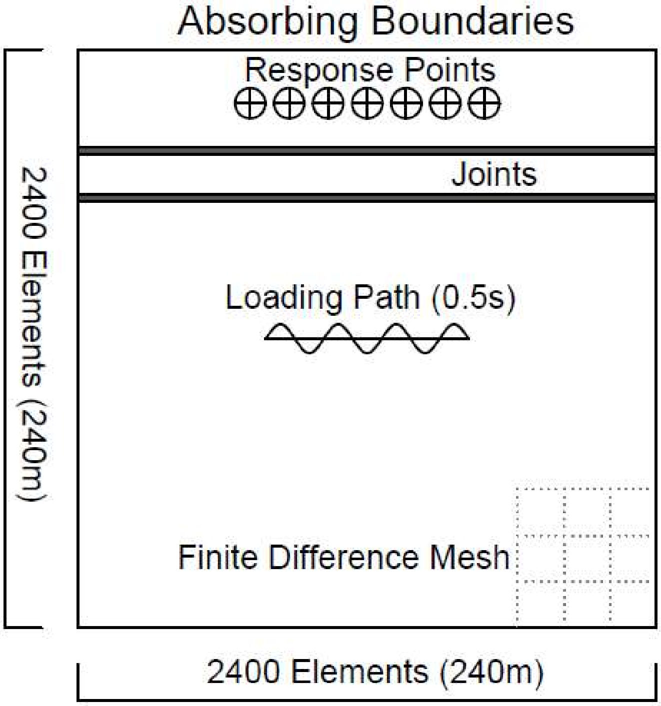

Figure 8-19 Schematic diagram of the WAVE2D moving load model

The loading path is located in the centre of the model, with the loading travelling from left to right. A range of different source velocities are used, with the same model run time of 0.5 s. As the source is in the centre of the model at half the run time, the sources start in different positions dictated by the source velocity. For example, a 100 m/s source velocity has a path length of 50 m, while a 50 m/s source velocity has a path length of 25 m.

8.3.2. Moving Load Source

The moving load modelled in this section is intended to be an impulse, much like in previous Chapters; however, in the time domain impulses cannot be easily modelled. Therefore, as described in Chapter 4, an impulse-like source is required. As used in previous Chapters, a modified Ricker wave is adopted for the moving load. Figure 8-20 a shows the input wave used and Figure 8-20 b the frequency spectrum, taken from an equivalent non-moving point load model. Due to the inbuilt moving load function in WAVE2D a band limited sine wave is not required, unlike in the previous section conducted in UDEC.

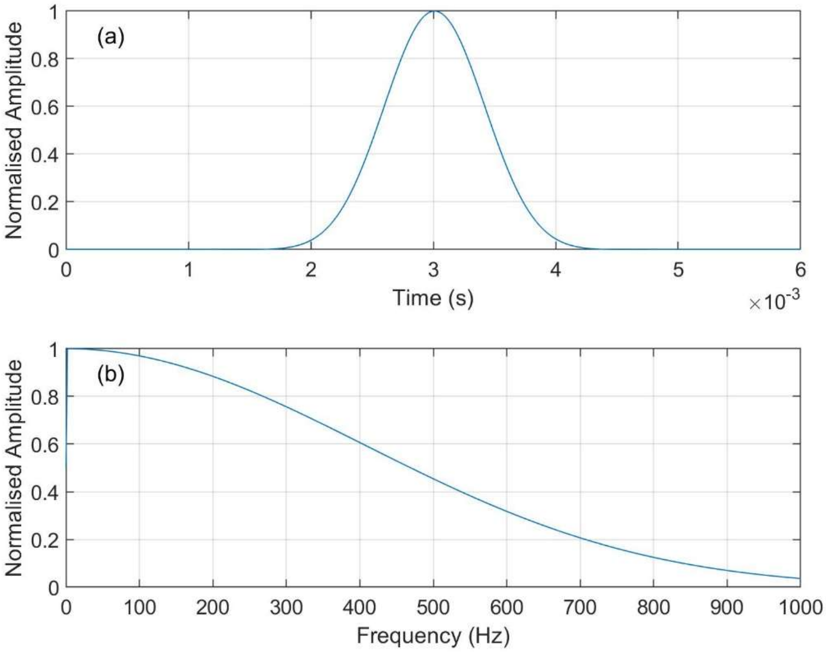

Figure 8-20 Input waves for moving point load models. Wave taken from an equivalent non-moving point load model. a) time series, b) frequency spectrum

A range of different wave speeds are investigated in this section. For a fair comparison of different models, it is necessary that all of these have the same waveform. This is shown in Figure 8-21, with data taken from the centre of the loading line in a continuum model. The subplots in Figure 8-21 all have the same waveform despite the wave speed ranging from 0 m/s, which is a non-moving point load source, to 100 m/s. Although it could be argued that changing the wave speed will cause the source to change, as shown by Zhang (2020), in order to generate the transfer functions the same source is required for all load speeds. Changing the waveform will change the frequency content, which will mask any frequency related effects within the model.

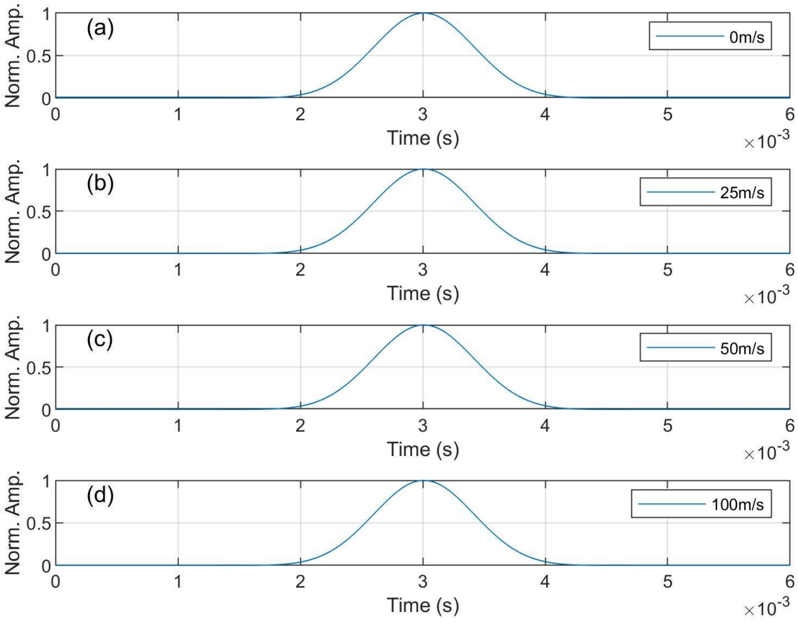

Figure 8-21 Waveforms from models with different wave speeds

8.3.3. Effect of a moving load and the load speed

For an initial analysis, the effect of a moving load is investigated by comparing the response of a non-moving point load model at a set distance from the source, with the response of a moving load model at the same position. The non-moving model is defined as an impulse applied to a single element which does not move. These results are derived from continuum models, allowing only the effect of the moving load to be established. This has been undertaken at a range of moving load speeds of 25, 50 and 100 m/s. The non-moving model gives u_{ref} for Equation 4-1, while the moving load models gives u.

Figure 8-22 shows the transfer function for the three load speeds. Each model shows a maximum at 0 Hz, followed by an almost zero transmission zone with a peak at a frequency which increases as the load speed increases. Past this, there is a high transmission zone with rapid oscillations. The peak is at 250, 500 and 1000 Hz for the 25, 50 and 100 m/s models, respectively. With a mesh size of 0.1 m, the moving load will move between elements every 0.004, 0.002 and 0.001 s for each of the load speeds (25, 50 and 100 m/s). This is calculated as $dt=dL/v$ (dL = mesh size, v = load speed). These values of dt correspond to frequencies of 250, 500 and 1000 Hz, which matches up with the peaks. This shows that an artefact in the numerical model causes this peak. This will only occur if the transfer function is calculated by comparing a moving model with a non-moving point load model, as is the case here, or a different velocity moving model.

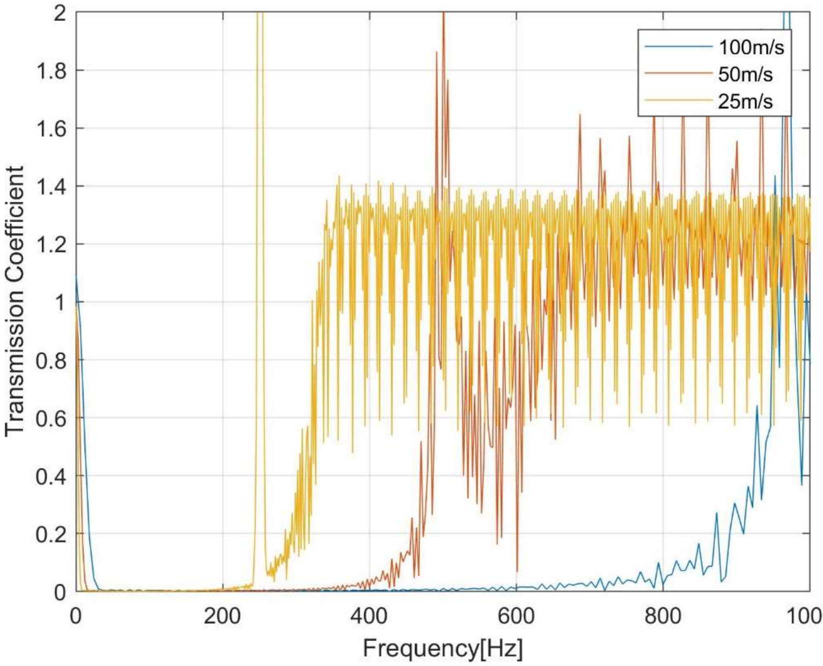

Figure 8-22 Transfer functions for 100, 50 and 25 m/s moving loads, compared to non-moving point loads (0 to 1000 Hz)

The frequency response past the maximum transmission cannot be thought of as being realistic. This gives a general trend of a peak at 0 Hz, which rapidly decays to a zero transmission zone. The low frequency portion of the transfer functions is shown in Figure 8-23.

Figure 8-23 shows that, for the low frequency response of a moving load, the load speed influences the relatively high transmission zone, with the 100 m/s load speed showing the greatest response over the greatest range, and the 25 m/s load speed showing the lowest and most confined range. This implies that a load moving at 0 m/s would show the lowest response, which cannot be the case, as that is effectively used as the input for the assessment. In fact, a 0 m/s load speed would show a transmission coefficient of one at all frequencies. A train travelling at 0 m/s would not cause an impulse; however, as the research is trying to determine the effect of load speed on the presence of potential resonance effects this nuance has been ignored.

Equally, an infinitely fast load would be expected to show a high transmission at all frequencies. This might be more likely, as an infinitely fast moving load would effectively load all parts of the transmission pathway at all times.

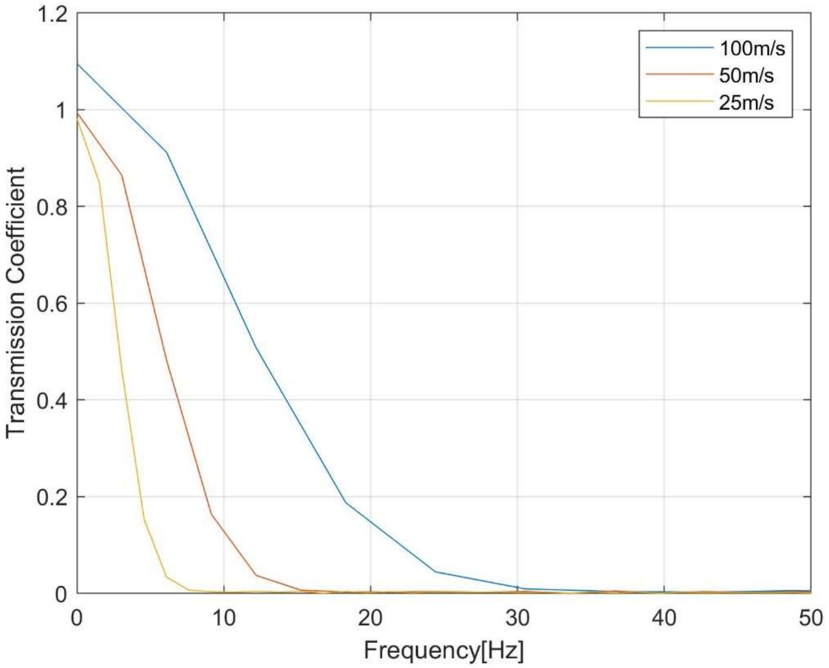

Figure 8-23 Transfer functions for 100, 50 and 25 m/s moving loads, compared to non-moving point loads (0 to 50 Hz)

8.3.4. Effect of a moving load with parallel joints

Figure 8-24 to Figure 8-27 show the transfer functions for moving loads models with two, three, four and five joints, respectively. The transfer functions in these Figures are compared to the spring resonant frequencies for the rock mass, defined in Chapter 4. The 0 m/s load speed is a non-moving point load and is presented as a comparison. The non-moving loading will act in the same way as the non-moving point loads in the previous section concerning 2D jointed rock masses.

The transfer functions show very clear high transmission zones at the frequencies predicted by the spring resonance Equation (Equation 4-18). The superposition resonance of this particular model should occur at over 832 Hz. This is evidence of the presence of the spring resonance effect in rock masses excited by moving loads.

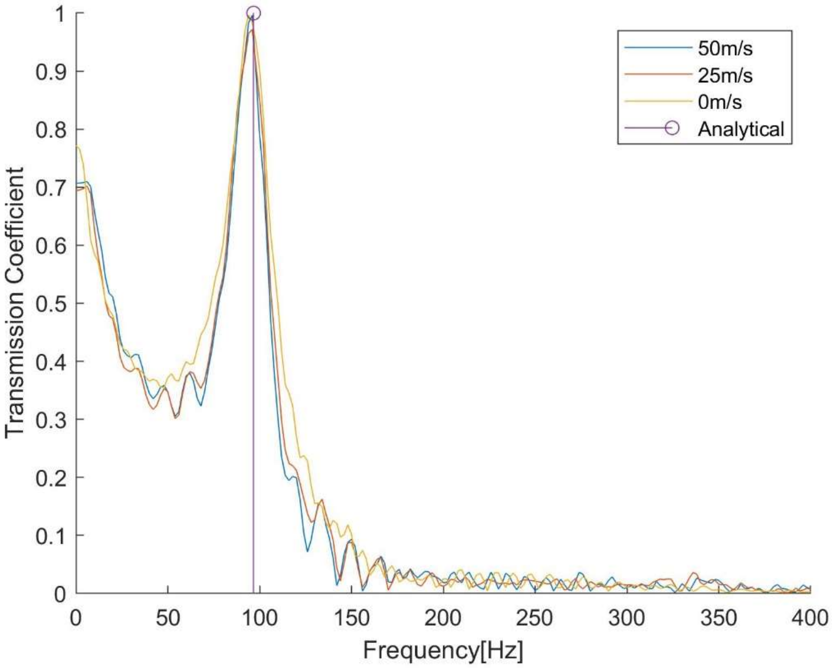

Figure 8-24 Two joints with loads of 0, 25 and 50 m/s

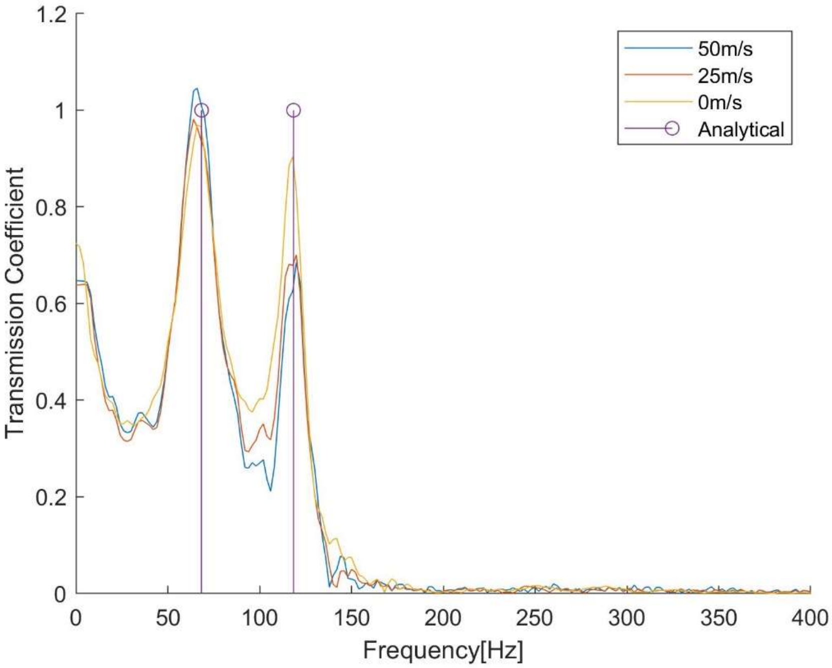

Figure 8-25 Three joints with loads of 0, 25 and 50 m/s

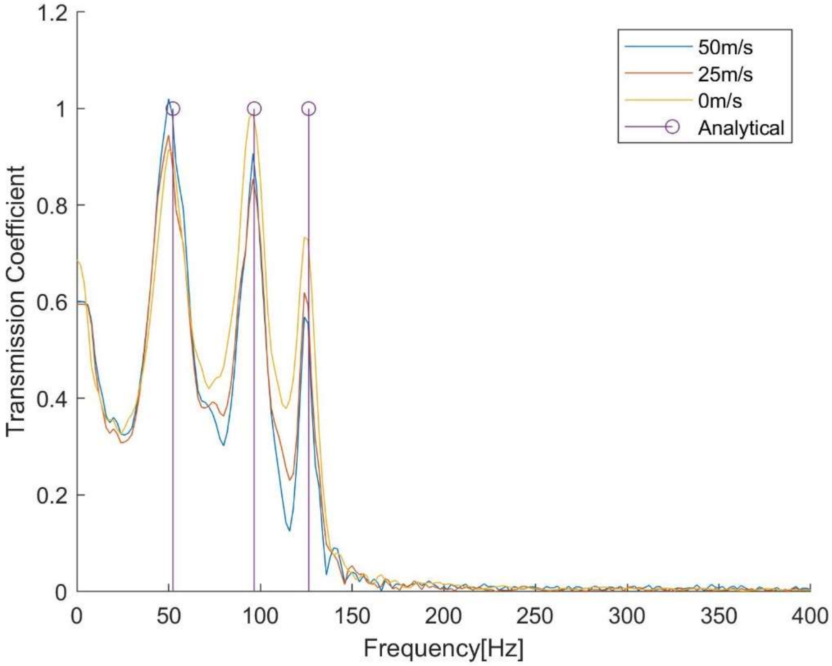

Figure 8-26 Four joints with loads of 0, 25 and 50 m/s

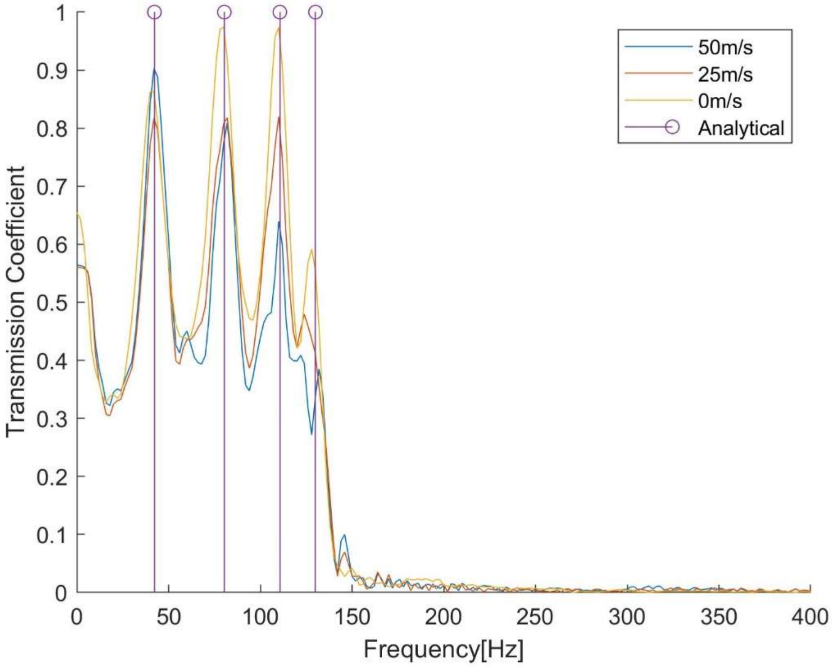

Figure 8-27 Five joints with loads of 0, 25 and 50 m/s

8.3.5. Moving Loads in Blocky Materials

The previous section investigates whether moving loads generate the spring resonance effect in parallel jointed materials, with the resonance mechanisms positively identified in transfer functions. Despite this, blocky rock masses, with more than one set of fractures, are often encountered in nature. Chapter 5 shows that the spring resonance effect exists when a non-moving point load excites a blocky rock mass; however, the interaction between a blocky material and a moving load is more complex. A plane wave exciting a blocky rock mass will only really encounter the joints which are orientated perpendicular to the direction which the wave is propagating in, while both the vertical and horizontal joints are encountered by a non-planar wave moving through a rock mass. This section examines simple blocky models and attempts to understand whether rock mass resonance mechanisms do exist in them. An example of a simple blocky rock mass model is shown in Figure 8-28. The simplest case of a blocky material is used, which is using two joints, giving a single block in the centre of the model. The x-velocity is recorded within the block as this is the block which will be oscillating due to the spring resonance.

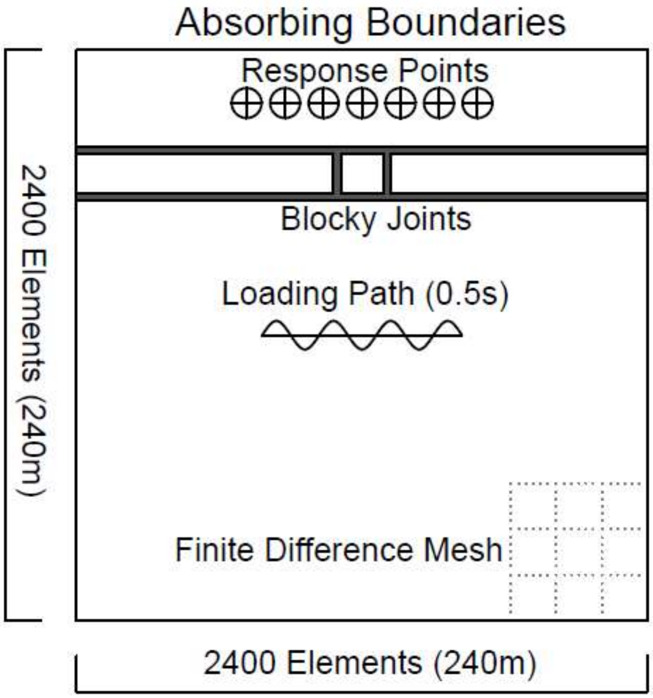

Figure 8-28 Schematic of blocky material model

A series of models are run using the set up shown in Figure 8-28. The vertical joints are spaced at 2, 5 and 10 m. The vertical joints are sandwiched between horizontal joints with a spacing of 2 m. The transfer functions are generated, using the insertion loss method, by comparing a model with (u) and without (u_{ref}) the blocks between the parallel joints. The results of this are shown in Figure 8-29. As the insertion loss method is used, the resonances of the horizontal joints should not affect the transfer functions shown, and instead only the effect of the blocks are being analysed. It is clear from the Figure that there are large regions of the transfer functions which show transmission coefficients of greater than 1. This effect increases when the joint spacing reduces. The model with a 2 m joint spacing between the vertical joints has a twin peak high transmission zone centred at 700 Hz (Figure 8-29 a), with the 5 m spacing model with a clear peak at 600 Hz (Figure 8-29 b). There are no clear high transmission zones in the model with a 10 m joint spacing (Figure 8-29 c). These peak transmissions do not seem to be affected to a significant degree by the joint stiffness, so they are unlikely to be created by the spring resonances, which occurs between 13 and 99 Hz, depending on the model properties. Equally, they are not at the correct frequency for the superposition resonance mechanism, which would occur at 832, 333 and 166 Hz for the 2, 5 and 10 m models, respectively. These also have not been created by superposition of S-waves, which would occur at 480, 192 and 96 Hz for the models in Figure 8-29. The causes of the interactions within these models remain unclear.

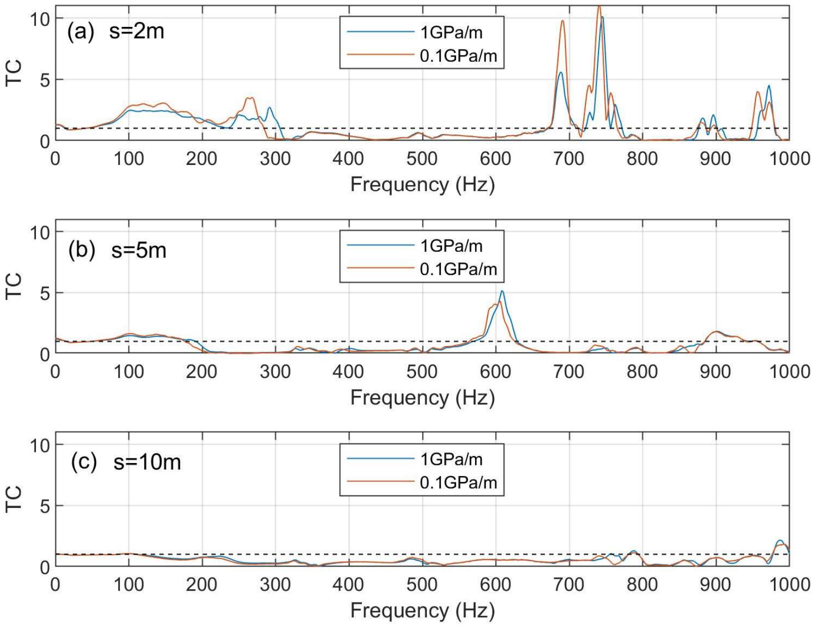

Figure 8-29 Transfer functions for blocky materials. Dashed black line shows Transmission Coefficient =1.

Figure 8-29 represents a very brief investigation into whether the spring resonance effect occurs in loads moving parallel to a blocky rock mass. From this, it looks unlikely that this resonance effect is occurring in this scenario.

Masonry tunnel linings are constructed of blocks, such as brick or stone, held together using cement. Such a structure can be thought of as an artificial blocky rock mass, with the brick or stone being the equivalent of blocks and the cement being a joint infilling. This is similar to the model shown for the above sensitivity analysis or Figure 7-4. The masonry structure is to all intents a periodic material, which will therefore exhibit a resonant frequency related to the spring resonance effect, as described in Chapter 7. If the spring resonance occurs in the walls of a masonry tunnel, it is possible that the oscillation of the blocks could lead to the deterioration of the strength of the masonry joint. Over time this reduction in strength could lead to a tunnel collapse. Such effects could be exacerbated by changes in vibration source, such as an upgrading of line speed. Changes in line speed could be brought about by re-using existing railway tunnels for new high speed rail lines. However, Figure 8-29 has shown that a blocky rock mass orientated perpendicular to the direction of a moving load, which is similar to the orientation of a tunnel wall in relation to a train track, does not show a clear spring resonance effect. Therefore, train vibrations are unlikely to affect the stability of a masonry tunnel lining, through the spring resonance mechanism.

8.4. Conclusions for moving loads

This Chapter investigates moving loads using the combined DEM-FDM, as well as the FDM. A DEM-FDM model is generated, and the maximum displacement of the rock mass recorded at two different locations, one on the loading path (the near field) and another located above the loading path (the far field). It is found that stress waves, generated by moving loads are affected by joints, which vary depending on the orientation of the joint and the direction of the moving load. The joint stiffness and joint spacing also influence wave transmission. This indicates that it may not be appropriate to use an equivalent continuum instead of a discretely jointed material model, which is found in previous Chapters related to wave transmission in non-moving point load models.

Following this an FDM model is used to determine whether the spring resonance effect occurs in parallel jointed and blocky rock masses. The spring resonance effect is found to occur in parallel jointed rock masses, although it is not identified in blocky rock masses. This indicates that a moving load travelling within a jointed rock mass will have a preferentially transmitted frequency, polarised with the direction of vibration perpendicular to the moving load direction. However, the spring resonance effect does not appear to occur within a blocky rock mass, with the direction of vibration polarised perpendicular to the moving load direction. As such, masonry joints in masonry lined tunnels will not show additional degradation due to the passage of trains through the tunnel.

9. Conclusions

"This concludes this projects scope,
With the findings which are kinda dope.
From a beginning with numerical models,
The outcomes finally viewed from realistic goggles.

Spring and superposition resonance occurs,
Giving the frequencies a material prefers.
These are found in various situations,
And discussed for different applications.

I hope this summary was illuminating,
A novel way of a study communicating.
I thank you for your perusal,
And I hope it has your approval."

© Army of Cats 2023

9.1. Synopsis

"Education never ends, Watson. It is a series of lessons with the greatest for the last." – Sherlock Holmes
(Doyle, 2014, pg. 782)

This chapter covers the main findings of this thesis, as well as their contribution to the current state of the art research. The limitations of the research and potential further works are summarised.

The research question originally posed for this project was titled "Modelling high-speed railway induced vibrations around tunnels (ground support)", although this has subsequently morphed into "Modelling high-speed rail induced vibrations around tunnels (jointed rock masses)" during the research. Jointed rock masses are by no means a less compelling field than tunnel support, and if anything, represent an area of research which is applicable to a wider audience than merely high speed rail tunnels. The outcome of this research is applicable to anything which cause vibrations, from manmade sources, such as rail vibrations and machine foundations, to natural sources, such as earthquakes.

The project methodology was focused around adding complexity at each stage of analysis, with early conceptual models including an unlined cavity within a jointed rock mass (Figure 1-1). The simplest way to view this was using a 1D model, which represents the transmission pathway of stress waves through a rock mass, moving directly from a source to a receiver. It was intended that, after moving to a 2D model, it would be possible to add in tunnel support in the form of liners and rock bolts to the models to determine the effect of these additions on vibrations and vice versa. In fact, the intention to model rock bolts motivated the study of jointed rock masses. However, rock support was never added into models. Out of the numerical codes used in this thesis, UDEC is the only one which is capable of modelling rock support such as those previously mentioned. However, again in early models developed for this research work, which are not included here, rock support was found to be difficult to model in a dynamic situation, causing models to crash. Therefore, efforts were devoted to the study of jointed rock masses alone, although unlined cavities were also modelled in later Chapters (Chapter 6).

Much of the work in this thesis took on a similar theme, using transfer functions to determine how stress waves are transmitted through jointed rock masses. This was initially done using a simplistic 1D model, although additional complexity was introduced as the work progressed.

The initial intention of the first transfer function Chapter (Chapter 4) was to merely present a new method of looking at jointed rock mass transmission, which the transfer function approach represents. However, clear trends could be seen in the data with peaks in transmission of certain frequencies. The frequency of the peaks were found to change when the properties of the rock mass changed. It was also found that the peak transmissions could be split into two groups, a low frequency group and a high frequency group, which appeared to be controlled by different factors (Section 4.6). With the use of a large systematic database of peak transmissions, the mechanisms behind these were identified. The low frequency high transmission operated on a mechanism related to masses between springs while the high frequency high transmissions were controlled by a mechanism related to superposition of reflected waves. The high transmissions were identified to be resonant frequencies of the rock mass. The low frequency resonance has been referred to as spring resonance and the high frequency resonance as superposition resonance.

Spring resonance occurs when blocks oscillate like masses between springs. This gives an equal number of resonant frequencies as there are blocks within a rock mass. The joints in the rock mass are equivalent to springs and the intact blocks are equivalent to masses. The blocks only relate to unbounded blocks, which are those which have joints on either side of them in the numerical models used in this study, and not the blocks which are at the ends of the model. Equation 4-18 is presented which can predict the frequency of the spring resonant frequencies (Section 4.6.1). The accuracy of the analytical equations was improved by altering the joint stiffness by incorporating the stiffness of the blocks using equation 4-17. In idealised mass between spring systems the masses are rigid; however, in the numerical models the blocks have a stiffness. Therefore, the introduction of the stiffness of the blocks into the term related to the stiffness of the joint was a reasonable step, which had a sound engineering principle behind it. Spring resonance, despite being based on classical mechanics, has not previously been identified in studies of stress wave transmission through jointed rock masses.

The superposition resonance occurs through reflections which take place when stress waves are incident upon a joint. Some energy is transmitted through the joint while the rest is reflected. Multiple reflections from the joints on either side of the block cause multiple waves within the block. These waves superimpose on one another, causing both destructive and constructive interference. At wavelengths which are multiples of half the block size, constructive interference occurs. This behaves in a similar way to standing waves on a string. Equation 4-20 is presented to predict the frequency of superposition resonance (Section 4.6.2). Theoretically, there are an unlimited number of super position resonant frequencies. This effect has previously been identified in stone blocks, has its own British Standard, and is exploited in resonance enhanced drilling. Superposition of reflected waves was also the mechanism proposed which caused high transmissions in previous studies of jointed materials; however, these occur at much lower frequencies than the ones identified in this study and would theoretically be occurring at frequencies which would generate destructive interference (Section 5.4).

Chapters 5 to 8 study the spring resonance mechanism and attempt to understand how it operates and whether it has been brought about by the highly simplified models used in the Chapter 4. To do this more complex models were generated, changing the boundary conditions (Section 5.3.2), introducing blocky rock masses (Section 5.3.1) as well as generating a non-plane wave source in a 2D model (Chapter 6). In addition to this, a new numerical modelling code, the finite difference method, and a new source wave form were used. All of this helps to determine whether the spring resonance mechanism is a real effect in jointed materials or whether it is merely a modelling artefact. The spring resonance effect was identified in each model, with the frequency of the resonances matching the results shown by Equation 4-18. The 2D models showed that the spring resonance effect does not just occur directly above a source, where waves will be normally incident upon a joint, but also when the wave is not normally incident (Section 6.5.2). 2D models also showed that when a cavity is modelled the resonance effect persists (Section 6.5.3). All this shows that the spring resonance effect is quite robust to changes in the modelling scenario. Evidence is presented showing that if a full waveform were modelled in previous studies, the resonance mechanisms would have been identified (Section 5.4).

Equivalent material models are analysed to determine whether these can show the identified resonance effects (Section 5.3.3). Homogenous equivalent media show no resonance effects due to the resonance effects being generated by the presence of joints within the material. A homogenous equivalent medium averages out the effect of the joints over the entire material, so the individual reflective and low stiffness zones which generate the resonance are not present. A localised equivalent medium, which applies equivalent medium properties to the nodes in the finite difference mesh which would represent joints, does show the resonance effects. This is because, despite a discrete fracture and an equivalent medium fracture being modelled in slightly different ways, both methods do have a low stiffness reflective boundary present in the model; therefore, generating the resonance effects.

The resonance mechanisms identified in this study were investigated for their influence on vibrations generated by trains (Section 6.6). It was found that a high transmission zone will be generated at low frequencies when there are a large number of joints as the spring resonances will all occur below a cut off frequency, which is related to the properties of the rock mass. This cut off frequency is compared for a range of common rock types, and it is shown that vibrations related to the train itself are likely to not be affected by the resonance mechanisms with vibrations being transmitted unopposed, while some vibrations related to sources from the track will fall outside the high transmission zone and be reduced (Figure 6-23).

The resonance mechanisms in jointed rock masses are shown to be similar to frequency response effects in periodic metamaterials (Chapter 7). Evidence from literature is presented which shows that a physical experiment of a periodic metamaterial shows a peak in transmission at the frequency predicted by the spring resonance effect (Figure 7-3). This provides the first proof of such an effect occurring in reality. Despite similarities with the frequency response of periodic metamaterials, jointed rock masses cannot be thought of as being a type of periodic metamaterial due to the derivation of the term metamaterial. Instead, it is suggested that a jointed rock mass is a natural periodic material, while metamaterials are artificial periodic materials.

Despite the semantic differences between jointed rock masses and periodic metamaterials, the similarity in their frequency response led to an investigation into a theoretical wave barrier (Section 7.5). This employed the predictable high and low transmissions of the spring resonance mechanism to cut out a significant degree of the frequency content of a signal. The principle is similar to locally resonant phononic cell wave barriers already in existence. However, those in use now use identical phononic cells, while the proposed barrier would use two different phononic cells. The two different cells would complement each other with the resonant frequency (pass band) of one falling within the low transmission (band gap) of the other. The proposed wave barrier was found to cut out a significant degree of the frequency content of a wave; however, it did not outperform the wave barrier composed of multiple identical cells, except at the resonant frequency of the cell. The proposed barrier is a less optimum set up because the resonant frequency of a single cell can be designed to fit within an area of low amplitude vibrations from the source.

The resonance effects are finally explored in models containing moving loads (Chapter 8). The spring resonance effect is identified in models where joints run parallel to the moving load direction (Section 8.3.4). However, the spring resonance does not occur in a blocky rock mass orientated perpendicular to this (Section 8.3.5). Furthermore, an alternative moving load analysis was also presented which results from a DEM-FDM analysis of equivalent materials (Section 8.2). Discontinuum analyses containing a single joint set were excited by a moving load. The response of these models were compared to equivalent transversely isotopic continua, whose plane of isotropy ran parallel to the dip of the joints, and an isotropic continuum with the same properties as the intact blocks in the discontinuum model. It was found that the transversely isotropic continua have a different response to their equivalent discontinuum models. It was also found that the moving load direction in relation to the dip of the joints can affect the response of a rock mass. This has implications for vibration analysis of tunnels in industrial practice, where the load would need to travel in both directions through a tunnel to ensure the correct vibration levels are captured by a scoping study.

This study has extensively used numerical modelling and has identified interesting and original effects within jointed rock masses. It would have been of benefit to this thesis to have successfully performed a physical experiment which identified the resonance effects. However, despite attempts being made this was not possible (Section 5.3.4). This is a clear omission from the research presented in this thesis and would be of value for any future research.

9.2. Key Findings

The key findings of this thesis are summarised below:

- Jointed rock masses show two types of resonance mechanism with analytical equations presented for each of these;
    - Mass between spring type resonance (spring resonance);
    - Superposition of multiple reflections (superposition resonance).
- The resonance mechanisms have been found to be robust to changing modelling assumptions and load types, including non-moving and moving loads.
- Spring resonances can form a high transmission zone at low frequencies;
    - The high transmission zone will cause much of the vibration spectrum from trains to be transmitted unhindered.
- The spring resonance mechanism has can be identified from physical experiments of periodic metamaterials;
    - Periodic metamaterials have similar resonance characteristics as jointed rock masses;

    - Jointed rock masses are defined as being a class of periodic metamaterials, natural periodic metamaterials. Conventional periodic metamaterials are manmade periodic metamaterials.
- Equivalent materials do not show the same response to excitation sources, when compared to their explicitly jointed and localised equivalent medium comparisons.

9.3. Limitations

Despite the best attempts of the author, this thesis does have its limitations. The work conducted in this thesis is entirely based upon numerical modelling results, solved in either 1D or 2D. The addition of 3D modelling would add an additional dimension to the work, figuratively and literally; although, with a simple 3D rock mass, it is unlikely that anything new will be identified and instead the presence of the resonance mechanisms will be more robustly identified. However, results from physical modelling would add gravity to the conclusions of this thesis. While results from a physical model from published literature were re-analysed and used as proof of the physical presence of the resonance mechanisms the model was not strictly a jointed rock mass. Identifying the resonance mechanisms in a physical sample composed blocks with unfilled joints would provide very convincing proof that the resonance mechanisms could occur in almost any jointed rock mass. The use of more advanced constitutive models for joints, such as the non-linear Barton-Bandis joint model, would be of scientific interest. Damping is another factor which has been largely omitted from this work. Its addition would make the results from the research more realistic.

9.4. Further Work

This thesis has tried to address transmission of train vibrations through jointed rock masses which surround tunnels. Some additional questions and omissions in this study exist and are areas of future work.

- A physical experiment to verify the presence of the resonance effects in jointed rocks. Although this was attempted it was never successfully completed (Section 5.3.4);
- An investigation into the role of damping on the resonance mechanisms. This could be incorporated into all models included in this work and would be expected to give some degree of spatial limit of the maximum number of blocks which could be included in the spring resonance mechanism in a continuous rock mass;
- Investigate the effect of non-linear joint stiffnesses on the resonance mechanisms;
- An investigation of resonance in tunnel support. There has been some discussion about the role of the jointed rock mass resonance mechanisms in masonry tunnels

(Section 8.3.5); however, this does not study how segmental linings and rock bolts interact with jointed materials;

- Three dimensional models of transmission through joints. This is considered to be a natural further step from the work shown in this study, which has progressed from 1D into 2D already.

9.5. Publications

The following publications have been produced during the course of this research work.

1. Holmes, H.T., Paraskevopoulou, C. and DeMoraes, R. 2020. Determining the Relative Influence of Joint and Rock Properties on the Propagation of Planar Waves in Jointed Rock Masses Using Multivariate Statistical Techniques In: 54th US Rock Mechanics/Geomechanics Symposium.
2. Holmes, H., Paraskevopoulou, C., Hildyard, M., Neaupane, K. and Connolly, D.P. 2023. Jointed rock masses as metamaterials-implications for railway tunnel vibrations. Transportation Geotechnics. 41, p.101033.
3. Holmes, H., Paraskevopoulou, C., Hildyard, M., Neaupane, K. and Connolly, D.P. 2023b. Numerical modelling of resonance mechanisms in jointed rocks using transfer functions. Journal of Rock Mechanics and Geotechnical Engineering. 15(5), pp.1076–1089.
4. Holmes, H., Paraskevopoulou, C., Hildyard, M., Neaupane, K. and Connolly, D.P. 2023c. Equivalent material modelling of fractured rock mass resonance effects In: Expanding Underground-Knowledge and Passion to Make a Positive Impact on the World: Proceedings of the ITA-AITES World Tunnel Congress 2023 (WTC 2023), 12-18 May 2023, Athens, Greece., p.268.
5. Holmes, H., Paraskevopoulou, C., Hildyard, M., Neaupane, K. and Connolly, D.P. 2023d. Effect of joint dip on the transmission of stress waves from a moving point load in a parallel jointed rock mass (in press) In: 15th ISRM Congress.

"I think we've outgrown full-time education ... Time to test our talents in the real world,
d'you reckon?" – Fred Weasley
(Rowling, 2003, pg. 861)

References

Ai, Z.Y. and Ren, G.P. 2016. Dynamic analysis of a transversely isotropic multilayered half-plane subjected to a moving load. *Soil Dynamics and Earthquake Engineering*. **83**, pp.162–166.

Albino, C., Godinho, L., Amado-Mendes, P., Alves-Costa, P., Dias-da-Costa, D. and Soares Jr, D. 2019. 3D FEM analysis of the effect of buried phononic crystal barriers on vibration mitigation. *Engineering Structures*. **196**, p.109340.

Andersen, L. and Jones, C.J.C. 2006. Coupled boundary and finite element analysis of vibration from railway tunnels-a comparison of two- and three-dimensional models. *Journal of Sound and Vibration*. **293**(3–5), pp.611–625.

Andrews, S.D., Trewin, N.H., Hartley, A.J. and Weedon, G.P. 2010. Solar variance recorded in lacustrine deposits from the Devonian and Proterozoic of Scotland. *Journal of the Geological Society*. **167**(5), pp.847–856.

Atkinson, C., Paraskevopoulou, C. and Miller, R. 2020. Investigation of Rehabilitation Methods of Victorian Tunnels *In*: *WTC 2020, Word Tunnelling Congress on Innovation and Sustainable Underground Serving Global Connectivity, September 2020, Kuala Lumpur, Malaysia.*

Avci, O., Bhargava, A., Nikitas, N. and Inman, D.J. 2020. Vibration annoyance assessment of train induced excitations from tunnels embedded in rock. *Science of The Total Environment*. **711**, p.134528.

Awdry, W. 1993. *Thomas the Tank Engine*. London: Reed Childrens Books.

Ba, Z., Liang, J., Lee, V.W. and Gao, Y. 2019. A semi-analytical method for vibrations of a layered transversely isotropic ground-track system due to moving train loads. *Soil Dynamics and Earthquake Engineering*. **121**, pp.25–39.

Bandis, S.C., Lumsden, A.C. and Barton, N.R. 1983. Fundamentals of rock joint deformation *In*: *International Journal of Rock Mechanics and Mining Sciences & Geomechanics Abstracts*., pp.249–268.

Barton, N., Løset, F., Lien, R. and Lunde, J. 1981. Application of Q-system in design decisions concerning dimensions and appropriate support for underground installations *In*: *Subsurface space* [Online]. Elsevier, pp.553–561. Available from: https://www.sciencedirect.com/science/article/pii/B9781483284217500806.

Barton, N. and Quadros, E. 2015. Anisotropy is Everywhere, to See, to Measure, and to Model. *Rock Mechanics and Rock Engineering*. **48**(4), pp.1323–1339.

Brady, B.H.G. and Brown, E.T. 2006. *Rock mechanics: for underground mining*. Springer science \& business media.

Bucher, K. and Grapes, R. 2011. *Petrogenesis of metamorphic rocks*. Springer Science & Business Media.

Cai, J.G. and Zhao, J. 2000. Effects of multiple parallel fractures on apparent attenuation of stress waves in rock masses. *International Journal of Rock Mechanics and Mining Sciences*. **37**(4), pp.661–682.

Calder, S. 2023. HS2 will reach central London only when line to Manchester is complete. *The Independent*. [Online]. Available from: https://www.independent.co.uk/travel/news-and-advice/hs2-manchester-london-train-mark-harper-b2322412.html.

Castanheira-Pinto, A., Alves-Costa, P., Godinho, L. and Amado-Mendes, P. 2018. On the application of continuous buried periodic inclusions on the filtering of traffic vibrations: A numerical study. *Soil Dynamics and Earthquake Engineering*. **113**, pp.391–405.

Chen, T. 2021. Seismic response analysis of loess site under far-field bedrock ground motion of the Wenchuan earthquake. *Plos one*. **16**(7), p.e0254871.

Cheng, Z. and Shi, Z. 2014. Vibration attenuation properties of periodic rubber concrete panels. *Construction and Building Materials*. **50**, pp.257–265.

Chua, K.H., Balendra, T. and Lo, K.W. 1992. Groundborne vibrations due to trains in tunnels. *Earthquake engineering & structural dynamics*. **21**(5), pp.445–460.

Clot, A., Arcos, R., Romeu, J. and Pàmies, T. 2016. Dynamic response of a double-deck circular tunnel embedded in a full-space. *Tunnelling and Underground Space Technology*. **59**, pp.146–156.

Coates, R.T. and Schoenberg, M. 1995. Finite-difference modeling of faults and fractures. *Geophysics*. **60**(5), pp.1514–1526.

Connolly, D.P. and Forde, M.C. 2015. Use of conventional site investigation parameters to calculate critical velocity of trains from Rayleigh waves. *Transportation Research Record*. **2476**(1), pp.32–36.

Connolly, D.P., Galvin, P., Olivier, B., Romero, A. and Kouroussis, G. 2019. A 2.5 D time-frequency domain model for railway induced soil-building vibration due to railway defects. *Soil Dynamics and Earthquake Engineering*. **120**, pp.332–344.

Connolly, D.P., Kouroussis, G., Laghrouche, O., Ho, C.L. and Forde, M.C. 2015. Benchmarking railway vibrations--Track, vehicle, ground and building effects. *Construction and Building Materials*. **92**, pp.64–81.

Connolly, D.P., Kouroussis, G., Woodward, P.K., Costa, P.A., Verlinden, O. and Forde, M.C. 2014. Field testing and analysis of high speed rail vibrations. *Soil Dynamics and Earthquake Engineering*. **67**, pp.102–118.

Connolly, D.P., Kouroussis, G., Woodward, P.K., Giannopoulos, A., Verlinden, O. and Forde, M.C. 2014. Scoping prediction of re-radiated ground-borne noise and vibration near high speed rail lines with variable soils. *Soil Dynamics and Earthquake Engineering*. **66**, pp.78–88.

Connolly, D.P., Marecki, G.P., Kouroussis, G., Thalassinakis, I. and Woodward, P.K. 2016. The growth of railway ground vibration problems — A review. *Science of the Total Environment*. **568**, pp.1276–1282.

Craig, R.F. 2004. *Craig's soil mechanics*. CRC press.

Crouch, S.L., Starfield, A.M. and Rizzo, F.J. 1983. Boundary element methods in solid mechanics.

Cummer, S.A., Christensen, J. and Alù, A. 2016. Controlling sound with acoustic metamaterials. *Nature Reviews Materials*. **1**(3), pp.1–13.

Deng, X.F., Zhu, J.B., Chen, S.G. and Zhao, J. 2012. Some fundamental issues and verification of 3DEC in modeling wave propagation in jointed rock masses. *Rock mechanics and rock engineering*. **45**(5), pp.943–951.

Dertimanis, V.K., Antoniadis, I.A. and Chatzi, E.N. 2016. Feasibility analysis on the attenuation of strong ground motions using finite periodic lattices of mass-in-mass barriers. *Journal of Engineering Mechanics*. **142**(9), p.4016060.

Di, H., Zhou, S., He, C., Zhang, X. and Luo, Z. 2016. Three-dimensional multilayer cylindrical tunnel model for calculating train-induced dynamic stress in saturated soils. *Computers and Geotechnics*. **80**, pp.333–345.

Dominguez, J. 1993. *Boundary elements in dynamics*. Wit Press.

Doyle, A.C. 2014. The Complete Sherlock Holmes. [Accessed 4 July 2023]. Available from: https://sherlock-holm.es/.

Eitzenberger, A. 2012. *Wave propagation in rock and the influence of discontinuities*. Luleåtekniska universitet.

Eitzenberger, A., Zhang, P. and Nordlund, E. 2011. Numerical simulation of train-induced vibrations in rock masses *In*: *12th ISRM Congress*.

EN, B.S. 2004. 14146: 2004 Natural stone test methods--Determination of the dynamic modulus of elasticity (by measuring the fundamental resonance frequency). *Brussels, CEN*.

Fan, L.F., Wang, L.J. and Wu, Z.J. 2018. Wave transmission across linearly jointed complex rock masses. *International Journal of Rock Mechanics and Mining Sciences*. **112**, pp.193–200.

Forrest, J.A. and Hunt, H.E.M. 2006a. A three-dimensional tunnel model for calculation of train-induced ground vibration. *Journal of sound and vibration*. **294**(4–5), pp.678–705.

Forrest, J.A. and Hunt, H.E.M. 2006b. Ground vibration generated by trains in underground tunnels. *Journal of Sound and Vibration*. **294**(4–5), pp.706–736.

Gao, G., Xu, C., Chen, J. and Song, J. 2018. Investigation of ground vibrations induced by trains moving on saturated transversely isotropic ground. *Soil Dynamics and Earthquake Engineering*. **104**, pp.40–44.

Garcia, B. 2014. London underground maps: art, design and cartography.

Gasparre, A. 2005. *Advance Laboratory Characterization of London Clay*. University of London London, UK.

Gazetas, G. 1983. Analysis of machine foundation vibrations: state of the art. *International Journal of soil dynamics and earthquake engineering*. **2**(1), pp.2–42.

Germanovich, L.N. and Astakhov, D.K. 2004. Fracture closure in extension and mechanical interaction of parallel joints. *Journal of Geophysical Research: Solid Earth*. **109**(B2).

Gupta, S., Stanus, Y., Lombaert, G. and Degrande, G. 2009. Influence of tunnel and soil parameters on vibrations from underground railways. *Journal of Sound and Vibration*. **327**(1–2), pp.70–91.

Hamad, W.I., Hunt, H.E.M., Talbot, J.P., Hussein, M.F.M. and Thompson, D.J. 2015. The dynamic interaction of twin tunnels embedded in a homogeneous half-space.

Hanson, C.E., Ross, J.C., Towers, D.A., Harris, M. and others 2012. *High-speed ground transportation noise and vibration impact assessment.*

He, C., Zhou, S., Guo, P., Di, H. and Zhang, X. 2018. Analytical model for vibration prediction of two parallel tunnels in a full-space. *Journal of Sound and Vibration*. **423**, pp.306–321.

He, C., Zhou, S., Guo, P., Di, H., Zhang, X. and Yu, F. 2019. Theoretical modelling of the dynamic interaction between twin tunnels in a multi-layered half-space. *Journal of Sound and Vibration*. **456**, pp.65–85.

Hildyard, M.W. 2007. Manuel Rocha Medal Recipient Wave interaction with underground openings in fractured rock. *Rock Mechanics and Rock Engineering*. **40**(6), pp.531–561.

Hildyard, M.W. 2001. *Wave interaction with underground openings in fractured rock*. Citeseer.

Hildyard, M.W., Daehnke, A., Cundall, P.A. and others 1995. WAVE: A computer program for investigating elastodynamic issues in mining *In*: *The 35th US symposium on rock mechanics (USRMS)*.

Holmes, H., Garcia-Taengua, E. and Fuentes, R. 2019. Meta-analysis of ground movements associated with deep excavations using a data mining approach. *Journal of Rock Mechanics and Geotechnical Engineering*. **11**(2), pp.409–416.

Holmes, H., Paraskevopoulou, C., Hildyard, M., Neaupane, K. and Connolly, D.P. 2023a. Jointed rock masses as metamaterials-implications for railway tunnel vibrations. *Transportation Geotechnics*. **41**, p.101033.

Holmes, H., Paraskevopoulou, C., Hildyard, M., Neaupane, K. and Connolly, D.P. 2023b. Numerical modelling of resonance mechanisms in jointed rocks using transfer functions. *Journal of Rock Mechanics and Geotechnical Engineering*. **15**(5), pp.1076–1089.

Hood, R.A., Greer, R.J., Breslin, M. and Williams, P.R. 1996. The calculation and assessment of ground-borne noise and perceptible vibration from trains in tunnels. *Journal of sound and vibration*. **193**(1), pp.215–225.

Huang, H.W., Wang, J., Zhao, C. and Mo, Y.-L. 2021. Two-dimensional finite-element simulation of periodic barriers. *Journal of Engineering Mechanics*. **147**(2).

Hussein, M.F.M. 2004. *Vibration from underground railways*. University of Cambridge Cambridge, MA, USA.

Hussein, M.F.M., François, S., Schevenels, M., Hunt, H.E.M., Talbot, J.P. and Degrande, G. 2014. The fictitious force method for efficient calculation of vibration from a tunnel embedded in a multi-layered half-space. *Journal of sound and vibration*. **333**(25), pp.6996–7018.

Hussein, M.F.M. and Hunt, H.E.M. 2009. A numerical model for calculating vibration due to a harmonic moving load on a floating-slab track with discontinuous slabs in an underground railway tunnel. *Journal of Sound and Vibration*. **321**(1–2), pp.363–374.

Hussein, M.I., Leamy, M.J. and Ruzzene, M. 2014. Dynamics of phononic materials and structures: Historical origins, recent progress, and future outlook. *Applied Mechanics Reviews*. **66**(4).

Itasca Consulting Group Inc. 2014. UDEC - Universal Distinct Element Code Version 6.0.

Jones, S. and Hunt, H. 2011. Voids at the tunnel--soil interface for calculation of ground vibration from underground railways. *Journal of Sound and Vibration*. **330**(2), pp.245–270.

Jones, S., Kuo, K., Hussein, M. and Hunt, H. 2012. Prediction uncertainties and inaccuracies resulting from common assumptions in modelling vibration from underground railways. *Proceedings of the Institution of Mechanical Engineers, Part F: Journal of Rail and Rapid Transit*. **226**(5), pp.501–512.

Koziol, P., Mares, C. and Esat, I. 2008. Wavelet approach to vibratory analysis of surface due to a load moving in the layer. *International Journal of Solids and Structures*. **45**(7–8), pp.2140–2159.

Krödel, S., Thomé, N. and Daraio, C. 2015. Wide band-gap seismic metastructures. *Extreme Mechanics Letters*. **4**, pp.111–117.

Kuhlemeyer, R.L. and Lysmer, J. 1973. Finite element method accuracy for wave propagation problems. *Journal of the Soil Mechanics and Foundations Division*. **99**(5), pp.421–427.

Kuo, K.A., Hunt, H.E.M. and Hussein, M.F.M. 2011. The effect of a twin tunnel on the propagation of ground-borne vibration from an underground railway. *Journal of Sound and Vibration*. **330**(25), pp.6203–6222.

Kurzweil, L.G. 1979. Ground-borne noise and vibration from underground rail systems. *Journal of Sound and Vibration*. **66**(3), pp.363–370.

Li, S., Tian, S., Li, W., Yan, T. and Bi, F. 2019. Research on the resonance characteristics of rock under harmonic excitation. *Shock and Vibration*. **2019**.

Long, M. 2001. Database for retaining wall and ground movements due to deep excavations. *Journal of Geotechnical and Geoenvironmental Engineering*. **127**(3), pp.203–224.

Lu, F., Gao, Q., Lin, J.H. and Williams, F.W. 2006. Non-stationary random ground vibration due to loads moving along a railway track. *Journal of Sound and Vibration*. **298**(1–2), pp.30–42.

Lysmer, J. and Kuhlemeyer, R.L. 1969. Finite dynamic model for infinite media. *Journal of the engineering mechanics division*. **95**(4), pp.859–877.

Ma, G.W., Fan, L.F. and Li, J.C. 2013. Evaluation of equivalent medium methods for stress wave propagation in jointed rock mass. *International Journal for Numerical and Analytical Methods in Geomechanics*. **37**(7), pp.701–715.

Meighan, C. 2022. Liz Truss won't commit to restoring plans for HS2 line between East Midlands and Leeds. *The National*. [Online]. Available from: https://www.thenational.scot/news/20586312.liz-truss-wont-commit-restoring-plans-hs2-line-east-midlands-leeds/.

Menard, K.P. and Menard, N. 2020. *Dynamic mechanical analysis*. CRC press.

Metrikine, A. V and Vrouwenvelder, A. 2000. Surface ground vibration due to a moving train in a tunnel: two-dimensional model. *Journal of Sound and vibration*. **234**(1), pp.43–66.

Milne, D.R.M., Le Pen, L.M., Thompson, D.J. and Powrie, W. 2017. Properties of train load frequencies and their applications. *Journal of Sound and Vibration*. **397**, pp.123–140.

Nakagawa, S. 1998. *Acoustic resonance characteristics of rock and concrete containing fractures*. University of California, Berkeley.

Ouakka, S., Verlinden, O. and Kouroussis, G. 2022. Railway ground vibration and mitigation measures: benchmarking of best practices. *Railway Engineering Science*. **30**(1), pp.1–22.

Parastatidis, E. 2019. *How do seismic waves respond to fractures in rock? Evaluation of effective media versus discrete fracture representations.* University of Leeds.

Parastatidis, E., Hildyard, M.W. and Stuart, G.W. 2017. Modelling P-Wave Propagation in a Medium With Multiple Parallel Fractures and Direct Comparison With Experimental

Recordings. *In*: *51st US Rock Mechanics/Geomechanics Symposium*.

Patmore, J.A. 1965. The British railway network in the Beeching era. *Economic Geography*. **41**(1), pp.71–81.

Phillips, J.C., Humphreys, M.C.S., Daniels, K.A., Brown, R.J. and Witham, F. 2013. The formation of columnar joints produced by cooling in basalt at Staffa, Scotland. *Bulletin of volcanology*. **75**(6), p.715.

Pyrak-Nolte, L.J., Myer, L.R. and Cook, N.G.W. 1990a. Anisotropy in seismic velocities and amplitudes from multiple parallel fractures. *Journal of Geophysical Research: Solid Earth*. **95**(B7), pp.11345–11358.

Pyrak-Nolte, L.J., Myer, L.R. and Cook, N.G.W. 1990b. Transmission of seismic waves across single natural fractures. *Journal of Geophysical Research: Solid Earth*. **95**(B6), pp.8617–8638.

Rieckh, G., Kreuzer, W., Waubke, H. and Balazs, P. 2012. A 2.5 D-Fourier-BEM model for vibrations in a tunnel running through layered anisotropic soil. *Engineering Analysis with Boundary Elements*. **36**(6), pp.960–967.

Rowling, J.K. 1998. *Harry Potter and the Chamber of Secrets (Harry Potter, #2)*. Bloomsbury.

Rowling, J.K. 2007. *Harry Potter and the Deathly Hallows (Harry Potter, #7)*. Bloomsbury Books.

Rowling, J.K. 2005. *Harry Potter and the Half-Blood Prince (Harry Potter, #6)*. Scholastic Paperbacks.

Rowling, J.K. 2003. *Harry Potter and the Order of the Pheonix (Harry Potter, #5)*. Bloomsbury Books.

Ruiz, J.F., Soares, P.J., Costa, P.A. and Connolly, D.P. 2019. The effect of tunnel construction on future underground railway vibrations. *Soil Dynamics and Earthquake Engineering*. **125**, p.105756.

Schoenberg, M. 1980. Elastic wave behavior across linear slip interfaces. *The Journal of the Acoustical Society of America*. **68**(5), pp.1516–1521.

Schoenberg, M. and Sayers, C.M. 1995. Seismic anisotropy of fractured rock. *Geophysics*. **60**(1), pp.204–211.

Shen, S.-L., Wu, H.-N., Cui, Y.-J. and Yin, Z.-Y. 2014. Long-term settlement behaviour of metro tunnels in the soft deposits of Shanghai. *Tunnelling and Underground Space Technology*. **40**, pp.309–323.

Sheng, X., Jones, C.J.C. and Thompson, D.J. 2005. Modelling ground vibration from railways using wavenumber finite- and boundary-element methods. *Proceedings of the Royal Society A: Mathematical, Physical and Engineering Sciences*. **461**(2059), pp.2043–2070.

Tadeu, A.J.B. and Kausel, E. 2000. Green’s Functions for Two-and-a-Half-Dimensional Elastodynamic Problems. *Journal of Engineering Mechanics*. **126**(10), pp.1093–1097.

Tan, Thiam Soon and Tan, T S 2003. *Characterisation and engineering properties of natural soils*. CRC Press.

Tsinidis, G., de Silva, F., Anastasopoulos, I., Bilotta, E., Bobet, A., Hashash, Y.M.A., He, C., Kampas, G., Knappett, J., Madabhushi, G. and others 2020. Seismic behaviour of tunnels: From experiments to analysis. *Tunnelling and underground space technology*. **99**, p.103334.

Varma, M., Maji, V.B. and Boominathan, A. 2017. A Study on Ultrasonic Wave Propagation Across Fractures in Jointed Rocks *In*: *51st US Rock Mechanics/Geomechanics Symposium*.

Witarto, W., Wang, S.J., Yang, C.Y., Nie, X., Mo, Y.L., Chang, K.C., Tang, Y. and Kassawara, R. 2018. Seismic isolation of small modular reactors using metamaterials. *AIP Advances*. **8**(4), p.045307.

Wynn, M. 2004. *Driffield: The Growth and Developmnet of Driffield and the Surrounding Landscape* 1st ed. Driffield: David Marley.

Yang, Y.B., Liang, X., Hung, H. and Wu, Y. 2017. Comparative study of 2D and 2.5 D responses of long underground tunnels to moving train loads. *Soil Dynamics and Earthquake Engineering*. **97**, pp.86–100.

Yau, J.-D. 2001. Resonance of continuous bridges due to high speed trains. *Journal of Marine Science and Technology*. **9**(1), p.2.

Yuan, Z., Boström, A. and Cai, Y. 2019. An analytical model for calculating vibrations from twin tunnels in a saturated poroelastic half-space. *Soil Dynamics and Earthquake Engineering*. **120**, pp.23–27.

Yuan, Z., Boström, A. and Cai, Y. 2017. Benchmark solution for vibrations from a moving point source in a tunnel embedded in a half-space. *Journal of Sound and Vibration*. **387**, pp.177–193.

Yuan, Z., Boström, A., Cai, Y. and Cao, Z. 2019a. Analytical solution for calculating vibrations from twin circular tunnels. *Soil Dynamics and Earthquake Engineering*. **117**, pp.312–327.

Yuan, Z., Boström, A., Cai, Y. and Cao, Z. 2019b. Analytical wave function method for modelling a twin tunnel embedded in a saturated poroelastic full-space. *Computers and Geotechnics*. **114**, p.103114.

Yuan, Z., Cai, Y. and Cao, Z. 2016. An analytical model for vibration prediction of a tunnel embedded in a saturated full-space to a harmonic point load. *Soil Dynamics and Earthquake Engineering*. **86**, pp.25–40.

Yuan, Z., Cao, Z., Boström, A. and Cai, Y. 2018. The influence of pore-fluid in the soil on ground vibrations from a tunnel embedded in a layered half-space. *Journal of Sound and Vibration*. **419**, pp.227–248.

Yuan, Z., Xu, C., Cai, Y. and Cao, Z. 2015. Dynamic response of a tunnel buried in a saturated poroelastic soil layer to a moving point load. *Soil Dynamics and Earthquake Engineering*. **77**, pp.348–359.

Zeng, C., Sun, H.L., Cai, Y.Q. and Wang, P. 2014. Analysis of three-dimensional dynamic response of a circular lining tunnel in saturated soil to harmonic loading. *Rock Soil Mech*. **35**(4), pp.1147–1156.

Zhan, Y., Yao, H., Lu, Z. and Yu, D. 2014. Dynamic analysis of slab track on multi-layered transversely isotropic saturated soils subjected to train loads. *Earthquake Engineering and Engineering Vibration*. **13**(4), pp.731–740.

Zhang, F. 2020. *Ground vibration caused by high-speed trains - when is 3D modelling needed?* University of Leeds.

Zhang, P., Nordlund, E., Swan, G. and Yi, C. 2019. Velocity Amplification of Seismic Waves

Through Parallel Fractures Near a Free Surface in Fractured Rock: A Theoretical Study. *Rock Mechanics and Rock Engineering*. **52**(1), pp.199–213.

Zhao, J., Cai, J.G., Zhao, X.B. and Li, H.B. 2006. Experimental study of ultrasonic wave attenuation across parallel fractures. *Geomechanics and Geoengineering*. **1**(2), pp.87–103.

Zhao, J, Zhao, X.B. and Cai, J.G. 2006. A further study of P-wave attenuation across parallel fractures with linear deformational behaviour. *International Journal of Rock Mechanics and Mining Sciences*. **43**(5), pp.776–788.

Zhao, X., Zhao, J., Cai, J. and Hefny, A.M. 2008. UDEC modelling on wave propagation across fractured rock masses. *Computers and Geotechnics*. **35**(1), pp.97–104.

Zhou, S., He, C., Di, H., Guo, P. and Zhang, X. 2017. An efficient method for predicting train-induced vibrations from a tunnel in a poroelastic half-space. *Engineering Analysis with Boundary Elements*. **85**, pp.43–56.

Zhu, J.B., Deng, X.F., Zhao, X. and Zhao, J. 2013. A numerical study on wave transmission across multiple intersecting joint sets in rock masses with UDEC. *Rock mechanics and rock engineering*. **46**(6), pp.1429–1442.

Zymnis, D.M., Chatzigiannelis, I. and Whittle, A.J. 2013. Effect of anisotropy in ground movements caused by tunnelling. *Géotechnique*. **63**(13), pp.1083–1102.

Appendix A – Database of High Transmissions

Spacing	Stiffness	Jn	Rock	Cp	Peak Number														
(m)	(MPa/m)			(m/s)	1	2	3	4	5	6	7	8	9	10	11	12	13	14	15
8	1.00E+05	2	Shale	2365	0	81	221	366	512	657	803	949	1094	1238	1375				
8	1.00E+05	2	Original	3328	0	107	306	511	716	913	1118	1321	1524	1726	1929				
8	1.00E+05	2	Quartzite	5910	0	173	518	867	1216	1572	1928	2286							
8	1.00E+04	2	Shale	2365	0	66	198	336	477	619	762	907	1051	1195	1340	1484	1629	1772	1915
8	1.00E+04	2	Original	3328	0	83	261	454	653	856	1060	1261	1470	1667	1872	2078			
8	1.00E+04	2	Quartzite	5910	0	104	416	770	1123	1490	1865	2220							
8	1.00E+03	2	Shale	2365	0	42	159	302	448	595	742	886	1033	1180	1326	1472	1617		
8	1.00E+03	2	Original	3328	0	41	217	422	626	834	1039	1247	1455						
8	1.00E+03	2	Quartzite	5910	0	43	374	742	1108										
8	5.00E+02	2	Shale	2365	0	29	154	300	445	593	738	886	1034	1179	1326				
8	5.00E+02	2	Original	3328	0	30	212	419	625	833	1038	1246							
8	5.00E+02	2	Quartzite	5910	0	31	371	740	1109										
5	1.00E+05	2	Shale	2365	0	122	351	581	807	1041	1264	1496							
5	1.00E+05	2	Original	3328	0	163	483	802	1126	1445	1762								
5	1.00E+05	2	Quartzite	5910	0	266	800	1350	1906										
5	1.00E+04	2	Shale	2365	0	97	303	522	748	976	1205	1435	1664	1893	2125				
5	1.00E+04	2	Original	3328	0	117	399	710	1031	1356	1673	2001	2328						
5	1.00E+04	2	Quartzite	5910	0	162	635	1206	1788	2373									
5	1.00E+03	2	Shale	2365	0	51	249	480	714	947	1181	1415							
5	1.00E+03	2	Original	3328	0	54	342	670	1001	1330									
5	1.00E+03	2	Quartzite	5910	0	55	596	1185											
5	5.00E+02	2	Shale	2365	0	38	242	476	712	944	1179	1414							
5	5.00E+02	2	Original	3328	0	39	337	669	998	1329									
5	5.00E+02	2	Quartzite	5910	0	39	594	1181											
2	1.00E+05	2	Shale	2365	0	284	840	1374	2151										
2	1.00E+05	2	Original	3328	0	385	1146	1886											
2	1.00E+05	2	Quartzite	5910	0	579	1824												
2	1.00E+04	2	Shale	2365	0	203	696	1244	1804	2370									
2	1.00E+04	2	Original	3328	0	232	927	1700	2514										
2	1.00E+04	2	Quartzite	5910	0	267	1535												
2	1.00E+03	2	Shale	2365	0	86	604	1187											
2	1.00E+03	2	Original	3328	0	87	841	1663											
2	1.00E+03	2	Quartzite	5910	0	88	1481												

2	5.00E+02	2	Shale	2365	0	61	598	1182											
2	5.00E+02	2	Original	3328	0	62	837	1661											
2	5.00E+02	2	Quartzite	5910	0	62	1480												
1	1.00E+05	2	Shale	2365	0	540													
1	1.00E+05	2	Original	3328	0	708													
1	1.00E+05	2	Quartzite	5910	0	980													
1	1.00E+04	2	Shale	2365	0	334	1309	2400											
1	1.00E+04	2	Original	3328	0	363	1740	2681											
1	1.00E+04	2	Quartzite	5910	0	387	3000												
1	1.00E+03	2	Shale	2365	0	123	1193												
1	1.00E+03	2	Original	3328	0	124	1669												
1	1.00E+03	2	Quartzite	5910	0	125													
1	5.00E+02	2	Shale	2365	0	87	1186												
1	5.00E+02	2	Original	3328	0	88	1664												
1	5.00E+02	2	Quartzite	5910	0	88													
8	1.00E+04	8	Shale	2365	0	16	33	50	66	82	99	114	200	337	477	618	762	906	1050
8	1.00E+04	8	Original	3328	0	22	42	65	87	105	124	140	264	454	652	853	1057	1261	1466
8	1.00E+04	8	Quartzite	5910	0	30	58	87	113	139	158	172	414	764	1125	1489			
8	1.00E+03	8	Shale	2365	0	10	20	29	39	46	53	56	155	298	447	594	741	888	1034
8	1.00E+03	8	Original	3328	0	11	22	32	41	49	55	59	217	420	627	833			
8	1.00E+03	8	Quartzite	5910	0	12	23	34	43	51	57	60	376	741					
8	5.00E+02	8	Shale	2365	0	8	15	23	29	35	38	42	157	299	446	593			
8	5.00E+02	8	Original	3328	0	8	16	24	30	36	39	42	213	418	626				
8	5.00E+02	8	Quartzite	5910	0	9	16	24	31	36	40	43	372						
5	1.00E+04	8	Shale	2365	0	25	49	75	99	123	147	167	306	523	747	975	1204	1434	1663
5	1.00E+04	8	Original	3328	0	30	63	93	124	152	178	197	400	707	1027	1351	1677		
5	1.00E+04	8	Quartzite	5910	0	41	81	120	155	185	211	227	639	1207	1788				
5	1.00E+03	8	Shale	2365	0	14	27	39	51	61	69	74	244	483	714	948	1182	1413	1646
5	1.00E+03	8	Original	3328	0	14	28	42	53	63	71	75	342	670	1001				
5	1.00E+03	8	Quartzite	5910	0	15	30	43	55	65	72	76	594	1182					
5	5.00E+02	8	Shale	2365	0	10	20	29	38	45	50	53	243	475	711				
5	5.00E+02	8	Original	3328	0	11	21	30	38	46	51	54	337	668					
5	5.00E+02	8	Quartzite	5910	0	11	21	31	39	46	51	55	592						
2	1.00E+05	8	Shale	2365	0	67	143	214	281	353	423	493	846	1409					
2	1.00E+05	8	Original	3328	0	97	192	289	383	476	569	656	1146	1918					

2	1.00E+05	8	Quartzite	5910	0	143	297	441	583	717	840	936	1825			
2	1.00E+04	8	Shale	2365	0	53	107	160	209	254	295	324	692	1240	1806	
2	1.00E+04	8	Original	3328	0	62	122	180	237	287	326	352	914	1705		
2	1.00E+04	8	Quartzite	5910	0	72	140	206	264	313	351	375	1527			
2	1.00E+03	8	Shale	2365	0	23	45	67	86	101	113	120	604	1184		
2	1.00E+03	8	Original	3328	0	24	47	68	87	102	114	121	841			
2	1.00E+03	8	Quartzite	5910	0	24	47	69	88	103	115	122	1479			
2	5.00E+02	8	Shale	2365	0	17	33	48	61	72	81	86	597	1183		
2	5.00E+02	8	Original	3328	0	17	33	49	62	73	81	86	836			
2	5.00E+02	8	Quartzite	5910	0	17	34	49	62	73	81	87				
1	1.00E+05	8	Shale	2365	0	134	274	412	547	675	808	928				
1	1.00E+05	8	Original	3328	0	183	356	537	710	878	1038	1177				
1	1.00E+05	8	Quartzite	5910	0	252	500	745	976	1190	1370	1497				
1	1.00E+04	8	Shale	2365	0	88	175	258	335	406	461	498	1296			
1	1.00E+04	8	Original	3328	0	98	190	281	362	433	488	522	1748			
1	1.00E+04	8	Quartzite	5910	0	105	207	299	384	453	506	539				
1	1.00E+03	8	Shale	2365	0	34	66	96	123	145	161	171	1193			
1	1.00E+03	8	Original	3328	0	34	67	97	124	146	162	172				
1	1.00E+03	8	Quartzite	5910	0	34	67	98	125	146	163	173				
1	5.00E+02	8	Shale	2365	0	24	47	69	88	103	115	122	1186			
1	5.00E+02	8	Original	3328	0	24	48	69	88	103	115	122				
1	5.00E+02	8	Quartzite	5910	0	24	48	69	88	104	115	123				
8	1.00E+03	3	Shale	2365	0	26	50	165	299	446	592	742	888	1034	1181	1327
8	1.00E+03	3	Original	3328	0	28	51	213	418	625	888	1041	1248	1454		
8	1.00E+03	3	Quartzite	5910	0	31	53	372	740	1109						
8	5.00E+02	3	Shale	2365	0	20	36	151	297	445	592	740	887	1033	1180	
8	5.00E+02	3	Original	3328	0	21	37	211	418	625	833	1040	1247			
8	5.00E+02	3	Quartzite	5910	0	22	38	370	740	1109						
5	1.00E+03	3	Shale	2365	0	36	64	243	476	711	999	1180				
5	1.00E+03	3	Original	3328	0	37	66	337	668	946	1331					
5	1.00E+03	3	Quartzite	5910	0	39	68	593	1182							
5	5.00E+02	3	Shale	2365	0	26	47	240	474	711	946	1180				
5	5.00E+02	3	Original	3328	0	27	48	335	668	999	1329					
5	5.00E+02	3	Quartzite	5910	0	28	48	592	1183							

2	1.00E+03	3	Shale	2365	0	59	106	597	1189							
2	1.00E+03	3	Original	3328	0	61	107	836	1666							
2	1.00E+03	3	Quartzite	5910	0	62	108	1484								
2	5.00E+02	3	Shale	2365	0	43	76	600	1184							
2	5.00E+02	3	Original	3328	0	44	76	834								
2	5.00E+02	3	Quartzite	5910	0	44	76									
1	1.00E+03	3	Shale	2365	0	87	151	1199								
1	1.00E+03	3	Original	3328	0	88	152	1664								
1	1.00E+03	3	Quartzite	5910	0	88	153									
1	5.00E+02	3	Shale	2365	0	62	107	1183								
1	5.00E+02	3	Original	3328	0	62	108	1663								
1	5.00E+02	3	Quartzite	5910	0	62	108									
1	1.00E+03	6	Shale	2365	0	45	86	123	151	169	1192					
1	1.00E+03	7	Shale	2365	0	38	75	108	136	157	170	1196				
1	1.00E+03	9	Shale	2365	0	30	59	87	111	133	151	164	171	1196		
8	1.00E+03	4	Shale	2365	0	20	39	53	160	302	448	594	741	887	1035	1181
8	1.00E+03	4	Original	3328	0	21	41	55	217	421	627	834	1041	1247		
8	1.00E+03	4	Quartzite	5910	0	23	43	57	374	714	1110					
8	5.00E+02	4	Shale	2365	0	15	29	39	154	299	445	593	740	887	1034	1180
8	5.00E+02	4	Original	3328	0	16	30	40	212	419	626	832	1040			
8	5.00E+02	4	Quartzite	5910	0	17	31	40	372	740						
5	1.00E+03	4	Shale	2365	0	27	51	69	249	479	713	948	1182	1415		
5	1.00E+03	4	Original	3328	0	28	54	71	342	670	1001	1331				
5	1.00E+03	4	Quartzite	5910	0	30	55	72	596	1184						
5	5.00E+02	4	Shale	2365	0	20	38	50	243	476	711	946	1180			
5	5.00E+02	4	Original	3328	0	21	39	51	337	668	999					
5	5.00E+02	4	Quartzite	5910	0	21	39	51	593	1183						
2	1.00E+03	4	Shale	2365	0	46	85	113	604	1186						
2	1.00E+03	4	Original	3328	0	47	87	114	841	1664						
2	1.00E+03	4	Quartzite	5910	0	48	88	115	1482							
2	5.00E+02	4	Shale	2365	0	33	61	81	597	1183						
2	5.00E+02	4	Original	3328	0	33	62	81	836							
2	5.00E+02	4	Quartzite	5910	0	34	62	81	1478							
1	1.00E+03	4	Shale	2365	0	66	123	161	1192							

1	1.00E+03	4	Original	3328	0	67	124	162	1670						
1	1.00E+03	4	Quartzite	5910	0	67	124	163							
1	5.00E+02	4	Shale	2365	0	48	87	115	1186						
1	5.00E+02	4	Original	3328	0	48	88	115							
1	5.00E+02	4	Quartzite	5910	0	57	88	115							
8	1.00E+03	5	Shale	2365	0	17	32	45	55	156	300	446	594	741	888
8	1.00E+03	5	Original	3328	0	17	34	47	57	220	419	627	834		
8	1.00E+03	5	Quartzite	5910	0	19	36	49	58	373	741				
8	5.00E+02	5	Shale	2365	0	13	24	34	40	152	299	445	593	739	
8	5.00E+02	5	Original	3328	0	13	25	35	41	211	419	626	832		
8	5.00E+02	5	Quartzite	5910	0	13	26	35	41	372	741				
5	1.00E+03	5	Shale	2365	0	22	42	59	71	245	478	715	948	1181	1414
5	1.00E+03	5	Original	3328	0	23	45	61	73	345	672	1000	1332		
5	1.00E+03	5	Quartzite	5910	0	24	46	63	74	598	1184				
5	5.00E+02	5	Shale	2365	0	16	31	44	51	241	476	711	946		
5	5.00E+02	5	Original	3328	0	17	1	45	52	336	668	999			
5	5.00E+02	5	Quartzite	5910	0	17	33	45	53	594					
2	1.00E+03	5	Shale	2365	0	37	70	98	116	600	1183				
2	1.00E+03	5	Original	3328	0	38	72	99	117	844					
2	1.00E+03	5	Quartzite	5910	0	38	73	101	118						
2	5.00E+02	5	Shale	2365	0	26	51	70	83	596	1182				
2	5.00E+02	5	Original	3328	0	27	51	71	83	838					
2	5.00E+02	5	Quartzite	5910	0	27	52	71	84	1479					
1	1.00E+03	5	Shale	2365	0	54	102	141	166	1196					
1	1.00E+03	5	Original	3328	0	54	102	142	167						
1	1.00E+03	5	Quartzite	5910	0	54	103	142	168						
1	5.00E+02	5	Shale	2365	0	38	73	100	118	119					
1	5.00E+02	5	Original	3328	0	38	73	101	118						
1	5.00E+02	5	Quartzite	5910	0	38	73	101	119						

Appendix B – Green’s Functions

Green's Functions for Displacement and Tractions in 2D plane strain from Tadeu & Kausel (2000).

Green's Functions for Displacement (H):

$$H_{xx} = \frac{1}{4i\rho\omega^2}\left[k_s^2 H_{0\beta} - \frac{1}{r}B_1 + \gamma_x^2 B_2\right] \qquad \text{[Equation A-1]}$$

$$H_{yy} = \frac{1}{4i\rho\omega^2}\left[k_s^2 H_{0\beta} - \frac{1}{r}B_1 + \gamma_y^2 B_2\right] \qquad \text{[Equation A-2]}$$

$$H_{xy} = H_{yx} = \frac{1}{4i\rho\omega^2}\left[\gamma_x \gamma_y B_2\right] \qquad \text{[Equation A-3]}$$

Green's Functions for Tractions (G):

$$\varepsilon_{vol}^{l} = \gamma_l \frac{1}{4i\rho\omega^2}\left[-k_s^2 k_\beta H_{1\beta} + \frac{4}{r}B_2 - B_3\right] \qquad \text{[Equation A-4]}$$

$$\varepsilon_{xx}^{l} = \gamma_l \frac{1}{4i\rho\omega^2}\left[(\frac{2}{r}B_2 - k_s^2 k_\beta H_{1\beta})\delta_{xl} + \frac{1}{r}B_2 - \gamma_x^2 B_3\right] \qquad \text{[Equation A-5]}$$

$$\varepsilon_{yy}^{l} = \gamma_l \frac{1}{4i\rho\omega^2}\left[(\frac{2}{r}B_2 - k_s^2 k_\beta H_{1\beta})\delta_{yl} + \frac{1}{r}B_2 - \gamma_y^2 B_3\right] \qquad \text{[Equation A-6]}$$

$$G_{ij}^{l} = \lambda \varepsilon_{vol}^{l} \delta_{ij} + 2\mu \varepsilon_{ij}^{l} \qquad \text{[Equation A-7]}$$

Auxiliary Functions and Definitions:

$$B_n = k_\beta^n H_{n\beta} - k_\alpha^n H_{n\alpha} \qquad \text{[Equation A-8]}$$

$$H_{ni} = H_n^{(2)}(k_i r)\ (i = \alpha, \beta) \qquad \text{[Equation A-9]}$$

$$\gamma_i = \frac{x_i}{r}\ \ (i = 1, 2)(1 = x, 2 = y) \qquad \text{[Equation A-10]}$$

$$r = \sqrt{x^2 + y^2} \qquad \text{[Equation A-11]}$$

$$k_\alpha = \frac{\omega}{\alpha} \qquad \text{[Equation A-12]}$$

$$k_\beta = \frac{\omega}{\beta} \qquad \text{[Equation A-13]}$$

$$\alpha = \sqrt{\frac{\lambda + 2\mu}{\rho}} \qquad \text{[Equation A-14]}$$

$$\beta = \sqrt{\frac{\mu}{\rho}} \qquad \text{[Equation A-15]}$$

H_n^2 = second Hankel function of order (n); α = P-wave velocity; β = S-wave velocity; δ_{ij} = Kronecker delta function (i = 1,2; j=1,2); l = direction of load (l=1,2); λ = Lame's constant; μ = Shear Modulus, ρ = density.

Green’s Functions for Displacement in 2D plane strain from (Dominguez, 1993).

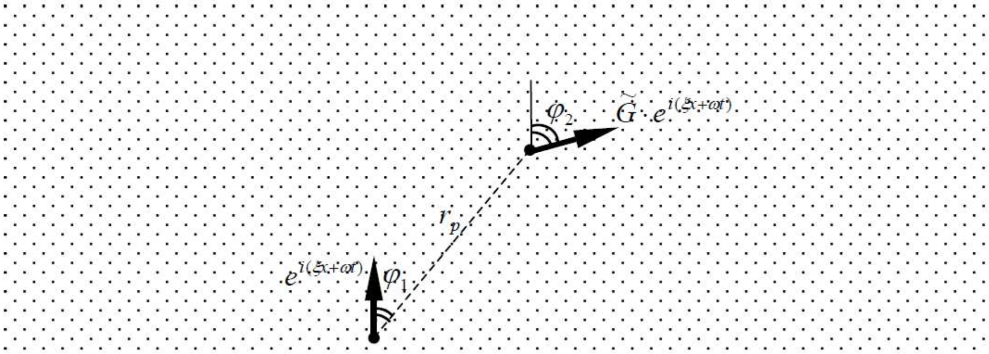

Figure B1 Schematic of equation parameters for Green’s Functions from (Dominguez, 1993). *From* Hussein (2004) *Figure D.1*

$$\begin{aligned}\tilde{G}(\omega, r, \varphi_1, \varphi_2) = \frac{1}{2\pi\beta^2\rho}&[-0.5\chi\sin 2\varphi_1 sin\,\varphi_2 + \psi cos\varphi_2 \\ &- \chi cos^2\varphi_1 cos\varphi_1]\end{aligned} \qquad \text{[Equation A-16]}$$

$$\psi = H_0^{(2)}\left(\frac{i\omega r}{\beta}\right) + \left(\frac{\beta}{i\omega r}\right)\left[H_1^{(2)}\left(\frac{i\omega r}{\beta}\right) - \frac{\beta}{\alpha}H_1^{(2)}\left(\frac{i\omega r}{\alpha}\right)\right] \qquad \text{[Equation A-17]}$$

$$\chi = H_2^{(2)}\left(\frac{i\omega r}{\beta}\right) - \left(\frac{\beta^2}{\alpha^2}\right)H_2^{(2)}\left(\frac{i\omega r}{\alpha}\right) \qquad \text{[Equation A-18]}$$

Where φ_{l} is the angle of the impulse (1) and response (2) from vertical. Other variables have the definitions shown for equations from Tadeu and Kausel (2000).

Appendix C – Moving Load FISH Function

```
;Fish Function for Moving Load in UDEC Model

def _pos
 whilestepping
 _v=100 ;velocity of load
 _a=0.0001
 _pos1=(time*_v)-10
 _pos2=((time-_a)*_v)-10
 _pos3=((time-(2*_a))*_v)-10
 _pos4=((time-(3*_a))*_v)-10
 _pos5=((time-(4*_a))*_v)-10
 _pos6=((time-(5*_a))*_v)-10
 _pos7=((time-(6*_a))*_v)-10
 _pos8=((time-(7*_a))*_v)-10
 _pos9=((time-(8*_a))*_v)-10
 _pos10=((time-(9*_a))*_v)-10
 _pos11=((time-(10*_a))*_v)-10
 _pos12=((time-(11*_a))*_v)-10
 _pos13=((time-(12*_a))*_v)-10
 _pos14=((time-(13*_a))*_v)-10
 _pos15=((time-(14*_a))*_v)-10
 _pos16=((time-(15*_a))*_v)-10
 _pos17=((time-(16*_a))*_v)-10
 _pos18=((time-(17*_a))*_v)-10
 _pos19=((time-(18*_a))*_v)-10
 _pos20=((time-(19*_a))*_v)-10
 if _pos1>-10 then
  command
   boundary interior yload -0.024471742 range annulus (_pos1,-100) 0 0.1
 endcommand
 endif
 if _pos2>-10 then
  command
   boundary interior yload -0.071019761 range annulus (_pos2,-100) 0 0.1
 endcommand
 endif
 if _pos3>-10 then
  command
   boundary interior yload -0.110615871 range annulus (_pos3,-100) 0 0.1
 endcommand
 endif
 if _pos4>-10 then
  command
   boundary interior yload -0.139384129 range annulus (_pos4,-100) 0 0.1
 endcommand
 endif
 if _pos5>-10 then
  command
   boundary interior yload -0.154508497 range annulus (_pos5,-100) 0 0.1
 endcommand
 endif
```

```
if _pos6>-10 then
 command
  boundary interior yload -0.154508497 range annulus (_pos6,-100) 0 0.1
endcommand
endif
if _pos7>-10 then
 command
  boundary interior yload -0.139384129 range annulus (_pos7,-100) 0 0.1
endcommand
endif
if _pos8>-10 then
 command
  boundary interior yload -0.110615871 range annulus (_pos8,-100) 0 0.1
endcommand
endif
if _pos9>-10 then
 command
  boundary interior yload -0.071019761 range annulus (_pos9,-100) 0 0.1
endcommand
endif
if _pos10>-10 then
 command
  boundary interior yload -0.024471742 range annulus (_pos10,-100) 0 0.1
endcommand
endif
if _pos11>-10 then
 command
  boundary interior yload 0.024471742 range annulus (_pos11,-100) 0 0.1
endcommand
endif
if _pos12>-10 then
 command
  boundary interior yload 0.071019761 range annulus (_pos12,-100) 0 0.1
endcommand
endif
if _pos13>-10 then
 command
  boundary interior yload 0.110615871 range annulus (_pos13,-100) 0 0.1
endcommand
endif
if _pos14>-10 then
 command
  boundary interior yload 0.139384129 range annulus (_pos14,-100) 0 0.1
endcommand
endif
if _pos15>-10 then
 command
  boundary interior yload 0.154508497 range annulus (_pos15,-100) 0 0.1
endcommand
endif
if _pos16>-10 then
```

```
  command
   boundary interior yload 0.154508497 range annulus (_pos16,-100) 0 0.1
 endcommand
 endif
 if _pos17>-10 then
  command
   boundary interior yload 0.139384129 range annulus (_pos17,-100) 0 0.1
 endcommand
 endif
 if _pos18>-10 then
  command
   boundary interior yload 0.110615871 range annulus (_pos18,-100) 0 0.1
 endcommand
 endif
 if _pos19>-10 then
  command
   boundary interior yload 0.071019761 range annulus (_pos19,-100) 0 0.1
 endcommand
 endif
 if _pos20>-10 then
  command
   boundary interior yload 0.024471742 range annulus (_pos20,-100) 0 0.1
 endcommand
 endif
end
```